

January 2013

# Synthesis of Titanium Dioxide Photocatalyst with the Aid of Supercritical Fluids

Haitao Li

University of South Florida, hli7@mail.usf.edu

Follow this and additional works at: <http://scholarcommons.usf.edu/etd>

 Part of the [Chemical Engineering Commons](#)

---

## Scholar Commons Citation

Li, Haitao, "Synthesis of Titanium Dioxide Photocatalyst with the Aid of Supercritical Fluids" (2013). *Graduate Theses and Dissertations*.

<http://scholarcommons.usf.edu/etd/4912>

This Dissertation is brought to you for free and open access by the Graduate School at Scholar Commons. It has been accepted for inclusion in Graduate Theses and Dissertations by an authorized administrator of Scholar Commons. For more information, please contact [scholarcommons@usf.edu](mailto:scholarcommons@usf.edu).

Synthesis of Titanium Dioxide Photocatalyst  
with the Aid of Supercritical Fluids

by

Haitao Li

A dissertation submitted in partial fulfillment  
of the requirements for the degree of  
Doctor of Philosophy  
Department of Chemical and Biomedical Engineering  
College of Engineering  
University of South Florida

Major Professor: Aydin Sunol, Ph.D.  
Sermin Sunol, Ph.D.  
Abla Zayed, Ph.D.  
John Kuhn, Ph.D.  
Mike Zaworotko, Ph.D.  
Vinay Gupta, Ph.D.

Date of Approval:  
November 20, 2013

Keywords: titania, aerogel, nanostructure, visible light, photocatalytic degradation

Copyright © 2013, Haitao Li

## **DEDICATION**

Dedicated to My Mom and My Brother who I love most.

## **ACKNOWLEDGMENTS**

This project would not have been possible without the support of many people. Special sincere gratitude and thanks go to Dr. Aydin Sunol, and Dr. Sermin Sunol their continuous guidance, moral support, especially in my toughest time in USF. Special thanks to the late Dr. John Wolan. I would like to express my gratitude to my lab colleagues who have helped and supported me throughout my project: Raquel, Brandon, Keyer, Wade, Nada, and Rosanna. Also thanks to my committee members, Dr. Abla Zayed, Dr. Vinay Gupta, Dr. John Kuhn, and Dr. Mike Zoworanko, who offered guidance and support. Finally, thanks to my wife, sons, parents, and numerous friends who endured this long process with me, and always offer support and love.

## TABLE OF CONTENTS

LIST OF TABLES	iv
LIST OF FIGURES	vi
ABSTRACT	xii
CHAPTER 1: INTRODUCTION	1
1.1 Introduction	1
1.2 Objectives	8
CHAPTER 2: BACKGROUND: HETEROGENEOUS PHOTOCATALYST	11
2.1 Mechanism of Photocatalysis	13
2.2 Affecting Factors of Photocatalysis	18
2.2.1 Intrinsic Factors	19
2.2.1.1 Particle Size	19
2.2.1.2 Surface Area	21
2.2.1.3 Crystal Structure and Properties	22
2.2.2 Extrinsic Factors	27
2.3 Titanium Dioxide Photocatalyst	30
2.3.1 Introduction of Titanium Dioxide	30
2.3.2 Improving Photocatalytic Activity of TiO <sub>2</sub>	36
CHAPTER 3: BACKGROUND: SUPERCRITICAL FLUIDS AND SOL-GEL	54
3.1 Supercritical Fluid Technology	54
3.1.1 Properties of Supercritical Fluids	56
3.1.2 Supercritical Fluid Extraction and Drying	59
3.1.3 Supercritical Fluid Impregnation	62
3.1.4 Solubility in Supercritical Fluids	64
3.2 Sol-gel Technology	72
3.2.1 Sol-gel Chemistry	73
3.2.2 Aging and Heat Treatment	76
3.2.3 Surfactant Templates	79
CHAPTER 4: EXPERIMENTAL	83
4.1 Sol-gel Preparation	83
4.1.1 Titanium Dioxide Sol-gel Preparation	84
4.1.2 Co-precipitated Titanium Dioxide/Tungsten Oxide Sol-gel Preparation	88
4.1.3 Co-precipitated Titanium Dioxide/Tungsten Oxide/Iron Ion Sol-gel Preparation	89

4.2 Supercritical Fluids Extraction and Drying	92
4.2.1 Experimental Setup	92
4.2.2 Experimental Procedure for Supercritical Fluids Extraction and Drying	95
4.3 Supercritical Impregnation	96
4.3.1 Experimental Setup	96
4.3.2 Experimental Procedure for Supercritical Impregnation	97
4.4 Heat Treatment	101
4.5 Photocatalyst Characterization	103
4.5.1 Nitrogen Physisorption Measurement	104
4.5.2 Scanning Electron Microscopy (SEM), Energy Dispersion Spectroscopy (EDS) and Focused Ion Beam (FIB)	108
4.5.3 X-ray Diffraction (XRD)	109
4.5.4 X-ray Photoelectron Spectroscopy (XPS)	111
4.5.5 Diffuse Reflectance Spectroscopy (DRS)	111
4.6 Photocatalytic Activity	112
4.6.1 Under UV Light	114
4.6.2 Under Visible Light	116
4.6.3 UV-Vis Spectroscopy	117
CHAPTER 5: PHOTOCATALYST PREPARATION RESULTS AND DISCUSSION	119
5.1 TiO <sub>2</sub> Aerogel Preparation	120
5.1.1 Effect of Composition	120
5.1.2 Effect of Aging	127
5.1.3 Effect of Sol-gel Drying Conditions	129
5.1.4 Heat Treatment	135
5.1.5 XPS Survey	137
5.2 Co-precipitated Aerogel Preparation	139
5.2.1 TiO <sub>2</sub> /WO <sub>3</sub> Co-precipitated Aerogel	139
5.2.2 TiO <sub>2</sub> /Fe <sup>3+</sup> Co-precipitated Aerogel	142
5.2.3 TiO <sub>2</sub> /WO <sub>3</sub> /Fe <sup>3+</sup> Co-precipitated Aerogel	143
5.3 Supercritical Impregnation	149
CHAPTER 6: PHOTOCATALYST CHARACTERIZATION AND PHOTOCATALYTIC ACTIVITY RESULTS AND DISCUSSION	162
6.1 Photocatalyst Characterization	162
6.1.1 Crystal Structure	163
6.1.1.1 Templated Pure TiO <sub>2</sub> Photocatalyst	163
6.1.1.2 Co-precipitated TiO <sub>2</sub> /WO <sub>3</sub> /Fe <sup>3+</sup> Aerogel	165
6.1.1.3 Supercritical Impregnated TiO <sub>2</sub> /WO <sub>3</sub> /Fe <sup>3+</sup> Aerogel	167
6.1.2 Band gap	168
6.2 Photocatalytic Activity	172
6.2.1 Under UV Light	173
6.2.2 Under Visible Light	177
6.2.3 Supercritical Impregnated Aerogel Photocatalysts	178
6.2.4 Kinetics of Photocatalytic Reaction	180
CHAPTER 7: CONCLUSIONS AND RECOMMENDATIONS	182
7.1 Conclusions	182
7.2 Recommendations	184

REFERENCES	186
APPENDICES	203
Appendix A: Nomenclature	204
Appendix B: Textural Properties Analysis Results	207
Appendix C: Additional XPS Surveys Patterns	212
Appendix D: Additional SEM/FIB Images	214
Appendix E: Additional XRD Patterns	220
Appendix F: Photocatalytic Activity Evaluation	222

## LIST OF TABLES

Table 2.1	Some Bulk Properties of the Three Main Polymorphs of TiO <sub>2</sub> (Anatase, Rutile, Brookite)	22
Table 3.1	Properties of Gases, Supercritical Fluids and Liquids	57
Table 3.2	Mole Fraction Solubility (x) of Transition Metal Complexes in Supercritical CO <sub>2</sub>	67
Table 4.1	Possible Residue Chemicals Left in Aerogel after Supercritical Extraction and Drying	102
Table 5.1	Textural Properties for Degussa P25, Sigma-Aldrich 99% Pure TiO <sub>2</sub> Powder and Two Templated TiO <sub>2</sub> Aerogel with Different Ethanol Usage	121
Table 5.2	Gelation Time and SSA for Templated TiO <sub>2</sub> Aerogels with Different HNO <sub>3</sub> Addition	124
Table 5.3	Textural Properties for Regular TiO <sub>2</sub> Aerogel and Templated TiO <sub>2</sub> Aerogel (Uncalcined and Calcined)	125
Table 5.4	Textural Properties for Templated TiO <sub>2</sub> Aerogel with Different Aging Time (Uncalcined)	127
Table 5.5	Observed Cloud Point Pressures of Triton X-114 Mixtures	132
Table 5.6	Textural Properties for Templated TiO <sub>2</sub> Aerogel with Different CO <sub>2</sub> Flow Rate (Uncalcined)	135
Table 5.7	Textural Properties for Templated TiO <sub>2</sub> Aerogel after Calcination	136
Table 5.8	Textural Properties for Regular TiO <sub>2</sub> /WO <sub>3</sub> 3 mol% Aerogel and Templated TiO <sub>2</sub> /WO <sub>3</sub> 3 mol% Aerogel (Uncalcined and Calcined)	140
Table 5.9	Textural Properties for Templated TiO <sub>2</sub> /Fe <sup>3+</sup> 3 mol% Aerogel (Uncalcined and Calcined)	143
Table 5.10	Textural Properties for Templated TiO <sub>2</sub> /3%WO <sub>3</sub> /Fe <sup>3+</sup> Aerogel with Different Amount of Iron Ion (Uncalcined and Calcined)	144
Table 5.11	Ferrocene Solubility in Supercritical Carbon Dioxide	150
Table 5.12	Textural Properties of Different Titania Based Photocatalysts under Different Conditions	151

Table 6.1	FWHM of Photocatalyst Samples at Anatase Phase Diffraction Peak and Anatase/Rutile Phase Ratio	165
Table 6.2	Bang-gap of Different Photocatalysts (Co-precipitated)	169
Table 6.3	Bang-gap of Different Photocatalysts (Supercritical Impregnated)	171

## LIST OF FIGURES

Figure 2.1	Schematic Description of the Change in a Catalytic Reaction Pathway	12
Figure 2.2	Main Processes in Semiconductor Photocatalysis: (A) Photon Absorption and Electron-Hole Generation; (B) Oxidation of Donor ( $D_{ads}$ ); (C) Reduction of Acceptor ( $A_{ads}$ ); and, (D) Electron-Hole Recombination at Surface and in Bulk.	15
Figure 2.3	3D Balls and Sticks Models of Anatase and Rutile Atomic Structures	23
Figure 2.4	Band Edge Position of Common Semiconductor Photocatalyst in Contact at pH=1	27
Figure 2.5	Photoinduced Processes on $TiO_2$	31
Figure 2.6	Energy Diagrams Illustrating $TiO_2$ Doped with Pt	39
Figure 2.7	Energy Diagrams Illustrating $TiO_2$ Doped with Anion under UV and Visible Light	41
Figure 2.8	Energy Diagrams Illustrating $TiO_2$ Doped with Iron Ions under UV and Visible Light	47
Figure 2.9	Schematic Representation of Charge Carrier Separation in the Photoexcited $WO_3/TiO_2$ Photocatalyst	49
Figure 2.10	Possible Mechanisms for Transition Electron Transfers Involving Composite Semiconductor Catalyst and Transition Metal Ion	53
Figure 3.1	Phase Diagram for Carbon Dioxide ( $CO_2$ )	55
Figure 3.2	Schematic Diagram for Sol-gel Routes, Preparation of Metal Oxide Gel through Sol-gel Method	74
Figure 4.1	Schematic Diagram for Synthesizing and Processing Templated Titanium Dioxide Sol-gel	85
Figure 4.2	Basic Properties of the Templating Surfactant Triton X-114	86
Figure 4.3	Schematic Diagram for Synthesizing and Processing Templated Co-precipitated Titanium Dioxide/Tungsten Oxide ( $TiO_2/WO_3$ ) Sol-gel	90

Figure 4.4	Schematic Diagram for Synthesizing and Processing Templated Coprecipitated Titanium Dioxide/Tungsten Oxide/Iron(III) Ion ( $\text{TiO}_2/\text{WO}_3/\text{Fe}^{3+}$ ) Sol-gel	91
Figure 4.5	Prepared Template $\text{TiO}_2$ Based Sol-gel Samples	92
Figure 4.6	Supercritical Fluid Extraction and Drying Pilot Plant	94
Figure 4.7	Basic Information of Ferrocene (Iron Ion Precursor)	97
Figure 4.8	Supercritical Impregnation Pilot Plant	98
Figure 4.9	Supercritical Impregnation Processes (a) Continuous Process; (b) Batch Process	100
Figure 4.10	Designed Sample Calcination Device in Horizontal Position	102
Figure 4.11	3-stage Aerogel Calcination Schedule	103
Figure 4.12	Quantachrome Autosorb-1C	105
Figure 4.13	Methylene Blue Chemical Structure	113
Figure 4.14	Batch Reactor for Photocatalytic Experiment under UV Light	115
Figure 4.15	Measured UV-A Light Intensity vs. Distance	115
Figure 4.16	Batch Reactor for Photocatalytic Experiment under Visible Light	116
Figure 4.17	Intensity Distribution of UV-A Lamp and Mercury Lamp with UV Cut-off Filter	117
Figure 5.1	SSA, APV and APD of Degussa P25, Sigma-Aldrich 99% Pure $\text{TiO}_2$ and Two Templated $\text{TiO}_2$ Aerogel Prepared with Different Ethanol Usage (A,B,C,and D)	121
Figure 5.2	Pore Size Distribution of Two Templated $\text{TiO}_2$ Aerogels With Different Ethanol to Solid Ratios (30:1 for A and B, 20:1 for C and D)	123
Figure 5.3	SSA, APV and APD of Regular $\text{TiO}_2$ Aerogel and Templated $\text{TiO}_2$ Aerogel (Uncalcined and Calcined)	126
Figure 5.4	Pore Size Distribution of Regular $\text{TiO}_2$ Aerogel (Uncalcined and Calcined)	126
Figure 5.5	SSA, APV and APD of Templated $\text{TiO}_2$ Aerogel with Different Aging Time (Uncalcined)	128
Figure 5.6 (a)	$\text{TiO}_2$ Templated Uncalcined Aerogel (Left) and Xerogel (Right) SEM Images	130
Figure 5.6 (b)	$\text{TiO}_2$ Templated Calcined Aerogel (Left) and Xerogel (Right) SEM Images	131

Figure 5.7	Mass Balance Calculations with Different CO <sub>2</sub> Flow Rate	134
Figure 5.8	SSA, APV and APD of Templated TiO <sub>2</sub> Aerogel before Calcination and after Calcination at Different Temperature	137
Figure 5.9	XPS Elemental Survey of Different Sample (a) Degussa P25; (b) Calcined Templated TiO <sub>2</sub> Aerogel	138
Figure 5.10	Textural Properties for Regular TiO <sub>2</sub> /WO <sub>3</sub> 3 mol% Aerogel and Templated TiO <sub>2</sub> /WO <sub>3</sub> 3 mol% Aerogel (Uncalcined and Calcined)	140
Figure 5.11	Pore Size Distribution of Regular TiO <sub>2</sub> /WO <sub>3</sub> 3 mol% Aerogel and Templated TiO <sub>2</sub> /WO <sub>3</sub> 3 mol% Aerogel (Uncalcined and Calcined)	141
Figure 5.12	XPS Elemental Survey of Calcined Co-precipitated TiO <sub>2</sub> /WO <sub>3</sub> Aerogel	142
Figure 5.13	Textural Properties of Templated TiO <sub>2</sub> /3%WO <sub>3</sub> /Fe <sup>3+</sup> Aerogel with Different Amount of Iron Ion (Uncalcined and Calcined)	144
Figure 5.14	Pore Size Distribution of Templated TiO <sub>2</sub> /3%WO <sub>3</sub> /3%Fe <sup>3+</sup> Aerogel before and after Calcination at 450 °C, 550 °C and 750 °C	145
Figure 5.15	Isotherm Plots of Uncalcined Templated Co-precipitated TiO <sub>2</sub> /WO <sub>3</sub> /Fe <sup>3+</sup> Aerogel	146
Figure 5.16	SEM-FIB Images of Templated Co-precipitated Aerogel Photocatalyst at Varying Magnifications	147
Figure 5.17	Textural Properties of Different Titania Based Photocatalysts under Different Conditions	151
Figure 5.18	SEM-FIB Images of Templated Supercritical Impregnated Aerogel Photocatalyst at Varying Magnifications	153
Figure 5.19(a)	EDS Elemental Analysis of Uncalcined TiO <sub>2</sub> /WO <sub>3</sub> Aerogel after Supercritical Impregnation with Ferrocene (Calcined)	158
Figure 5.19(b)	EDS Elemental Analysis of Calcined TiO <sub>2</sub> /WO <sub>3</sub> Aerogel after Supercritical Impregnation with Ferrocene (Calcined)	159
Figure 5.20(a)	SEM-EDS Elements Mapping Images of Uncalcined TiO <sub>2</sub> /WO <sub>3</sub> Aerogel after Supercritical Impregnation with Ferrocene (Calcined)	160
Figure 5.20(b)	SEM-EDS Elements Mapping Images of Calcined TiO <sub>2</sub> /WO <sub>3</sub> Aerogel after Supercritical Impregnation with Ferrocene (Calcined)	161
Figure 6.1	XRD Patterns of Uncalcined Templated TiO <sub>2</sub> Aerogel	163
Figure 6.2	XRD Patterns of Calcined Aerogel and Xerogel	164
Figure 6.3	XRD Patterns of Photocatalyst Samples.	166

Figure 6.4	XRD Patterns of Co-precipitated TiO <sub>2</sub> /WO <sub>3</sub> /Fe <sup>3+</sup> Aerogel Photocatalyst Samples Calcined at Different Temperatures	167
Figure 6.5	XRD Patterns of Co-precipitated TiO <sub>2</sub> /WO <sub>3</sub> /Fe <sup>3+</sup> Aerogel Photocatalyst and Supercritical Impregnated TiO <sub>2</sub> /WO <sub>3</sub> /Fe <sup>3+</sup> Aerogel Photocatalyst	168
Figure 6.6	Diffuse Reflectance Spectra of Different Photocatalysts	169
Figure 6.7	Diffuse Reflectance Spectra of Co-precipitated TiO <sub>2</sub> /WO <sub>3</sub> with Different Amount of Iron	170
Figure 6.8	Diffuse Reflectance Spectra of Co-precipitated TiO <sub>2</sub> /WO <sub>3</sub> /Fe <sup>3+</sup> with Different Calcination Temperatures	171
Figure 6.9	Diffuse Reflectance Spectra of Supercritical Impregnated TiO <sub>2</sub> /WO <sub>3</sub> /Fe <sup>3+</sup> with Different TiO <sub>2</sub> /WO <sub>3</sub> Conditions	172
Figure 6.10	Calibration Curve for Methylene Blue Absorption Peak at 297nm in UV-Vis Spectrum	173
Figure 6.11	Typical UV-Vis Absorbance Peak of MB (wavelength = 297nm) Reduction during Photodegradation under UV Light	174
Figure 6.12	Color Fading of MB Solution during Photodegradation under UV Light	174
Figure 6.13	Methylene Blue Degradation under UV Light (P25 and Co-precipitated Aerogel)	175
Figure 6.14	Methylene Blue Degradation under Visible Light (P25 and Co-precipitated Aerogel)	178
Figure 6.15	Methylene Blue Degradation under UV Light (P25, Supercritical Impregnated Aerogel and Co-precipitated Aerogel)	179
Figure 6.16	Methylene Blue Degradation under Visible Light (P25, Supercritical Impregnated Aerogel and Co-precipitated Aerogel)	179
Figure 6.17	Kinetics of Photodegradation of MB with Different Photocatalysts under (a) UV Light; (b) Visible Light	180
Figure B.1	BET and BJH Plots of TiO <sub>2</sub> Aerogel after Aging 120 Hours	207
Figure B.2	BET and BJH Plots of TiO <sub>2</sub> Aerogel after Supercritical Extraction and Drying (8 hours @ R <sub>CO2</sub> = 5 ml/min)	208
Figure B.3	BJH Pore Size Distribution Plots of TiO <sub>2</sub> Aerogel at Different Calcination Temperature (a: 350 °C; b: 400 °C; c: 450 °C)	209
Figure B.4	BJH Pore Size Distribution Plots of TiO <sub>2</sub> /Fe <sup>3+</sup> 3 mol% Aerogel (Uncalcined (Red) and Calcined (Blue))	210

Figure B.5	BJH Pore Size Distribution Plots of $\text{TiO}_2/3\%\text{WO}_3/\text{Fe}^{3+}$ Aerogel with Different Amount of Iron ion (1% (Red), 3% (Blue), and 5% (Green))	210
Figure B.6	BJH Pore Size Distribution Plots of Different Titania Based Photocatalysts under Different Conditions ( $\text{TiO}_2/\text{WO}_3$ Uncalcined+SFI Uncalcined(Red), $\text{TiO}_2/\text{WO}_3$ Uncalcined+SFI Calcined (Blue), $\text{TiO}_2/\text{WO}_3$ Calcined+SFI Uncalcined (Green) and $\text{TiO}_2/\text{WO}_3$ Calcined+SFI Calcined(Orange))	211
Figure C.1	XPS High Resolution Elemental Survey of Sol-gel Synthesized $\text{TiO}_2$ Aerogel	212
Figure D.1	SEM-FIB Images of Templated Co-precipitated Aerogel Photocatalyst at Varying Magnifications and Processes	214
Figure D.2	SEM-FIB Images of Templated Supercritical Impregnated Aerogel Photocatalyst at Varying Magnifications	216
Figure E.1	XRD Pattern of Degussa P25	220
Figure E.2	XRD Pattern of Co-precipitated $\text{TiO}_2/\text{WO}_3/\text{Fe}^{3+}$ Aerogel after Calcination at 450 °C	220
Figure E.3	XRD Pattern of Co-precipitated $\text{TiO}_2/\text{WO}_3/\text{Fe}^{3+}$ Aerogel after Calcination at 550 °C	221
Figure E.4	XRD Pattern of Supercritical Impregnated $\text{TiO}_2/\text{WO}_3/\text{Fe}^{3+}$ Aerogel after Calcination	221
Figure F.1	Methylene Blue Degradation under UV Light with P25	222
Figure F.2	Methylene Blue Degradation under UV Light with $\text{TiO}_2$ Aerogel	222
Figure F.3	Methylene Blue Degradation under UV Light with $\text{TiO}_2/\text{WO}_3$ Aerogel	223
Figure F.4	Methylene Blue Degradation under UV Light with $\text{TiO}_2/\text{Fe}^{3+}$ Aerogel	223
Figure F.5	Methylene Blue Degradation under UV Light with Co-precipitated $\text{TiO}_2/\text{WO}_3/\text{Fe}^{3+}$ Aerogel	224
Figure F.6	Methylene Blue Degradation under UV Light with Supercritical Impregnated $\text{TiO}_2/\text{WO}_3/\text{Fe}^{3+}$ Aerogel	224
Figure F.7	Methylene Blue Degradation under Visible Light with P25	225
Figure F.8	Methylene Blue Degradation under Visible Light with $\text{TiO}_2$ Aerogel	225
Figure F.9	Methylene Blue Degradation under Visible Light with $\text{TiO}_2/\text{WO}_3$ Aerogel	226
Figure F.10	Methylene Blue Degradation under Visible Light with $\text{TiO}_2/\text{Fe}^{3+}$ Aerogel	226

Figure F.11	Methylene Blue Degradation under Visible Light with Co-precipitated TiO <sub>2</sub> /WO <sub>3</sub> /Fe <sup>3+</sup> Aerogel	227
Figure F.12	Methylene Blue Degradation under Visible Light with Supercritical Impregnated TiO <sub>2</sub> /WO <sub>3</sub> /Fe <sup>3+</sup> Aerogel	227

## ABSTRACT

Titanium Dioxide ( $\text{TiO}_2$ ) emerged as one of the most popular photocatalysts since 1970's. However, its photocatalytic activity requires UV irradiation due to its large band gap unless further functionalization or modifications are performed. Furthermore, recovery issue has always been a major drawback, if the more effective form nano particles are utilized.

The key objectives of this research were synthesizing new  $\text{TiO}_2$  based photocatalyst systems that are effective with both the UV and the visible light while utilizing novel superior environmentally friendly techniques enabling development of nano-structured photocatalysts that can be easily recovered. In this dissertation research, highly porous nano-structured  $\text{TiO}_2/\text{WO}_3/\text{Fe}^{3+}$  aerogel composite photocatalyst are prepared, characterized, and tested for model photocatalytic reactions. The photocatalyst structure is tailored to capture environmental pollutants and enable their decomposition in-situ under both UV and visible light through photodecomposition to smaller benign substances.

A novel and green method is applied to prepare unique surfactant templated aerogel photocatalysts with highly porous nano-structure, high surface area, and tailored pore size distribution. Sol-gel process followed by supercritical fluids extraction and drying allowed synthesis of highly porous composite  $\text{TiO}_2/\text{WO}_3$  aerogel. The surfactant template was completely removed with the aid of a supercritical solvent mixture followed with heat treatment.  $\text{Fe}^{3+}$  ion was incorporated within the composite aerogel photocatalyst as dopant either at the sol-gel co-precipitation step or at a subsequent supercritical impregnation process. Supercritical drying followed with heat treatment results in titanium dioxide with the most profound anatase crystal structure. Neutral templates were used to further enhance retention and tuning of the

nano-pore structure and the surface properties. The Nitrogen adsorption-desorption isotherms methods were used to follow the removal of solvents and templates as well as tracking the textural properties of the synthesized aerogel. Surfactant-templated aerogels, which show remarkable thermal stability and uniform pore size distribution, exhibit specific surface areas three times more than the highly optimized commercial nano-particles, industry standard TiO<sub>2</sub> photocatalyst *Degussa P-25*, even after heat treatment.

The synthesized catalysts were characterized by using SEM, FIB, EDS, XRD, XPS and porosimetry prior to post photocatalytic activity evaluation through a model photocatalytic reaction. The band gaps of the catalysts were also determined by using diffuse reflectance spectroscopy.

The model reaction employed Methylene Blue (MB) photo-oxidation under UV and visible light. Resulting aerogel TiO<sub>2</sub>/WO<sub>3</sub>/Fe<sup>3+</sup> photocatalyst exhibited comparable photocatalytic capability to Degussa P25 under UV light exposure and offered much superior photocatalytic capability under visible light exposure.

## CHAPTER 1

### INTRODUCTION

#### 1.1 Introduction

Photocatalyst, one of the most important components and special types of the catalyst family, had a phenomenal growth since its first introduced and described by Plotnikov in 1930's [1]. According to a new technical market research report [2], the global market value for photocatalysts was an estimated \$847.5 million in 2009, but is expected to increase to nearly \$1.7 billion in 2014, for a 5-year Compound Annual Growth Rate (CAGR) of 14.3%. Photocatalysts, also known as a class of semiconductors, can be irradiated by light with higher energy than their band gaps. The excited energy-rich electron-hole pairs result in direct production of photo-electricity (such as in solar cells), or the electron-hole pairs can be used to activate oxidative chemical reactions, with such reactants characterized by superior oxidizing properties and super-hydrophilicity. Photocatalyst offers various pathways to water decontamination [3, 4], air disinfection [5, 6], decomposition of crude oil spills [7, 8], reduction of carbon dioxide with water [9], self-cleaning green construction [10], and even hydrogen generation from water splitting [11]. This research focused on use of photocatalysis for destruction of environmentally hazardous compounds. Unlike costly and difficult removal and isolation of toxic chemicals, photocatalysis leads to destruction of toxic through degradation at ambient temperature and pressure, through use of readily available materials and established techniques. By comparison, photocatalysis is inexpensive and low energy consumption, and is applicable to a wide range of pollutants (VOC, bacteria, and mold) make this class of catalyst attractive for a portfolio of environmental applications.

Titanium dioxide photocatalyst dates back to the 1970s [12] and has been the subject of various nanocrystalline photocatalytic materials research studies summarized in many reviews [13–28]. The popularity of titanium oxide photocatalysts is due to its commercial availability, non-toxicity, chemical inertness, environmental benignity and biocompatibility as well as high photocatalytic activity. Because it is considered as an ideal photocatalyst, there has been continuous interest and academia and industry has consistently attempted to improve its photocatalytic activity (PCA) and explore new applications in various applicable areas since the 1970's.

Material properties such as surface area, pore size, particle size and crystal structure and properties are responsible for its photocatalytic performance.  $\text{TiO}_2$  based photocatalysts with various morphologies including nanotubes [29,30], nano-spheres [31,32], nanowires [33-35], nano-rods [36-38], nano-ribbons [39,40] and films [41, 42] have been successfully synthesized via different routes and developed with outstanding performance in diverse areas ranging from environmental treatment to clean energy production. However, its wide band gap (3.2eV) has primarily limited pure  $\text{TiO}_2$  based photocatalyst such as commercialized *Degussa P-25* to only be utilized under Ultraviolet (UV) light. The efficient use of sunlight (4% UV light vs. 55% visible light), especially of the visible light region of the spectrum, appears as an exciting challenge for developing next generation photocatalysts which can be used in both UV light and visible light.

Many recent published research works have mainly focused on improving photocatalytic activity through various mechanisms.

Optimizing structural and morphological aspects via different synthesis routes and materials may achieve defined crystalline structure, larger surface area with more active sites

that are available and accessible, more charges trap sites, higher density of hydroxyl •OH groups, increased surface acidity or better adsorption /desorption capacity.

A large surface area plays an important role in photocatalytic reaction efficiencies. It can provide a large amount of active sites, and absorb more target molecules in order to promote the photoinduced reaction rates. At nano-scale range, physical and chemical properties of semiconductors are easily modified and optimized by changing their diameters. Nanoparticles usually not only offer desired crystalline structure but also come with a large surface area. However, it also has obvious drawbacks coming from the size issue. Electron-hole pair recombination rates are higher when particles size is less than 10nm [43]. Nanoparticles alone are not easy to be recovered from aqueous system after used without extra filtration or centrifugation process. There is also evidence that indicates that high concentrations of powdered and ultrafine titanium dioxide dust causes respiratory tract cancer in animals exposed by inhalation and intratracheal instillation, which make titanium dioxide nanoparticles classified as possibly carcinogenic to humans [44].

Doping the semiconductor with various dopants may lead to an enhanced efficiency of photocatalytic system and achieve visible light sensitive photocatalysts. Dopants include anions, cations, transition metal ions, and rare earth metal ions.

Dopant content either changes the interfacial charge transfer rate, which directly influences the rate of  $e^-/h^+$  pair recombination, or reduces the space-charge region of doped photocatalyst. However, the concentration of dopant needs to be optimized to a certain level to avoid creation of new recombination centers. Impregnation, co-precipitation and sol-gel methods are normally used to introduce dopants. To induce visible light activated  $TiO_2$ , non-metallic anions and cations are utilized to substitute oxygen in  $TiO_2$  in order to narrow the band gap. However, valence band (VB) upward shift results in not only a narrowing of the band gap

but also a reduction in “oxidizing” holes. Meanwhile, electron-hole recombination probability is also higher. The induced alteration of the photocatalytic activity by adding p-type metal ion dopants is made up from changes of light-adsorption capability, adsorption capacity of the substrate molecules on the surface and the interfacial charge transfer rate of the TiO<sub>2</sub> photocatalyst. As metal ions are incorporated into the TiO<sub>2</sub> lattice, impurity energy levels in the band gap of TiO<sub>2</sub> are formed, the modified band gap becomes narrower.

Metal loading on photocatalyst surface creates certain metal–semiconductor regions, which leads photoinduced electrons to transfer from photocatalyst surface to metal particles to avoid e<sup>-</sup>/h<sup>+</sup> recombination.

If the work function of the metal is higher than that of Titania, electrons are removed from the TiO<sub>2</sub> particles into the vicinity of each metal particle that leads to a decrease in electron–hole recombination, as well as to an efficient charge separation. There is also an optimum loading value of metal particles. Metal loading methods include sol-gel methods [45, 46], mechanical mixing [47, 48], chemical deposition [49], precipitation-reduction [47] and photodeposition [50-52]. Noble metals such as Pt, Pd, Ag, Au, Rh and Cu, Ni have been reported for metal coating.

Sensitizing photocatalyst surface with dye/metal complex can increase the efficiency of the excitation processes and exploit the more abundant source of light energy coming from sun light. Dye sensitization is performed by anchoring sensitizer (dye) onto the surface of semiconductor materials. Covalent bonding, ion-pair type association, physisorption, entrapment in cavities or pores and hydrophobic self-assembly of a monolayer are generally used in the dye sensitization process. However, loose dye particles may also cause secondary contamination, especially in aqueous system or block active sites on the photocatalyst surface.

Coupling of two semiconductors, which possess different energy levels for their corresponding conduction band and valence band, enhances charge separation and increases life of the excited electron-holes pairs. It allows more electrons or holes transfer to adsorbed substrates.

When a large band gap semiconductor (For example  $\text{TiO}_2$ ) is coupled with a small band gap semiconductor (for example CdS) with a more negative conduction band (CB) level, CB electrons can be injected from the small band gap semiconductor to the large band gap semiconductor. Thus, a wide electro-hole separation is achieved. Direct mixing of two semiconductors, or precipitating one over another, are normally used to create such composite semiconductors.  $\text{TiO}_2$  coupling with CdS [53, 54], CdSe [55, 56],  $\text{WO}_3$  [57- 60],  $\text{Fe}_2\text{O}_3$  [61, 62], ZnO [62-64],  $\text{SnO}_2$  [65] were studied. From a practical standpoint, the second semiconductor should be photocorrosion free and physically and chemically stable to avoid any undesirable toxic by-product to release to the environment.

Using different support materials can immobilize the  $\text{TiO}_2$  photocatalysts, increase the illuminated specific catalyst area, increase surface area and adsorption capacity of the photocatalytic system, and influence the selectivity of the photocatalytic reactions.

Different kinds of porous material can be used as support materials, silica [66-68], Zeolite [69, 70], activated carbon [71, 72], fiber glass [73], clays [74],  $\gamma\text{-Al}_2\text{O}_3$ [75], quartz beads [76], polymer matrix [77] or film, fabrics [78,79] and papers [80]. Coupling, immobilization in porous matrix, electrophoretic deposition on conducting substrate and spray coating are considered as common immobilization techniques. In addition, sol-gel synthesis combines chemical and physical transformation by in situ catalyst generation and coating of support.

Many recent research works also involved using more than one dopant or multiple ways to enhance  $\text{TiO}_2$  based photocatalytic activity. Work by Ohno et al. [81] shows  $\text{C}^{4+}$  and  $\text{S}^{4+}$  co-

doped TiO<sub>2</sub> shows better PCA than single component doping. Kim et al. [82] demonstrated that sol-gel synthesized Zr and S co-doped TiO<sub>2</sub> are very effective in visible-light.

In this research work, we choose to combine composite semiconductor, transition metal ion doping with aid of both sol-gel synthesis and environmentally friendly supercritical fluid aided process technique to produce a novel high surface area and uniformly tailored nanoporous TiO<sub>2</sub> based photocatalyst system that can be utilized in UV and visible light, which also has stable porous structure.

The chosen deposited second semiconductor Tungsten Oxide (WO<sub>3</sub>) was determined by virtue of its physical and chemical properties, conduction-valence bands potential compared to TiO<sub>2</sub> and the preferable resultant surface acidity. The concentration of composite semiconductor is critical to photocatalyst photocatalytic activity since an appropriate concentration of second semiconductor causes better charge separation.

Transition metal Fe ions can trap not only electrons but also holes, and the impurity energy levels introduced are near to conduction band as well as valence band edges of TiO<sub>2</sub>. Iron-doped TiO<sub>2</sub> photocatalysts have shown good results in photoreduction of nitrogen, water splitting, and photooxidation of different organic compounds. In addition, the availability and variety of organic iron compounds provide better choices based on actual cost and experimental feasibility.

Sol-gel chemistry is currently applied as one of the most widely used methods for synthesis of porous materials [83]. The sol-gel method offers several advantages in making catalysts and catalyst supports. This process provides aerogels with favorable properties such as high purity, high porosity, and high surface area in addition to homogeneity at the molecular level [84]. However, different drying processes after sol-gel synthesis determines the final textural and functional properties of synthesized products. When the liquid inside the sol-gel

system is dried at atmosphere pressure or vacuum conditions, capillary force produces shrinkage and cracking which cause loss of the major porous structure of the gel and tremendous reduction of porosity and surface area. Aerogels were first developed by Kistler [85] and were defined as a gel dried at a temperature and pressure higher than the critical point of the pore fluid. A supercritical fluids drying process largely increases the porosity and surface area of the aerogel by eliminating the liquid-vapor interface and capillary forces, which minimizing the shrinkage associated with drying. With newly accessible supercritical regimes ( $T_c = 31.1\text{ }^\circ\text{C}$ ,  $P_c = 72.8\text{ atm}$ ), supercritical carbon dioxide ( $\text{SCCO}_2$ ), when used as the supercritical drying medium, enables synthesis of aerogels at relative lower temperatures and pressures [86]. Supercritical carbon dioxide becomes well-known as an excellent candidate for replacement of traditional organic solvents in many different processes due to its outstanding characteristics and properties: mild critical conditions, low cost, non-toxicity, non-flammability, highly available and easy recycled, low surface tension, low viscosity, gas-like diffusivities and liquid-like solvation power.

Controlled pore size distribution is another favorable property for catalysts. Recently, new pathways have been studied to prepare porous materials. Introducing surfactants as template molecules to the synthesis of the sol-gel allows better control over the properties of the porous materials [87]. In the research reported here, a refined and optimized non-ionic surfactant-templated pathway was utilized to produce  $\text{TiO}_2$  based photocatalyst with mesoporous structure. The basic advantages of the surfactant-templated porous material are high porosity and tunable unimodal nanoporosity [88] Also, removal of the solvent and surfactant using supercritical fluids ensures retaining the pore structure [89]. The final heat treatment achieves desired crystal structure with enhance the thermal, chemical and morphological stability of  $\text{TiO}_2$  based catalyst in the same step.

Currently, Supercritical fluid (SCF) aided impregnation was widely applied for various product functionalization purposes including catalysts [90, 91], polymers [92-94], thin films [95, 96], porous semiconductors [97, 98] and wood products [99]. The low viscosities of SCFs and high diffusivities of solutes in SCFs generally results in superior mass transfer characteristics compared to conventional solvents. This is an accomplishment through controlling the solute's solubility in which is dependent on process operating conditions, thus allowing solutes of Fe ion precursor to be uniformly impregnated and precipitated into the pores of the TiO<sub>2</sub> based aerogels.

## **1.2 Objectives**

The objectives of this research were to

- a. Synthesize TiO<sub>2</sub> base photocatalyst with environmentally friendly green process techniques
- b. Design a porous photocatalyst matrix with tailored nano-structure and properties that can capture environmental pollutants and decompose them into benign chemicals, and also be easily recovered and reused.
- c. Synthesize TiO<sub>2</sub> based photocatalytic system that are preferably activated with both UV and visible light.

In order to meet these objectives, specific steps were followed in a logical and organized sequence.

A fundamental background of heterogeneous photocatalyst is presented in Chapter 2, which includes a brief introduction of mechanism of photocatalysis, the intrinsic and extrinsic

affecting factors of photocatalytic activity, and a fundamental introduction of chemical and physical properties of each component in a designed TiO<sub>2</sub> based photocatalyst.

In Chapter 3, a broad review of supercritical fluid techniques is presented. The specific details of supercritical fluids extraction and drying, and supercritical fluids impregnation are further discussed. The sol-gel synthesis technique is reviewed in this chapter as well as inclusion of some previous works results. The heat treatment and surfactant template selection are also explained in this section.

In Chapter 4, all the experimental systems setups and procedures employed during this research are described in full detail. Initially, sol-gel preparations of titanium dioxide and co-precipitated TiO<sub>2</sub>/WO<sub>3</sub>/Fe<sup>3+</sup> system are presented. Secondly, supercritical fluids aided processes including supercritical fluids extraction and drying and supercritical fluids impregnation are described. Both processes share a similar experimental setup, which includes supercritical fluids feeding unit, high pressure autoclave, temperature control unit and back pressure control unit, for a total of 4 units. However, the supercritical fluids impregnation setup employed an add-on metal complex feeding cell. All characterization techniques employed in this research are discussed. Surface analysis techniques Brunauer-Emmett-Teller Surface Area Analysis (BET) and Barrett-Joyner-Halenda Pore Size Distribution (BJH) are used to identify samples' specific surface area, total pore volume, average pore size and distribution before and after heat treatment. Scanning Electron Microscopy (SEM), Energy-Dispersion X-ray Spectroscopy (EDS) and Focused Ion Beam (FIB) images and elemental maps vividly showed fine details about nanoporous structure. X-ray Diffraction Spectroscopy (XRD) spectra determined the desired crystal structures presenting in proposed samples. Diffuse reflectance spectra described light wavelength absorption of samples and predicted the band gap change. The final sub-section presented are the photocatalytic activity experimental setups. All setup diagrams and experimental procedures are explained in detail.

Chapter 5 focuses on presenting and comparing the experimental results from two different photocatalyst preparation routes. The first synthesis route discussed is the preparation of composite semiconductor  $\text{TiO}_2$  based photocatalysts ( $\text{TiO}_2/\text{WO}_3$ ) doped with Fe ion using sol-gel co-precipitation. The second and final synthesis route discussed was based upon preparation of catalyst using supercritical fluids, with Fe ion introduced into existing  $\text{TiO}_2/\text{WO}_3$  aerogel structure via supercritical fluids impregnation. The factors effecting preparation and synthesis of aerogel are discussed.

In Chapter 6, photocatalysts characterization results are presented. Photocatalytic activities of synthesized  $\text{TiO}_2$  based photocatalyst under UV light and visible light are evaluated and compared to performance results of commercial photocatalyst *Degussa* P25 under the same test and evaluation conditions.

Finally, the conclusions of this dissertation are summarized in Chapter 7, which further includes recommendations for future work.

## CHAPTER 2

### BACKGROUND: HETEROGENEOUS PHOTOCATALYST

Catalysis is a certain chemical phenomenon where the rate of chemical reaction(s) is (are) accelerated due to the participation of a substance called a catalyst. Kinetically, a chemical reaction is introduced a less difficult pathway towards thermodynamically favored completion with consuming lower activation energy. Unlike the reactants in the reaction, a catalyst participates, but is not consumed, and can be recovered at the end of the reaction as shown in Figure 2.1. A catalyst may participate in multiple chemical transformations and undergo a temporary change during reactions, for example binding with other function groups, intermediate substances or carrying an extra charge, but it will be regenerated quantitatively after the catalytic cycle ends. The production of most industrially important chemicals involves catalysis. Additionally, most biochemically significant processes are catalyzed as well. Hydrogen ion ( $H^+$ ) is the most common catalyst. Many transition metals such as Iron (Fe), Cobalt (Co), Platinum (Pt), Palladium (Pd) and transition metal complexes are used in catalysis as well. Enzymes as catalysts are very important in biology.

Homogeneous catalysts are the type of catalysts which are in the same physical phase as the other reactants in the reaction. Heterogeneous catalysts are those in a different physical phase to the rest of the reactants. The most common is a solid catalyst and a liquid solution, or a solid catalyst and a mixture of gases. The Haber process shown in equation 2.1 is one of the best-known reactions involving a transition metal catalyst. This process generates ammonia from nitrogen gas and hydrogen gas using metallic iron as the catalyst. This is a heterogeneous catalysis system.



As the name implies, photocatalysis is the acceleration of a photoinduced reaction in the presence of a catalyst. After years of research and development, the definition of photocatalysis has grown and evolved along with all involved areas. In its most simplistic description, it denotes the acceleration of a photoreaction by the action of a catalyst [100]. In photocatalytic reactions, light, as reaction activation energy source, is absorbed by an adsorbed substrate (the catalyst or initiator) which excites energy-rich electron-hole pairs ( $e^-/h^+$ ), which in turn generate free radicals (e.g. hydroxyl radicals:  $\bullet\text{OH}$ ) which then participate in secondary reactions. Heterogeneous photocatalysis is a technology based on the irradiation of a photocatalyst, usually a semiconductor such as ZnO, CdS,  $\text{TiO}_2$ ,  $\text{WO}_3$ , CdSe, whose irradiation with photon with energy equal to or greater than its band gap energy ( $E_g$ ) causes electrons to be excited from the valence band to the conduction band, meanwhile leaving a hole in valence band.

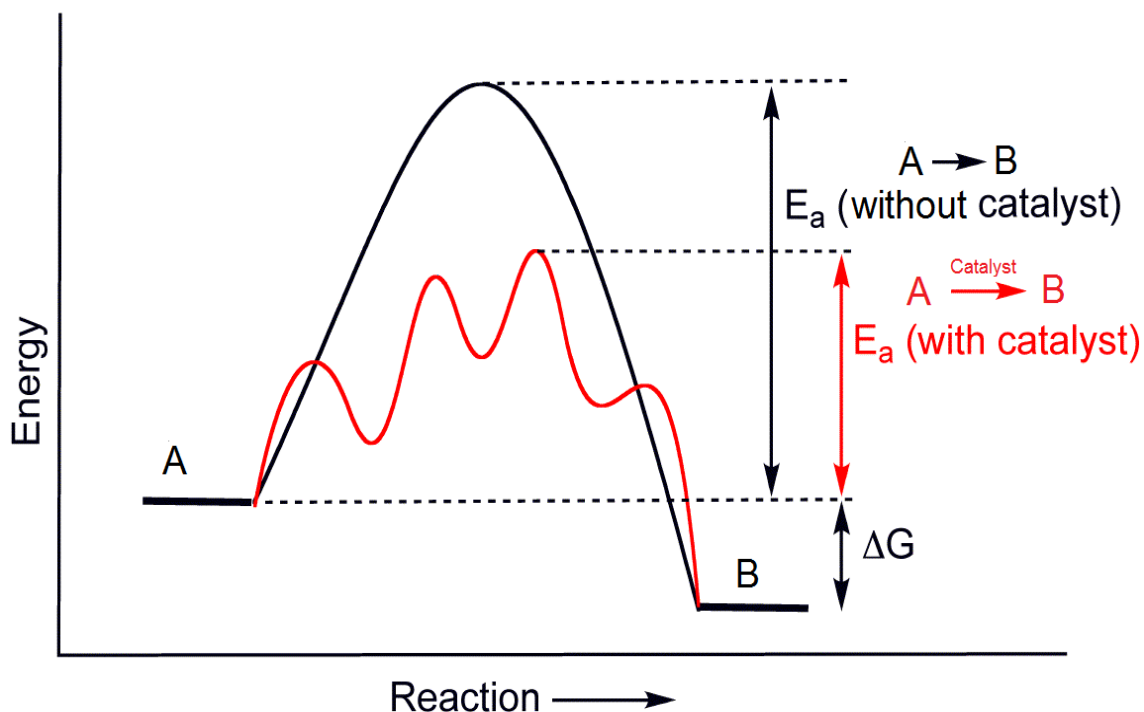


Figure 2.1 Schematic Description of the Change in a Catalytic Reaction Pathway

## 2.1 Mechanism of Photocatalysis

Similar to complicated thermal catalytic reactions, photocatalysis can vary with respect to the mechanism of a given reaction. Salomon et al. [101] proposed that photocatalysis could be further classified into two main types.

### a. Photogenerated catalysis

The light-induced generation of ground state catalyst interacts with ground state substrate to carry out a chemical reaction in a thermodynamically spontaneous catalytic step, such as photoinduced catalytic reaction, photoinitiated catalytic reaction.

### b. Catalyzed photolysis

Either the catalyst or the substrate or both are in an excited state during the catalytic step. Thus, light is used to raise the efficiency of a reaction, such as catalyzed photochemistry, catalyzed photoreaction, photosensitization, photo-assisted catalysis.

Photocatalytic reactions are initiated by the absorption of light and use energy from electromagnetic radiation in the form of photon to provide the activation energy for the reaction. Planck's equation (2.2 or 2.3) shows the relation between the light frequency,  $\nu$ , and wavelength,  $\lambda$ , and the energy associated with the incident photon,  $E$ .

$$E = h\nu \quad (2.2)$$

$$E = \frac{hc}{\lambda} \quad (2.3)$$

where  $h$  is the Planck's constant and  $c$  is the speed of light.

Most heterogeneous photocatalysis involve solid semiconductor dispersed in the reactant medium such as liquid solution or gas mixture. The electronic structure of a semiconductor plays a key role in semiconductor heterogeneous photocatalysis. A semiconductor consists of the highest occupied energy band, called the valence band (VB) and the lowest empty band, called the conduction band (CB). The energy difference between these two levels is called the band gap energy ( $E_g$ ). Without light excitation, both the electrons and holes are in valence band. When semiconductors are excited by photons with energy equal to or larger than their band gap, electrons receive energy from the photons and are thus promoted from VB to CB with simultaneous generation of holes in valence band. For semiconductor  $\text{TiO}_2$ , whose band gap energy is 3.2 eV for the anatase phase with indirect band gap, the corresponding absorbed light wavelength is 387.5 nm, which is within the UV light range. To be able to generate an electron-hole ( $e^-/h^+$ ) pair, the semiconductor must be irradiated with light of this frequency or higher. The reaction is simply expressed as:



where  $D_{ads}$  are donors and  $A_{ads}$  are acceptors.

After the pairs of electrons/holes are created in the semiconductor, the charge will transfer between electron-hole pairs and adsorbed species (reactants) on the semiconductor surface to create different radicals with different reduction or oxidation power. The photo-excited electrons and holes can also recombine in bulk or on the surface of semiconductor in a few nanoseconds, thus releasing energy in the form of heat or photons. The efficiency of a photocatalyst depends on the competition of electrons and holes transfer to absorbed species at

different interfaces and their deactivation by recombination. Electrons and holes that migrate to the surface of the semiconductor to create active sites without recombination can, respectively, react with donor (D) or acceptor (A) species adsorbed on or close to the surface of the semiconductor. Thereby, subsequent anodic and cathodic redox reactions can be initiated. The energy level at the bottom of the CB is actually the reduction potential of electrons and the energy level at the top of the VB determines the oxidizing ability of holes, each value reflecting the ability of the system to promote reductions and oxidations.

In general, the main processes occurring on a photocatalyst particle include (a) photon absorption and electron-hole generation; (b) oxidation of donor ( $D_{ads}$ ); (c) reduction of acceptor ( $A_{ads}$ ); (d) electron-hole recombination at surface and in bulk (shown in Figure 2.2). The reduction and oxidation reactions are the basic mechanisms of photocatalytic hydrogen production (water splitting) and photocatalytic decomposition, respectively.

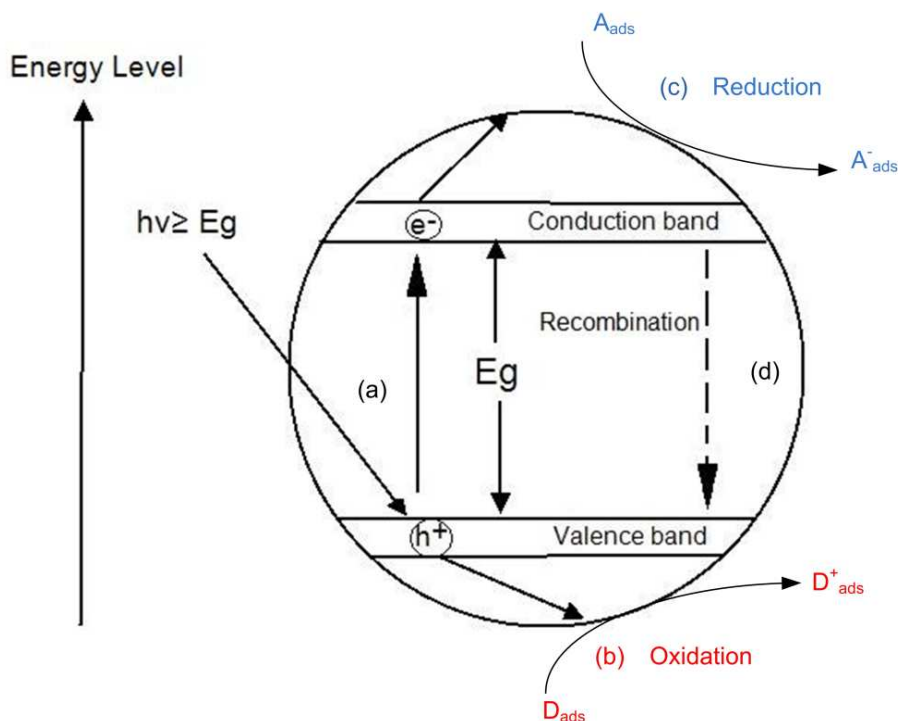


**Figure 2.2 Main Processes in Semiconductor Photocatalysis: (A) Photon Absorption and Electron-Hole Generation; (B) Oxidation of Donor ( $D_{ads}$ ); (C) Reduction of Acceptor ( $A_{ads}$ ); and, (D) Electron-Hole Recombination at Surface and in Bulk.**

After the solid semiconductor material is dispersed in the reactant medium, the reactant/pollutant molecules adsorb onto the surface of photocatalyst. During the photocatalysis reaction, reactant/pollutant molecules undergo chemical transformation, oxidation, reduction, or both, immediately after they contact with the active sites on the surface of photocatalyst. The intermediate byproduct or final product may be desorbed from the active sites or continue precipitating onto the surface of photocatalyst.

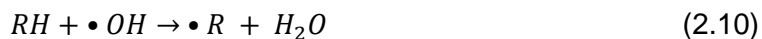
The adsorption of the reactant/pollutant onto the surface of the catalyst can be categorized as chemisorption or physisorption. Chemisorption is adsorption of the reactant/pollutant through strong chemical bond at the interface of the catalyst and reactant/pollutant. Alternatively, physisorption is a physical bond between the reactant/pollutant and catalyst due to forces such as Van der Waals forces. During the photocatalysis process, the adsorption of reactant/pollutant molecule and intermediate molecule may undergo both chemisorption and physisorption steps. Extreme strong chemical bonding or weak bonding will degrade or even eliminate photocatalytic activity. The bond between the catalyst and reactant/pollutant need to be strong enough to provide appropriate time for photocatalysis to be completed, while both adsorption and desorption occur.

The heterogeneous photocatalytic process with TiO<sub>2</sub> based photocatalyst is a complex sequence of reactions that can be expressed by the following two sets of simplified pathways with photogenerated hole ( $h_{VB}^+$ ) and electron ( $e_{CB}^-$ ) participation.

a. Photooxidation

The highly oxidizing characteristics of the VB holes and the generated hydroxyl radicals, •OH are responsible for the decomposition of organic reactants when water is available.

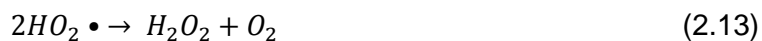




The adsorbed reactant/pollutant RH can be oxidized directly with the photogenerated holes when the concentration of reactant/pollutant is high enough or reactant/pollutant molecules are strongly adsorbed to the surface of photocatalyst. The hydroxyl groups on the photocatalyst surface and water itself also can react with holes  $h^+$  to generate hydroxyl radicals  $\bullet OH$  which have sufficiently high oxidation power to oxidize the reactant/pollutant and intermediates. The oxidative pathway leads, in many cases, to complete oxidation of an organic substrate to  $CO_2$  and  $H_2O$ . Depending on the individual organic substance, the generated intermediate byproducts may initiate other redox reactions at the same time.

#### b. Photoreduction

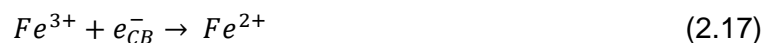
When  $O_2$  is present in reacting system, dissolved  $O_2$  which is transformed to the superoxide radical anion ( $O_2^{\bullet -}$ ) and which can lead to the additional formation of  $\bullet OH$ , and hydroperoxide radicals  $HO_2\bullet$ .





The essential role of oxygen as a acceptor of conduction band electron is to trap the electrons in order to prevent their recombination with the holes. Electrons trapped by oxygen, generating superoxide anions, will participate in a series of reactions, leading to the formation of hydrogen peroxide  $H_2O_2$  and the hydroxyl radical. Thus, reduction of  $O_2$  by electrons also helps the photo-oxidation reactions indirectly.

Also, an acceptor can be a metal ion species, which have a convenient redox potential suitable for transformation into a multiple oxidation states, for example Iron (III) ion can be converted to Iron (II) ion after accepting an electron



thus, providing an additional mechanism to avoid electron/hole recombination.

## 2.2 Affecting Factors of Photocatalysis

There are several different of factors that can influence the photocatalysis process due to its complexity. From a chemistry point of view, photocatalysis is a series of chemical reactions, which occur under exposure to light, among reactant, media and a photocatalyst. The inherent properties of photocatalyst and the experimental conditions can both affect the final photocatalytic activity. Factors related to the properties of the photocatalyst and the experimental conditions can be categorized as intrinsic and extrinsic variables that are affecting photocatalytic reactions in different ways.

## 2.2.1 Intrinsic Factors

### 2.2.1.1 Particle Size

The particle size of a photocatalyst is a very important parameter for photocatalytic efficiency. After many years and a variety of development research efforts in nano science, it is well-known that in the nanometer-size range, physical and chemical properties of semiconductors can be modified (compared with bulk) by simply manipulating particle size. Small variations in particle diameters lead to great modifications in the surface/ bulk ratio of photocatalysts, thus modifying the significance of both volume and surface electron-hole recombination, as well as the optical and electronic properties of photocatalyst.

Quantum size effects (QSE) occur for semiconductor particles (Q particles) whose size is on the order of 10-100 Å. The anomalies arise when the dimension of the semiconductor particles are commensurate with the de Broglie wavelength of the charge carriers in the semiconductor. The electron and hole produced in Q-particles are confined in a potential well of small geometrical dimensions [102]. Due to this confinement, the conduction band electrons and the valence band holes do not experience the electronic migrations that present in a bulk semiconductor. Instead, the confinement produces a quantization of discrete electronic states and increases the effective band gap of the semiconductor, which can be observed experimentally as a blue shift in the absorption and emission spectra.

On the other hand, the most important electronic property influenced by particle size is the space charge layer. When semiconductor particles are in contact with an electrolyte having acceptor or donor species, surface band bending happens at the semiconductor/liquid interface which requires establishment of a new electrochemical equilibrium. The Fermi level of the semiconductor is equal to the potential of the redox couple in electrolyte. The movement of Fermi level is facilitated by the transfer of electrons from semiconductor to the electrolyte which

leaves the interface negatively charged. In this electric charged region, on each side of interface, the charge distribution differs from the bulk materials. For example, in  $\text{TiO}_2$  anatase, surface hole trapping dominates because spatial charge separation is achieved by the migration of photogenerated holes toward the particle surface due to the strong upward band bending. The driving force to separate the charge carriers is proportional to the magnitude of the potential drop within the space charge layer. Potential difference is higher for large particle size ( $>100$  nm) thus allowing for effective charge separation. However, the transmit time of charge carriers from particle interior to the surface can be significantly increased as the particle diameter increases. The charge carriers may therefore tend to recombine in the bulk before they can migrate to the surface if the transmit time is too long. For optical properties, light absorption and scattering on semiconductor particle are influenced by particle size too. Light scattering ability of particles depends on their size relative to the wavelength of the light. Light absorption coefficient is much higher and scattering coefficient is much lower when nano-particles are used, and maximum scattering is observed when the sizes of particles are close to half of the wavelength of the incident light. Moreover, for large particles, irradiation is primarily absorbed in the outer layer of the particle and the interior bulk is not fully utilized.

To sum up, over-reducing the size of photocatalyst particles ( $<10$  nm) may result in negative consequences to the photocatalysis process, such as band gap increase and faster surface recombination of charge carriers. Larger particle size ( $>100\text{nm}$ ) may result in longer transmit time of charge carriers to the surface, increase recombination of electron-hole pairs before reaching the surface, as well as larger light scattering coefficients. Optimized particle size is desirable for improving photocatalytic activity. From practice industrial perspective, nanoparticles utilized in aqueous systems also has present problems with catalyst recovery for photocatalyst recycle.

### 2.2.1.2 Surface Area

The photocatalytic activity of  $\text{TiO}_2$  catalysts depends strongly on two factors: absorbability and the separation efficiency of electron-hole pairs. In heterogeneous catalysis, reaction takes place at the active surface of the solid catalyst. The PCA of modified  $\text{TiO}_2$  photocatalysts can be further enhanced if photocatalyst absorbs more targeted reactants/pollutants along with effective charge separation. High surface area is desirable for the photocatalytic system where adsorption on the surface is the rate-controlling step [103]. Adsorption of pollutants in the vicinity of the photocatalytic active sites promotes the photodegradation of reactants/pollutants that normally do not or in low concentrations adsorb on the photocatalyst surface. The basic concept is based on the physisorption of reactants on inert substrates followed by their surface diffusion to the interface between the adsorptive sites and photocatalytic sites. The adsorption capacity can be generally improved by increasing the specific surface area (SSA) and pore volume of catalysts. However, when several intermediate products appear and intend to re-adsorb strongly during photocatalysis, surface active site may be blocked for further interfacial charge transfer. Meanwhile, surface hydroxyl concentration and distribution influence adsorption step and selectivity significantly.

Nano particles and thin film are usually associated with higher specific surface area. Sol-gel synthesized mesoporous materials have demonstrated more advantages, such as purity, homogeneity, felicity and flexibility in introducing dopants in various concentrations, stoichiometry control, and the ability to manipulate composition and coating in large and complex area than other high surface materials. Pore structure of highly porous material also plays a key role in photocatalytic activity. Pores must be fabricated as an open cell that can be accessible during the entire photocatalysis reaction process. Pore size distribution and mesopore volume percentage describe the homogeneity of material and uniformity of porous structure.

### 2.2.1.3 Crystal Structure and Properties

In photocatalysis, a critical issue to be addressed is the crystallographic structure of the metal oxide that is related to its photocatalytic activity. Titanium dioxide has been known to exist in three main polymorphic phases: rutile (tetragonal), anatase (tetragonal) and brookite (orthorhombic). All of them have the same fundamental octahedral structural units, but their arrangements are different. They differ by the assembly patterns of the octahedral chains. Rutile's crystal structure is built up from octahedrals that are connected by their edges, in anatase, the vertices are connected, and in brookite, both vertices and edges are connected. The lattice structure for anatase and rutile is demonstrated in terms of distorted  $\text{TiO}_6$  octahedra (shown in Fig 2.3). Differences in crystal structures of each type of titanium dioxide induce the different thermodynamic properties i.e. stability, and physical properties i.e. optical refractivity, density (Table 2.1) [104].

**Table 2.1 Some Bulk Properties of the Three Main Polymorphs of  $\text{TiO}_2$  (Anatase, Rutile, Brookite)**

Phase	Refractive Index	Z	Density ( $\text{g.cm}^{-3}$ )	Band Gap (eV)	Light wavelength threshold (nm)	Crystal Structure
Anatase	2.49	4	3.895	3.26	384	Tetragonal
Rutile	2.903	2	4.2743	3.02	410	Tetragonal
Brookite	2.583	8	4.123	2.96	401	Orthorhombic

Rutile is predicted to be the most stable phase over the entire temperature and pressure region based on thermodynamic calculation [105]. However, there is only 4~12 KJ/mol Gibbs free energy difference among these three phases. That means at room temperature and pressure all of these three phases are almost equally thermodynamically stable.

Due to surface free energy and surface stress, when particle size reduces to the nanoscale level, the relative stability phase may reverse. Anatase is most thermodynamically stable at sizes less than 11 nm, brookite is most stable between 11 and 35 nm, and rutile is most stable at sizes greater than 35 nm.

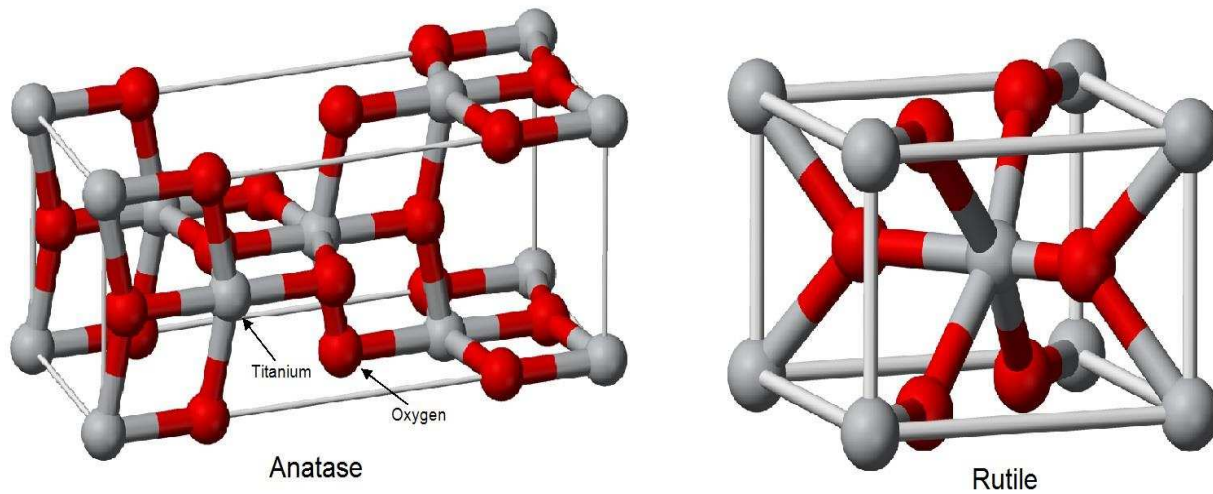


**Figure 2.3 3D Balls and Sticks Models of Anatase and Rutile Atomic Structures**

Due to oxygen vacancies, TiO<sub>2</sub> works as an n-type transition metal oxide semiconductor in which the density of holes in the valence band is exceeded by the density of electrons in the conduction band. In n-type semiconductors, electrons are the majority carriers, and holes are the minority carriers. Both the anatase and the rutile have a tetragonal crystal structure with the anatase unit cell having higher volume compared to the rutile. The differences in lattice structures of anatase and rutile TiO<sub>2</sub> cause different densities and electronic band structures, leading to different band gaps (for bulk materials: anatase 3.20 eV and rutile 3.02 eV). Therefore, the absorption thresholds correspond to 384 and 410 nm wavelength for the two titania forms, respectively [106]. Higher wavelengths are usually obtained for weakly crystallized thin films or nanosized materials [107]. Both crystal structures, anatase and rutile, are commonly used as photocatalysts, with anatase showing a greater photocatalytic activity for

most reactions. The mechanism responsible for this behavior is a controversial subject. Considerable research is in progress to gain complete understanding into this phenomenon. However, at present there are three hypotheses trying to explain higher photocatalytic activity of anatase.

a. Higher Fermi level

The anatase has higher Fermi level over the rutile by 0.1 eV. This leads to lower capacity to absorb oxygen and higher degree of hydroxylation (a higher number of hydroxyl groups) on the surface. These hydroxyl groups contribute to the higher photocatalytic activity.

b. Indirect band gap

The anatase possesses an indirect band gap while the rutile has a direct band gap. In a direct band gap material, the minimum in the conduction band coincides with the maximum in the valence band, thus facilitating an early recombination of the electrons with the valence band holes. In the indirect band gap materials, the minimum in the conduction band is away from the maximum in the valence band. This enables the excited electron to stabilize at the lower level in the conduction band itself leading to its longer life and greater mobility.

c. Excitation electron mass

Anatase possesses a wider absorption gap. Hence, it is proposed that excitation electron mass of the outer shell electrons in the anatase may be lower than in the case of the rutile. This may explain higher mobility of electrons in the anatase.

It has been suggested that this increased photoreactivity is due to anatase's slightly higher Fermi level, lower capacity to absorb oxygen and higher degree of hydroxylation (i.e., number of hydroxyl groups on the surface). Furthermore, there are also studies which claim that

a mixture of anatase (70-75%) and rutile (30-25%) is more active than pure anatase [108-110]. The mixture is considered as a kind of composite semiconductor where the photoexcited electrons transfer from anatase conduction band to rutile conduction band thus achieving a wide charge separation that prevents early recombination. The current commercialized photocatalyst, *Degussa P25*, is a mixture of anatase and rutile phases (anatase/rutile ratio $\approx$ 80/20) with a nominal particle size of 50nm and a surface area of  $50\pm 15$  m<sup>2</sup>/g.

The photogenerated electrons and holes migrate to the interface between photocatalyst and adsorbed reactant/pollutant and participate in reduction and oxidation reactions. Band edge position and the redox potential of the adsorbed species determine the possibility of certain types of reactions. Band edge positions of different semiconductor materials in contact with aqueous electrolyte at pH=1 are shown in Figure 2.4. For an oxidation reaction to occur, the potential level of the donor species must be higher (more negative) than the maximum position in valence band of the semiconductor catalyst. Likewise, for a reduction reaction to take place, the potential level of the acceptor species must be lower (more positive) than the minimum position in conduction band of the semiconductor catalyst.

For TiO<sub>2</sub> anatase, the redox potential for photogenerated holes is +2.53 eV which is regarded as possessing strong oxidative decomposing power. The surface of a photocatalyst can absorb a certain amount of water. When this water is oxidized by positive holes, hydroxyl radicals are formed. Then, the hydroxyl radicals react with the organic compound and partially degrade it. If oxygen is present at the same time, the intermediate radicals in the organic compounds and oxygen can undergo radical chain reactions and consume oxygen in some cases. In such a case, the original organic compound eventually completely decomposes, ultimately becoming CO<sub>2</sub> and H<sub>2</sub>O. Under some conditions, organic compounds can react directly with the positive holes, resulting in oxidative decomposition. The redox potential for conduction band electrons is -0.52 eV, which is negative enough to reduce di-oxygen to

superoxide, or to hydrogen peroxide. Depending upon the exact conditions, the holes, •OH radicals,  $O^{2-}$ ,  $H_2O_2$  and  $O_2$  itself can all play important roles in the photocatalytic reaction mechanisms. Usually it is simply assumed that oxidative and reductive photocatalytic reactions take place simultaneously on  $TiO_2$  particles, however it is very difficult to confirm this assumption by direct experimental measurements.

The  $TiO_2$  crystal structure phase is one of the most critical parameters determining the application as a photocatalyst, or as other purpose material. This monotropic anatase to rutile transformation, achieved by increased temperature or pressure, is influenced by several factors.

a. Concentration of lattice and surface defects

An increase of surface defects enhances the rutile transformation rate as these defects act as nucleation sites. The presence of dopants also affects this transformation. Ions with valency less than four (e.g.,  $Cu^{2+}$ ,  $Fe^{3+}$ ) and having small radii increase the transformation rate and ions with valency higher than four (e.g.,  $S^{6-}$ ,  $P^{6-}$ ) or negative charge (e.g.,  $Cl^-$ ,  $F^-$ ) decrease and inhibit the transformation.

b. Particle size

Smaller grain size (e.g., nanoparticle) with high specific surface areas increases the total boundary energy of  $TiO_2$  powder so that the tendency of particles sintering together and growth increases. However, selection of synthesis method, wide dispersion on the support, and addition of certain compounds can retard the particle from reaching each other, making anatase more stable.

c. Applying pressure

An increase of environmental pressure will lower the transformation temperature.

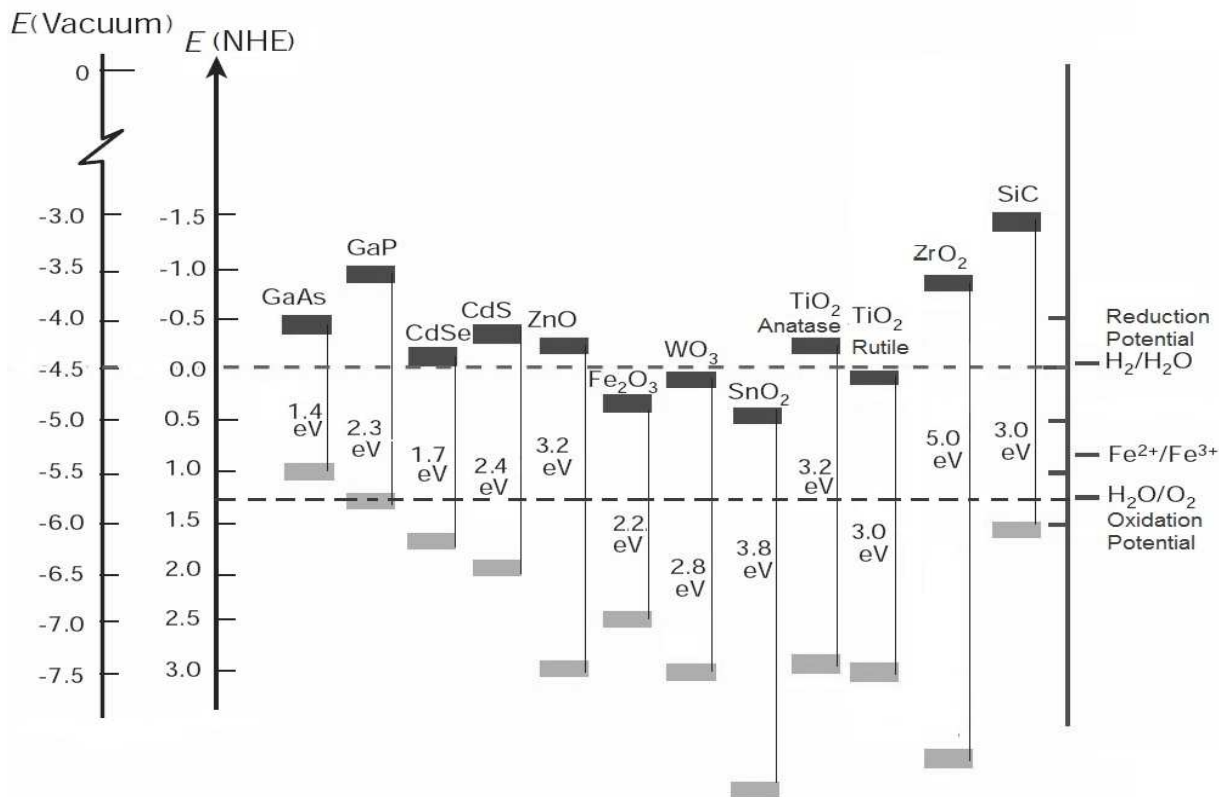


**Figure 2.4 Band Edge Position of Common Semiconductor Photocatalyst in Contact at pH=1**

### 2.2.2 Extrinsic Factors

In photocatalysis, in addition to the physical and chemical properties of photocatalysts, the operational parameters also influence the total photocatalytic activity. Parameters such as photocatalyst dosage, type and initial concentration of the target compound, coexisting reagents, temperature, light intensity, oxygen concentration, circulating flow rate, and pH value are the main parameters affecting the reaction rate and result.

#### a. Photocatalyst dosage

Generally, decomposition rate increases initially with photocatalyst dosing due to increases in the number of the available surface active sites for adsorption and interfacial

charge transfer. Beyond a certain optimum concentration, the solution opacity increases (due to increased light scattering of the photocatalyst particles) causing a reduction of light penetration in the solution and a consequent rate decrease [111]. The optimal amount of photocatalyst varies with the employed reactor design, dimension and other parameters of the reacting system. For all practical purpose, the limit of photocatalyst dosage should be preferentially maintained under 1 g/L when photocatalyst particles are dispersed in an aqueous solution.

b. Concentration of the target reactant/pollutant

The degradation rate of organic substrates usually exhibits saturation behavior: At high initial concentration of reactant/pollutant, all surface active sites are occupied. A further increase of the concentration of reactant/pollutant does not affect the actual catalyst surface concentration. Instead of increase the PCA, the increase of reactant/pollutant may reduce desorption of intermediate products and thus block the active sites on the photocatalyst surface, which will cause a decrease the PCA. Meanwhile, at low concentrations, the degradation rate increases linearly with reactant/pollutant concentration. It is favorable for kinetic study of photocatalysis.

c. Temperature

Like most photoreactions, photocatalytic reactions are not dramatically sensitive to minor variations in temperature [112]. This is due to the low thermal energy (0.026 eV at room temperature) has almost no contribution to the activation energy of photocatalysts with wide band gap, such as  $\text{TiO}_2$  (3.26 eV). On the other hand, these activation energies are quite close to that of hydroxyl radical formation, indicating that the photodegradation of organic compounds is controlled by rate of hydroxyl radical reactions. The potentially temperature dependent steps, such as adsorption, desorption, charge carriers surface migration and rearrangement do not appear to be rate determining in this case.

d. Light intensity

Light intensity is an important parameter of reactor design and final photocatalytic activity evaluation of photocatalysis. To some degree, the number of excited electron-hole pairs depends on the photon flux. Some previous work had reported that light intensity found a non-linear dependence on kinetics of photocatalysis process. The variation of reaction rate as a function of the used wavelength follows the adsorption spectrum of the catalyst with a threshold corresponding to its band energy [17]. Increasing light intensity above the optimum value does not show increase in photodegradation rate since the photon absorption for a certain concentration of photocatalyst has been saturated.

e. Oxygen

Oxygen is commonly considered to scavenge electrons. Adding Oxygen to a reacting system was found to be essential for photocatalytic degradation of organic compounds. In a liquid reacting system, dissolved molecular oxygen becomes a strong electrophile and thus an increase of its content probably traps more electrons and reduces electron-hole recombination rate. However, higher concentration of dissolved molecular oxygen may lead to a decrease of the reaction rate. This phenomenon could be attributed to the fact that the concentration of hydroxyl groups on  $\text{TiO}_2$  surface becomes higher, which inhibits the adsorption of reactant/pollutant at active sites.

f. pH value

The surface charge, band edge positions and dispersion of  $\text{TiO}_2$  are strongly influenced by pH when  $\text{TiO}_2$  photocatalyst particles are utilized in aqueous solution due to the presence of hydroxyl groups on the  $\text{TiO}_2$  surface. Positive surface charge is expected at lower pH and negative surface charge is predicted at higher pH values. With pH value increasing the negative

charged hydroxyl groups concentration is raising which will be of benefit to the adsorption and subsequent degradation rate of cationic reactant/pollutant molecules.  $\text{TiO}_2$ 's flat band potential position also changes with pH value variation. The flat band potential dictates the ability of electrons to reduce the adsorbed electrolyte. pH also influence the isoelectric point of the  $\text{TiO}_2$  particles, Agglomeration of photocatalyst particles may occur if a poor dispersion happens due to pH change. Consequently, the effective surface area and adsorbility of  $\text{TiO}_2$  will decrease.

## **2.3 Titanium Dioxide Photocatalyst**

### **2.3.1 Introduction of Titanium Dioxide**

Titanium (Ti), well known as the world's fourth most abundant metal and the ninth most abundant element, was discovered in 1791 by Reverend William Gregor in England. Pure titanium dioxide does not occur in nature, it is primarily found in various minerals like rutile, ilmenite, leucoxene, anatase, brookite, perovskite, and sphene, and in titanates and many iron ores as well.

Titanium Dioxide or Titania--- $\text{TiO}_2$ , characterized by the presentation of an amazing photoinduced phenomenon, has attracted more and more research and work on this field. With a wide band gap (3.2 eV), titanium dioxide is able to be excited using light with wavelength from visible light through UV light which have higher photon energy than the band gap. An electron is promoted to the conduction band leaving a hole in the valence band. The excited electron can either be used directly to create electricity as in photovoltaic solar cells or used to drive a chemical reaction, which is called photocatalysis. Excited electron-hole pairs can be applied in water photo-splitting for hydrogen generation or in chemical process to create or degrade specific organic, inorganic and biological compounds. The strong oxidative potential of the positive holes oxidize water to create hydroxyl radicals. This oxidative potential can also oxidize oxygen or organic materials directly. Recently, another interesting newly discovered property,

photoinduced super-hydrophilicity of titanium dioxide film surface has been exploited for anti-fogging coatings or self-cleaning windows. The types of photochemistry responsible for photocatalysis and super-hydrophilicity are totally different, even though both can occur simultaneously on the same surface.  $\text{TiO}_2$  incorporated into outdoor building materials can substantially reduce concentrations of airborne pollutants such as volatile organic compounds. Figure 2.5 shows the main photoinduced processes on  $\text{TiO}_2$  material based on the difference of aspects and applications of applied reactions.

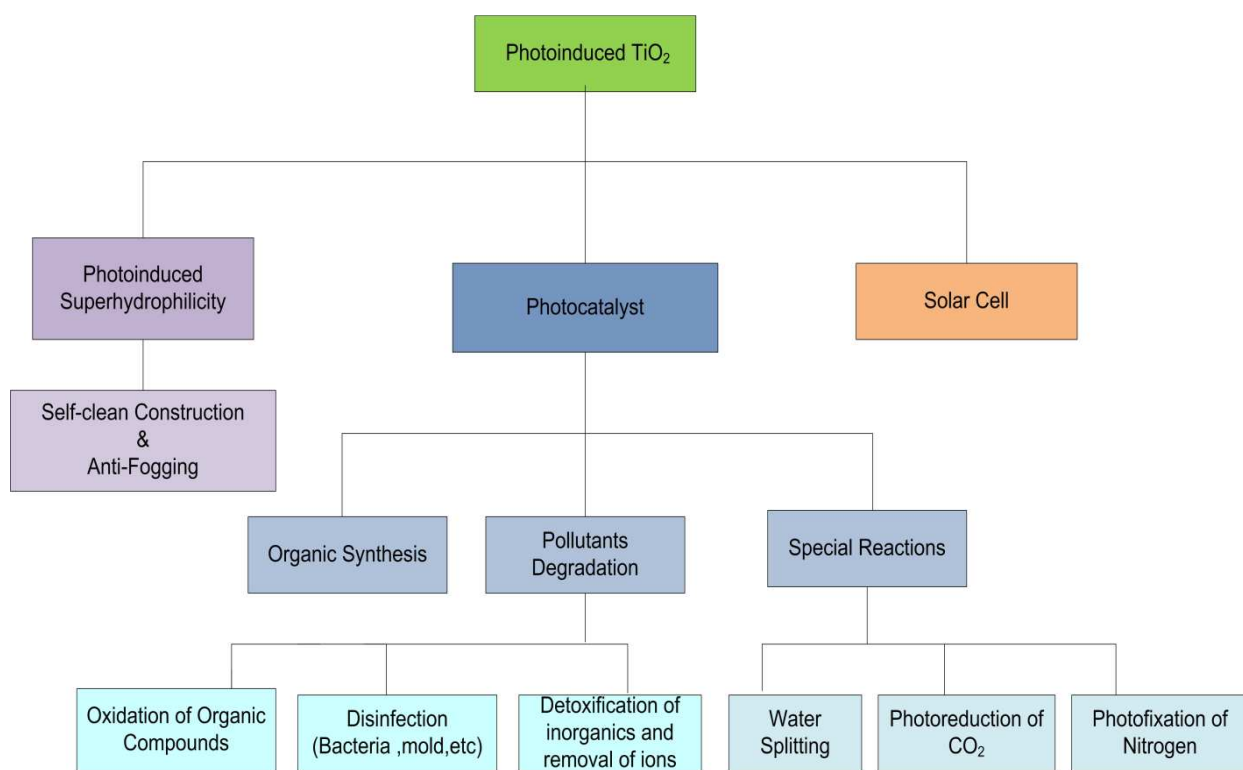


**Figure 2.5 Photoinduced Processes on  $\text{TiO}_2$**

To obtain high purity  $\text{TiO}_2$  products, several artificial synthesis routes have to be taken. Powder, crystal and thin film are three major forms of synthesized  $\text{TiO}_2$ , both powders and films can be built up from crystallites ranging from a few nanometers to several micrometers. Many novel methods lead to nanoparticle formation without need of deagglomeration process. Some synthesis routes have been industrialized since the titanium dioxide industry was established,

while others are still confined to the laboratory due to the high cost of initial materials and apparatus.

There are two industrial manufacturing methods for the production of titanium dioxide: the sulfate route and the chloride route. Both processes involve a number of stages and are not environmental friendly processes.

a. Sulfate route

Ilmenite is transformed into titanium sulfates by reaction with sulfuric acid. In the final step, the titanium sulfate is reacted with water resulting in formation of titanium oxide and sulfuric acid:

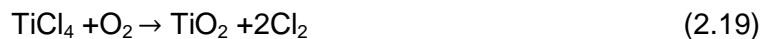


After the titanium sulfate has been heated and hydrolyzed, the precipitated titanium oxide or titanium hydroxide is calcined at 800–1000 °C to eliminate the amorphous structure and produce a crystalline structure. Straight hydrolysis yields only anatase phase on calcination.

The sulfate process benefits from cheap raw materials, but the final product needs a post-heat treatment to achieve crystalline products. The sulfate process yields a substantial amount of waste iron sulfides and a poor quality TiO<sub>2</sub>.

b. Chloride route

The rutile is reacted with chlorine to produce titanium tetrachloride, which is purified and re-oxidized. The precursor, TiCl<sub>4</sub>, is oxidized in the gaseous phase at high temperature (985 °C) in a H<sub>2</sub>/O<sub>2</sub> flame yielding very pure TiO<sub>2</sub>, the chlorine gas is recycled:



The chloride route is less environmentally invasive but requires more complex process steps. TiO<sub>2</sub> nanoparticles can be produced by the gas-to-particle conversion in flame reactors. This method provides good control of particle size, particle crystal structure and purity. TiO<sub>2</sub> nanoparticles made by this flame synthesis ranged from 10 to 130 nm in average particle diameter, and the mass fraction of anatase synthesized was 40 to 80%. Many variables for the synthesis of nanoparticles in the flames, such as the configurations of the flame, the concentration of precursor, gas composition, and gas flow rate, affect particle formation, particle aggregation, sintering, and phase composition of particles.

The laboratory methods can be categorized based on the involved reaction phase.

a. Solution routes

Liquid-phase processing route is attributed to be one of the most convenient and easiest methods of synthesis. It can produce homogenous materials, complex shape, and controlled composite materials. The downside is residue of solvent may remain as impurity in final products.

By adding alkali solution (NaOH, NH<sub>4</sub>OH, urea), the hydroxides are precipitated from raw material (e.g. TiCl<sub>3</sub>, TiCl<sub>4</sub>) followed by calcination to crystallized oxide (Precipitation Methods). Large anatase particles are the normal product from fast precipitation.

Chemical reactions occur in aqueous (hydrothermal method) or organic media (solvothetical method) such as methanol, butanol, or toluene at relatively low temperature (about 250 °C). The solvothetical treatment could be useful to control grain size, particle morphology, crystalline phase, and surface chemistry by regulating the solution composition, reaction temperature, pressure, solvent properties, additives, and ageing time. TiOSO<sub>4</sub>, H<sub>2</sub>TiO(C<sub>2</sub>O<sub>4</sub>)<sub>2</sub>, H<sub>2</sub>Ti<sub>4</sub>O<sub>9</sub>•0.25 H<sub>2</sub>O, TiCl<sub>4</sub> in acidic solution are reported as Ti sources in hydrothermal synthesis. Hydrothermal methods have proved to be a mild and effective

alternative of nanoparticle and nanocrystallite TiO<sub>2</sub> synthesis. The relatively lower temperatures (usually <250 °C) favor a decrease in agglomeration of particles, and changes in reaction conditions (temperature, pH, reactant concentration, presence of mineralizers) can lead to products with specific characteristics. A final hydrothermal heating treatment is needed to achieve the crystal structure transformation.

Sol-gel process generally involve the use of inorganic or organic salts as well as metal alkoxides or nitrates as precursors. The non-alkoxide route uses inorganic salts (such as nitrates, chlorides, carbonates, acetates, acetylacetonates, etc.), which requires an additional removal of the inorganic anion; while the alkoxide route (the most employed) uses metal alkoxides as precursors.

The sol-gel process under ambient pressure starts with the hydrolysis of a precursor, when it encounters water. The hydrolysis continues simultaneously with the poly-condensation of the hydrolyzed monomers leading to the formation of a three-dimensional network, which is a solid phase encapsulating solvent. Porous materials, thin film and powder can be prepared via sol-gel route. The gel materials are referred as aqua-gel when water is used as the solvent and alco-gel when alcohol is used as solvent. The encapsulated solvent can be removed from a gel by either conventional evaporative drying or supercritical fluid drying in the drying step. This supercritical fluid aided sol-gel synthesis process provides aerogels with favorable properties such as high purity, high porosity, and high surface area in addition to homogeneity at the molecular level. To get a crystalline product, the powder obtained from the normal sol-gel process needs to be calcined at relatively high temperatures (>400 °C). As titanium sources, Ti(O-E)<sub>4</sub>, Ti(*i*-OP)<sub>4</sub>, and Ti(O-nBu)<sub>4</sub> are most commonly used. The general formula for the sol-gel synthesis of TiO<sub>2</sub> is:



A key desired property for both catalysts and sorbents is pore size distribution. A recent pathway, compatible with sol-gel technique, utilizes surfactants as template to prepare large surface area titania phases, which exhibit a desirable mesoporous structure. The choices in template selection are vast and extensively reviewed in the literature [113, 114]. Block copolymers can also be used as templates to direct formation of mesoporous structure.  $\text{TiO}_2$  Thin films can be achieved by dip coating. For aerogels, use of nonionic surfactants avoid extra electrical charge which limit the cross-linking of the units and compromise the thermal stability of the porous framework as well as enable ease in their subsequent removal with or without heat treatment [115]. Obviously, heat removal is the less desirable option in terms of retaining pore structure, but is very often unavoidable, especially when precursor transformation, such change from hydroxides to oxides, is necessary.

There are also several synthesis methods of  $\text{TiO}_2$  particle or thin film fabrication such as microemulsion route, combustion route, and electrochemical deposition route which are hindered by critical reaction conditions, low productivity, or high time and energy cost. Meanwhile, some novel methods, which involved using supercritical fluid systems (e.g., RESS), have been applied on the production of  $\text{TiO}_2$  nanoparticles. Details on these processes will be presented in the next chapter.

#### b. Gas phase method

Most synthesis routes for making a thin film are carried out in gas phase. Those processes can be divided into those that are chemical and physical of nature. The gas phase method can produce powder product as well if a collection step included.

Chemical Vapor Deposition (CVD) is a widely used versatile technique designed to coat large surface areas in a short span of time. Precursor, pressure and activation method are the

key factors of CVD process. Compound formed from chemical reaction or decomposition of precursors is the main source of the thin film.

Instead of a chemical reaction, gasified material is directed toward the substrate. The most commonly employed Physical Vapor Deposition (PVD) technique is thermal evaporation, in which a material is evaporated and deposited onto a substrate. The heating source includes electron beam and laser beam. Most PVD process takes place under reduced pressure to minimize impurity and collisions of gas molecules.

Aerosol-based methods are hybrid methods because such routes start from precursors in solutions, which can be further processed in a number of different ways. Spray Pyrolysis Deposition is another technique being used to manufacture thin film. The size of the particles formed and the morphology of the resulting film are strongly dependent on deposition parameters like substrate temperature, composition and concentration of the precursor, gas flow, and substrate-nozzle distance.

Other techniques including Molecular beam epitaxy (MBE), Sputtering, and Dynamic ion beam mixture, Ion implantation are used to produce TiO<sub>2</sub> thin film as well.

The crystal structure and electronic properties of TiO<sub>2</sub> material have been discussed in previous section.

### **2.3.2 Improving Photocatalytic Activity of TiO<sub>2</sub>**

Although the pure form of titanium dioxide offers unique performance particularly at the nanosize,  $e^-/h^+$  recombination, fast backward reactions ( $\text{Water} \rightarrow \text{H}_2 + \text{O}_2 \rightarrow \text{Water}$ ), and ineffective performance under visible light (Band gap energy of pure TiO<sub>2</sub> is 3.2 eV) necessitate continued search for superior photocatalysts. Solutions to improving photocatalytic reactions with TiO<sub>2</sub> imply development of defined crystalline size and structure, larger surface area,

enhanced sorption capability and tunable nanoporosity, and incorporation of various dopants to modify the surface activity. In this section, performance modifications based on different doping methods will primarily be discussed.

TiO<sub>2</sub> has a photonic efficiency of less than 10% for most photodegradation processes. TiO<sub>2</sub> photocatalysis, which is governed by free radical mechanism, are non-selective reactions. In other words, target reactant/pollutant and intermediate molecules may experience the same decomposition rate during photocatalysis. However, some intermediate compounds show even higher toxicity than the parent compound. Therefore, it is necessary to develop a TiO<sub>2</sub> based photocatalyst system that can utilize UV and visible light to increase photonic efficiency. The modification of TiO<sub>2</sub> to improve its efficiency have been carried out in various ways, all modifications need to solve at least one or maybe all of these three major existing disadvantages.

a. Recombination of photo-generated electron/hole pairs

Conduction band electrons can recombine with valence band holes very quickly and release energy in the form of unproductive heat or photons.

b. Inability to utilize visible light

Since the UV light only accounts for about 4% of the solar radiation energy while the visible light contributes about 55%, the inability to utilize visible light limits the efficiency of solar photocatalytic reactions.

c. For water splitting, fast backward reaction

Decomposition of water into hydrogen and oxygen is an energy intensive process, thus the thermodynamics preferred backward reaction (recombination of hydrogen and oxygen into water) proceeds easily.

Organic compounds adsorbed by the photocatalysts are decomposed mainly by the VB holes and radicals induced by holes. Therefore, the mechanism involved in transferring these photogenerated holes to the interface is of paramount importance. On the other hand, for photocatalytic water splitting, the transfer of CB electrons to the interface and their energy levels are the most important factors that affect the hydrogen production rate. Hence, the results based on environmental remediation applications cannot be directly applied to water splitting.

Incorporation of  $e^-$  donors, carbonate salts, noble metals, anions or cations, transition metal ions, composite semiconductors, and dye sensitization are all possible pathways to modify band-gap, promote the photocatalytic activity, induce an effective charge separation and enhance the visible light response [17]. However, none of above pathways, in and of themselves, is capable of solving all existing issues.

a. Addition of electron donors (sacrificial reagents or hole scavengers)

Adding electron donors (sacrificial reagents or hole scavenger) to react with VB holes can enhance the photocatalytic  $e^-/h^+$  separation. Organic compounds (hydrocarbons, such as EDTA, methanol, ethanol, Lactic acid) are widely used as electron donors which can be oxidized by VB holes, meanwhile, the remaining strongly reducing CB electrons can reduce  $H^+$  to  $H_2$ . Other inorganic ions  $S^{2-}/SO_3^{2-}$ ,  $Ce^{4+}/Ce^{3+}$ ,  $Fe^{3+}/Fe^{2+}$  and  $IO_3^-/I^-$  can also be used as sacrificial reagents.

*Advantage:* Adding electron donors to react irreversibly with the photo-generated VB holes can enhance the photocatalytic electron/hole separation.

*Disadvantage:* Since electron donors are consumed in photocatalytic reaction, continual addition of electron donors is required.

b. Noble metal and group VIII metal loading ( Metal coating)

If the Fermi level of the metal is lower than that of titania, electrons are migrated from the  $\text{TiO}_2$  particles in the vicinity of each metal particle. This results in formation of a Schottky barrier (Pt produces the highest Schottky barrier) at each metal–semiconductor region, which leads to a decrease in electron–hole recombination rate, as well as to an increase in charge carriers separation. As a consequence of the improved separation of electrons and holes, metal deposition on the  $\text{TiO}_2$  surface enhances photocatalytic reactions by accelerating the transfer of electrons to dissolved oxygen molecules.

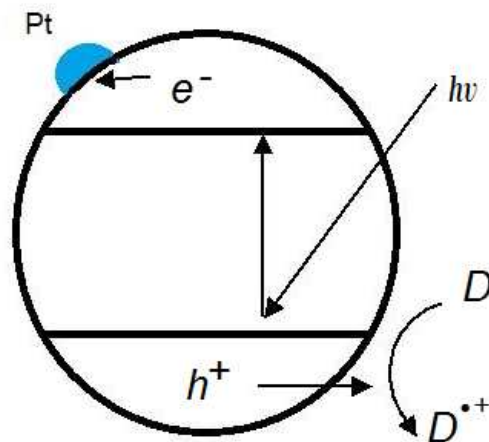


**Figure 2.6 Energy Diagrams Illustrating  $\text{TiO}_2$  Doped with Pt**

*Advantage:* Noble metals (Ag, Pt, Au, Cu, Pd, Rh, Ir, Os and Ni) [116-123] or combined mixed metals work as electron scavengers or electron sinks to trap electrons, while photo-generated VB holes remain on the  $\text{TiO}_2$ . These activities greatly reduce the possibility of electron-hole recombination, resulting in efficient separation and stronger photocatalytic reactions.

*Disadvantage:* The cost of noble metal loading is one of obvious disadvantages. Also, there is an optimum loading value of metal particles, if metal loading is above optimum values, several harmful effects could happen. First, a decrease in electron density occurs, due to electron attraction by numerous metal particles, which has a detrimental effect on the charge separation, lowering the photocatalytic activity of the catalyst. Second, excessive coverage of TiO<sub>2</sub> catalyst limits the amount of light reaching the surface, reducing the number of photogenerated hole-electron pairs and consequently lowering the photodegradation rate. Third, once negatively charged, metal particles, especially for highly loaded samples (%M >5%), attract holes and subsequently recombine them with electrons. In this case, the metal deposits become recombination centers.

Platinum usually is the number one choice for noble metal loading of TiO<sub>2</sub> due to its activity, wide application and best photocatalytic efficiency. The UV-illumination of an aqueous TiO<sub>2</sub> suspension in the presence of PtCl<sub>6</sub><sup>2-</sup> and electron donors results in the deposition of Pt<sup>0</sup> on the TiO<sub>2</sub> surface. Research work has shown that Pt/TiO<sub>2</sub> is active in the photodecomposition of benzene, trichloroethylene, phenol, methanol, ethanol tert-butyl-alcohol acetone, methyl-butyl-ether, acetaldehyde, EDTA, ethyl acetate, ozone, and azodyes.

Metal loading methods include sol-gel methods, mechanical mixing, chemical deposition, precipitation-reduction and photodeposition. The resulting PCA of doped photocatalyst depends on the preparation method and on the final physicochemical properties of the material.

#### c. Anion doping

Substituting oxygen sites in TiO<sub>2</sub> with anions (N<sup>3+</sup>, C<sup>4+</sup>, S<sup>4+</sup>, B<sup>3+</sup>, X<sup>-</sup> (F<sup>-</sup>, Cl<sup>-</sup>, Br<sup>-</sup>)) leads to a band gap narrowing which could shift its light response region into the visible spectrum. Increasing the width of the valence band causes the upper edge of TiO<sub>2</sub> VB moving upward, meanwhile the lower edge of conduction band position remains unchanged. Therefore, the

anion-doped  $\text{TiO}_2$  should be able to reduce protons for hydrogen production under visible light due to the narrowed band gap. On the other hand, the upward shift of VB may reduce the oxidation power of doped photocatalyst under visible light. The electron-hole recombination possibility becomes higher. However, anions are less likely to form recombination centers than metal cations.

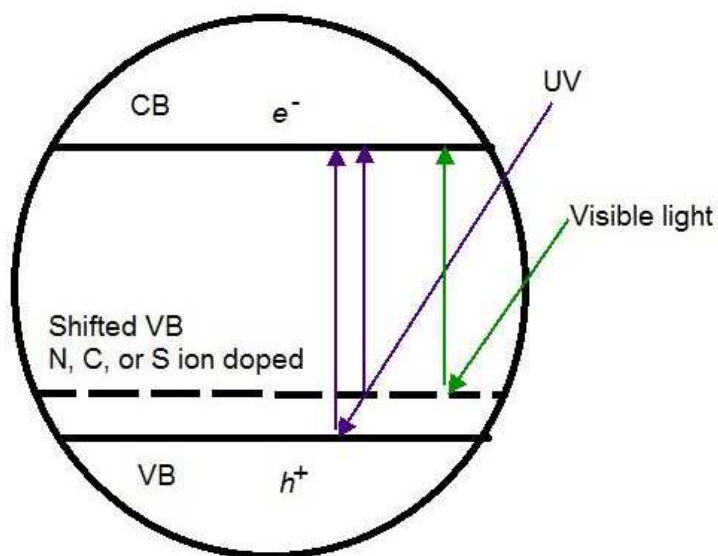


**Figure 2.7 Energy Diagrams Illustrating  $\text{TiO}_2$  Doped with Anion under UV and Visible Light**

*Advantage:* Anions are less likely to form recombination centers and are more effective to enhance the photocatalytic activity under visible light by narrowing the band gap through shifting the VB edge upwards.

*Disadvantage:* VB upward shift not only results in a narrow band gap, but also produces holes with less oxidation power. Additionally, the electron-hole recombination possibility is higher. For efficient photocatalytic reaction, coupling with other technologies, such as noble metal loading or electron donor addition, is necessary. Normally Over-doping (>1%) will reduce the photocatalytic efficiency.

Among anions, N, C, and S are the most researched substances utilized as dopant in improving TiO<sub>2</sub> photocatalyst.

Nitrogen was introduced by hydrolytic or sol-gel process using TiCl<sub>4</sub> [124] or Ti(SO<sub>4</sub>)<sub>2</sub> [125] and NH<sub>3</sub> solution. The N-doped TiO<sub>2</sub> was capable of decomposing acetaldehyde or 2-propanol to CO<sub>2</sub> under visible light illumination. Also NH<sub>3</sub> annealing is widely used to dope N into TiO<sub>2</sub> by using temperature to control the percentage of N substitution [126].

In N-doped TiO<sub>2</sub> oxygen sites were substituted by nitrogen atoms, TiO<sub>2-x</sub>N<sub>x</sub>, the substitutional doping of N contributes to the band gap narrowing by mixing of N 2*p* and O 2*p* states together. The quantum efficiency of the system was higher under UV light than that observed under visible light. This may be explained as formation of an isolated narrow N 2*p* band above the valence band of the TiO<sub>2-x</sub>N<sub>x</sub> photocatalyst. Illumination with UV light causes excitation of electrons in both the valence band and narrow band, but irradiating with visible light only excites electrons in the narrow band (Figure 2.7). The decrease in quantum yield of TiO<sub>2-x</sub>N<sub>x</sub> photocatalytic system with increasing *x* values in organic photodecomposition could be explained in terms of recombination of holes and electrons promoted by extra oxygen vacancies/doping sites. The same theory also can be used as a reasonable explanation for similar anion doping such as S<sup>4+</sup>, C<sup>4+</sup>. It is also possible that the upper edge of the narrow band has been shifted too close to CB, and the recombination of electron and holes is much easier. Therefore, an optimal value of the amount of loaded anion is necessary. Research found that PCA of the N-doped TiO<sub>2</sub> with anatase phases was found to be higher than that of the commercial TiO<sub>2</sub> photocatalyst *Degussa* P25 for phenol decomposition under visible light irradiation, while *Degussa* P25 showed higher PCA under sunlight irradiation.

C-doped TiO<sub>2</sub> method resulted in the shifting of the upper level of the valence band towards negative potential during band gap narrowing in the carbon-doped TiO<sub>2</sub> powder, which

led to a decrease in the oxidizing power. Several synthesis methods had been applied to achieve C-doped TiO<sub>2</sub>. Irie H. et al. research showed carbon-doped anatase phase TiO<sub>2</sub> powders were obtained by oxidizing commercial TiC powders [127]. The carbon substitution caused the absorbance edge of TiO<sub>2</sub> to be shifted to the higher wavelength region. Carbon-doped TiO<sub>2</sub> showed PCA for the decomposition of IPA to CO<sub>2</sub> via acetone under visible light (400-530nm) irradiation. Pyrolysis of the alcohols employed in the sol-gel process by using different alkoxide precursors lead to carbonaceous species embedded in the TiO<sub>2</sub> matrix.[128,129]. TiCl<sub>4</sub> and tetrabutylammonium hydroxide were used in preparation of C-doped TiO<sub>2</sub> via hydrolysis process, after calcined at 400C completely mineralize 4-CP under visible light 455nm [130], sample also can be supported on filter paper and photocatalyze the oxidation of gaseous benzene, acetaldehyde and CO.

S-doped TiO<sub>2</sub> can be achieved in similar ways as C, N doped. For example, heating TiS<sub>2</sub> powder at 300-600 °C in air, the product shows have an anatase structure [131], the mixing of the S 3p states with TiO<sub>2</sub> VB increases the width of the VB itself. This results in a decrease in the band gap energy. The band gap energies calculated for TiO<sub>2-x</sub>S<sub>x</sub> and TiO<sub>2</sub> are 1.4 and 2.3 eV, respectively. The oxidation state of the S atoms incorporated into the TiO<sub>2</sub> particles were determined to be mainly S<sup>4+</sup> from X-ray photoelectron spectra (XPS) spectra. In addition, thiourea has been used in a sol-gel process to introduce S into TiO<sub>2</sub> for decomposition of methylene blue and 2-propanol under visible light [132]. However, decreasing of PCA due to catalytic poison caused by oxidation of SO<sub>2</sub> to SO<sub>4</sub><sup>2-</sup> has also been reported.

#### d. Metal ion (cation) doping

Doping TiO<sub>2</sub> by using metal ions has been widely studied. Similar to metal particles loaded on TiO<sub>2</sub> surface, metal ions work as electron traps that reduce the possibility of electron-

hole recombination, consequently resulting in efficient separation. There are many ways of depositing metal ions on to the TiO<sub>2</sub> semiconductor, but the two major ways of doing so are:

*Ion Implantation:* Physical implantation by bombarding the photocatalyst with high-energy metal ion beams, these highly energized ions are injected into the lattice and interact with TiO<sub>2</sub> and substitute with Ti<sup>4+</sup> ions. This process modifies TiO<sub>2</sub> electronic structure and cause redshift to the visible region (up to 600 nm); the mixing of Ti *d* orbital of Ti-O with metal *d* orbital of the implanted metal ions leads to band gap narrowing.

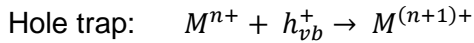
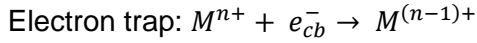
The order of effectiveness in resulted redshift was found to be V>Cr>Mn>Fe>Ni in ion implantation. Such redshift were observed only after calcination of the metal ion implanted TiO<sub>2</sub> photocatalyst was done in oxygen at around 450~550 °C. It implied that metal ion implantation modified the electronic structure of TiO<sub>2</sub> in a way different from chemical doping that formed impurity energy levels in the band gap of TiO<sub>2</sub>. Presently metal ion implanted TiO<sub>2</sub> is believed to be the most effective photocatalyst for solar energy utilization and is in general referred as the “second generation photocatalyst”.

*Chemical doping:* Metal ions are chemically doped into the TiO<sub>2</sub> semiconductor through the chemical synthesis processes such as the sol–gel, co-precipitation and impregnation.

The total induced modification of the photocatalytic activity is made up from the sums of changes, which occur in the light-absorption capability, adsorption capacity of the substrate molecules, and interfacial charge transfer rate.

Helping photocatalyst absorb light in the visible region of the spectrum is the most desirable effect of this process. As metal ions are embedded into the TiO<sub>2</sub> lattice, impurity energy levels in the band gap of TiO<sub>2</sub> are formed, in another words, it introduces intra-band gap

states to exist within the band gap. Furthermore, electron (hole) transfer between metal ions and TiO<sub>2</sub> can alter electron-hole recombination as



The energy level of M<sup>n+</sup>/M<sup>(n-1)+</sup> should be more positive (lower) than the CB lower edge of TiO<sub>2</sub>, while the energy level of M<sup>n+</sup>/M<sup>(n+1)+</sup> should be more negative (higher) than the VB upper edge of TiO<sub>2</sub>. The typical examples of M<sup>n+</sup>/M<sup>(n-1)+</sup> are Fe<sup>3+</sup>/Fe<sup>2+</sup>; Cu<sup>2+</sup>/Cu<sup>+</sup>/Cu; Ag<sup>+</sup>/Ag, Cr<sup>6+</sup>/Cr<sup>3+</sup>.

In photocatalytic reactions, interfacial charge carrier transferring is as important as carrier trapping. Only if the trapped electron and hole are transferred to the surface, photocatalytic reactions can occur. Therefore, metal ions should be doped near the surface of TiO<sub>2</sub> particles for better charge transferring. In case of deep doping, metal ions likely become new recombination centers, since electron/hole transferring to the interface is more difficult and slower. For photodegradation, the electron trap type metal ion is preferred, because holes and radicals generated by holes are the dominant factors in photooxidation of organic compounds, on the contrary, for hydrogen generation, hole trap is preferred since protons need to be reduced by e<sup>-</sup> to generate hydrogen.

*Advantage:* Doping of metal ions, serving as an electron scavenger, could expand the photo-response of TiO<sub>2</sub> into visible light spectrum (redshift). hν due to embedding metal ion into TiO<sub>2</sub> lattice.

*Disadvantage:* Near the surface doping of TiO<sub>2</sub> particles is necessary for a better charge transference, while deep doping of metal ions will likely behave as recombination centers. Meanwhile, there is an optimum concentration of doped metal ion (normally < 1 at%), above which the photocatalytic activity decreases due to the increase in recombination.

Different rare earth metal ions (La, Ce, Er, Pr, Gd, Nd and Sm) had been used as dopant into TiO<sub>2</sub>. Enhanced PCA and redshift of photo-response were observed at certain doping content. Doping with Gd ions were found to be most effective in enhancing the photocatalytic activity due to its highest ability to transfer charge carriers to the interface.

Except rare earth metal ions doping, transition metal ion doping has attracted more attention on improving the TiO<sub>2</sub> photocatalyst.

Fe<sup>3+</sup>, Mo<sup>5+</sup>, Ru<sup>3+</sup>, Os<sup>3+</sup>, Re<sup>5+</sup>, V<sup>4+</sup>, and Rh<sup>3+</sup> ions doping concentration at 0.1-0.5 at% level can increase photocatalytic activity, while dopants Co<sup>3+</sup> and Al<sup>3+</sup> ions cause detrimental effects [133]. The different effects of metal ions result from their abilities to trap and transfer electrons/holes. For example, Cu and Fe ions can trap not only electrons but also holes, and the impurity energy levels introduced are near to CB as well as VB edges of TiO<sub>2</sub>. Therefore, doping of either Cu or Fe ions is recommended. Metal salts used as precursors for dopant ions are listed as follows: LiOH, Mg(ClO<sub>4</sub>)<sub>2</sub>, AlCl<sub>3</sub>, VCl<sub>3</sub>, VOSO<sub>4</sub> • 3H<sub>2</sub>O, VOCl<sub>3</sub>, Cr(NO<sub>3</sub>)<sub>3</sub>, MnF<sub>3</sub>, Fe(NO<sub>3</sub>)<sub>3</sub>•9H<sub>2</sub>O, CoF<sub>3</sub>, NiCl<sub>2</sub>, Zn(ClO<sub>4</sub>)<sub>2</sub>, Ga(NO<sub>3</sub>)<sub>3</sub>, Zr(OCH(CH<sub>3</sub>)<sub>2</sub>)<sub>4</sub>, NbCl<sub>5</sub>, MoCl<sub>5</sub>, RuCl<sub>3</sub>, Rh(NO<sub>3</sub>)<sub>3</sub>•2H<sub>2</sub>O, SnCl<sub>4</sub>, SbCl<sub>5</sub>, TaCl<sub>5</sub>, ReCl<sub>5</sub>, and OsCl<sub>3</sub>.

Fe<sup>3+</sup>, Ru<sup>3+</sup>, Os<sup>3+</sup>, and Gd<sup>3+</sup> represent a special position among the metallic dopants. These four metal ions have a half-filled electronic configuration (*d5* and *f7*) that is known to be more stable. When these metal ions trap electrons, the half-filled electronic configuration is destroyed and their stability decreases. The trapped electrons can easily be transferred to adsorbed oxygen molecules on the surface of the TiO<sub>2</sub> catalyst while the metallic ions return to the original stable half-filled electronic configuration. This might promote charge carrier transfer and efficient separation of the electrons and holes.

For  $\text{Fe}^{3+}/\text{Fe}^{2+}$ ,  $\text{TiO}_2$  particles can be doped by iron(III) ions, form mixed oxides or mixtures of simple and mixed oxides. Various Fe–Ti mixed oxides can be formed, like  $\text{Fe}_2\text{TiO}_5$  (pseudobrookite),  $\text{Fe}_2\text{Ti}_3\text{O}_9$  (pseudorutile), and  $\text{Fe}_2\text{Ti}_2\text{O}_7$ . Iron ion doping has several important advantages compared to other transition metal ions.

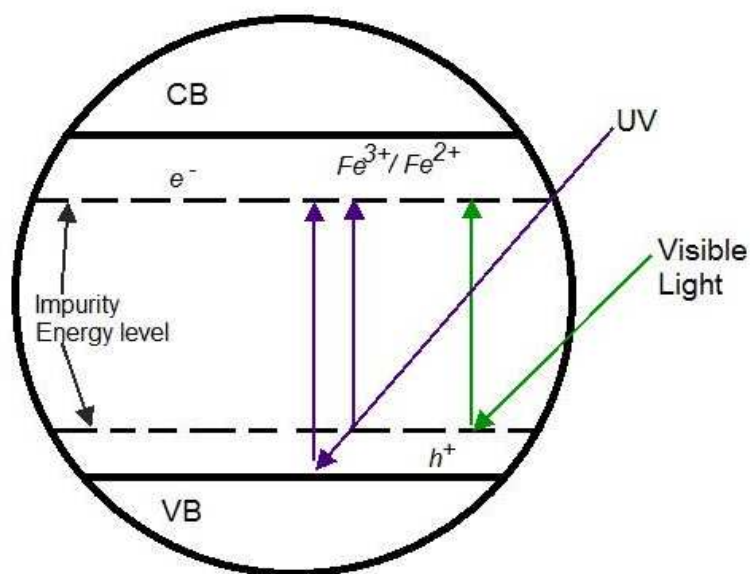


**Figure 2.8 Energy Diagrams Illustrating  $\text{TiO}_2$  Doped with Iron Ions under UV and Visible Light**

First, iron cations have a large influence on the charge-carrier recombination time. Doping with 0.5 at%  $\text{Fe}^{3+}$  drastically increases the charge-carrier lifetime, which can be extended to minutes and even hours. But in intrinsic  $\text{TiO}_2$ , the mean lifetime of an electron–hole pair is about 30 ns.

Second, iron ion doping induces a batho-chromic effect (Red Shift). An enhancement of photo-response edge of  $\text{TiO}_2$  from 380 nm to higher wavelengths and a higher absorbance in the range 400–650 nm compared to pure titania is observed.

Third, using iron-doped photocatalyst is efficient in several important photocatalytical reduction and oxidation reactions, which include photoreduction of nitrogen to ammonia, water splitting in the absence of  $N_2$  with high yields on Fe-TiO<sub>2</sub> catalyst, photooxidation of neat toluene towards benzaldehyde with O<sub>2</sub> presence, and photooxidation of oligocarboxylic acids, 4-nitrophenol, o-cresols, and dichloroacetic acid.

e. Composite Semiconductor (Coupled Photocatalysts)

The coupling of two semiconductors, possessing different energy levels for their corresponding conduction bands and valence bands (different band gap position), provides an approach to achieve a more efficient charge separation, an increased lifetime of the charge carriers and an enhanced interfacial charge transfer to adsorbed substrates. Direct mixing of these two semiconductors physically (blending, ball milling) and precipitation of one semiconductor over another (support, thin film) including sol-gel dip coating are main preparation methods. For example, a MO<sub>x</sub>-TiO<sub>2</sub> composite thin film electrodes obtained by a sol-gel process has two aims: (A) extending the light adsorption spectrum and improving the efficiency of the light; (B) suppressing the recombination of photogenerated electron/hole pairs. The current commercialized photocatalyst *Degussa P25* has been reported that it is composed of 70-75% anatase TiO<sub>2</sub> (E<sub>g</sub>= 3.2 eV) and 20-25% rutile TiO<sub>2</sub> (E<sub>g</sub>=3.0 eV), it is a simple composite semiconductor with two different crystal structure phases of the same chemical.

*Advantage:* When a large band gap semiconductor (For example TiO<sub>2</sub>) is coupled with a small band gap semiconductor (For example CdS, WO<sub>3</sub>), photoexcited CB electrons on the semiconductor which has the higher conduction band will transfer to another semiconductor's CB which has the lower conduction band in this composite semiconductors catalyst. Meanwhile, photoexcited VB holes on the semiconductor which has lower valence band will transfer to

semiconductor's which has the higher valence band in the composite semiconductor system, Thus, a wide electron-hole separation is achieved (Shown in Figure 2.9).

Successful coupling two semiconductors for photocatalytic water-splitting (hydrogen production) under visible light irradiation can be achieved, when (a) all semiconductors are photocorrosion free; (b) the small band gap semiconductor can be excited by visible light; (c) the CB of the small band gap semiconductor should be more negative than that of the large band gap semiconductor; (d) the CB of the large band gap semiconductor should be more negative than  $E_{H_2/H_2O}$ ; (e) electron injection should be fast as well as efficient.

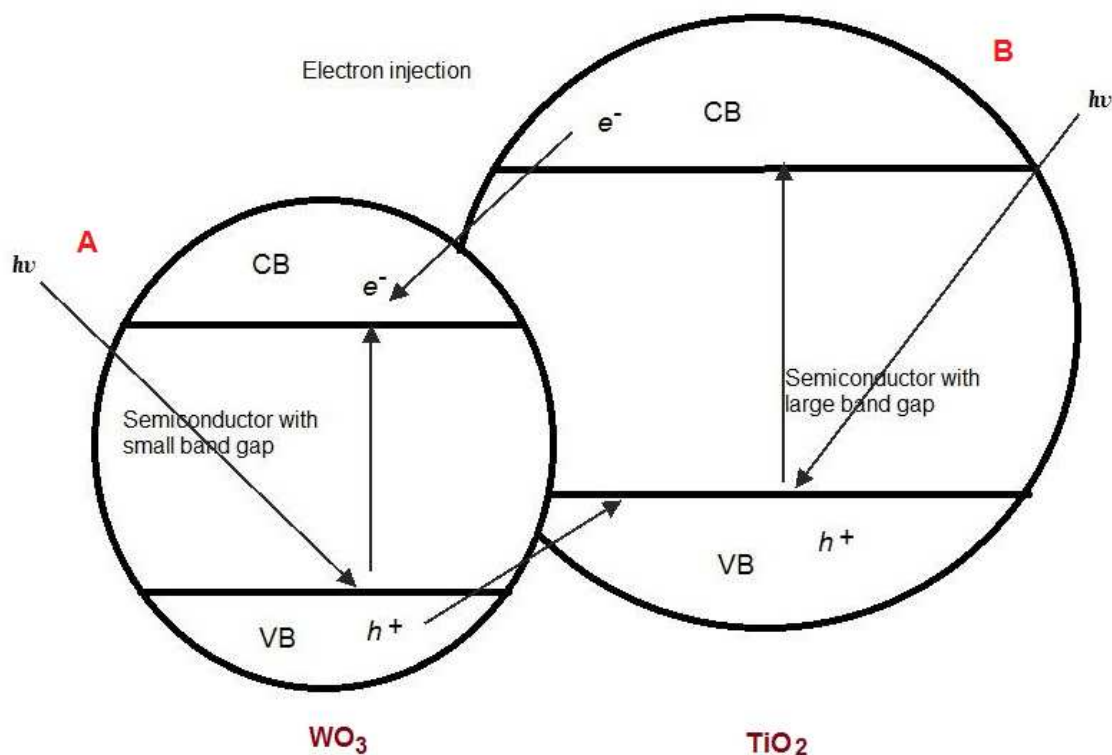


**Figure 2.9 Schematic Representation of Charge Carrier Separation in the Photoexcited  $WO_3/TiO_2$  Photocatalyst.**

*Disadvantage:* In some case, sacrificial agent, EDTA, has to be added to scavenge VB holes on small band gap semiconductors; otherwise, photocorrosion of the small band gap

semiconductor would occur, and more toxic compound would release and remain in target remediation system and cause secondary contamination.

Two possible cases could occur when a composite semiconductor is exposed to light. In first case, only the small band gap semiconductor (A) is illuminated but the other semiconductor (B) is non-activated. If incident photons that are not energetic enough to excite the large band gap semiconductor are energetic enough to excite the small band gap semiconductor, photoexcited electron/hole pairs are only created in the small band gap semiconductor's CB and VB, the electron is transferred to the conduction band of B, while the hole remains on A's VB. This inter-particle electron transfer therefore yields an irreversible vectorial electron transfer, under certain conditions, for example, only visible light is incident. In second case, both A and B are illuminated. A vectorial transfer of  $e^-$  and  $h^+$  from one semiconductor to another occurs: electrons are accumulated at the lower lying CB of one semiconductor, while the holes accumulate at the VB of the other semiconductor. For example, when solar light is incident, the smaller band gap semiconductor determines the capability of visible light absorption on composite semiconductor. The crucial parameters of composite SC for efficient charge separation include a proper placement of the individual semiconductors, optimal thickness of the covering semiconductor, geometry of particles, surface texture, and particle size.

CdS, CdSe,  $WO_3$ ,  $Bi_2S_3$ ,  $Fe_2O_3$ , ZnO and  $SnO_2$  have been studied as coupling SC with  $TiO_2$ . [134-139]. ZnO has been reported to be photoactive for phenol and nitrophenol degradation in spite of some photocorrosion effects in the liquid–solid phase [78]. From a practical viewpoint, utilization of CdS alone or in coupled systems is not desirable owing to the significant quantities of toxic cadmium that are released into aqueous media from the photoanodic corrosion of the CdS-based system [63].

Tungsten(VI) oxide, also known as Tungsten trioxide ( $\text{WO}_3$ ), has received more attention because of its potential for many applications such as manufacturing tungstates for x-ray screen phosphors, for fireproofing fabrics, in gas sensors or novel electrochromic windows. Experimental data determined that hexagonal  $\text{WO}_3$  has 2.8 eV indirect band gap. The conduction band potential ( $E_{\text{CB}}$ ) of  $\text{WO}_3$  is less negative than the reduction potential of aqueous electrolyte  $E(\text{H}^+/\text{H}_2)$ , which make it less favorable to be used as an efficient photocatalyst alone. However, it becomes a favorable choice for coupling with another large band gap semiconductor material (such as  $\text{TiO}_2$ ), which has less photo-response to visible light, to achieve a better charge separation in a composite semiconductor system. In addition,  $\text{WO}_3$  has high photocorrosion stability and as low a toxicity as  $\text{TiO}_2$ .

Both  $\text{WO}_3$  and  $\text{TiO}_2$  are n-type semiconductors alone and when they are coupled. The electron transport properties across the junction are similar to those across a Schottky barrier. After two semiconductors are in contact, thermal equilibrium is reached, and formation of space charge layer associated with necessary band bending in the junction zone is achieved. The electrons transferred from the high conduction band edge of  $\text{TiO}_2$  to the less negative conduction band edge of  $\text{WO}_3$  also help create the space charge zone. Recently,  $\text{TiO}_2/\text{WO}_3$  coupling photocatalyst has attracted more attention for creating a new photocatalyst that can work in both UV and visible light environments. Lin et al. [140] produced  $\text{WO}_3/\text{TiO}_2$  by incipient wetness method. The resultant photocatalyst powder had shifted the band gap to 2.62 eV and decomposed 4-chlorophenol under visible light irradiation; however, it had low photo activity under UV region. Chai et al. [141] also used incipient wetness method to manufacture  $\text{WO}_3/\text{TiO}_2$  nanoparticles that were able to decompose VOC and 2-propanol gas under visible light.  $\text{WO}_3/\text{TiO}_2$  film prepared by Song et al. [142] was 2.8-3 times more effective than pure  $\text{TiO}_2$  film in decomposing gas-phase 2-propanol.

#### f. Co-doping

When only one method or one dopant has obvious advantage and disadvantage, then a second method or additional second dopant may work as complementary to the first one when using them together. Recently, co-doped  $\text{TiO}_2$  showed better photocatalytic activity than one made by single component doping such as anion doping, transition metal ion doping, or composition semiconductor. Ohno, T et al. [91] used  $\text{C}^{4+}$  and  $\text{S}^{4+}$  cation co-doped  $\text{TiO}_2$ , atomic percentage of  $\text{C}^{4+}$  and  $\text{S}^{4+}$  are 0.2% and 0.1% respectively. The absorption edge of rutile  $\text{TiO}_2$  powder was largely shifted from 400 to 700 nm. Results of photocatalytic oxidation of 2-methylpyridine and methylene blue (MB) by using the  $\text{C}^{4+}$  and  $\text{S}^{4+}$  co-doped  $\text{TiO}_2$  photocatalyst with rutile phase showed the superior efficacy of the system than fine anatase  $\text{TiO}_2$  photocatalyst under a wide range of incident light including visible light. Another Ohno's work showed that the photocatalytic activities of S or N-doped  $\text{TiO}_2$  photocatalysts combined with adsorbed Iron(III) ion doping were significantly improved for oxidation of 2-propanol compared to those of S or N-doped  $\text{TiO}_2$  without metal ion doping under both UV light and visible light [143,144]. Kim, S.W. et al. [92] reported that Zr- $\text{TiO}_2$ -S systems which were synthesized by a modified sol-gel method are very effective visible-light active photocatalysts for degradation of toluene. All reactions follow pseudo 1<sup>st</sup>-order kinetics with the decomposition rate reaching as high as 77% within 4h. The catalytic activity decreases in the following order: Zr- $\text{TiO}_2$ -S >  $\text{TiO}_2$ -S > Zr- $\text{TiO}_2$  >  $\text{TiO}_2$  = *Degussa P-25*, and the catalytic performance is found to be a function of Zr-contents as follows: 3 wt% Zr- $\text{TiO}_2$ -S > 0.5 wt% Zr- $\text{TiO}_2$ -S > 5 wt% Zr- $\text{TiO}_2$ -S > 1 wt% Zr- $\text{TiO}_2$ -S.

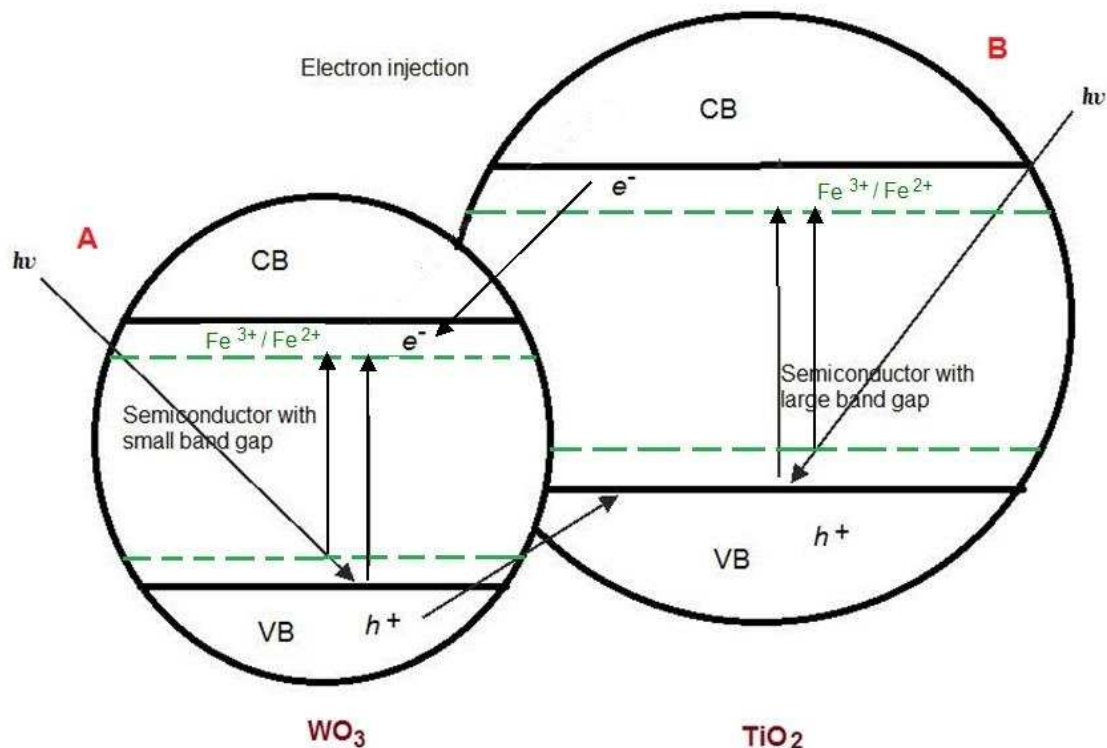


**Figure 2.10 Possible Mechanisms for Transition Electron Transfers Involving Composite Semiconductor Catalyst and Transition Metal Ion**

As previously mentioned,  $\text{TiO}_2$  doping with transition metal ions chooses trapping the electrons to facilitate an effective charge separation. The novel work we performed in this report involves combining both composite semiconductor and transition metal ions together in one single synthesis step.  $\text{WO}_3$  has high photo-corrosion stability and low toxicity like or similar to  $\text{TiO}_2$ , and smaller band gap (2.8 eV) and a suitable conduction band potential to allow photo excited electron transfer to  $\text{WO}_3$  conduction band from  $\text{TiO}_2$  conduction band. The composite photocatalyst features a smaller band gap which is more desirable for photodegradation under visible light. Iron (III) ion enables electron transfer to  $\text{Fe}^{3+}$  ( $\text{Fe}^{3+} + \text{e}^- \rightarrow \text{Fe}^{2+}$ ) to avoid the fast  $\text{e}^-/\text{h}^+$  recombination. Possible mechanisms are shown in Figure 2.10. There may be two possible ways for electrons to be excited from the valence band to the conduction band and leave a positive hole in the conduction band when the sample is exposed to the light [145].

## CHAPTER 3

### BACKGROUND: SUPERCRITICAL FLUIDS AND SOL-GEL

In this chapter, a broad literature review of supercritical fluid (SCF) technology including properties of SCF, supercritical fluid extraction and drying, supercritical fluid impregnation and solubility of organometallic complexes and non-ionic surfactant in SCFs is first given. Lastly, in the second section, sol-gel chemistry, sol-gel aging, drying and heat treatment, and surfactant as template selection are discussed.

#### 3.1 Supercritical Fluid Technology

For any pure substance, there is a transition state called the “critical state”: for temperatures below the critical temperature  $T_C$  or for pressures below the critical pressure  $P_C$ , two phases co-exist, liquid and vapor. As the critical state is approached, the density of the liquid begins to decrease while the density of the vapor increases until a single point is reached. This point at a certain pressure and temperature is called the critical point (CP). On a phase diagram, it is the point where the liquid phase-gas phase boundary disappears. The critical point represents the highest temperature and pressure at which the substance can exist as a vapor and liquid in equilibrium. When temperature and (or) pressure exceed the critical temperature and pressure ( $T > T_C$ ,  $P > P_C$ ) the two phases, liquid and vapor become indistinguishable, and only one phase exists. This is called the supercritical phase. Supercritical fluid (SCF) is defined as a substance above its critical temperature ( $T_C$ ) and critical pressure ( $P_C$ ). Figure 3.1 shows the phase diagram of pure carbon dioxide to explain the phase boundaries and changes.

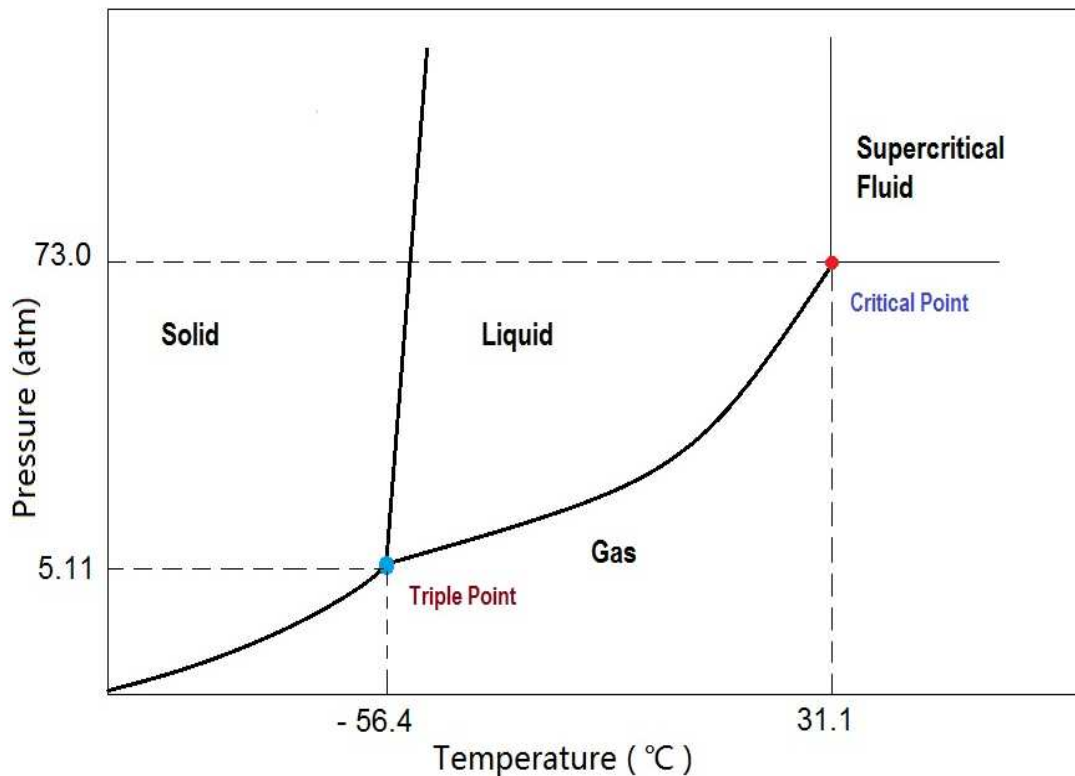


**Figure 3.1 Phase Diagram for Carbon Dioxide (CO<sub>2</sub>)**

Compared with traditional liquid solvents, supercritical fluids reveal several unique physical properties including a greater diffusivity ( $D$ ), a tunable equivalent density ( $\rho$ ), and a lower viscosity ( $\mu$ ) [146]. Supercritical fluid technology has become very attractive for these stated reasons. Even though the first plant using supercritical fluid technology was built over 40 years ago in North America, it is only now that we see its wide applications in many fields. Supercritical fluid technology offers numerous advantages compared to conventional processes, such as high mass transfer rate, reduced unit, and lower operating costs and environmentally benign processing [147]. Extraction and purification, particle production, impregnation, analytical application, solvent replacement and green chemistry are the most popular attributes of supercritical fluid processing [148].

### 3.1.1 Properties of Supercritical Fluids

Properties of supercritical fluids (SCFs) are different from those of ordinary liquids and gases being tunable simply by changing the pressure and temperature. In particular, density and viscosity change drastically at conditions close to the critical point which greatly affects the solvent activity. Mass transport properties such as viscosity and diffusivity are similar to those of gases; therefore, improved mass transport rates are achieved in supercritical fluids. Indeed, the viscosities of supercritical fluids are lower than liquid solvents, but higher than gases. The diffusivities of the solute in SCFs are also intermediate between those of gases and liquids. Both of these properties reveal that the density of SCFs is also in between those of gases and liquids, but closer to liquids. Therefore, SCFs is capable of dissolving many organic and inorganic compounds which might not be soluble in gases at relatively low temperature. Furthermore, the solvating power of SCFs is tunable because the density of SCFs is also easily tunable with merely changing the pressure at a constant temperature.

In general, supercritical fluids have the mobility of gases and the solvating power of liquid solvents resulting in efficient permeation into porous matrices, high mass transport rate and high solvency. A general comparison of the magnitude of some of the important properties for liquids, gases, and supercritical fluids in the near critical region is listed [149] in Table 3.1.

The thermodynamic properties of supercritical mixtures are very complex. The Peng-Robinson (PR) equation of state [150] has been one of the models of choice used to describe chemical system behavior. The PR equation of state is a slight adjustment to the attractive and repulsive forces represented by Van der Waals' hard sphere equation. Peng-Robinson EOS (Equation 3.1) does very well in correlating the experimental data and representing the phase behaviors.

The PR equation of state takes the following form:

$$P = \frac{RT}{v-b} - \frac{a(T)}{v(v+b)+b(v-b)} \quad (3.1)$$

PR equation also can be rewritten as cubic form

$$Z^3 - (1 - B)Z^2 + (A - 3B^2 - 2B)Z - (AB - B^2 - B^3) = 0 \quad (3.2)$$

where

$$Z = \frac{Pv}{RT} \quad (3.3)$$

$$A = \frac{aP}{R^2T^2} \quad (3.4)$$

$$B = \frac{bP}{RT} \quad (3.5)$$

Equation (3.2) yields one or three roots depending upon the number of phases in the system. In the two-phase region, the largest root of Z is for the compressibility factor or molar volume of vapor while the smallest positive root corresponds to that of the liquid.

**Table 3.1 Properties of Gases, Supercritical Fluids and Liquids**

<b>Physical Properties</b>	<b>GAS</b>	<b>Supercritical Fluid</b>	<b>Liquid</b>
Density $\rho$ , (kg/m <sup>3</sup> )	0.6-2.0	200-500	600-1600
Diffusivity, D, (10 <sup>-6</sup> m <sup>2</sup> /s)	10-40	0.07	0.0002-0.002
Dynamic Viscosity, $\eta$ , (mPa s)	0.01-0.3	0.01-0.3	0.2-3
Kinematics' Viscosity, $\nu$ , (10 <sup>-6</sup> m <sup>2</sup> /s)	5-500	0.02-0.1	0.1-5
Surface Tension, $\sigma$ , (dynes/cm)	-	-	10-400
Thermal Conductivity, k, (W/m K)	0.01	0.1	0.1

The three most popular supercritical fluids are carbon dioxide, propane and water. Among them, special attention and research have been paid to carbon dioxide (CO<sub>2</sub>) because of its convenient critical parameters ( $T_c=31.1$  °C and  $P_c=73$  atm), non-toxicity, inflammability, availability, physiological compatibility, low cost, recyclability and environmental benignancy.

Carbon dioxide is not classified as a volatile organic chemical (VOC), instead, supercritical CO<sub>2</sub> is considered as a green solvent by its nature. At near ambient temperature, under acceptable pressure, carbon dioxide, operates as an excellent supercritical solvent, and is typically used to process low-volume and high-value products. This includes food, pharmaceuticals, fine chemicals, and cosmetics, which should be carried out at temperatures as close as possible to ambient temperature to avoid thermal degradation and without the use of hazardous chemicals [147]. There are also a number of practical advantages associated with the use of supercritical carbon dioxide as a processing solvent. For example, product isolation to total dryness is achieved by simple evaporation after pressure released. This could prove to be particularly useful in the final steps of pharmaceutical syntheses where even trace amounts of solvent residues are considered problematic. It is also commonly used as an antisolvent for active pharmaceutical compounds by means of recrystallization from organic solvents using such processes as gas antisolvent re-crystallization (GAS) [151], precipitation with compressed antisolvent [152] and supercritical antisolvent process (SAS) [153,154].

All solvents including pure supercritical fluids have their own selectivity. At certain temperatures and pressures, some substances are not soluble in supercritical fluids, for this reason the addition of a small amount of a co-solvent/entrainer will be helpful. Co-solvents have the ability to improve the solubility of desired components in supercritical fluid as they provide the required interactions for solubilizing the desired compound. Alcoholic solvent, methanol and ethanol are two popular choices for co-solvents as they are both soluble in supercritical CO<sub>2</sub> at relative low pressures and temperatures [155, 156]. Even ethanol and CO<sub>2</sub> can be considered

as miscible supercritical liquids at certain conditions. In this work, ethanol was already chosen as the solvent in sol-gel process, so ethanol inside alcogel would be considered as co-solvent in the supercritical extraction and drying step. In the supercritical impregnation step, extra ethanol was fed into system as co-solvent by the HPLC pump.

### **3.1.2 Supercritical Fluid Extraction and Drying**

The tunable density and compressibility make supercritical fluids adjustable solvents with a continuous transition between “excellent” solvents under supercritical conditions and “poor” solvents in the state of a compressed gas. Most processes are based on these solvent power variations [157].

Supercritical fluid extraction has been traditionally applied in the food and pharmaceutical industries, especially for the nutraceutical area where extraction is done with  $\text{SCCO}_2$  which does not leave any toxic residues in the final product. Nutraceuticals are natural extracts from plants or natural products that contain physiological or health benefits. The first industrial application of supercritical fluids was a coffee decaffeination plant in 1978, followed by a hops extraction plant in 1982. During the 80's and 90's industrial and lab research in supercritical fluids were mainly focused on extraction processes from liquid and solid matrices. Nowadays, Supercritical fluids techniques are being widely used and developed in many applications, such as, remediation of soil, chemical reaction and synthesis of polymers and organic compounds, impregnation and in situ encapsulation, removal of nicotine from tobacco, nucleation and particle size control, cleaning electronic parts and decaffeinating of green coffee beans.

In the method of extraction and drying using supercritical fluids, the selectivity and extractability of the objectives are highly determined by their solubility in supercritical fluids. This is accomplished by tuning the density of the supercritical fluid through minutely adjusting the

processing temperature or pressure, or by adding co-solvents to enhance the solvating power for specific compounds.

The approaches to drying of wet porous material like alcogel are conventional evaporation, freeze-drying, and supercritical drying. All pore templates and solvents within the porous matrix should be removed before further functionalization or end-use. Supercritical drying methods evolved considerably since the pioneering work of Kistler where excess alcohol was added to the autoclave and then, heat was supplied so that supercritical conditions were reached. Subsequently, supercritical solvent was removed from the autoclave by depressurization above the critical temperature of the solvent [95]. The process of supercritical drying is a specific example of supercritical fluid extraction and it utilizes another property of SCF--low surface tension. Low surface tension accompanied by high diffusivity allows the supercritical fluids to penetrate into a porous matrix very affectively.

When compared to conventional drying for removal of conventional solvents, supercritical drying establishes a sustained single supercritical phase where drying is free from liquid-vapor phase interfacial stresses. This facilitates the production of aerogels that have the same morphological properties as their alcogel precursors. Whereas traditional evaporative extraction and drying uses solvents to separate and extract certain solutes of interest under ambient pressure or vacuum either with or without heating. Traditionally wet gel materials resulting from non-critical evaporative drying methods are defined as xerogels. Conventional evaporative drying uses solvents to separate and extract certain solutes of interest that have a large affinity with interfering matrix materials. As a liquid-vapor interfacial phenomenon, the evaporation of solvent from a sample surface or matrix is associated with severe capillary pressures that could cause permanent collapsing of fragile samples such as sol-gel porous structures. The best approach to minimize the capillary pressure acting on the sol-gel network during drying is to examine the following Equation 3.6

$$P = \frac{2\sigma \cos(\theta)}{r} \quad (3.6)$$

where  $P$  is capillary pressure,  $\sigma$  is surface tension,  $\theta$  is the contact angle between liquid and solid and  $r$  the pore radius. For a given pore size the capillary pressure can be reduced by using a solvent with a lower surface tension than the original solvent in the gel network [98,158] and/or eliminating the liquid-vapor interface with supercritical drying [159,160]. On the other hand, supercritical carbon dioxide offers considerable potential as a replacement for solvents in many extraction and drying processes, such as, extraction of solvents and monomers from polymer solutions.

High purity  $\text{CO}_2$  is the supercritical fluid medium of choice for most extractions. For reasons already stated, in supercritical drying, the supercritical fluid being used as the drying medium can be tuned to perform different levels of extractions in supercritical fractionation because the supercritical solvating power is tightly tuned and adjustable. One of several available pathways is based upon varying the density of the supercritical fluid through either or both of temperature and pressure during the process, the higher the density of the supercritical fluid, the higher the solvating power of that supercritical fluid and hence the higher drying rate achieved. A very small increase in pressure at or slightly above the critical temperature results in a dramatic increase in the density of the supercritical fluid. This is important when gradual extraction of a certain liquid phase is desired in a fractionation mode where a small incremental change in density is invoked with successive extraction. Supercritical fluid's density also can be varied via change in temperature when pressure is held constant above the critical pressure. Meanwhile, the value of viscosity and diffusivity are both dependent on temperature and pressure. In the case of gases, as the temperature increases, it leads to an associated increase in the viscosity of the gas, the opposite is observed in the case of the supercritical fluids. Whereas the viscosity of the supercritical fluids decrease with increasing the supercritical fluid

temperature making the drying process fast and less mass transfer limited. However, in general, drying is best accomplished by modifying supercritical fluid pressure, which is much easier than introducing temperature fluctuation throughout the entire supercritical extraction and drying process.

Another method to tune the solubility of the supercritical fluid is to modify the supercritical fluids to be able to entrain the solute from the solid phase in the drying process. For example, enhanced non-polar supercritical CO<sub>2</sub> produced by adding a small amount of miscible polar modifier such as ethanol and/or methanol is able to dissolve certain polar molecules which pure supercritical CO<sub>2</sub> has limited solving power to dissolve. The added fluid is referred to in the literatures as an entrainer, co-solvent or modifier. However, it should be noted that while modifiers enhance the solving power of the mixed supercritical fluid, they also interfere with the solute and influence the mass transfer rate. Such phenomenon is a result of the miscibility of the modifier in the liquid solute making the diffusion coefficient for the solute in the supercritical fluid much smaller than without the use of the modifier. In practice, a careful choice of the modifier should be done so that the chemical affinity for the solute in the supercritical fluid is enhanced and at the same time the diffusivity of the solute to the supercritical fluid is not greatly hindered.

In general, selecting a supercritical fluid system for extraction and drying purposes should be chosen based on the following considerations: phase behavior, co-solvent effects, transport properties of the supercritical fluids, molecular structure, polarity, solvent-matrix interaction, porosity of the matrix and solvent location within the matrix.

### **3.1.3 Supercritical Fluid Impregnation**

Impregnation with supercritical fluid, such as impregnating the matrices with dopants, is the reverse process of SFE. Impregnating active reagent in porous media or polymer systems is more effective and timesaving with supercritical fluids than traditional liquid solvents due to the

higher diffusivity of supercritical fluids. Moreover, the greater diffusivity of supercritical fluids allows one to achieve a homogeneous distribution of active compounds inside various porous matrices.

A simple supercritical fluid impregnation normally occurs in three steps.

a. Dissolving step

A desired amount of dopant is dissolved into supercritical fluid, the composition of supercritical fluid is depended on co-solvent choice and operating conditions. Solubility of dopant in supercritical fluid can be tuned by modifying system pressure, temperature or the fraction of co-solvent in supercritical fluid, if co-solvent is being used.

b. Diffusion step

The targeted matrix is permeated by a supercritical solution containing the dopant. This is a typical diffusion controlled step. Appropriate and sufficient diffusion time required.

c. Depressurizing step

A fast depressurization causes an extreme decrease in the solubility of the supercritical fluid and permits the solute deposition inside the porous matrix and precipitation on the surface while the supercritical solvent is rapidly vented out of the reactor.

This step can be iterated several times or system pressure can be reduced in stage, to achieve multiple layers of impregnation of the porous substrate. However, high depressurization rates are expected to result in considerable stress formation. The fluid outside the gel flows out of the reactor at a higher rate than the fluid flowing out of the gel-network. Due to differential pressure, the fluid in the gel network expands and stresses develop in the gel. Cracking of the porous substrate may occur when the stress exceeds the strength of the gel-network.

Early application examples of this concept are impregnation of colorants, aromas and pesticides in various matrices [161, 162]. Similarly, supercritical fluid dyes of textiles, especially polyesters, can be used as substitute to classical aqueous dyes which results in water pollution. Recently, as a novel green environmentally friendly technique, supercritical fluid impregnation has been used in more and more areas, such as polymeric materials, thin films and membrane formation, drug delivery and production of catalytic porous materials. Impregnation of organic dyes into glassy polymers [163-165], polymeric substrates modification [166], impregnation of organometallic compounds into polymer (PVC, PE or PVA) films [167], carbon molecular sieve membrane [168] or fuel cell membrane [169], hydrogel-type ophthalmic drug delivery applications [170,171] and preparation of SiO<sub>2</sub> based aerogel [172,173] were reported.

In this study, an organometallic compound, Ferrocene or bis( $\eta^5$ -cyclopentadienyl) iron (C<sub>10</sub>H<sub>10</sub>Fe or Fe(C<sub>5</sub>H<sub>5</sub>)<sub>2</sub>) is utilized as Iron ion precursor dopant in supercritical fluid impregnation experiments where ethanol is used as co-solvent to increase the doping effectiveness. Since temperature fluctuations may also cause material thermal expansion stress, which may result substrate cracking and weak spots formation, all experimental works described in this report were performed at designed constant temperatures.

### **3.1.4 Solubility in Supercritical Fluids**

By increasing the pressure of the gas above the critical point, it is possible to give the supercritical solvent liquid-like densities and solvating strengths. Near the critical point, the density of the gas will increase rapidly with increasing pressure. Therefore, the solubility of many compounds is several orders of magnitude greater than predicted from the classical thermodynamics of ideal gases. As the average distance between molecules decreases, non-ideal gas behavior will begin to govern the interactions between the solvent and the sample accounting for a tremendous enhancement in solubility. In the supercritical region, solving

power is a direct function of density, which in turn is a function of system pressure and temperature. Solving power of supercritical fluids can be finely tuned to solubilize or separate solutes and solvents by minutely manipulating the pressure and/or temperature. Usually, the solvent power of a supercritical fluid increases with density and vice versa. The solvent power of supercritical fluids is enhanced as the fluid density increases with pressure increments at a given temperature, whereas the supercritical fluid density is reduced by temperature augmentation at constant pressure. This is favorable for desorption, extraction, impregnation or regeneration processes. Because of the non-compressibility of conventional liquids, this phenomenon is unique to supercritical fluids.

The solubility of a solute in a supercritical fluid is one of the most important thermo-physical mixture properties. The solubility information is needed for the determination of Equation of State (EOS) interaction coefficients to allow prediction of the phase distribution of the solute. This information is used to understand the temperature-pressure dependence of the solubility in order to determine the appropriate operating conditions and procedures for different type of process. Researchers [174-176] had developed a number of different approaches to measure solute solubility for pure or multi-component supercritical fluids. These techniques are either dynamic, where the solute is continually removed within supercritical fluids at equilibrium conditions, or static, where known amounts of solute and solvents are preloaded into a cell where the pressure, temperature and/or volume can be adjusted to obtain the cloud point or equilibrium conditions.

It is even possible, by adding small quantities of miscible co-solvent, to customize a supercritical fluid for a specific application. Polar co-solvents, also known as modifiers or entrainers in different research reports, the most frequently used of which are ethanol and methanol; lead to increases in the selectivity and solving power because of solute molecules interacting with the co-solvent. McHugh and Krukonis [177] have found that many of the

behaviors observed in phase diagrams for multi-component mixtures are very similar to the phase diagrams for binary mixtures, even if the components vary in molecular size, shape, structure and/or attractive potential.

Much work has been done on the modification of supercritical CO<sub>2</sub> by adding one or more modifiers to increase the solvating power and selectivity for specific solutes such as surfactants and organometallic complexes. A summary of recent research work on the mole fraction solubility of transition metal complexes in supercritical CO<sub>2</sub> is shown in Table 3.2.

In this research, a non-ionic surfactant template—Triton X-114 was used as aerogel porous structure template to create a highly porous matrix in sol-gel during the preparation of TiO<sub>2</sub> based aerogel which was removed as effectively as possible through supercritical extraction and drying process. Meanwhile, Ferrocene employed as Iron ion precursors was impregnated into synthesized aerogels through supercritical fluid impregnation process. The affinity study on solubility of the non-ionic surfactant X-114 in different supercritical mixtures and conditions has been done experimentally and accurate models for calculating the solubility of this compound were also achieved [178].

**Table 3.2 Mole Fraction Solubility (x) of Transition Metal Complexes in Supercritical CO<sub>2</sub>**

<b>Metal complex</b>	<b>P, atm</b>	<b>T, °C</b>	<b>Density, g/ml</b>	<b>Solubility, x</b>	<b>Reference</b>	<b>Available/Supplier/Price</b>
<b>GROUP 4</b>						
TiCl <sub>4</sub>	100	76	0.23	0.09	[1]. Bartle, K. D.; Clifford, A. A.; Jafar, S. A.; Shilstone, G. F. <i>J. Phys. Chem. Ref. Data</i> <b>1991</b> , 20, 713-756.	SA, 89541,500ml,>98%,\$35.4
<b>GROUP 6</b>						
Cr(acac) <sub>3</sub>	200	60~40	0.73~0.85	1.2~1.1×10 <sup>-4</sup>	[2]. M. Ashraf-Khorassani, M.T. Combs and L.T. Taylor, Solubility of metal chelates and their extraction from an aqueous environment via supercritical CO <sub>2</sub> . <i>Talanta</i> <b>44</b> (1997), p. 755-763..	SA,202231,100g,>97%,\$31.2
	175	40	0.81	9.1×10 <sup>-5</sup>	[3]	
Cr(acacBr) <sub>3</sub>	200	40	0.85	1.3×10 <sup>-5</sup>	[3]	Synthesized [3]
	175	40	0.81	1.0×10 <sup>-5</sup>	[3]	
Cr(thd) <sub>3</sub>	200	40	0.85	4.5×10 <sup>-3</sup>	[3]	SA, 468223-1G,\$57.20
<i>trans</i> -Cr(thd) <sub>3</sub>	175	40	0.81	4.21×10 <sup>-3</sup>	[3]	Synthesized [3]
<i>mer</i> -Cr(tfa) <sub>3</sub>	200	40	0.85	2.0×10 <sup>-3</sup>	[3]	Synthesized [3]
<i>fac</i> -Cr(tfa) <sub>3</sub>	200	40	0.85	1.4×10 <sup>-3</sup>	[3]	Synthesized [3]
<i>cis</i> -Cr(tfa) <sub>3</sub>	175	40	0.81	1.139×10 <sup>-3</sup>	[3]	Synthesized [3]
Cr(hfa) <sub>3</sub>	200	60	0.73	>8.0×10 <sup>-3</sup>	[2]	
Mo(CO) <sub>6</sub>	103	51	0.39	9.2×10 <sup>-3</sup>	[4]. Warzinski, R. P.; Lee, C.-H.; Holder, G. D. <i>J. Supercrit. Fluids</i> , <b>1992</b> , 5, 71.	Pressure Chemicals, Pittsburgh, PA,

**Table 3.2 Continued**

GROUP 7						
Mn(acac) <sub>3</sub>	290	60	0.83	1.9×10 <sup>-7</sup>	[5]. Saito, N.; Ikushima, Y.; Goto, T. <i>Bull. Chem. Soc. Jpn.</i> 1990, 63, 1532-1534.	F-A, ac34378-0250,25g,\$42.1
Mn(acac) <sub>2</sub>	290	60	0.83	8.5×10 <sup>-8</sup>	[5]	
CpMn(CO) <sub>3</sub>	100	40	0.62	8.1×10 <sup>-3</sup>	[6]. Fedotov, A. N.; Simonov, A. P.; Popov, V. K.; Bagratashvili, V. N. <i>J. Phys. Chem. B</i> , 1997, 101, 2929-2932.	SA, 288055-1G,\$31.6
GROUP 8						
Fe(C <sub>5</sub> H <sub>5</sub> ) <sub>2</sub>	241	50	0.83	4.0×10 <sup>-3</sup>	[7]. Cowey, C. M.; Bartle, K. D.; Burford, M. D.; Clifford, A. A.; Zhu, S.; Smart, N. G.; Tinker, N. D. <i>J. Chem. Eng. Data</i> 1995, 40, 1217-1221. [8] Bartle, K. D.; Burford, M. D.; Clifford, A. A.; Cowey, C. M. <i>Measurement of the solubility of metal complexes in supercritical fluids</i> ; Bartle, K. D., Burford, M. D., Clifford, A. A., Cowey, C. M., Eds.; International Society for the Advancement of Supercritical Fluids: Strasbourg, 1994; Vol. 1, pp 419-422	SA
GROUP 9						
Co(fddc) <sub>2</sub>	100	50	0.41	8.8×10 <sup>-5</sup>	[9]. Lin, Y. H.; Smart, N. G.; Wai, C. M. <i>Trends Anal. Chem.</i> 1995, 14, 123-133. [10]. Laintz, K. E.; Wai, C. M.; Yonker, C. R.; Smith, R. D. <i>J. Supercrit. Fluids</i> , 1991, 4, 194-198.	

**Table 3.2 Continued**

	100	50	0.40	$5.3 \times 10^{-5}$	[10]	
Co(ddc) <sub>2</sub>	100	50	0.41	$2.6 \times 10^{-7}$	[9],[10]	
	100	50	0.40	$1.6 \times 10^{-7}$	[10]	
Co(acac) <sub>3</sub>	290	60	0.83	$9.4 \times 10^{-8}$	[5]	SA,C83902,25g,98%,\$34.4
Co(acac) <sub>2</sub>	290	60	0.83	$5.2 \times 10^{-8}$	[5]	
<b>GROUP 10</b>						
Ni(fddc) <sub>2</sub>	100	50	0.41	$7.9 \times 10^{-5}$	[9], [10]	Synthesized [15]
	100	50	0.40	$4.8 \times 10^{-5}$	[10]	
Ni(ddc) <sub>2</sub>	100	50	0.41	$9.4 \times 10^{-8}$	[9], [10]	Synthesized [15]
	100	50	0.40	$6.0 \times 10^{-8}$	[10]	
Ni(hfa) <sub>2</sub>	200	60	0.73	$4.9 \times 10^{-4}$	[2]	SA, 339709-5G, 98%,\$43.5
	200	60	0.73	$8.0 \times 10^{-3}$	[2]	
NiCl <sub>2</sub> [P(C <sub>6</sub> H <sub>5</sub> ) <sub>3</sub> ] <sub>2</sub>	220	45	0.83	$3.6 \times 10^{-6}$	[11]. Palo, D. R.; Erkey, C. <i>J. Chem. Eng. Data</i> 1998, 43, 47-48.	SA, 15245-5G,>98%,\$14.6
<b>GROUP 11</b>						
Cu(fddc) <sub>2</sub>	100	50	0.41	$1.0 \times 10^{-4}$	[9], [10]	Synthesized [15]
	230	60	0.77	$4.0 \times 10^{-3}$	[13]. C.M. Wai, S. Wang and J.-J. Yu, Solubility parameters and solubilities of metal dithiocarbamates in supercritical carbon dioxide. <i>Anal. Chem.</i> 68 (1996), p. 3516.	[15]. Laintz, K. E.; Wai, C. M.; Yonker, C. R.; Smith, R. D. <i>Anal. Chem.</i> , 1992, 64, 2875-2878.
Cu(ddc) <sub>2</sub>	100	50	0.41	$1.2 \times 10^{-7}$	[9], [10]	Synthesized [15]
	230	60	0.77	$1.1 \times 10^{-5}$	[13]	
Cu(bdc) <sub>2</sub>	230	60	0.77	$7.2 \times 10^{-4}$	[13]	Synthesized [12]
Cu(hdc) <sub>2</sub>	230	60	0.77	$2.8 \times 10^{-3}$	[13]	Synthesized [12]

**Table 3.2 Continued**

Cu(acac) <sub>2</sub>	200~290	40~60	0.85~0.83	1.8×10 <sup>-5</sup> ~4.3×10 <sup>-8</sup>	[3], [5]	FA,AC11065-1000,100g
	175	40	0.81	1.6×10 <sup>-5</sup>	[3]	
Cu(bzac) <sub>2</sub>	200	40	0.85	6.0×10 <sup>-6</sup>	[3]	Commercial supplier
	175	40	0.81	5.0×10 <sup>-6</sup>	[3]	
Cu(tfzm) <sub>2</sub>	200	40	0.85	2.1×10 <sup>-5</sup>	[3]	Synthesized [3]
	175	40	0.81	1.4×10 <sup>-5</sup>	[3]	
Cu(dmhd) <sub>2</sub>	200	40	0.85	2.1×10 <sup>-4</sup>	[3]	Synthesized [3]
	175	40	0.81	1.5×10 <sup>-4</sup>	[3]	
Cu(dibm) <sub>2</sub>	200	40	0.85	4.6×10 <sup>-4</sup>	[3]	Synthesized [3]
	175	40	0.81	3.9×10 <sup>-4</sup>	[3]	
Cu(thd) <sub>2</sub>	200	40	0.85	5.8×10 <sup>-4</sup>	[3]	SA, 345083-1G,\$27
	175	40	0.81	4.5×10 <sup>-4</sup>	[3]	
Cu(tod) <sub>2</sub>	200	40	0.85	1.1×10 <sup>-3</sup>	[3]	Synthesized [3]
	175	40	0.81	7.8×10 <sup>-4</sup>	[3]	
Cu(hfa) <sub>2</sub>	200	40	0.85	3.8×10 <sup>-3</sup>	[3]	Aldrich, 335193-5G,\$32.3,
	175	40	0.81	3.54×10 <sup>-3</sup>	[3]	
Cu(tfa) <sub>2</sub>	200	40	0.85	4.2×10 <sup>-4</sup>	[3]	Commercial supplier
	175	40	0.81	3.5×10 <sup>-4</sup>	[3]	
Cu(hfa) <sub>2</sub> ·H <sub>2</sub> O	100	40	0.62	8.1×10 <sup>-3</sup>	[6]	Aldrich, 335193-5G,\$32.3,
Cu(pdc) <sub>2</sub>	230	60	0.77	4.0×10 <sup>-6</sup>	[13]	Synthesized [13]
Cu(p3dc) <sub>2</sub>	230	60	0.77	1.2×10 <sup>-4</sup>	[13]	Synthesized [13]
Cu(p5dc) <sub>2</sub>	230	60	0.77	1.8×10 <sup>-3</sup>	[13]	Synthesized [13]
Cu Kelex 100	200	60	0.74	5.0×10 <sup>-6</sup>	[14]. N.G. Smart, T.E. Carleson, S. Elshani, S. Wang and C.M. Wai,. <i>Ind. Eng. Chem. Res.</i> 36 (1997), p. 1819.	Synthesized [14]

**Table 3.2 Continued**

Cu Cyanex 301	200	60	0.74	$4.1 \times 10^{-4}$	[14]	Cytec Industries Inc.
Cu Cyanex 302	200	60	0.74	$1.5 \times 10^{-4}$	[14]	Cytec Industries Inc.
Cu Cyanex 272	200	60	0.74	$8.0 \times 10^{-6}$	[14]	Cytec Industries Inc.
<b>GROUP 12</b>						
Zn[SCSN( <i>n</i> -C <sub>4</sub> H <sub>9</sub> ) <sub>2</sub> ] <sub>2</sub>	237	55	0.80	$3.0 \times 10^{-5}$	[12]. Wang, J.; Marshall, W. D. <i>Anal. Chem.</i> 1994, 66, 1658-1663.	Synthesized [12]
Zn[SCSN(C <sub>2</sub> H <sub>5</sub> ) <sub>2</sub> ] <sub>2</sub>	237	55	0.80	$1.9 \times 10^{-6}$	[12]	Synthesized [12]
Zn(SCSNC <sub>4</sub> H <sub>8</sub> ) <sub>2</sub>	237	55	0.80	$2.8 \times 10^{-7}$	[12]	Synthesized [12]
Zn(acac) <sub>2</sub>	290	60	0.83	$2.1 \times 10^{-7}$	[5]	F, ICN219908, 100G, \$1175.8
Zn(pdc) <sub>2</sub>	230	60	0.77	$9.0 \times 10^{-6}$	[13]	Synthesized
Zn(ddc) <sub>2</sub>	230	60	0.77	$2.4 \times 10^{-5}$	[13]	SA, 329703-25g, 98%, \$17.6
Zn(p3dc) <sub>2</sub>	230	60	0.77	$1.5 \times 10^{-4}$	[13]	Synthesized [13]
Zn(bdc) <sub>2</sub>	230	60	0.77	$6.9 \times 10^{-4}$	[13]	F, ICN219924, \$587.05
Zn(p5dc) <sub>2</sub>	230	60	0.77	$3.2 \times 10^{-3}$	[13]	Synthesized [13]
Zn(hdc) <sub>2</sub>	230	60	0.77	$5.8 \times 10^{-3}$	[13]	Synthesized [13]
Zn(fddc) <sub>2</sub>	230	60	0.77	$9.0 \times 10^{-3}$	[13]	Synthesized
Hg(fddc) <sub>2</sub>	100	50	0.41	$5.5 \times 10^{-4}$	[9]	Synthesized
	230	60	0.77	$1.4 \times 10^{-2}$	[13]	
Hg(ddc) <sub>2</sub>	100	50	0.41	$9.0 \times 10^{-7}$	[9]	Synthesized
	230	60	0.77	$5.3 \times 10^{-5}$	[13]	
Hg(pdc) <sub>2</sub>	230	60	0.77	$3.4 \times 10^{-6}$	[13]	Synthesized
Hg(p3dc) <sub>2</sub>	230	60	0.77	$2.3 \times 10^{-4}$	[13]	Synthesized [12]
Hg(bdc) <sub>2</sub>	230	60	0.77	$5.6 \times 10^{-4}$	[13]	Synthesized [12]
Hg(p5dc) <sub>2</sub>	230	60	0.77	$2.0 \times 10^{-3}$	[13]	Synthesized [12]
Hg(hdc) <sub>2</sub>	230	60	0.77	$3.8 \times 10^{-3}$	[13]	Synthesized [12]

### 3.2 Sol-gel Technology

The interest in sol-gel processing can be traced back into the mid-1800s with the observation that the hydrolysis of tetraethyl orthosilicate (TEOS) under acidic conditions led to the formation of  $\text{SiO}_2$  in the form of fibers and monoliths. Sol-gel process generally involves the use of inorganic or organic salts such as metal alkoxides or monomers as precursors with solvent to form a colloidal solution (sol) , which is a liquid of solid particles ranging in size from 1 nm to 1 micron, that acts as an integrated network (or gel) of either discrete particles or continuous network polymers. Hydrolysis and poly- condensation reactions occur when the precursors are mixed with water and catalyst. The further condensation of sol particles into a three-dimensional network produces a gel-like diphasic system, which is a solid phase encapsulating liquid phase. The gel materials are referred to as aqua-gel when water is used as the solvent and alcogel when alcohol is used. The encapsulated solvent can be removed from a gel by either conventional evaporative drying or supercritical drying. The resulting solid products are known as a xerogel and an aerogel, respectively. Afterwards, a thermal treatment, or calcination process, is often necessary in order to favor further poly-condensation and enhance mechanical properties and structural stability via final sintering, densification and grain growth. If synthesized using supercritical processes. The precursor sol can be either simply deposited on a substrate to form a film by dip coating or spin coating, cast into a suitable container with the desired shape to obtain monolithic ceramics, glasses, fibers, membranes, aerogels, or used to synthesize powders (e.g. nanospheres). Sol-gel approach is a cheap and low-temperature technique that allows for the fine control of the product's chemical composition. Even small quantities of dopants can be introduced in the sol and end up uniformly dispersed in the final product.

The benefits of sol-gel based synthesis of aerogels are their high purity, microstructure, homogeneity at molecular level, and low temperature preparation. There are several outstanding advantages of the sol-gel route for making catalytic materials.

- a. Maintaining high purity materials because of the purity of the starting materials;
- b. Impacting some of the physical characteristics such as pore size distribution and pore volume;
- c. Varying compositional homogeneity at a molecular level;
- d. Synthesizing samples at low temperatures;
- e. Compositing several components in a single step;
- f. Producing samples in different physical forms and shapes.

Figure 3.2 schematically shows the five key steps in sol-gel synthesis from a metal alkoxides precursor to a designed final product: i, gel formation; ii, gel aging; iii, solvent removal; iv, gel drying; v, heat treatment. The versatility of this preparative approach lies in the number of parameters that can be manipulated in each of these steps.

### **3.2.1 Sol-gel Chemistry**

Metal alkoxides have been widely used as a precursor in sol-gel preparations because they are commercially available in high purity and their solution chemistry has been documented [179]. The sol-gel synthesis of metal oxides is based on the poly-condensation of metal alkoxides  $M(OR)_z$  in which R is usually an alkyl group ( $R=CH_3, C_2H_5, \dots$ ) and z the oxidation state of the metal atom  $M^{Z+}$ . Sol-gel chemistry with metal alkoxides can be described in terms of two classes of reactions known as hydrolysis reaction and condensation reactions as shown in

equations 3.7, 3.8 and 3.9. Metal alkoxides are not miscible with water and have to be dissolved in another solvent, currently the parent alcohol prior to hydrolysis.

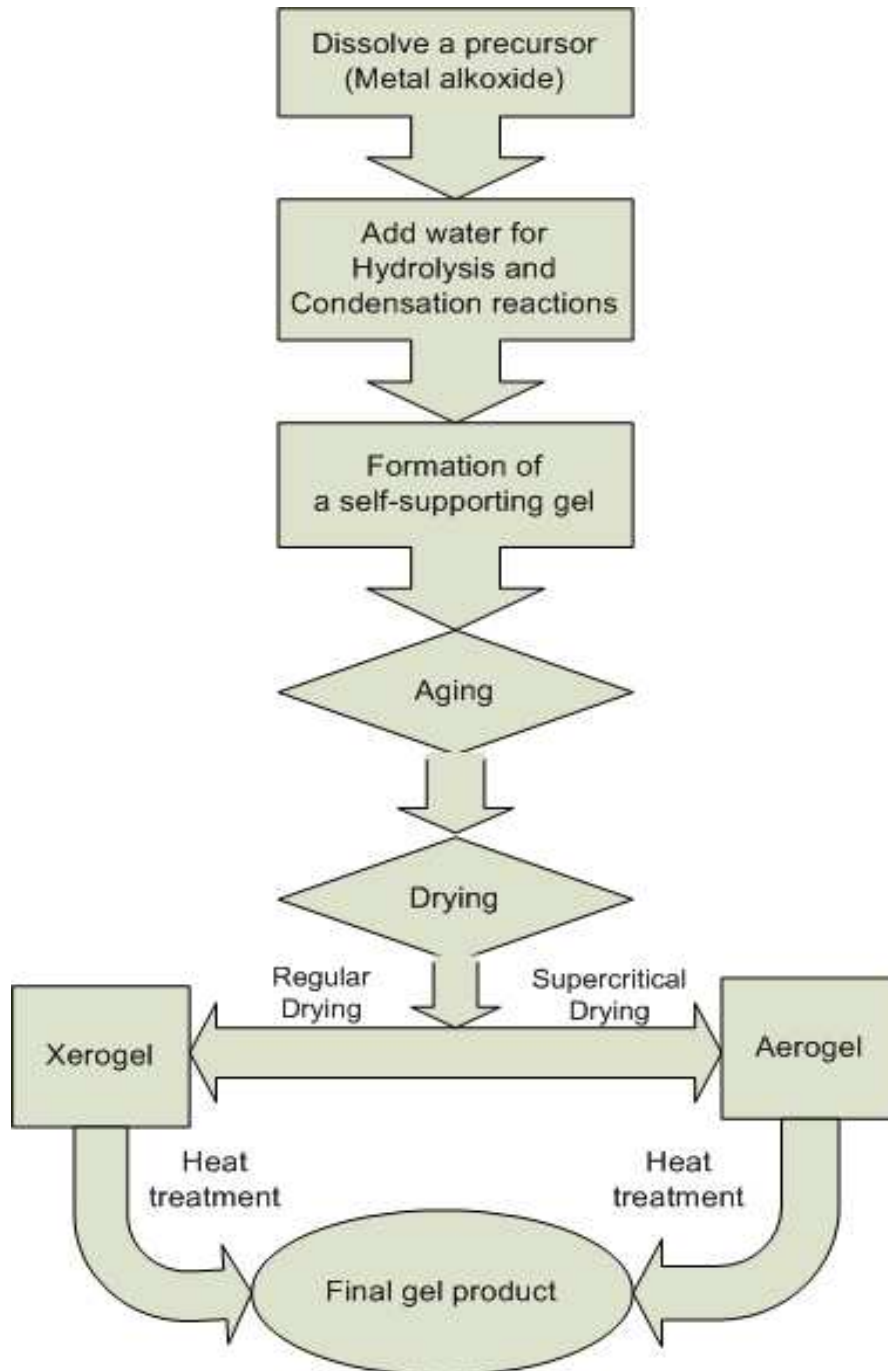


Figure 3.2 Schematic Diagram for Sol-gel Routes, Preparation of Metal Oxide Gel through Sol-gel Method

a. Hydrolysis reaction



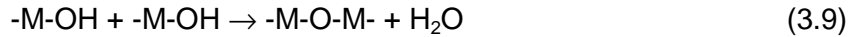
where M presents Si, Ti, Zr, Hf, Ta, Nb, or Al, etc., and R presents CH<sub>3</sub>, C<sub>2</sub>H<sub>5</sub>, C<sub>3</sub>H<sub>7</sub>, etc.

b. Condensation reaction

Leading to the formation of bridging oxygen



or



where X can either be H or R (an alkyl group).

The condensation of hydroxyl and or alkoxy groups can be considered as a type or class of inorganic polymerization. When the extent of polymerization and cross-linking of polymeric molecules become extensive, the entire solution becomes rigid and a gel is formed. The size and degree of branching and cross-linking of the inorganic polymer strongly impact the porosity of the gel, and later the surface area, pore volume, pore size distribution, and thermal stability of the final oxide after heat treatment. The relative rates of hydrolysis and condensation determine the extent of branching and cross-linking of the inorganic polymer and colloidal aggregation in the gelation mixture [180]. When the condensation reaction is relatively faster than the hydrolysis reaction, the resulting sol-gel is highly branched and the corresponding gel is more mesoporous in structure. On the contrary, if the hydrolysis reaction is relatively faster than the condensation reaction, the resulting sol-gel is weakly branched and the corresponding gel is more microporous in structure. Since hydrolysis and condensation are both nucleophilic

displacement reactions, the reactivity of metal alkoxides is dependent on the positive partial charge of the metal atom and its coordination number. In general, the longer and bulkier the alkoxide group attached to a particular metal atom, the less reactive that precursor is in hydrolysis and condensation. Both relative reaction rates are functions of many parameters including temperature and time, pH value, catalyst, concentration of precursor, and the amount of water present. It is possible to vary the structure and properties of the gel network by controlling these factors.

### **3.2.2 Aging and Heat Treatment**

The effect of gelation time on gel properties is significant and should be part of the experimental design. Gel time is defined as the time it takes for a solution to undergo a rapid rise in viscosity. This corresponds to a solution's transition from a viscous fluid to an elastic gel. At the gel point, there is a continuous solid phase with a structure where particles form and branch as dictated by the specific growth conditions. This particular phase has significant impact on the structural evolution. The material undergoes in all subsequent processing steps.

Aging is the process between the formation of a gel network and the removal of solvent from that solid gel network. When the pore liquid remains in the matrix, a gel is not static and can undergo many changes [181]. During the aging process, hydrolysis and poly-condensation continue to occur. Parameters such as temperature and pH value of the gel affect length of aging period and the properties of the sol-gel. This process can actually be desirable because it leads to an enhanced cross-linking network that is mechanically stronger and easier to handle, and also increases the viscosity of the mixture. Choosing appropriate aging time is one of the keys to a successful sol-gel synthesis. Not enough aging time may cause a fragile sol-gel, which has incomplete and unstable cross-link network. However, longer aging time can also lead to an over cross-link or even closed cells which is not accessible during the drying process.

Gel aging is an extension of the gelation step in which the gel network is reinforced through further condensation. Extensive condensation causes a phenomenon called syneresis, the expulsion of solvent due to gel matrix shrinkage can occur during gel aging. The shrinkage in alcoholic gel systems is attributed to formation of new bonds through condensation reactions, which increase the bridging bonds and cause contraction of the gel network.

During the following drying step, solvent trapped in the porous gel matrix is removed. As the solvent evaporates, surface tension or capillary force accompanying evaporation pulls on the walls of the pores. Therefore, the pore structure collapses during drying. In this research, supercritical drying was used for the drying of the aged sol-gel material to free it from its solvents in order to maintain the pore size and volume.

After the wet gel system has been dried and the solid phase has emerged from the drying process, further heat treatment, also called calcination, is needed to stabilize the physical and chemical properties of the solid gel and to make it suitable for future applications at severe temperature conditions [182].

Calcination is carried out in an oxidizing or inert atmosphere at a temperature slightly above the projected operating temperature of the catalyst. The aim of calcination is to stabilize the physical, chemical, and catalytic properties of the catalyst. During calcination several chemical reactions and physical changes can occur [183].

Thermally unstable compounds (carbonates, nitrates, hydroxides, and organic salts) decompose under gas evolution and are usually converted to oxides. Relevant reaction is shown in equations 3.10.



Decomposition products can form new compounds by solid-state reactions. Amorphous regions can become crystalline at very high temperatures. Various crystalline modifications can undergo reversible conversions. The pore structure and mechanical strength of precipitated catalysts can also change.

Various textural and chemical changes of the gel are associated with the calcination process. All organic groups such as the alkyl group ( $C_nH_{2n+1}$ ) will react with oxygen in air and eventually decompose to water, carbon dioxide and residual carbon. Iron complexes that have been impregnated into aerogel samples in supercritical impregnation experiments react with oxygen producing iron oxide that would be trapped within in the porous network. In co-precipitated aerogel synthesis where iron nitrate is used as iron ion dopant precursor, the by-product for Ferrocene and iron nitrate would be different because the  $C_5H_5$  group would convert to water and carbon dioxide. Nitrogen dioxide would be produced from the reaction between the nitrate group and oxygen. Some components inside the gel react with oxygen in the airflow or decompose to other compounds, which are more stable at high temperature. Heating rate is another parameter that can influence the final product's properties. At fast heating rate, due to pores sintering, some areas may become inaccessible with airflow before temperature reaches the compound decomposition point or even vaporization point. Residue of those compounds may decompose into unwanted substances without oxygen presented. Those unwanted substances could be harmful to the final product as toxic contaminants. A controlled temperature ramping rate is desirable to achieve better results.

The solid gel undergoes phase transformations under different temperature conditions resulting in different crystal and morphological structures that occur during different heating temperatures. The phase transitions of titania during calcination are non-reversible. Thus, the physical characteristics of the final product depend on several parameters such as heating temperature, time, and gaseous environment. It is common practice to subject the sample to a

more severe heat-treatment than it is likely to encounter in a reactor to ensure the stability of its structural and textural properties during future industrial operations.

A viscous sintering is a phenomenon of densification in which the solid particles of the gel are drawn toward each other by interfacial energy. Material moves by viscous flow or diffusion in such a way as to eliminate porosity and thereby reduce the solid-vapor interfacial area. Due to viscous sintering, micro-structural pores have been found to be diminish or even disappear completely during calcination, as determined by nitrogen adsorption isotherms. Micropores may be either sintered to close cells, or its walls collapse to connect or merge to others to make new mesopores or macropores. Pore size distribution becomes narrower after calcination [184] due to the reduction or elimination of the micropores in the solid gel. Pore volume also decreases slightly.

### **3.2.3 Surfactant Templates**

A template works as an instrument which is used as a guide in bringing any piece of work to the desired shape. For gels, the selection of the template material is of top priority in defining the final porosity, its distribution, orientation and the surface texture. The exploration of the supramolecular templating technique has created the ability to synthesize an array of mesoporous metal oxide materials with potential applications in various areas that include catalysis, separation, chemical sensing, environmental remediation, and optics [185]. The use of a template to affect the synthesis of new materials was first demonstrated by the pioneering work of Busch on exploration of the effect of metal templates in the synthesis of macro-compounds in the 1960s [186]. Many materials prepared by the sol-gel technique, especially the aerogels, are mesoporous with large surface area and high pore volume. However, those materials usually have a broad pore size distribution as well. Since the discovery of the M41S family of mesoporous molecular sieves by Mobil scientists in 1992, synthesis

and application of ordered mesoporous materials using surfactants as pore-directing agents has attracted wide attention.

Silica porous material was synthesized through using a neutral chemical templating material for the first time in 1995 [187]. This templating methodology had some advantages over the former templating methodology used for M41S material because the neutral templates are less attached to the solid structure and therefore can be removed easily. The template selection naturally dictates the processes that can be employed for its removal. Easy removal for the nonionic template from the templated solid network exhibits many advantages for the templated material, such as, improvement of the textural mesoporosity, sharper pore size distribution and thicker framework walls. By using the neutral template, it was possible to recycle the cost-intensive neutral chemical template. While the primary removal path of template is thermal decomposition, extractive processes, particularly supercritical fluid extraction, offer gentler and environmentally greener pathways, often with superior pore structure retention. Interplay between surfactant and solvent becomes significant particularly at the drying stage. Question of to what extent the template material should be removed in the supercritical extraction and drying stage, along with the solvent, needs to be addressed at the design stage.

The available options for surfactant and other materials to be removed supercritically are

a. Template is soluble in supercritical carbon dioxide.

CO<sub>2</sub> is non-polar, has low dielectric constant, and does not engage in Van der Waals type interactions. In other words, CO<sub>2</sub> is a poor solvent for polar and high molecular weight material. Special designed CO<sub>2</sub>-philic and amphiphilic surfactants are needed.

b. Template is soluble in a suitable entrainer plus supercritical carbon dioxide.

The advantages of supercritical fluids can be complied if entrainers (modifiers), such as alcohols, are used to enhance the solubility of the template material. The indigenous solvent employed in sol-gel synthesis can serve as entrainer or co-solvent. This path for removal of surfactants has been successfully employed in removal of templated material in several applications, particularly non-ionic ones [188-190].

c. Template is soluble in other supercritical systems.

In applications where intermediate or higher temperature template removal is acceptable or desirable, other supercritical solvents may also be employed. The initial aerogel synthesis methods utilized alcohols indigenous within the sol.

In many applications, removal of the residue of templating material using thermal means may be inevitable. These thermal operations may lead to sintering. To avoid the need of adding additional material (e.g. mixed metal oxides, silica, alumina) to reduce sintering, fine control of heat treatment step is found to be helpful.

Surfactants are classified on the nature of the hydrophobic groups. There are four general groups of surfactants, which are defined as

- a. Anionic. Where the hydrophilic group bears a negative total charge such as carboxylic (-COOH), sulfonate (R-SO<sub>2</sub>-O-) or sulfate (-SO<sub>4</sub><sup>2-</sup>) group.
- b. Cationic. Where the hydrophilic group bears a positive charge such as quaternary ammonium halides (NR<sub>4</sub><sup>+</sup>).
- c. Nonionic. Where the hydrophilic group of the surfactant bears no electrical charge, yet derives its molecular solubility from highly polar hydrocarbon groups, such as, polyoxyethylene (HO-(CH<sub>2</sub>CH<sub>2</sub>O)<sub>n</sub>-) groups.

- d. Amphoteric. Where the surfactant molecules contain both positive and negative charges, such as, the sulfobetaines ( $C_7H_{17}NO_3S$ ).

In all four classes, the hydrophobic group is generally a long-chain of hydrocarbon radicals which will influence the size and sharp of pores in the gel. The hydrophilic group will be an ionic or highly polar group that can impart some solvent solubility to surfactant molecules. Surfactants in the sol-gel process help to promote molecular assembling, which is defined as a spontaneous association of molecules into thermodynamically or kinetically stable, structurally well-defined aggregates joined by non-covalent bonds. Surfactant can be used in many different ways for templating. However, using nonionic surfactants seems to have more advantages than others, such as, a significantly lower sensitivity to the presence of electrolyte in the system and a small affect on the system pH value. Due to the neutral electrical property, nonionic surfactants do not provide the precursor with extra electrical charge which will limit the cross-linking of the units and compromise the thermal stability of the porous framework.

For purposes of the experimental work described and discussed in this dissertation, Triton X-114 was used as the nonionic surfactant template.

## CHAPTER 4

### EXPERIMENTAL

The main experimental steps involve: sol-gel preparation, supercritical fluids aided extraction and drying, supercritical fluid aided impregnation, calcination/heat treatment, characterization methods of the photocatalysts, and testing of the photocatalytic activity of produced photocatalysts through analysis of in methylene blue (MB) degradation reactions under UV light or visible light. In this chapter, the experimental methods, experimental setups and procedures, materials, characterization methods and procedures applied for this research will be described.

#### 4.1 Sol-gel Preparation

The sol-gel process involves the formation of a sol, which is a liquid suspension of solid particles. Hydrolysis of precursor and further condensation of sol particles into a multi-dimensional network are the main two steps to produce a gel. Preparation procedures for synthesizing regular and template titania based gel, templated co-precipitate Titanium dioxide/Tungsten Oxide ( $\text{TiO}_2/\text{WO}_3$ ) gel and templated co-precipitate Titanium dioxide/Tungsten Oxide/Iron Ion ( $\text{TiO}_2/\text{WO}_3/\text{Fe}^{3+}$ ) gel are described in sections 4.1.1, 4.1.2 and 4.1.3 respectively. The key variants of the prepared sol-gels involve incorporation of templating non-ionic surfactant, tungsten oxide and iron ion precursors. Regular gel in this study refers to the synthesis of the titanium dioxide based gel without using surfactants as template agent (or template) in the sol-gel preparation. On the contrary, a templated gel means one synthesized using surfactants as the template.

#### 4.1.1 Titanium Dioxide Sol-gel Preparation

Preparation procedure for regular and templated titanium dioxide will be discussed in this section. Different Titanium oxide gels were synthesized with similar recipes and procedures to evaluate the various photocatalysts. After the synthesis of sol-gel, xerogels and aerogels are obtained. Xerogel is achieved through ambient drying methods and the aerogel is achieved through supercritical fluid extraction and drying (SFE), respectively. A schematic diagram for the steps involved in the synthesis of sol-gel for templated alumina is shown in Figure 4.1.

In the templated titanium dioxide sol-gel preparation procedure, two solutions were separately prepared. Similarly, in regular TiO<sub>2</sub> sol-gel preparation, only one solution mixture was prepared. The first solution prepared for templated sol-gel contains Titanium Butoxide (Ti(OBu)<sub>4</sub>, C<sub>16</sub>H<sub>36</sub>O<sub>4</sub>Ti, MW:340.35, d:0.99 g/ml, Supplier: Aldrich) as titanium dioxide precursor, dissolved in high purity ethanol (EtOH, 200 proof, Supplier: Aldrich) under stirring. Golubko, N.V. et al. [191] reported hydrolysis of Ti(OBu)<sub>4</sub> is much slower than that of other Ti(OR)<sub>4</sub>. Ti(OBu)<sub>4</sub> hydrolysis products are multilevel systems, their structural elements are complex oligomeric molecules of titanium oxobutoxide— ultrafine particles (UFP) with the size of 1.6 nm. The second solution contains the surfactant template dissolved in a small portion of the required total amount of ethanol as well. The surfactant used in this solution was Triton® X-114 ((1,1,3,3-Tetramethylbutyl) phenyl-polyethylene glycol, *t*-Oct-C<sub>6</sub>H<sub>4</sub>-(OCH<sub>2</sub>CH<sub>2</sub>)<sub>x</sub>OH, x = 7-8, Supplier: Sigma-Aldrich) which is a non-ionic neutral surfactant. Its basic properties are shown in Figure 4.2. The second solution mix was slowly added to the first solution for 10 minutes under constant stirring. To ensure homogeneity of the mixture, the mixture was stirred for another half hour at room temperature under covered by parafilm.

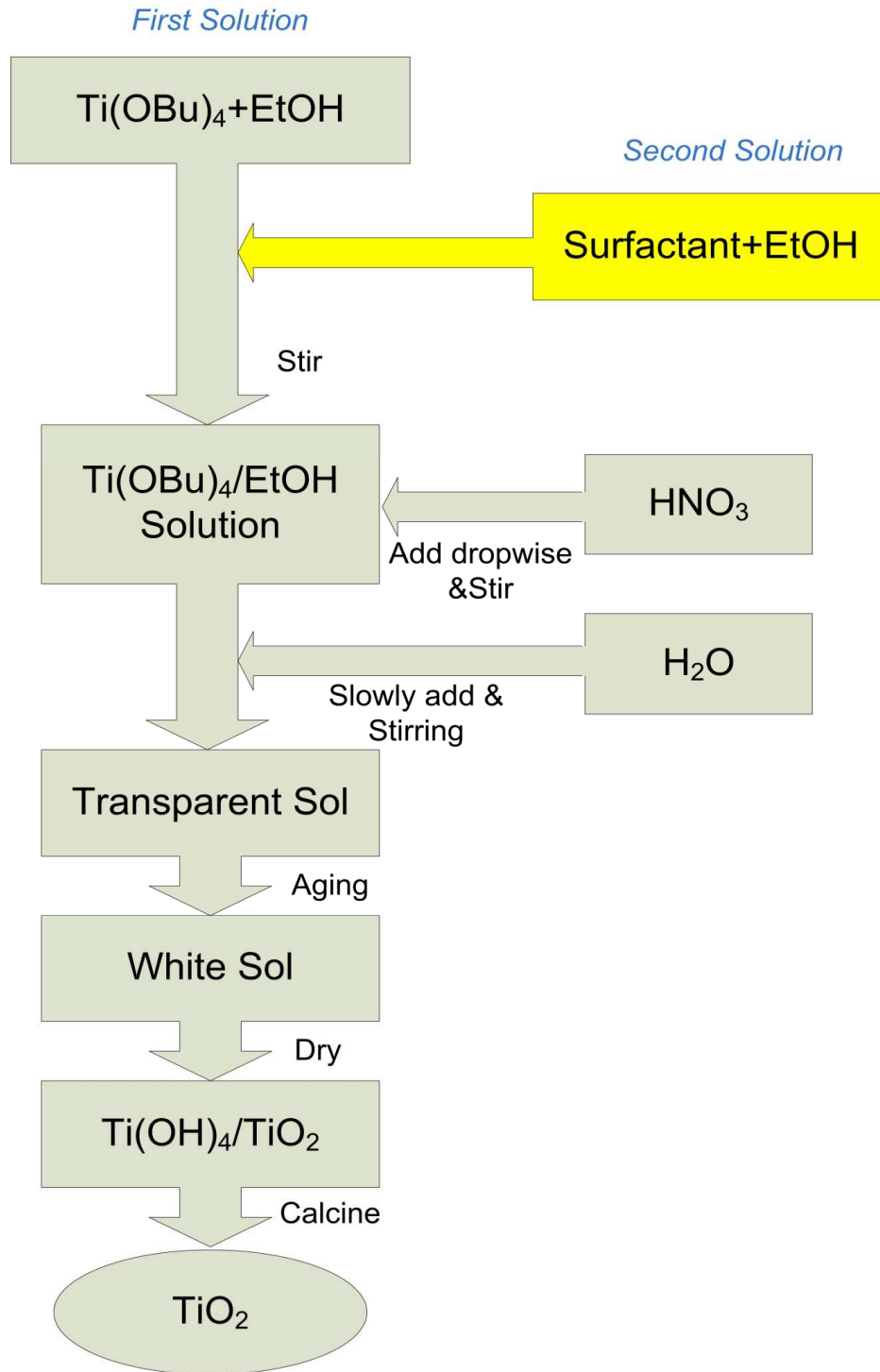
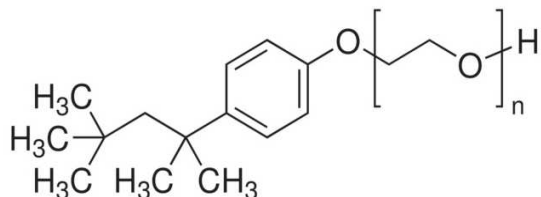


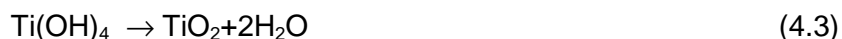
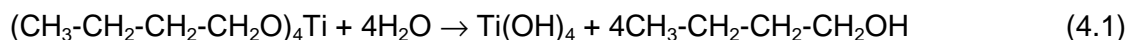
**Figure 4.1 Schematic Diagram for Synthesizing and Processing Templated Titanium Dioxide Sol-gel**



Triton® X-114  $C_8H_{17}(C_6H_4)(OC_2H_4)_nOH$  MW:426-558 D:1.022-1.058 g/ml Boiling Point:>177°C

**Figure 4.2 Basic Properties of the Templating Surfactant Triton X-114**

A small amount of Nitric acid ( $HNO_3$  70%, supplier: Aldrich) was dropwise added as catalyst to the mixture before adding water in order to avoid instant gelation. The next step is adding required amount of de-ionized water to the mixture dropwise while stirring continuously at room temperature. Adding water drop by drop decreases the rate of the solid-state formation, to regulate the particles morphology in a wide range [191]. The mixture was covered and stirred for another hour resulting in spontaneous gelation. Subsequently, the gel was stored at room temperature covered by parafilm. Titanium hydroxide/Titanium dioxide gel was formed according to the following hydrolysis reactions:



In fact, substitution of OR-group by OH is followed by immediate condensation with formation of titanium oxoalkoxides. The molar ratio of chemicals  $Ti(OBu)_4$  : Ethanol :  $H_2O$  :  $HNO_3$  : Triton X-114 is 1 : 30 : 7.5 : 0.3 : X. The required amount of water in this sol-gel preparation was according to the titanium butoxide hydrolysis reaction shown in Equation 4.1. The effect of surfactant concentration on aerogel pore structure was studied and optimized in a former study [172]. In this study, surfactant to titanium butoxide ratio X was fixed at 0.1.

Systematic procedure for making templated titanium dioxide sol-gel:

a. Preparing solution one

Ti(OBu)<sub>4</sub> (34.5 g) was dissolved in 200 proof ethanol (116 ml), and was stirred until Ti(OBu)<sub>4</sub> dissolved completely to form one a uniform liquid phase..

b. Preparing solution two

The Surfactant Triton X-114 (5.67 g) was dissolved in ethanol (59 ml). The solution was stirred until it also formed a uniform liquid phase;

c. Mixing the two solutions by slowly adding solution two into solution one;

d. Adding nitric acid to the mixture

Under continuous stirring, nitric acid 70% (2.0 ml) was added dropwise to mixture (about 15-20 drops per minute), with constant mixing maintained after addition for 30 minutes;

e. Adding de-ionized water to the mixture

De-ionized H<sub>2</sub>O (13.5 ml) was added dropwise to mixing solution.

f. Forming the templated sol-gel solution

The mixed sol-gel solution was stirred for another one hour covered with parafilm. The formed mixture was stored for aging purposes at room temperature for 48 hours.

The regular titanium dioxide sol-gel preparation procedure varies by only making the solution one with only the required amount of ethanol (175 ml).

#### 4.1.2 Co-precipitated Titanium Dioxide/Tungsten Oxide Sol-gel Preparation

For the synthesis of designed composite semiconductor Titanium Dioxide /Tungsten Oxide photocatalyst, tungsten oxide and titanium dioxide were co-precipitated in one step with surfactant template as described in this section. Tungsten chloride ( $WCl_6$ , supplier: Sigma) was used as tungsten oxide precursor. Tungsten hexchloride is quite moisture sensitive. Instead of dissolving in water, it readily hydrolyzes with water, yielding the orange oxychlorides  $WOCl_4$  &  $WO_2Cl_2$ , and upon further hydrolysis, yields tungsten trioxide  $WO_3$  according to the following hydrolysis reaction:



Compared to the sol-gel preparation procedure described in the former section, it is necessary to initially prepare a precursor solution three of tungsten chloride dissolved in a certain amount of ethanol. The dosage of  $WCl_6$  depends on the experimental design and may vary between 3~5 mol% of the amount of titanium dioxide. The amount of water used in  $WCl_6$  hydrolysis is negligible as compared to that used in the  $Ti(OBu)_4$  hydrolysis reaction. Only two additional steps were added to the procedure described in last section for preparing co-precipitated titanium dioxide/tungsten oxide sol-gel.

3 mol%  $WCl_6$  (1.19 g) was dissolved in ethanol (40 ml) under nitrogen purged environment, and was stirred until  $WCl_6$  dissolved completely to form a uniform liquid phase as solution three. This step is added after step b given in the last section. Additionally, the amount of ethanol used in preparing solutions one and two, detailed in the previous section, are both reduced 20 ml from original quantities of ethanol used previously.

Solution three was added to the mixture, and stirring was maintained for an additional 10 minutes to uniformly blend the solutions. This step is added after step d mentioned in previous section.

A schematic diagram for synthesizing templated co-precipitated Titanium Dioxide/Tungsten Oxide sol-gel is shown in Figure 4.3.

#### **4.1.3 Co-precipitated Titanium Dioxide/Tungsten Oxide/Iron Ion Sol-gel Preparation**

For the synthesis of Iron ion doped composite semiconductor Titanium Dioxide /Tungsten Oxide photocatalyst, Iron ion ( $\text{Fe}^{3+}$ ), tungsten oxide and titanium dioxide were co-precipitated in one-step with surfactant template as described in this section. Iron(III) nitrate (or ferric nitrate  $\text{Fe}(\text{NO}_3)_3 \cdot 9\text{H}_2\text{O}$  crystal, supplier: Fisher Scientific) was used as iron ion precursor. Iron nitrate is soluble in both water and ethanol. Mixing with water is preferable method in this sol-gel preparation. In these sol-gel compositions, Iron nitrate is non-reactive, and co-precipitates within the sol-gel network. However, it was anticipated that a portion of Iron Nitrate may be extracted with ethanol and surfactant during the supercritical fluid extraction and drying step. So a reasonable excessive initial loading of iron nitrate was used to account for possible losses. In this preparation, 1, 3 or 5 mol% Iron Nitrate relative to titanium dioxide was used for comparison. Compared to the sol-gel preparation procedure described in previous section, only step e will be divided into two individual steps:

- e.1. Dissolving 1.21g ( 3 mol%)  $\text{Fe}(\text{NO}_3)_3 \cdot 9\text{H}_2\text{O}$  in 13.5 ml de-ionized water.
- e.2. Adding the prepared iron nitrate solution dropwise to the mixture.

A schematic diagram for synthesizing templated co-precipitated Titanium Dioxide/Tungsten Oxide / Iron ion sol-gel is shown in Figure 4.4. Pictures of the prepared sol-gel samples are shown in Figure 4.5.

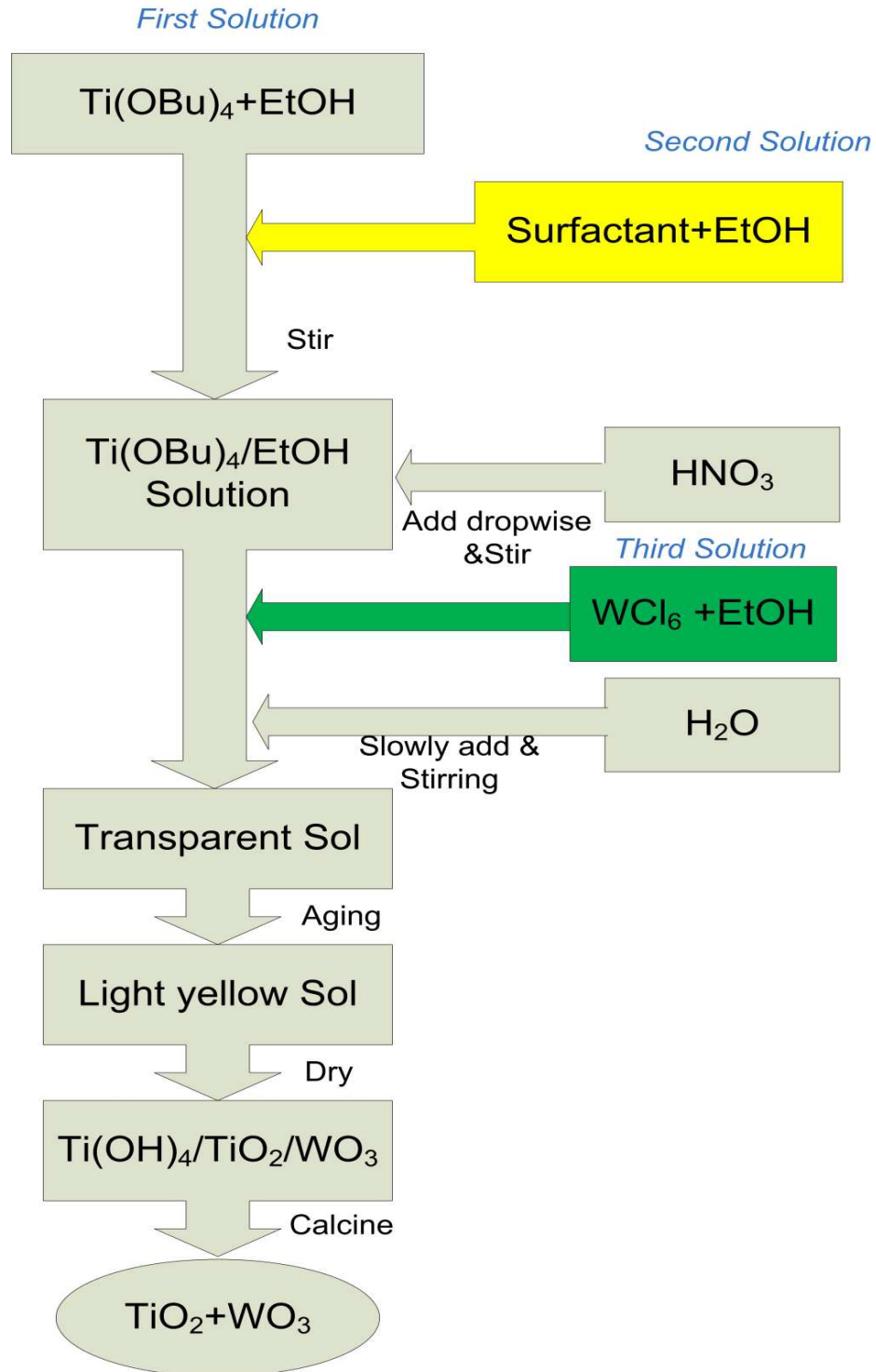


Figure 4.3 Schematic Diagram for Synthesizing and Processing Templated Co-precipitated Titanium Dioxide/Tungsten Oxide ( $\text{TiO}_2/\text{WO}_3$ ) Sol-gel

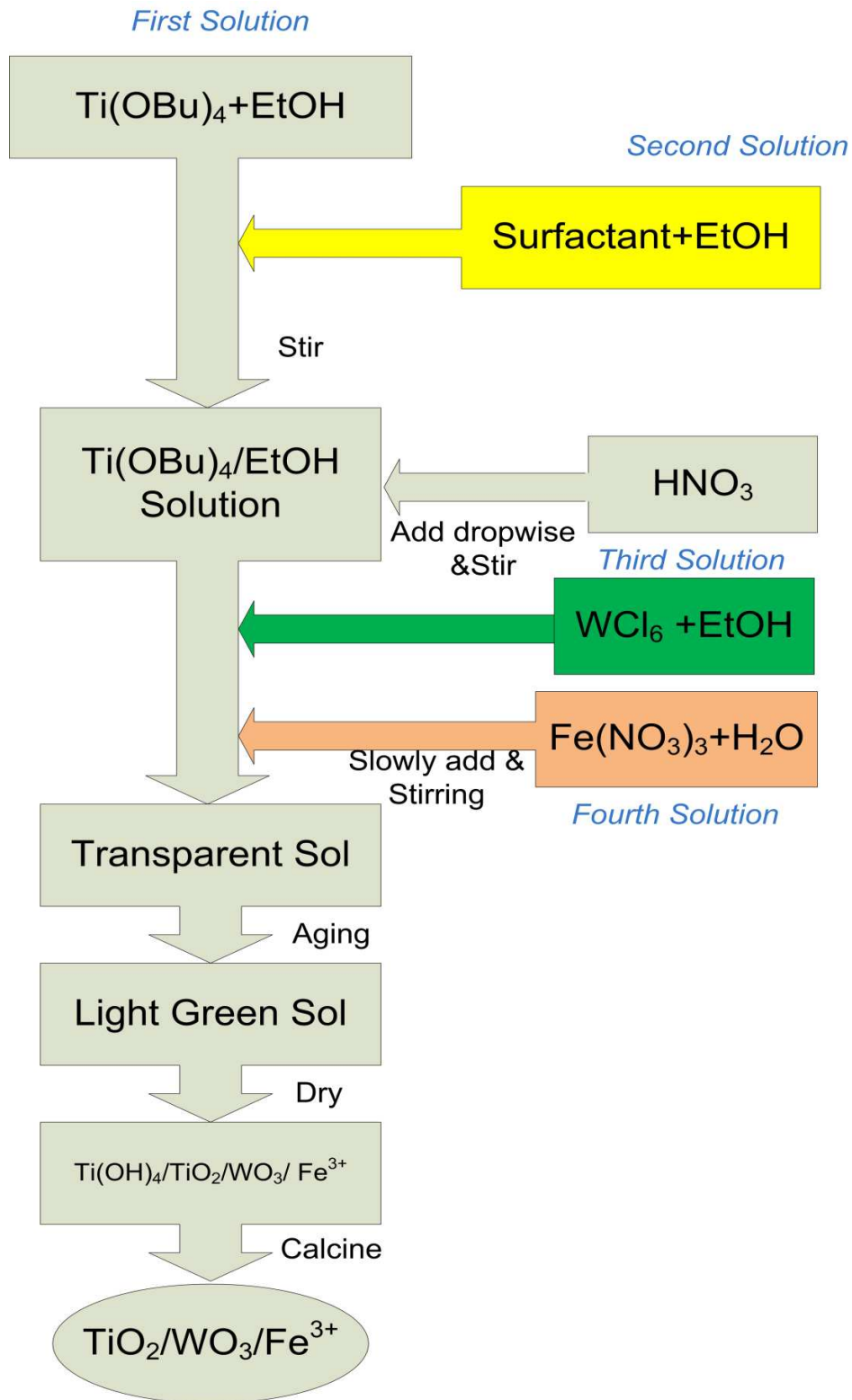
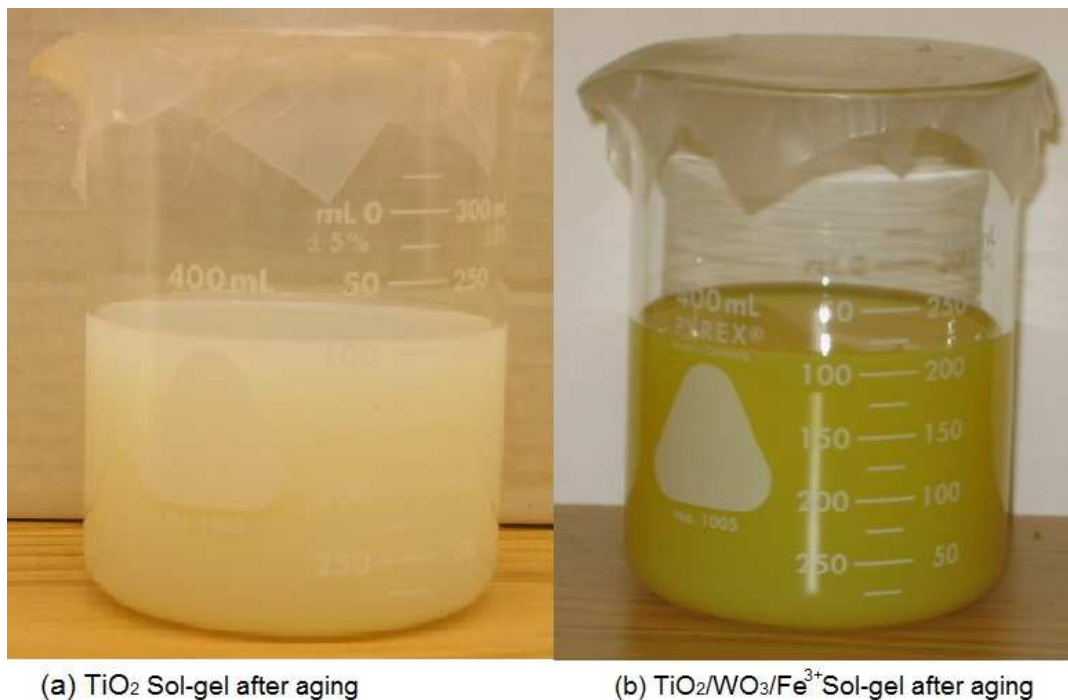


Figure 4.4 Schematic Diagram for Synthesizing and Processing Templated Co-precipitated Titanium Dioxide/Tungsten Oxide/Iron(III) Ion ( $\text{TiO}_2/\text{WO}_3/\text{Fe}^{3+}$ ) Sol-gel



**Figure 4.5 Prepared Template  $\text{TiO}_2$  Based Sol-gel Samples. (a) Template  $\text{TiO}_2$  Sol-Gel Sample after Aging; (b) Template  $\text{TiO}_2/\text{WO}_3/\text{Fe}^{3+}$  Sol-gel Sample after Aging**

## 4.2 Supercritical Fluids Extraction and Drying

Compared to xerogel which is produced by drying the wet gels under air at atmospheric pressure and  $100\text{ }^\circ\text{C}$  for 24 hours, aerogels are produced from prepared aged sol-gel samples through extractive supercritical drying to avoid collapse of pore structure. The supercritical fluid pilot plant used for supercritical extraction and drying is shown as Figure 4.6. Experimental setup and procedures used in this research are discussed in this section.

### 4.2.1 Experimental Setup

The entire system can be visualized in three interconnected functional sections; feeding section, high pressure drying/extraction section and gas-liquid separation and sample collection/recovery section. All parts, tubing and *Swagelock*® fittings are made of stainless

steel, (SS-316). The tubing used in the main fabrication of the SCF setup is primarily 1/4 inch in diameter, while augmented by some 1/8 inch in diameter.

The feeding section consists of compressed carbon dioxide feed tank (AIRGAS, CD-50) with associated pressure regulation, high pressure CO<sub>2</sub> pump (Thar, P-200), the head of which is chilled with the aid of a refrigerating circulator (Ecoline RE120, Lauda, Brinkmann) to ensure initial liquid feed, HPLC pump (Waters, model 600E) for possible co-solvent use, entrainer container, in-line mixer, and a number of plug and valves.

The high pressure drying extraction section consists of a 1000 ml autoclave (*Autoclave Engineer*) all within a constant temperature air environment controlled with a circulating water from a bath (HAAKE, model B81) fitted with stainless steel pipe coil, several electrical heating tapes (Omega), pressure gauges (Matheson), thermocouple probes (Omega, K-type) and two sets of radiators. A specially designed cylindrical stainless steel screened (200 mesh) sample holder/cage was used for easy sample loading and unloading purpose. The recovery and collection begins with a dome loaded backpressure regulator followed by low-pressure gas-liquid separator and venting system. A compressed nitrogen tank provides the necessary pressure to the backpressure regulator.

The gas-liquid separation and sample collection/recovery section consists of a compressed nitrogen tank (AIRGAS, NI200), backpressure regulator, and low-pressure gas-liquid separator and venting system.

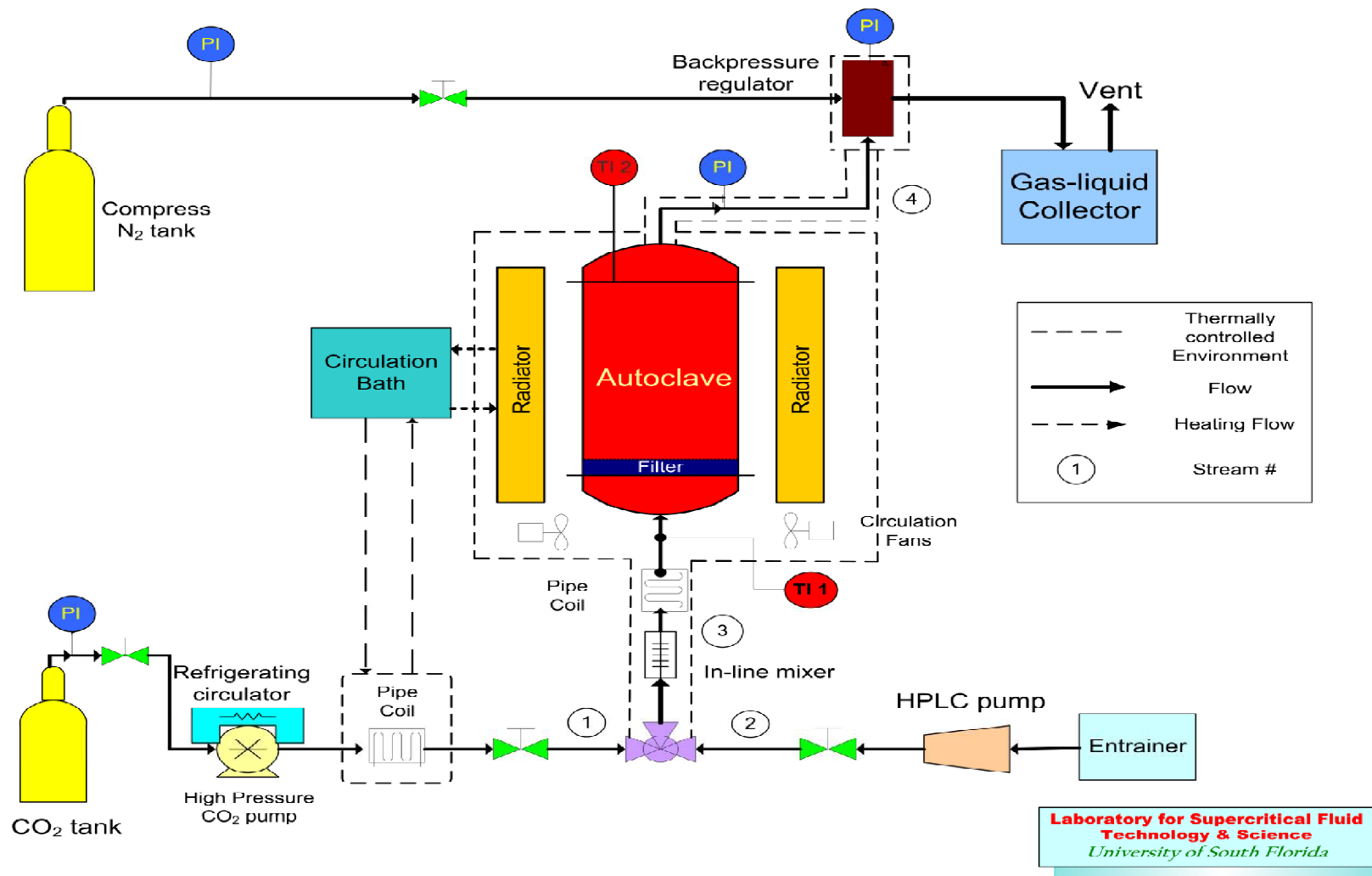


Figure 4.6 Supercritical Fluid Extraction and Drying Pilot Plant

#### 4.2.2 Experimental Procedure for Supercritical Fluids Extraction and Drying

Most of the solvent and surfactant in the alcogel was separated and removed from the system smoothly in this process without disturbing the porous structure. The trace amount of surfactant and solvent in aerogel is eliminated by calcination/ heat treatment, which will be discussed in section 4.4.

The drying procedure was described as follows. The alcogel sample was placed inside the sample holder and loaded into the autoclave which had been pre-heated to a temperature of 40 °C. The autoclave was closed tightly and then purged with carbon dioxide. All the vents and outlet valves were securely closed and the system pressure was initially raised to 850 psi. Meanwhile, the backpressure system was turned on and set at 1800 psi.

Carbon dioxide was compressed and cooled down to -4 °C, passed through high pressure CO<sub>2</sub> pump, and the system was pressurized until the desired set point pressure, as determined by the set point on the backpressure regulator at the start of each experimental run was achieved. The pressure used for these process runs was 1800 psi. Carbon dioxide, and any co-solvent if used, entered the in-line mixer unit just before being introduced to the autoclave through bottom feed. For these experimental runs, no co-solvent was needed since the amount of ethanol used in the sol-gel preparations was sufficient. When the processing pressure was achieved, the feeding flow rate of CO<sub>2</sub> was kept at 20 ml/min for about 8 hours. The flow rate is dictated primarily based on hydrodynamic considerations and mass balance while experimental duration ensures possible maximum removal of sol gel solvents and the surfactant template. Experimental evidence is combined with differential balance where solubility of the solvents is modeled using the Peng–Robinson equation of state with Wong-Sandler mixing rules. Further discussion on the affects of flow rate and other experimental conditions will be presented in next chapter.

Sol-gel solvents and residual templates were extracted throughout the volume of the autoclave up to the backpressure regulator which controls the upstream processing pressure. Heating the backpressure regulator avoids dry ice formation when the dense gas is expanded. The backpressure exit is under ambient pressure and feeds into a vessel in which the effluent mixture separated into both gas and liquid phases.

### **4.3 Supercritical Impregnation**

An alternate route for introduction of the iron ion dopant into the TiO<sub>2</sub> based sol-gel system other than thru co-precipitation is supercritical impregnation which offers feasible pathway to loading different dopants that are soluble in supercritical CO<sub>2</sub> or supercritical CO<sub>2</sub> with co-solvent.

After preparation of the highly porous TiO<sub>2</sub>/WO<sub>3</sub> aerogel, functionalization of the porous catalyst support needs to be performed. Using supercritical fluid unique properties, such as low viscosities, high diffusivities of solutes, and easily tunable solubility, supercritical impregnation has been widely applied for various product functionalization purposes. This pathway offers a very attractive and superior approach to achieve highly homogeneous dispersed surfaces functionalization. The amount of dopant loading on the aerogel surface can be controlled by modifying the solubility of dopant in supercritical fluids through change of process temperature and pressure. The aerogel samples used in supercritical impregnation process discussed here were obtained from experimental samples prepared as described in section 4.1.2, either before or after heat treatment.

#### **4.3.1 Experimental Setup**

The prepared TiO<sub>2</sub>/WO<sub>3</sub> aerogel was doped with Iron bis(cyclopentadienide) (Ferrocene, C<sub>10</sub>H<sub>10</sub>Fe, Supplier: Acros Organics) (Shown in Figure 4.7) as Iron ion precursor in supercritical

CO<sub>2</sub>. The experimental setup used in supercritical extraction and drying process was simply modified to meet supercritical impregnation process requirements by adding an optional organic metal complex feed cell on the feeding section. A 12 cm long stainless steel tube (D=1/2 inch) was cut and made into an organometallic complex feed cell, which had 200 mesh stainless steel screen installed on both ends as filters. The modified pilot plant is shown as Figure 4.8.

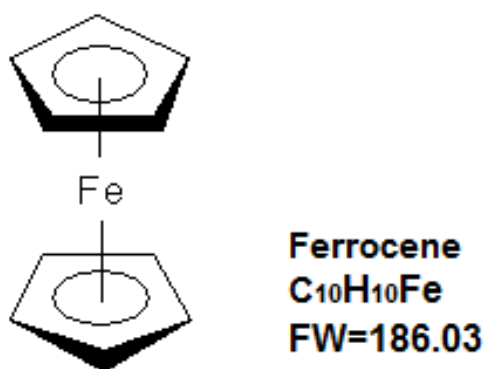


**Figure 4.7 Basic Information of Ferrocene (Iron Ion Precursor)**

#### **4.3.2 Experimental Procedure for Supercritical Impregnation**

Supercritical impregnation can be carried out in two different ways: continuous process or batch process (shown in Figure 4.9). Process choice is made on basis of what type of metal complex being used and the required solute loading concentration. In practice, batch process is preferable if a high cost metal complex is chosen.

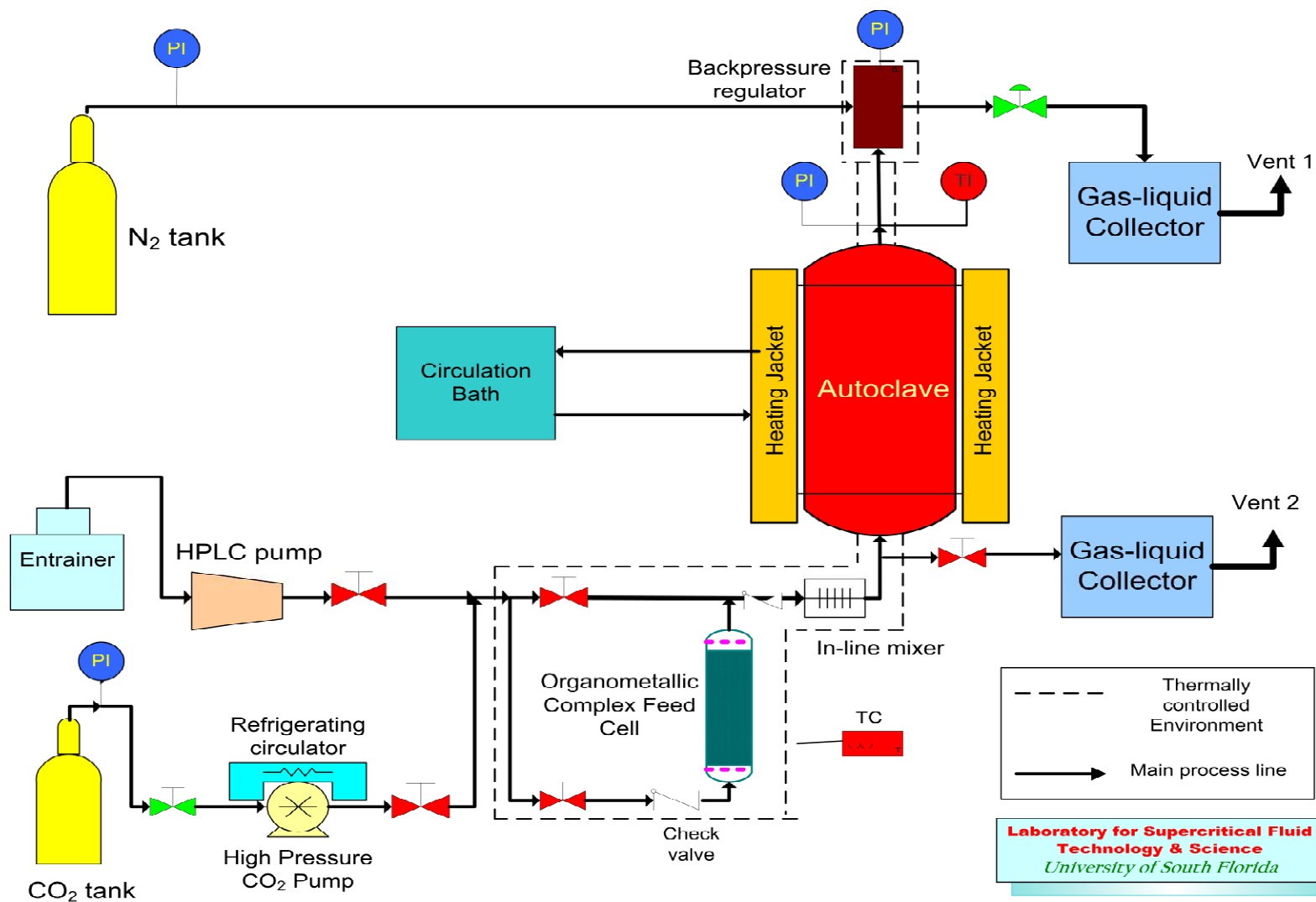
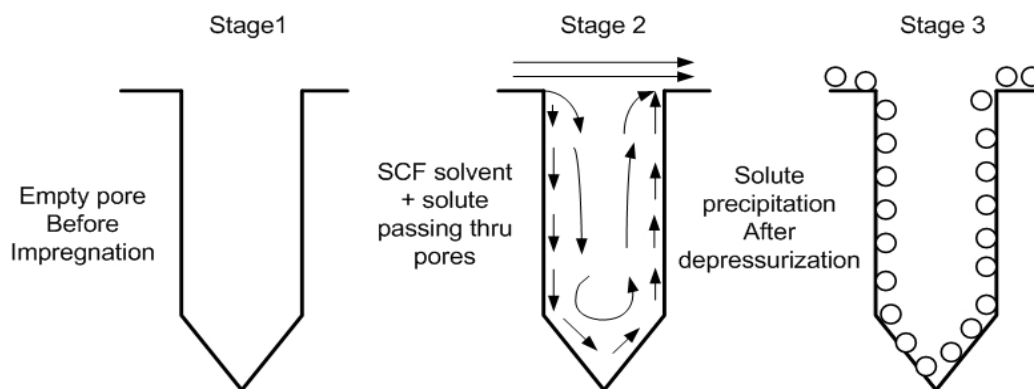


Figure 4.8 Supercritical Impregnation Pilot Plant

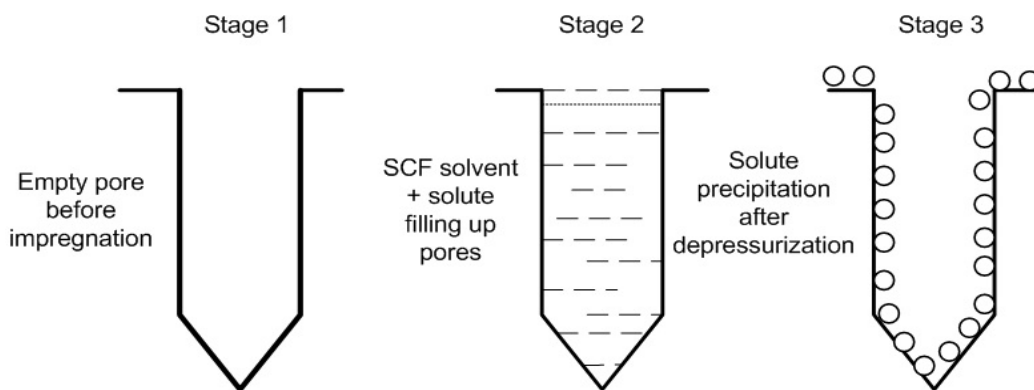
The batch impregnation pathway is a diffusion-dominated process. The adsorption of solute on the interior wall of the aerogel pores was dependent on diffusivity of the solute transferring into the pores. Solubility of the metal complex under various processing conditions is the key parameter to control in the entire impregnation procedure. The system was first pressurized to the desired pressure by supercritical CO<sub>2</sub>. After running for 30 minutes with high flow rates (CO<sub>2</sub> 10 ml/min), the flow rate was reduced to 2 ml/min. Another 30 minutes at constant flow was maintained in order to keep the system pressure stabilized. The CO<sub>2</sub> flow was subsequently switched to the metal complex feeding loop. During the low flow period, a relatively static homogeneous supercritical environment was maintained throughout the system. Solute was able to diffuse into the pores uniformly. After stopping all feeding flows and closing all inlet valves, depressurizing the entire system quickly caused the solubility of solute to dramatically decrease, resulting in precipitation of the metal complex into the pores and onto the surface of the aerogel. The process can be repeated 2 to 3 more times if high concentration loading of solute is required. Initial higher pressure is more preferable in batch processing in order to achieve higher solubility of solute. In this research, since only low concentration Fe<sup>3+</sup> loading is desired, continuous flow process with an initial excess amount of Ferrocene loading in the organic metal feed cell was used.

The supercritical impregnation procedure used in this research work was as follows. The prepared aerogel sample (2-3 g) was placed into a specially designed stirring basket with 4 individual meshed cases. The stirring basket was fixed onto a stirring system of the autoclave, and stirring speed was set to 30 rpm. The autoclave had been pre-heated to a regulated temperature of 50 °C. The backpressure regulator was set to achieve a processing pressure of 1650 psi (114 bar). No co-solvent was used in the reported results. The dopant feed cell loop with 1 g Ferrocene loaded was initially closed before system pressure set point was reached. When the process pressure was achieved and stable, supercritical solution flow was switched to

pass through the dopant cell loop and fed into the system. The feeding flow rate of CO<sub>2</sub> was kept at 5 ml/min for about 2 hours, and then was reduced to 1 ml/min as a makeup flow for another 3 hours to maintain the system pressure. System pressure was then further reduced to 1100 psi in order to lower the solubility of Ferrocene in SCCO<sub>2</sub>, and was held constant for 1 hour. After stopping all feed flow and closing all inlet valves, the entire system was depressurized rapidly to cause solute precipitation.



(a) Continuous Process



(b) Batch Process

**Figure 4.9 Supercritical Impregnation Processes (a) Continuous Process; (b) Batch Process**

#### 4.4 Heat Treatment

After removal of the liquid solvent from the porous structure of the aerogel sample at completion of the supercritical extraction and drying process, further heat treatment was necessary to convert the aerogel into a catalytically useful form and to achieve structural stability. Heat treatment was carried out in the presence of airflow in order to evaporate and decompose any residual solvent and surfactant from the aerogel [193].

A calcination device was designed to meet the following objectives: (1) holding enough quantity of the sample, (2) withstanding the high calcination temperatures, (3) allowing a direct temperature measurement through an inserted electronic temperature probe, (4) preventing the sample particle from being carried out of the device by the flowing air, and (5) loading and unloading the sample easily. The designed schematic diagram of calcination device is shown in Figure 4.10 for horizontal position settings.

The dried aerogel or impregnated TiO<sub>2</sub> base aerogel was placed in the calcination device. Sample was placed in the middle of a 1-inch diameter and 20 cm long stainless steel (SS-316) tube (*Swagelock*) in a horizontal setting. The tubing was then connected to the airflow lines and to a secondary temperature measurement probe device that works in conjunction with the temperature displayed on the control panel of the tube furnace for confirmation and better accuracy. After the whole calcination assembly was placed into the tube furnace (Thermodyne model 21100), the airflow was introduced from a compressed air tank (AIRGAS, breathing quality) regulated at 10 psig. The total calcination time was fixed to 6 hours; however, the calcination temperatures may vary for different samples for comparison purpose.

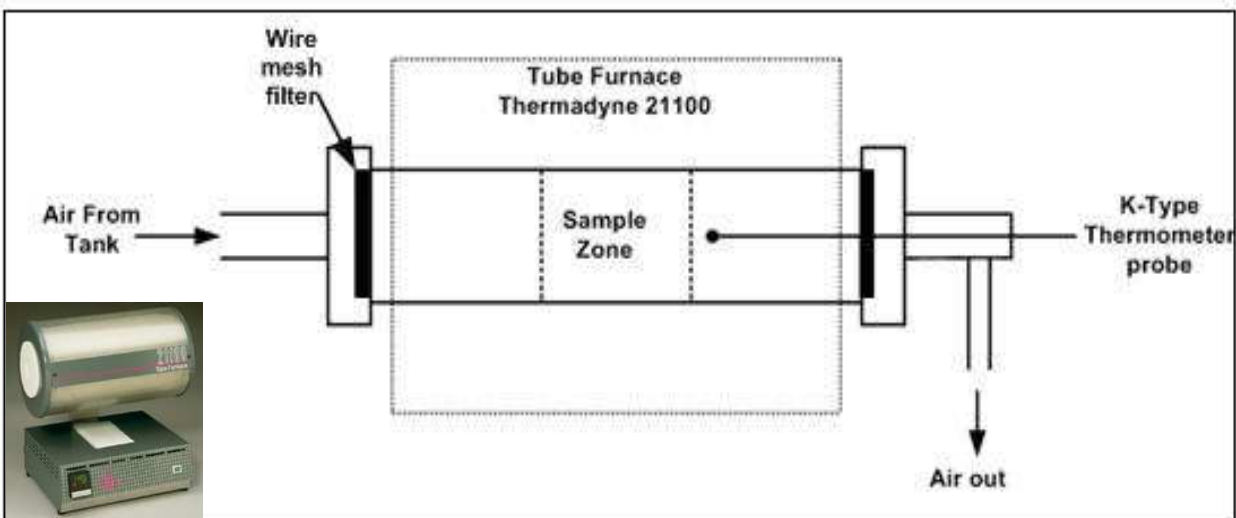


**Figure 4.10 Designed Sample Calcination Device in Horizontal Position**

Trace amount of volatile chemicals including ethanol and hydrochloric acid and non-volatile chemicals such as water and surfactant X-114 may remain inside the porous structure of aerogel. The possible contamination chemicals left inside the aerogel after SFE are listed in Table 4.1. A typical 3-stage aerogel calcination schedule is shown in Figure 4.11. The entire heat treatment procedure was designed to avoid unnecessary severe sintering and pore structure collapsing. Temperature ramps up gradually and holds at certain set temperatures for a period of time to initially allow evaporation of volatiles happen first. Set temperature 1 was for Ethanol, HCl, and water removal, set temperature 2 for HNO<sub>3</sub>, 1-Butanol and surfactant Triton X-114. The sample was calcined in set temperature 3 for three hours after the temperature reached 450 °C.

**Table 4.1 Possible Residue Chemicals Left in Aerogel after Supercritical Extraction and Drying**

<b>Chemical</b>	<b>Boiling point @ Ambient pressure (°C)</b>
Ethanol	78.4
Water	100.0
Triton X-114	170~200
1-Butanol	116~118
HNO <sub>3</sub> (70%)	120.5
HCl	-85.1

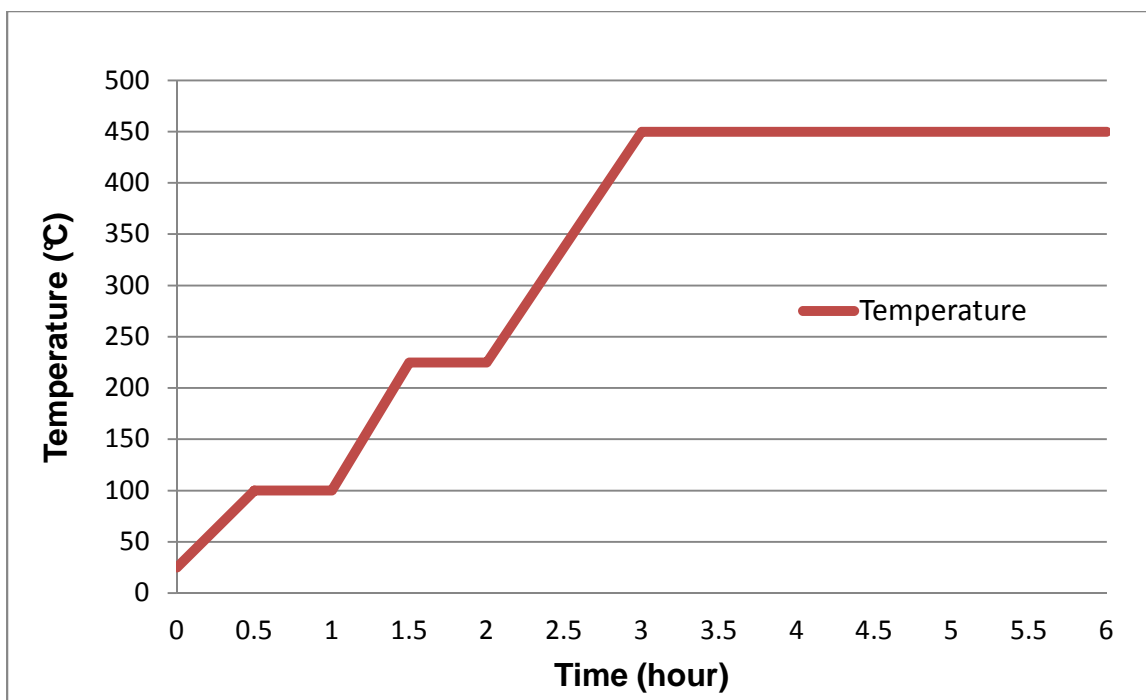


**Figure 4.11 3-stage Aerogel Calcination Schedule**

#### **4.5 Photocatalyst Characterization**

Nitrogen adsorption-desorption experiments were carried out in order to study the total surface area, total pore volume, average pore size, and pore size distribution. An Autosorb series machine along with Enhanced Data Reduction Software from Quantachrome Corp was used routinely for pore structure information development. BET multi-point method was used in order to determine total specific surface area. Pore size distribution and average pore size of the meso-pores were determined using BJH method. The samples' surface morphology, surface images, and elemental composition were characterized by Scanning Electron Microscope combined with energy dispersion spectrum (SEM-EDS). The surface images collected with Focused Ion Beam (FIB) further depict the uniform pore structure and diameter of the photocatalysts. X-ray photoelectron spectroscopy (XPS) analysis further characterized the elemental composition and chemical state. X-ray Diffraction spectra determined the types of crystallinity present in the prepared photocatalysts. Photocatalysts' band gap measurements

were done by using Diffuse Reflectance Spectroscopy (DRS). The typical results will be presented in the next chapter.

#### 4.5.1 Nitrogen Physisorption Measurement

The surface area (SSA), average pore size/diameter (APD), total pore volume (TPV) and pore size distribution were the vital properties of the structural and textural measurements which needed to be characterized. Quantachrome is a world leader in the design and manufacture of laboratory instruments for characterizing properties of porous materials and powders. Nitrogen adsorption-desorption experiments were carried out in order to study the SSA, TPV, APD, and pore size distribution for meso porosity of the gels. Autosorb-1C (shown in Figure 4.12) along with AS1WIN software from Quantachrome Corp. were used for routine pore structure information of TiO<sub>2</sub> based aerogel. Aerogel samples were prepared at the degassing station to remove any adsorbed volatile residues such as air, carbon dioxide, water, or organic solvents from the sample surface. The degassing procedure normally takes 3-12 hours at 80 °C under ultra high vacuum (UHV), degassing time was determined by sample condition, for example, aerogel samples before heat treatment (un-calcined) needs overnight degassing, but the calcined sample only needs 3-5 hours degassing.

##### a. Specific surface area (SSA)

The Brunauer-Emmett-Teller (BET) method [194] is the most widely used procedure for the determination of the surface area of solid materials and involves the use of the BET equation (4.5).

$$\frac{1}{W\left(\left(\frac{P_0}{P}\right)-1\right)} = \frac{1}{W_m C} + \frac{C-1}{W_m C} \left(\frac{P}{P_0}\right) \quad (4.5)$$



**Figure 4.12 Quantachrome Autosorb-1C**

where  $W$  is the weight of gas adsorbed at a relative pressure,  $P/P_0$ , and  $W_m$  is the weight of adsorbate constituting a monolayer of surface coverage. The term  $C$ , the BET  $C$  constant, is related to the energy of adsorption in the first adsorbed layer and consequently its value is an indication of the magnitude of the adsorbent/adsorbate interactions.

Equation 4.5 results in a linear plot of  $1/[W/(P_0/P)-1]$  vs.  $P/P_0$  for most solids using nitrogen as the adsorbate. Nitrogen adsorption-desorption data at 77 K which is the standard

boiling point of nitrogen were collected and analyzed. The total specific surface areas (SSA) for uncalcined and calcined aerogel samples were obtained by using a multi-point BET method which is restricted to a limited region of the adsorption isotherm, usually in the  $P/P_0$  range of 0.05 to 0.30. This linear region is shifted to lower relative pressures for microporous structures.

The standard multipoint BET procedure requires a minimum of three points in the appropriate relative pressure range. 7 points BET was chosen in this research in order to increase measurement accuracy. The weight of a monolayer of adsorbate  $W_m$  can then be obtained from the slope  $s$  and intercept  $I$  of the BET plot. From equation 4.5:

$$S = \frac{C-1}{W_m C} \quad (4.6)$$

$$I = \frac{1}{W_m C} \quad (4.7)$$

Thus, the weight of a monolayer  $W_m$  can be obtained by combining equations 4.6 and 4.7.

$$W_m = \frac{1}{s+I} \quad (4.8)$$

The second step in the application of the BET method is the calculation of the surface area. This requires knowledge of the molecular cross-sectional area  $A_{cs}$  of the adsorbate molecule. The total surface area  $S_t$  of the sample can be expressed as:

$$S_t = \frac{W_m N A_{cs}}{M} \quad (4.9)$$

where  $N$  is Avogadro's number ( $6.023 \times 10^{23}$  molecules/mol) and  $M$  is the molecular weight of the adsorbate. Nitrogen is the most widely used gas for surface area determinations since it exhibits

intermediate values for the C constant (50-250) on most solid surfaces, precluding either localized adsorption or behavior as a two dimensional gas. Since it has been established that the C constant influences the value of the cross-sectional area of an adsorbate, the acceptable range of C constants for nitrogen makes it possible to calculate its cross-sectional area from its bulk liquid properties. For the hexagonal close-packed nitrogen monolayer at 77 K, the cross-sectional area  $A_{cs}$  for nitrogen is  $16.2 \text{ \AA}^2$ .

The specific surface area SSA of the solid can be calculated from the total surface area  $S_t$  and the sample weight  $w$ , according to equation 4.10:

$$SSA = S_t/W \quad (4.10)$$

b. Porosity: Pore volume, Pore Size and Pore Size Distribution

It is expedient to characterize pores according to their sizes.

- Macropores: > 50 nm diameter
- Mesopore: 2 nm – 50 nm diameter.
- Micropore: < 2 nm diameter

Porosity of powders and other porous solids can be conveniently characterized by gas adsorption studies. Two common techniques for describing porosity are the determination of total pore volume and pore size distribution. For the evaluation of the porosity of most solid materials, nitrogen at 77 K is the most suitable adsorbate.

Total pore volumes, average pore size and pore size distributions of the aerogel porous network before and after heat-treatments were calculated by using the Quantachrome enhanced data reduction system through the BJH method, proposed by Barrett, Joyner and

Halenda, 1951 [195] utilizing the nitrogen desorption isotherm 40 points method between  $P/P_0$  range of 0.99 and 0.05. The results are presented and discussed in Chapters 5.

The total pore volume is derived from the amount of vapor adsorbed at a relative pressure close to unity, by assuming that the pores are then filled with liquid adsorbate. The average pore size can be estimated from the pore volume. For example, assuming cylindrical pore geometry, the average pore radius  $r_p$  can be expressed as

$$r_p = \frac{2V_{liq}}{S} \quad (4.11)$$

where  $V_{liq}$  is the volume of nitrogen contained in the pores converted from the volume of nitrogen adsorbed ( $V_{ads}$ ) and  $S$  is the BET surface area. The pore diameter was taken as the one where maximum differential pore volume occurred.

The distribution of pore volume with respect to pore size is called a pore size distribution. It is generally accepted that the desorption isotherm is more appropriate than the adsorption isotherm for evaluating the pore size distribution of an adsorbent due to the isotherm being closer to true thermodynamic stability.

#### **4.5.2 Scanning Electron Microscopy (SEM), Energy Dispersion Spectroscopy (EDS) and Focused Ion Beam (FIB)**

Scanning electron microscope (SEM) and energy dispersion spectroscopy (EDS) (Hitachi, Model S-800 SEM/EDAX-Phoenix EDS system with field emission electron gun) were used to obtain a sample's high-resolution surface images, elemental composition and for study of the distribution of coupling semiconductor and dopant on photocatalyst surface.

The SEM has a magnification power of 300,000 times actual size. The image is generated by scanning a small diameter focused beam of high-energy electrons over the specimen. These electrons are scattered from the solid sample surface, and are then collected

to generate an image. The electron beam is also used to reveal information on chemical composition of microstructures below 1  $\mu\text{m}$  in size using an x-ray spectrometer. The spectrometer collects x-rays which are also generated by the electron beam. The x-rays line intensities are characteristic of the quantity of each element present in the area scanned by the electron beam. EDS is used to acquire elemental maps or spot chemical analyses.

A small amount of dried sample was placed on the top of the SEM-EDS sample stub using carbon tape as the sample holding media. The sample was coated with a thin layer of gold (Ag) and palladium (Pd) via a Hummer X sputtering coater to prevent electron charging. The coating process was highly recommended when clear ultra high-resolution surface images are required. In this way, the samples are grounded and do not become highly electrically charged which will result in blurry images. However, the carbon tape and metallic coating can introduce other elemental signals when the SEM-EDS spectra are analyzed. Thus, in EDS elemental mapping and analysis, samples were uncoated.

Obtaining a highly porous structure is one of the goals in this research, it is important to show not only the image of sample surface but also its cross sections to unveil the real porous structure. The Quanta 200 3D Dual Beam is a combination of two systems: Scanning Electron Microscope (SEM) and Focused Ion Beam (FIB). It uses an energetic focused beam of ions as a “nano” milling machine and can mill cross sections and patterns. The two different sources (electrons and ions) enable high-resolution imaging of the surface structures.

### **4.5.3 X-ray Diffraction (XRD)**

Proper crystal structure is very important for photocatalyst, and X-ray Diffraction (XRD) is a powerful fundamental non-destructive technique for characterizing the atomic and molecular structure of crystalline materials. In this method, an incident beam of X-rays are diffract into many different directions by crystalline atoms, creating a diffraction pattern. This pattern

provides information on structures, phases, preferred crystal orientations (texture) and other structural parameters such as average grain size, crystallinity, strain and crystal defects. X-ray diffraction peaks are produced by constructive interference of a monochromatic beam of x-rays scattered from each set of lattice planes at specific angles. The peak intensities are affected by the atomic diffraction within those lattice planes. Consequently, the X-ray diffraction pattern is the fingerprint of periodic atomic arrangements in a given material.

Philips PANalytical's X'Pert Pro MRD X-ray diffractometer (X-Ray source Cu K $\alpha$  ( $\lambda=1.5405$  Å), 45 KW and 40mA) along with *X'pert Highscore* plus software was used to collect XRD patterns of doped and un-doped aerogel samples. In the X-ray diffraction measurement, the width of incident slit and diffraction slit used for all analysis were 1° and 2°, respectively. The incident beam mask used corresponds to 10 mm. A ground fine powder sample is mounted on a sample holder plate and gradually rotated from one starting diffraction angle to an ending diffraction angle (normally  $2\theta=20^\circ$  to  $80^\circ$ ) with step size of  $0.02^\circ$  while being bombarded with X-rays, which generate a diffraction pattern. The characteristic peak ( $2\theta=25.28^\circ$ ) of anatase (101) and the characteristic peak ( $2\theta=27.42^\circ$ ) of rutile (110) were used for comparative and quantitative analysis. Anatase/rutile ratio can be simply calculated from the resulting XRD patterns using the Spurr equation:

$$\text{Rutile \%} = 1 / \left\{ 1 + 0.8 \left[ \frac{I_A(101)}{I_R(110)} \right] \right\} \quad (4.12)$$

where  $I_A$  is the intensity of anatase (101) peak and  $I_R$  is the intensity of rutile (110) peak, or achieved by using Rietveld analysis with pattern simulation if pure anatase/rutile characteristic crystalline peaks reference data are available.

Grain size or the mean size of the ordered (crystalline) domains  $\tau$ . can be estimated from a XRD line broadening analysis using the Scherrer equation:

$$\tau = \frac{k\lambda}{\beta \cos \theta} \quad (4.13)$$

where  $k$  is the dimensionless shape factor,  $\lambda$  is the X-ray wavelength,  $\theta$  is the Bragg angle, and  $\beta$  is the line broadening at half the maximum intensity (FWHM).

#### 4.5.4 X-ray Photoelectron Spectroscopy (XPS)

X-ray Photoelectron Spectroscopy (XPS) is a relatively non-destructive technique that: (1) exposes the sample to ultra high vacuum (UHV) pressures with base pressures of  $1 \times 10^{-10}$  Torr, (2) increases the temperature by approximately 10-20 °C, and (3) exposes the sample to soft X-rays between approximately 1000~1500 eV. These conditions are considered nondestructive for most materials and systems with few exceptions. The uses of XPS are elemental analysis of surface and near-surface regions of all elements except hydrogen (H) and chemical state information of near-surface species. Samples were prepared by degassing under UHV for 24 hours. XPS elemental analysis was done using both Al K $\alpha$  and Mg K $\alpha$  radiation based on the binding energy range and resolution requirement. Some examples of the information gathered through the use of XPS are the determination of oxidation states of metal atoms in metal oxide surface films and the identification of their surface concentrations. The average analysis depth for XPS is 10-100 Å. Qualitative analysis can be performed in 5 to 10 minutes. Quantitative analysis requires 1 hour to several hours depending on the information desired. Equipment used in this research was Perkin Elmer PHI 560 UHV XPS/ SAM system with AugerScan 2 data . Due to limited access to this equipment, only few samples were analyzed on this equipment.

#### 4.5.5 Diffuse Reflectance Spectroscopy (DRS)

Diffuse Reflectance Spectroscopy (DRS), also known as Elastic Scattering Spectroscopy, is a non-destructive technique that measures the characteristic reflectance

spectrum produced when incident light is reflected from a medium surface at many angles rather than just one angle as in specular reflection. The DRS measurement mechanisms are light absorption and scattering on medium surface, which vary with wavelength to produce the reflectance spectrum. This spectrum demonstrates information about the optical properties and structure of the measured medium. The UV-Vis Diffuse reflectance spectra show that the sample absorbs certain wavelengths of light which are directly related to a material band gap, through the following relation:

$$E_G = E_{light} = \frac{hc}{\lambda} \quad (4.14)$$

where  $h$  is Planck's constant,  $c$  is the speed of light and  $\lambda$  is the wavelength. The typical DRS measurement setup was composed of a UV-Vis light source (DH-2000 Deuterium Tungsten Halogen light source UV-Vis-NIR, Ocean Optics), a UV-Vis spectrometer (USB4000-UV-VIS Miniature Fiber Optic Spectrometer, 200-850 nm Ocean Optics), ISP-I Integrating Spheres (ISP-50-8-R-GT, Ocean Optics) and a couple of optical fibers (QP600-1-SR, Ocean Optics). A set of Teflon sample holders were used to hold samples and reflectance standard (99.9% pure Barium sulfate, BaSO<sub>4</sub>, Sigma-Aldrich). Samples were ground to fine powders before measuring. Integrating sphere, with an internal PTFE-coating, measures the total integrated reflectance of surfaces placed against the sphere's sample port. The value obtained becomes the reflectance (relative reflectance) with respect to the reflectance of the reference white standard, which is taken to be 100%.

#### **4.6 Photocatalytic Activity**

After physical and chemical characterization, the photocatalytic performances of different aerogel photocatalysts were evaluated in comparison with *Degussa* P25 in the degradation of methylene blue (MB) as a model compound under UV and visible light. MB is an heterocyclic

aromatic chemical compound ( $C_{16}H_{18}N_3SCl \cdot 3H_2O$ , supplier: Acros Organic) (shown in Figure 4.13). It has been used in various applications. At room temperature, it dissolves in water and yields a blue solution.

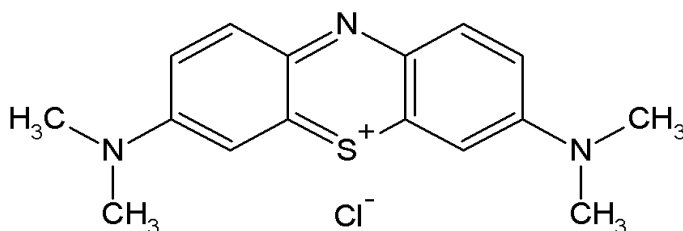
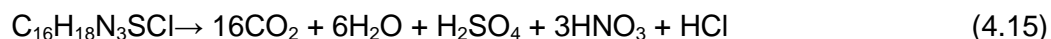


**Figure 4.13 Methylene Blue Chemical Structure**

When photodecomposition starts, the blue color of an aqueous solution of MB fades. Theoretically, MB can be completely converted, illustrated by the following reaction.



Experiments run at room temperature and pressure (STP) with 500 ml of 10 ppm MB water solution at neutral pH was used to evaluate the photocatalytic activities of different photocatalysts in the decomposition of MB. The experimental system consisted of a quartz water cooling jacketed batch stirred reactor (600ml,  $D_{out}= 9.5$  cm,  $D_{in}= 7.5$  cm ) manufactured by Schott Duran where 200 mg of catalysts was used. MB solution with photocatalyst added was stirred 30 minutes in the dark to achieve adsorption equilibrium before initiation of the photodecomposition experiment. The photodecomposition reaction is carried out for 12 hours. The initial MB solution concentration was measured and recorded with Ocean Optics USB4000 UV-Vis optical spectrometer. All experiments were run under constant temperatures which was maintained by continuous stirring and cooling water flow to avoid any Arrhenius effect on reaction rate. Experiments setups run under UV exposure and visible light were different.

#### 4.6.1 Under UV Light

The UV light source used was Spectroline ENB-260C UV hand lamp (6 W with UVA=365 nm and UVB=312 nm) Figure 4.14 shows the general configuration of the experimental system. A parafilm covered batch reactor was placed inside a cubic foil laminated enclosure (20 X 20 X 35 cm) which had an open window on the left-hand sidewall. The UV lamp was securely attached to the windows opening to avoid unnecessary radiation leakage. The UV lamp window was 10 cm away from of reactor center. UVA was used in this research work only. A flow meter (AALBORG Instrument) and an aerating stone was used to control the flow and diffusion of oxygen (Breathing quality, flow rate at 100 ml/min) into the MB-photocatalyst suspension, while a magnetic stirrer and stirring rod were used to uniformly disperse the catalyst particle throughout the solution. About 8 ml of suspension samples were drawn at each sampling point with sampling syringe at the top of enclosure. Sample was transferred into a centrifuge tube which was covered with aluminum foil to avoid further photodegradation. The experiment starting point,  $T_0$ , is the time when UV light was turned on. Figure 4.15 shows that the intensity of UV light varies with distance, the light intensity at 10 cm is  $0.6 \text{ mW/cm}^2$ . Samples were drawn at 30 minute intervals for the first 2 hours, then followed by one hour intervals from the 3<sup>rd</sup> to 8<sup>th</sup> hour, and 2 hours intervals from the 9<sup>th</sup> hour to the 12<sup>th</sup> hour.

The experimental procedure and conditions that may affect the photocatalytic activity have been addressed. Initial concentration of reactant/pollutant, photocatalyst concentration, incident light intensity, pH of the solution and concentration of oxygen are the major extrinsic variables. The main purpose of the experimental design was to control and optimize maximum number of extrinsic variables to maximize photocatalytic activity within the same and between experiments in order to maintain the consistency in each experiment and allow the reasonable comparison of the results from different experiments.

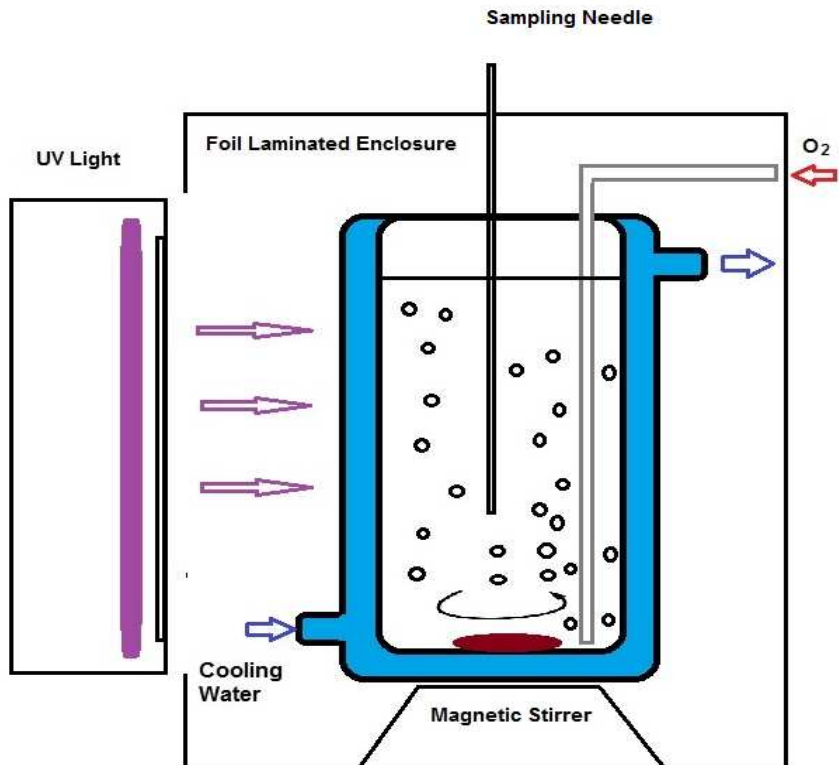


Figure 4.14 Batch Reactor for Photocatalytic Experiment under UV Light

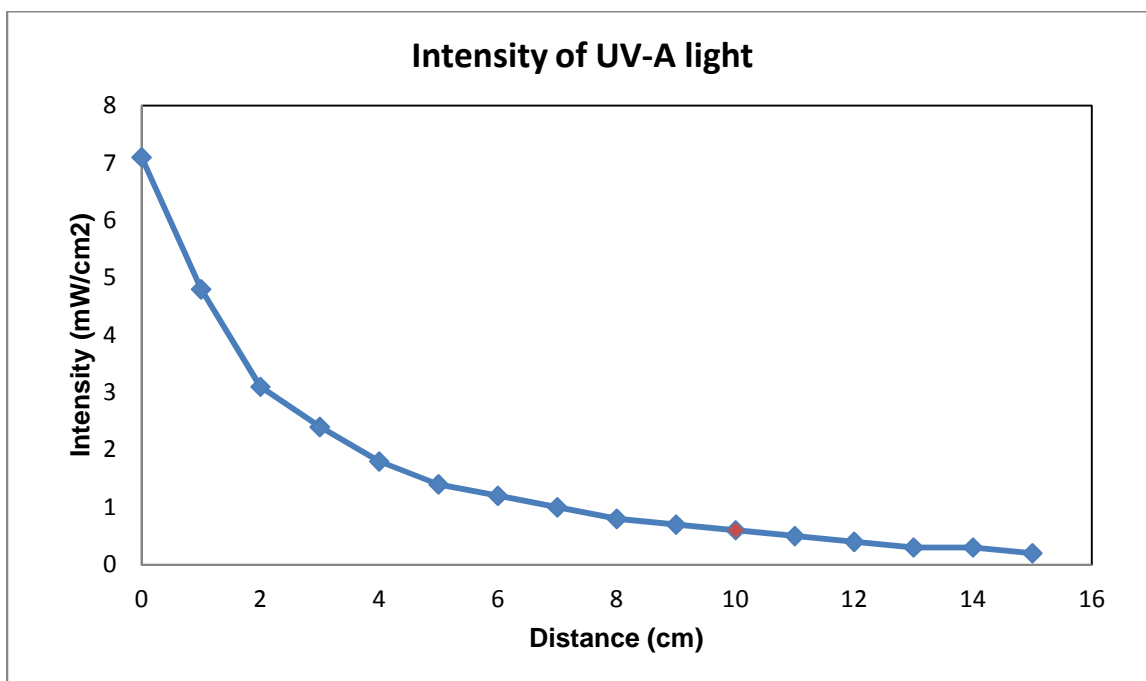


Figure 4.15 Measured UV-A Light Intensity vs. Distance

#### 4.6.2 Under Visible Light

The visible light source was 250 W IWASAKI EYE HID Self-ballasted mercury lamp (E28W26), the batch reactor was covered with UV cut-off filter film ( $>400$  nm). Figure 4.16 shows the general configuration of the experimental system. The parafilm covered batch reactor was placed inside a cubic aluminum enclosure (50 X 33 X 55 cm) with circulation cooling fan installed. The mercury lamp was fixed to top of enclosure 35 cm away from the center of the reactor. Experimental procedure was conducted in the same manner as the one for UV light tests. Samples were drawn at one-hour intervals. Figure 4.17 shows the intensity distribution of UV A light and visible light with wavelength change.

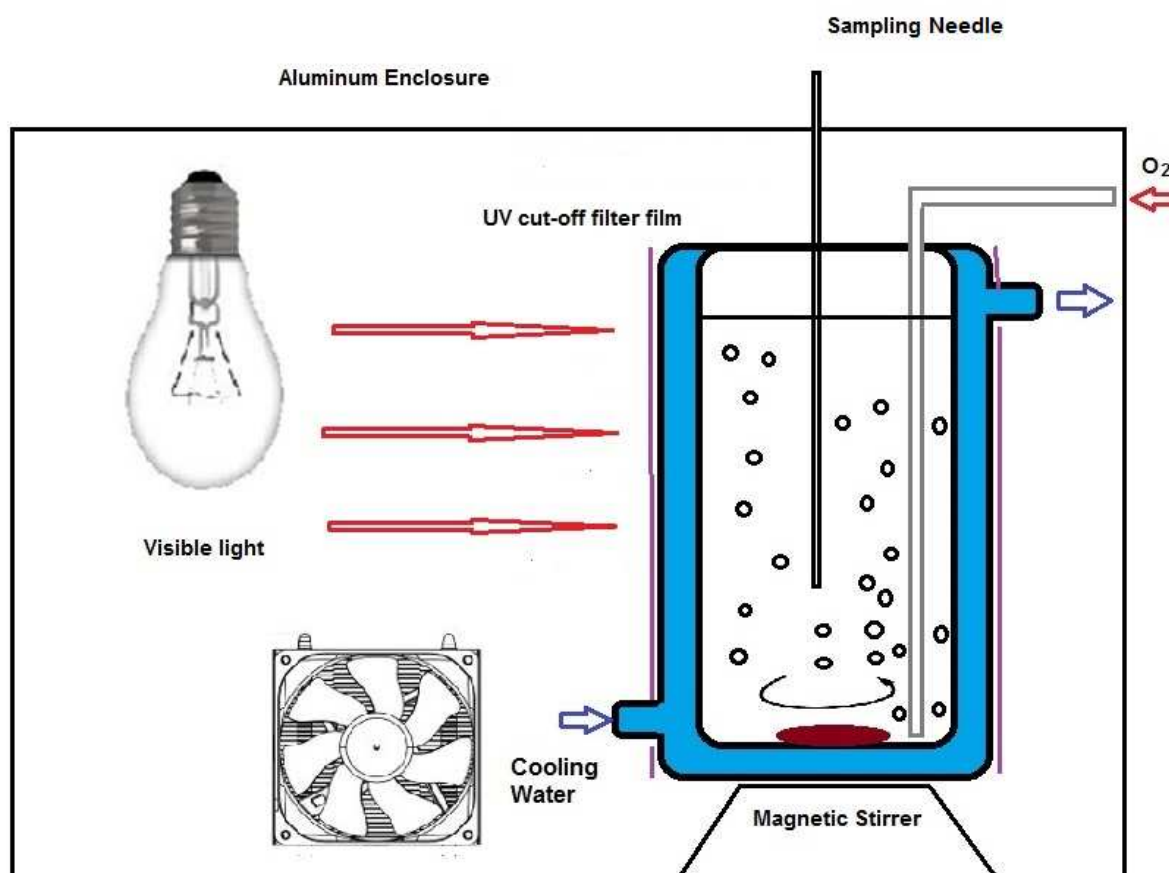
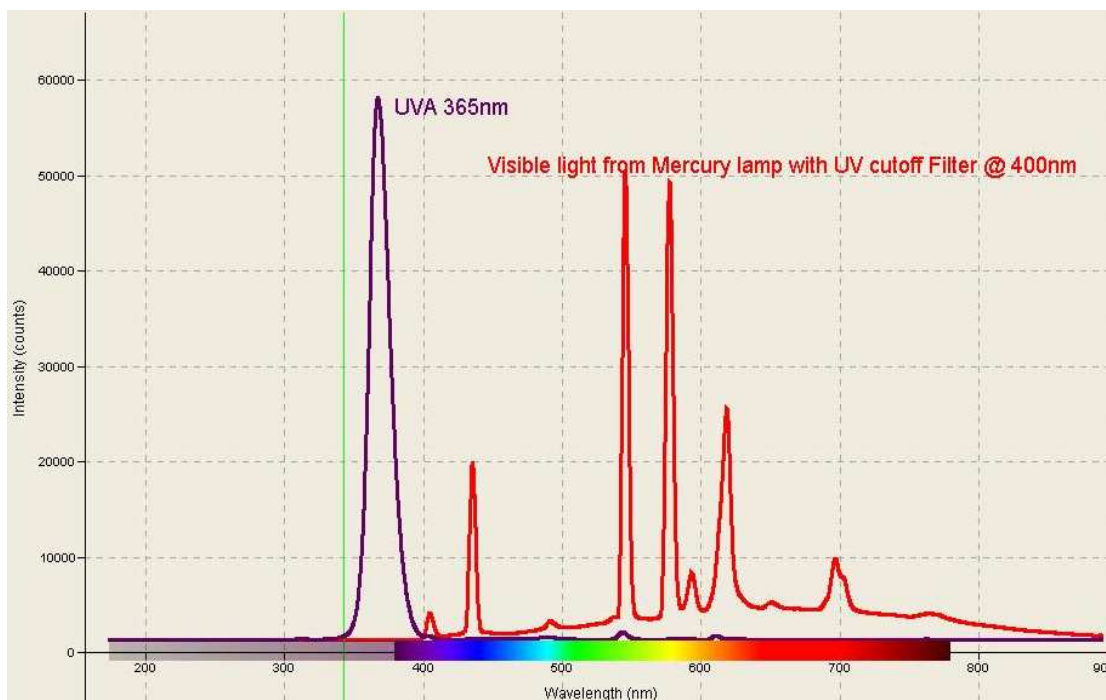


Figure 4.16 Batch Reactor for Photocatalytic Experiment under Visible Light



**Figure 4.17 Intensity Distribution of UV-A Lamp and Mercury Lamp with UV Cut-off Filter**

### 4.6.3 UV-Vis Spectroscopy

Many substances absorb UV or visible light, the wavelength of light absorbed varies from compound to compound which can be used to identify the absorbing species within the compound. A UV-Vis absorption spectrum may show a number of absorption bands corresponding to structural groups within the compound. Meanwhile, Beer's law states that the absorbance of a solution is directly proportional to the path length,  $b$ , and the concentration of the absorbing species,  $c$ , as shown in following equation (4.16)

$$A = \epsilon bc \quad (4.16)$$

where  $\epsilon$  is a constant of proportionality, known as absorptivity. UV-Vis absorption spectra are a measure of how much light a sample absorbs. For most samples, absorbance relates linearly to the concentration of the substance. MB's UV absorption peak is at 297 nm. Before measuring any MB concentration change from collected samples, a standardized calibration curve of MB

solution (0-10 ppm) was prepared. UV-Vis concentration measurement setup is similar to the one used in DRS except the light sensor was switched from integrating sphere to UV-Vis transmission dip probe (T300-RT-UV-VIS, Ocean optics) and a light intensity attenuator (FVA-UV, Ocean Optics) Coupling with UV-Vis USB4000 spectrometer and light source. This combination of instrumentation creates small-footprint optical-sensing system for measuring in situ transmission in chemical solution and other liquids. The probe was fixed onto a designed probe holder to minimize the system deviation. This probe was carefully dipped into sample vial during concentration measurement, and was rinsed at least twice with de-ionized water between each measurement.

The collected MB-photocatalyst suspension samples were centrifuged at 8500 rpm for 30 minutes in order to completely separate the solid particles from the liquid solution. Only clear solution was transferred into the UV-Vis testing sample cells for concentration measurement. Experimental results will be discussed in chapter 6.

## CHAPTER 5

### PHOTOCATALYST PREPARATION RESULTS AND DISCUSSION

In this chapter, the experimental results are presented and discussed in four main related sections: pure  $\text{TiO}_2$  aerogel preparation, co-precipitated aerogel preparation, supercritical impregnation, and, finally comparison between the co-precipitated and supercritical fluids impregnated  $\text{TiO}_2$  based photocatalyst system.

The details of the procedure for  $\text{TiO}_2$  based aerogel preparation are described in Chapter 4. Templated  $\text{TiO}_2$  xerogel samples and regular (non-templated)  $\text{TiO}_2$  aerogel samples had also been synthesized for comparison purposes only. Some procedural or analytical conditions and parameters had been studied and optimized in previous work [192] or suggested in the instrument's standard procedure. For example, keeping the molar ratio of surfactant template used in sol-gel preparation at 0.1 had been found to be the best choice for obtaining a highly porous aerogel with uniform pore size distribution. The choice of analysis points in BET and BJH analysis were suggested as 7-point BET (0.05 to 0.30  $P/P_0$ ) and 20-20 BJH adsorption-desorption points, respectively.

The initial composition of reagents used in the pure  $\text{TiO}_2$  sol-gel preparation obviously impact the final textural and chemical properties of the aerogel, including aerogel surface area, porosity, chemical and thermal stability, crystal structure, etc. Different composition results in variances in gelation rates, hydrolysis and condensation reaction rates, and degree of cross-linking. This chapter discusses optimization of the  $\text{TiO}_2$  based aerogel photocatalyst preparation

process. The effects on textural and chemical properties of photocatalysts by coupling with  $\text{WO}_3$  co-precipitate, and finally doping with iron ion precursor are also discussed in this chapter.

## 5.1 $\text{TiO}_2$ Aerogel Preparation

### 5.1.1 Effect of Composition

In the study described in the following sections, the molar ratio of ethanol and  $\text{HNO}_3$  were varied during the process optimization study. Meanwhile, regular  $\text{TiO}_2$  aerogel and templated xerogel were prepared for comparison purpose.

#### a. The amount of ethanol

Sol is a colloidal solution that solid particles disperse in a liquid. Ethanol was used as the liquid solvent of sol, which will be encapsulated inside a multi-dimensional integrated network of solid particles (gel) after hydrolysis and further condensation. An appropriate amount of solvent is required to allow a sufficient reaction volume for metal alkoxide hydrolysis reaction and network cross-linking. During formation of the gel, a solid network spans the volume of the liquid medium. The use of very small amount of solvent will limit the degree of cross-linking, accelerate the gelation rate, and result in lower porosity and smaller pore size. Conversely, too much of solvent will cause isolated cross-linking, form a weaker porous nanostructure with larger pore sizes and extend the gelation time.

Recipes for two different  $\text{TiO}_2$  sol-gel preparations and comparison textural analysis results are shown in table 5.1. Here, the dosage ratio of all other reagents and experiment conditions were kept the same for each aerogel preparation. The molar ratios of each component in the first and second sample preparation were  $\text{Ti}(\text{OBU})_4$  : Ethanol :  $\text{H}_2\text{O}$  :  $\text{HNO}_3$  : Triton X-114 is 1 : 30 : 7.5 : 0.3 : 0.1 and 1 : 20 : 7.5 : 0.3 : 0.1, respectively. BET multi-point method ( $P_0/P=0.05-0.30$ ) was used in order to determine total surface area of aerogel samples

before and after calcination. Results comparison is shown in Figure 5.1. Pore size distribution results for four samples characterized through The BJH dV/dD desorption method are also shown in Figure 5.2.

**Table 5.1 Textural Properties for Degussa P25, Sigma-Aldrich 99% Pure TiO<sub>2</sub> Powder and Two Templated TiO<sub>2</sub> Aerogel with Different Ethanol Usage**

Sample		BET surface area (m <sup>2</sup> /g)	Total Pore Volume (cc/g)	Average Pore (Å)
Molar ratio	Condition			
Degussa P25	N/A	59.7	0.149	19.3
Sigma-Aldrich 99% Pure TiO <sub>2</sub>	N/A	10.7	0.126	24.4
EtOH: Ti(OBu) <sub>4</sub> 30 : 1	Uncalcined (A)	365.0	2.652	290.7
	Calcined (B)	150.5	1.255	273.7
EtOH: Ti(OBu) <sub>4</sub> 20 : 1	Uncalcined (C)	315.4	1.093	138.6
	Calcined (D)	127.0	0.516	123.6

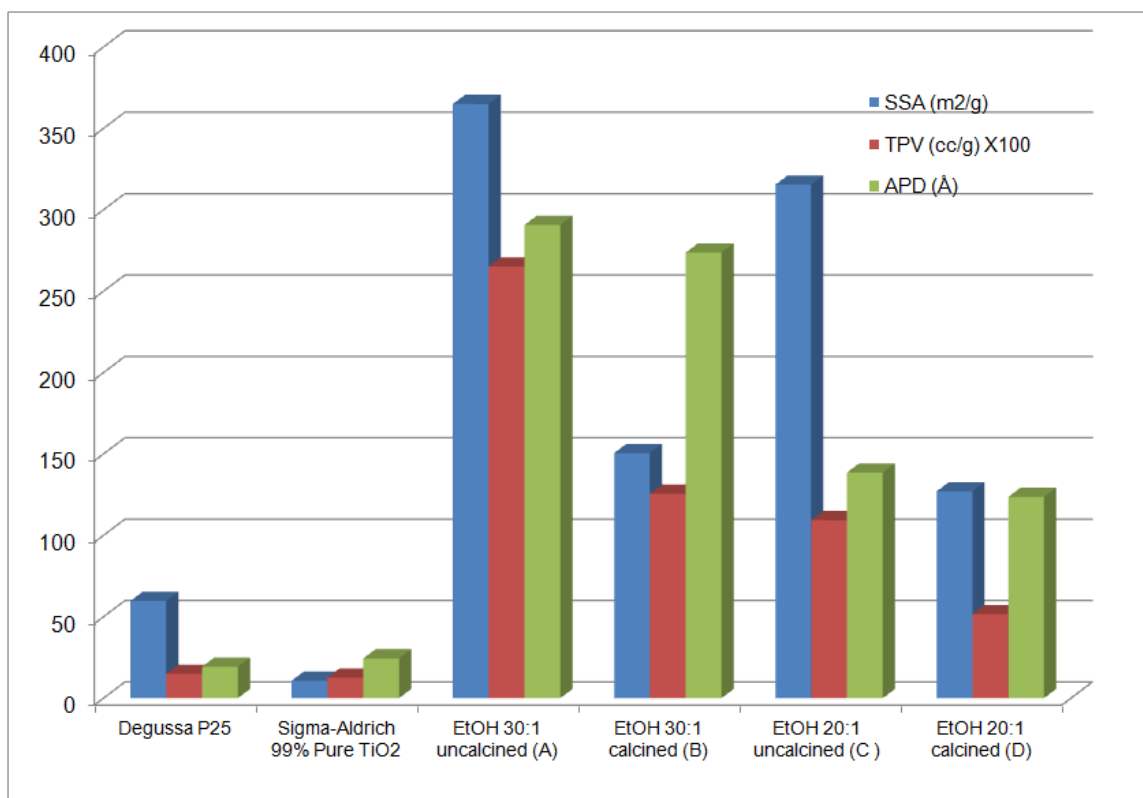


**Figure 5.1 SSA, APV and APD of Degussa P25, Sigma-Aldrich 99% Pure TiO<sub>2</sub> and Two Templated TiO<sub>2</sub> Aerogel Prepared with Different Ethanol Usage (A,B,C,and D)**

Specific surface area (SSA) is a vital property of porous catalyst. The higher SSA the catalyst has, the greater the number of actual reacting sites is available for catalytic reaction. However, micropores are not totally accessible during photocatalytic reaction due to higher surface tension compared to other larger pores. Thus, the inaccessible portion of micropores in a photocatalyst may be considered as non-porous material, especially in liquid system such as water remediation.

The pore structure of the materials is compared with Degussa P25 nanoparticle catalyst and Titanium dioxide from Sigma-Aldrich. As shown in Figure 5.1, the surface area, pore volume per gram and average pore size of the product aerogels are about an order of magnitude higher in comparison to the industry standard. The surface area was about 3 to 10 times greater for aerogels while pore volume per gram increased by about five times. With using different amounts of solvent, compared to sample C and D, sample A and B has similar SSA change patterns before and after calcination but very different TPV and APD in value. This phenomenon can be explained as evidence that a sufficient amount of solvent will provide enough reaction volume which allows hydrolysis and cross-linking maximized, thus generating a highly porous matrix. Also evidenced was that less solvent led to less porous matrix. The entrapped template surfactant molecules did not completely expand in the pore liquid and thus produced higher percentage of micropores which caused the smaller average pore diameter. Also noted is that, unstable micropores and mesopores in as-made aerogels tended to sinter and loss pore volume during heat treatment. Sample A and B synthesized with appropriate amount of solvent shows stronger structure throughout the entire mesopore region. The pore size distribution shown in Figure 5.2 clearly indicated that the pore volume of the pores with diameters less than 2 nm dramatically decreased after calcination. Also, the average pore size of the samples showed some decrease due to sintering of pores. It was further experimentally observed that too much solvent increasing aging time and requires more supercritical fluid to be

used to remove the ethanol from the alcogel during the drying process, a drawback in this process that must be considered in final process design.

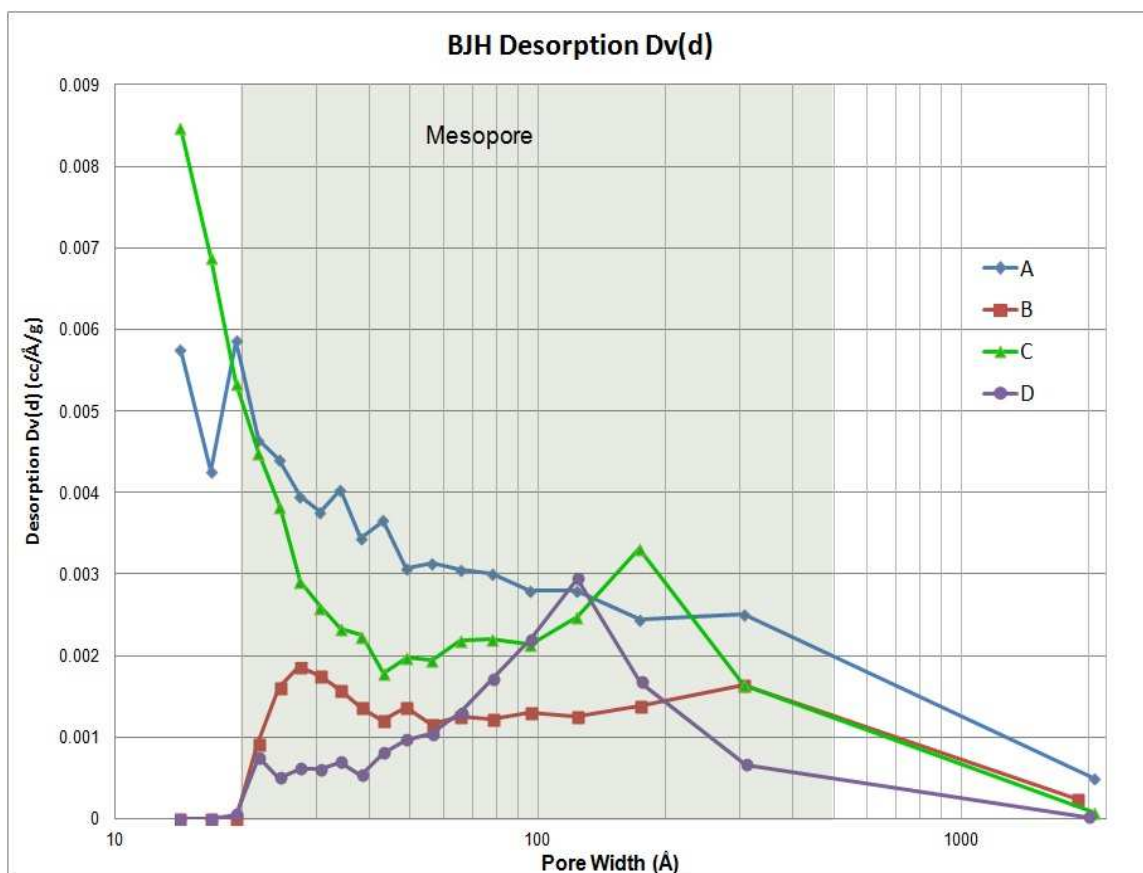


**Figure 5.2 Pore Size Distribution of Two Templated TiO<sub>2</sub> Aerogels With Different Ethanol to Solids Ratios (30:1 for A and B, 20:1 for C and D)**

b. The amount of HNO<sub>3</sub>

Extensive research works have been performed on hydrolysis of various titanium alkoxides (Ti(OR)<sub>4</sub>) as precursors in sol-gel synthesis of titanium dioxide. Livage et al. [180] proposed that the entire hydrolysis reaction of titanium alkoxides can be simply divided into two steps. First, one of alkoxy groups (•OR) is quickly substituted by hydroxyl group (•OH) from water in the hydrolysis reaction; second, oxo- and hydroxo- bridges are formed in polycondensation reactions. Both steps are very quick if there is sufficient water present. As

condensation reactions progress, oligomeric oxoalkoxides are formed with various compositions  $TiO_x(OR)_{4-2x}$ . Aging of the condensation will allow the completion of condensation reactions and multilevel cross-linked network is obtained upon completion. Immediately upon water addition to the alcohol/titanium alkoxide solution, submicron species (monodisperse colloids) are created and start growing, with the growth described by LaMer theory [196]. Even when water is slowly being added dropwise, quick condensation reactions result in rapid precipitation of solid particles which generates small porous structures. In order to decrease the rate of solid precipitation formation, a small amount of acid can be added to the alcohol/titanium alkoxide solution before water addition. However, too much acid may cause extremely slow gelation rates and longer aging times which are undesirable. The effect of gelation time on gel properties is significant. Gelation time is defined as the time it takes a solution to undergo a rapid rise in viscosity. This corresponds to a solution's transition from a viscous fluid to an elastic gel. At the gel point, there is a continuous solid phase with a structure where particles form and branch as dictated by the specific growth conditions. This particular phase has significant impact on the structural evolution the material undergoes in all subsequent processing steps.

**Table 5.2 Gelation Time and SSA for Templated  $TiO_2$  Aerogels with Different  $HNO_3$  Addition**

<b>Molar ratio (Uncalcined)</b>	<b>Gelation time (hour)</b>	<b>BET Specific Surface Area SSA (<math>m^2/g</math>)</b>
<b><math>Ti(OBu)_4: HNO_3=1:0.25</math></b>	< 2	266.9
<b><math>Ti(OBu)_4: HNO_3=1:0.3\sim 0.35</math></b>	4~6	365.0
<b><math>Ti(OBu)_4: HNO_3=1:0.5</math></b>	> 36	98.1

The results shown in Table 5.2 indicate that using either less or more than appropriate amount of acid resulted in a decrease of synthesized aerogel surface area. However, the SSA

decrease with less acid is due to fast gelation, while the SSA decrease with more acid is caused by a low degree of network cross-linkage.

c. Surfactant

The main purposes of using surfactant as a template in sol-gel synthesis are for defining the final porosity, pore distribution, orientation and the surface texture. Regular TiO<sub>2</sub> aerogel and templated TiO<sub>2</sub> aerogel textural properties comparison are shown in Table 5.3 and Figure 5.3. Pore size distribution change of regular TiO<sub>2</sub> aerogel before and after calcination is shown in Figure 5.4.

**Table 5.3 Textural Properties for Regular TiO<sub>2</sub> Aerogel and Templated TiO<sub>2</sub> Aerogel (Uncalcined and Calcined)**

Sample		BET surface area (m <sup>2</sup> /g)	Total Pore Volume (cc/g)	Average Pore (Å)
Templated TiO <sub>2</sub> Aerogel	Uncalcined	365.0	2.652	290.7
	Calcined	150.5	1.255	273.7
Regular TiO <sub>2</sub> Aerogel	Uncalcined	283.8	0.527	74.3
	Calcined	25.4	0.146	310.0

Regular TiO<sub>2</sub> aerogel has a relatively high surface area before undergoing heat treatment. However, the majority of the porous structure is composed of micropores and small mesopores (> 5 nm). After calcination, almost all multilevel porous structures vanished due to crystalline growth, pore sintering or collapse. By comparison, templated TiO<sub>2</sub> aerogel still maintained the mesoporous structure after heat treatment. In other words, using a non-ionic surfactant template not only defines the porosity and pore size distribution without limiting the cross-linking and gelation, but also provides more thermally stable textural properties to the aerogel and protects the pores from collapsing during the calcination step. It is worth mentioning that the choice of surfactant is very important. It is important to select a surfactant template with

necessary co-solvent that can be easily and completely removed during supercritical fluid extraction and drying to ensure the superior pore structure retention.

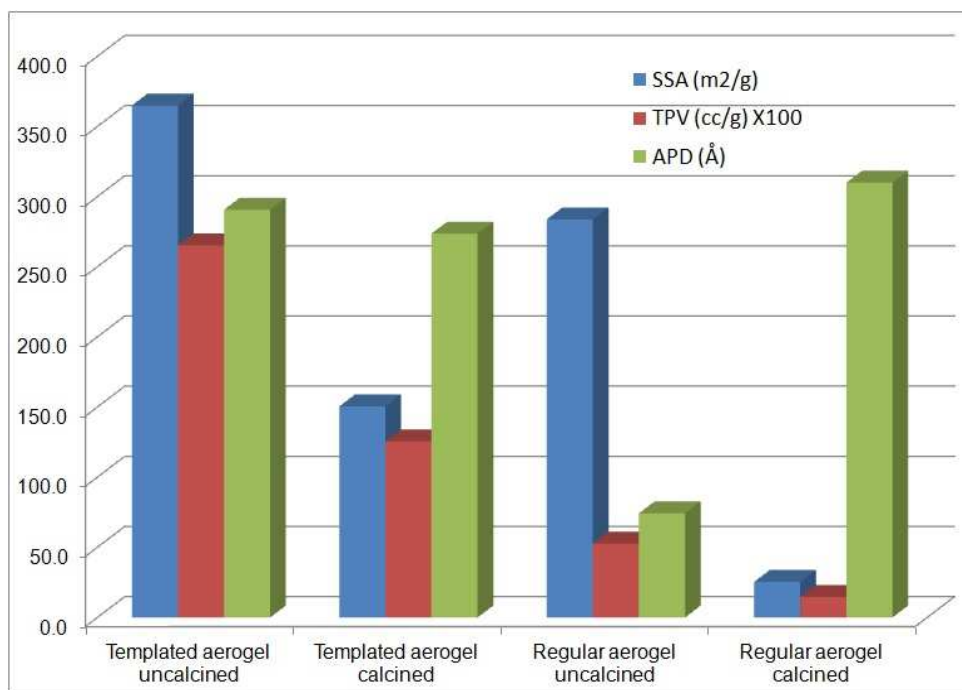


**Figure 5.3 SSA, APV and APD of Regular TiO<sub>2</sub> Aerogel and Templated TiO<sub>2</sub> Aerogel (Uncalcined and Calcined)**

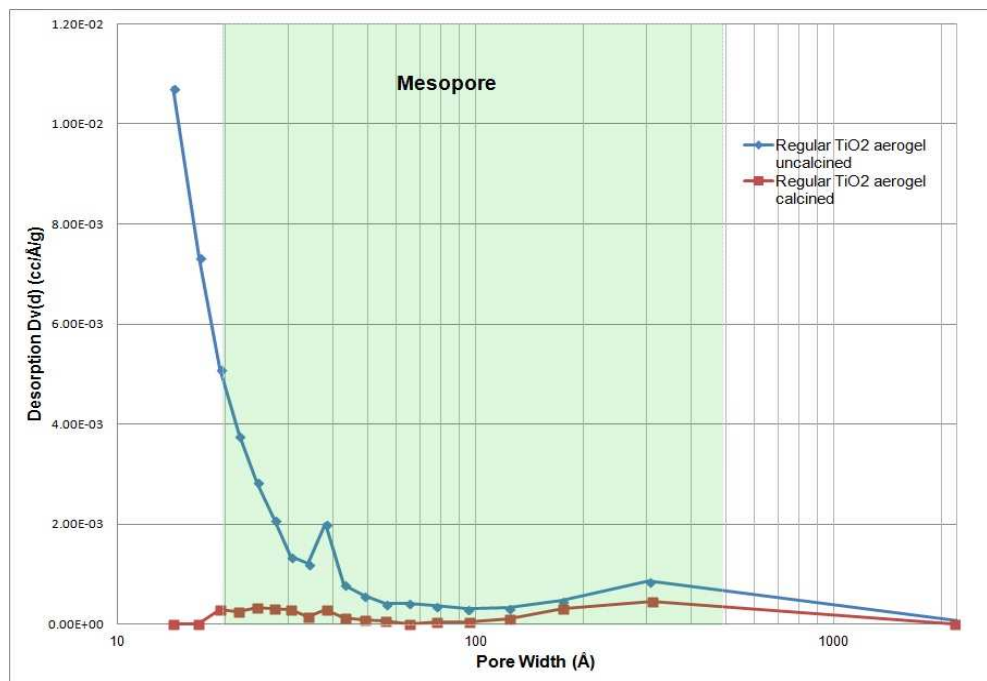


**Figure 5.4 Pore Size Distribution of Regular TiO<sub>2</sub> Aerogel (Uncalcined and Calcined)**

### 5.1.2 Effect of Aging

Aging is the time between the formation of a solvent encapsulated gel network and the removal of solvent from the gel network. As long as the solvent remains in the matrix, a gel is not static and can undergo many changes. After a sol-gel was prepared, it was divided into two identical samples, sample one was left to age for 48 hours at room temperature before the next extraction and drying stage; sample two aged for 120 hours in order to study the effects of aging time on the textural properties of the aerogels. Sol-gel samples were prepared in the same composition and under the same drying conditions. A comparison of results is shown in Table 5.4 and Figure 5.5, respectively.

**Table 5.4 Textural Properties for Templated TiO<sub>2</sub> Aerogel with Different Aging Time (Uncalcined)**

Sample	Multiplepoint BET surface area (m <sup>2</sup> /g)	Total Pore Volume (cc/g)	Average Pore (Å)
48 hours Aging (uncalcined)	365.0	2.652	290.7
120 hours Aging (uncalcined)	3.88	0.0314	323.9

Parameters that affect these aging processes include temperature, time, and pH of the pore liquid. For alkoxide-derived gels, the poly-condensation reactions continue the formation of the gel into a rigid multi-dimension network built of polymeric solid particle and encapsulated solvent, even long after onset of the gel point. This process is actually favorable to final gel characteristics because it leads to a more cross-linked network that is mechanically stronger and easier to handle. However, extensive condensation causes a phenomenon called syneresis, in which, the gel is reinforced with extra cross-linking which contracts and shrinks the matrix, forcing the expulsion of solvent from the pores. The shrinkage in alcoholic gel systems is

attributed to formation of new bonds through condensation reactions, which increase the bridging bonds and cause contraction of the gel network [197]. Coarsening or ripening is a physical phenomenon driven by solubility differences associated with surfaces that have different radii of curvature. Coarsening basically involves the dissolution and re-precipitation of particles, resulting in an increase in the average pore size of the gel and a decrease in its specific surface area [99].

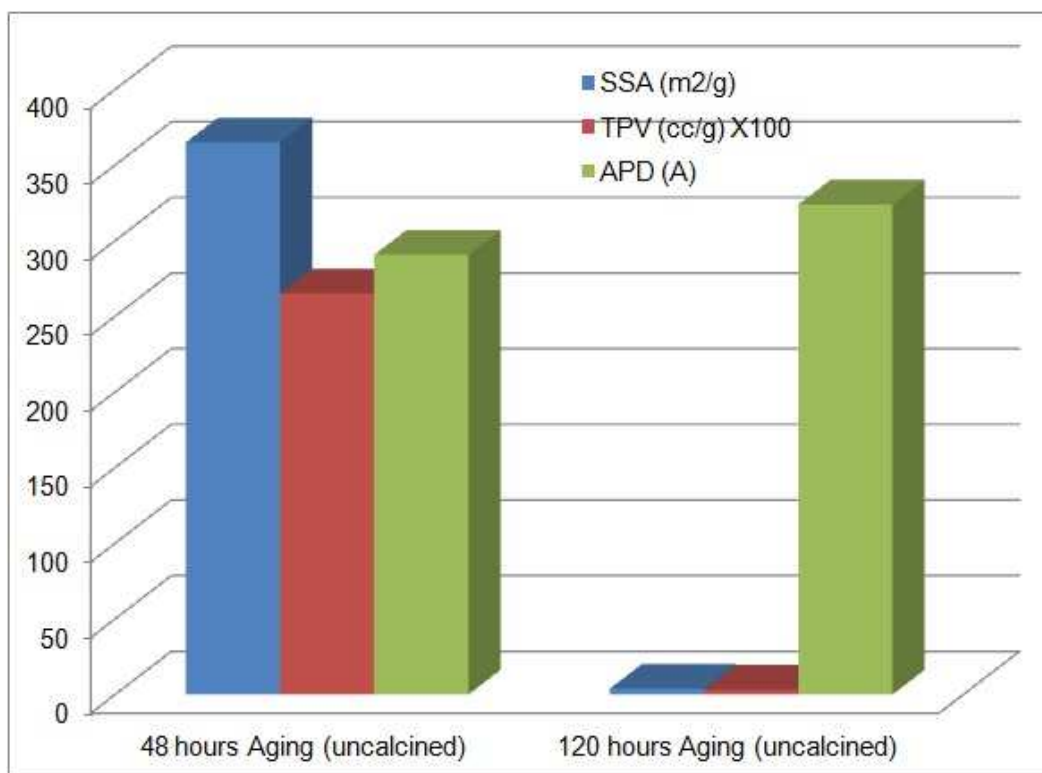


**Figure 5.5 SSA, APV and APD of Templated TiO<sub>2</sub> Aerogel with Different Aging Time (Uncalcined)**

With the same supercritical fluid extraction and drying conditions, a longer aging time resulted in extra gel shrinkage, which caused extreme low specific surface area, and larger average pore sizes in the sample before calcination. For the 120 hours aging time sample, significant liquid solution was observed floating on top of aged gel, which became a direct evidence of the solvent expulsion phenomenon.

### 5.1.3 Effect of Sol-gel Drying Conditions

#### a. Drying method

The solvent and other liquids and components entrapped within the porous gel structure are removed during the extraction and drying stage. After drying at ambient pressure or vacuum conditions, sol-gel converts into a monolith microporous structure known as xerogel. Drying under supercritical conditions, which intends to prevent porous structure collapsing due to lower surface tension and elimination of capillary forces exerted on the walls of the pores, resulted in a formation of a highly porous structure known as an aerogel. Figure 5.6 shows SEM images comparison of aerogel and xerogel samples uncalcined and calcined at different magnifications. Xerogel sample were prepared for simple physical appearance and crystallographic structure comparison purpose only, no other characterization or analysis were performed with  $\text{TiO}_2$  xerogels in this research.

Oven dried xerogel sample looks very similar to light yellow sugar crystals, The coloration was assume to be attributed to non-volatile solutes, such as nitric acid, still entrapped within the gel network. When the pores collapsed and shrunk, the avenues of escape of these contaminants were blocked before those substances totally vaporized. Trapped solutes may physically or chemically bind to xerogel structure, which would alter characteristics and properties of product xerogel. These sets of images clearly show that aerogel sample has a very amorphous pattern with a rough surface, while xerogel shows a crystal sharp pattern with a smooth surface both before and after calcination.

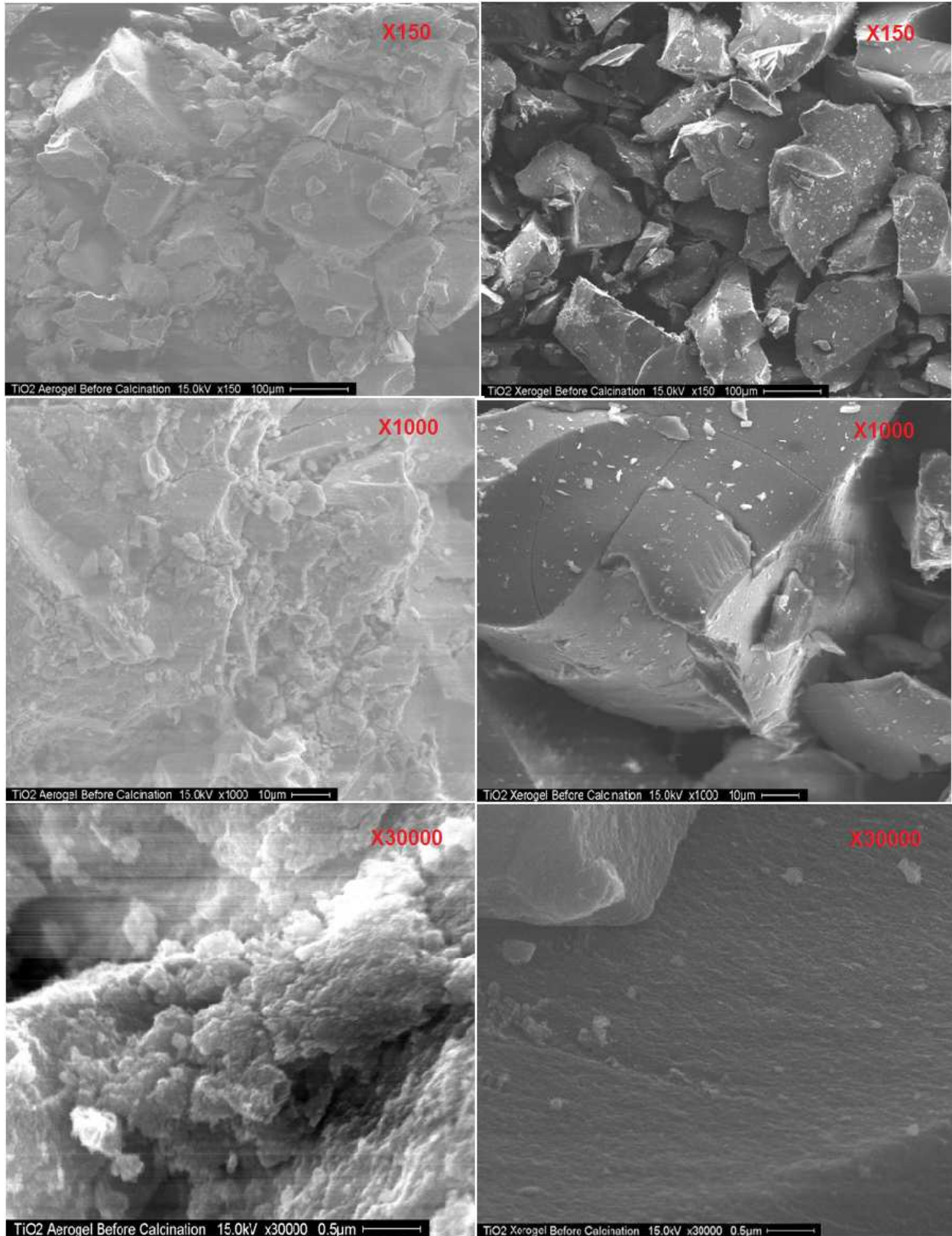


Figure 5.6 (a) TiO<sub>2</sub> Templated Uncalcined Aerogel (Left) and Xerogel (Right) SEM Images

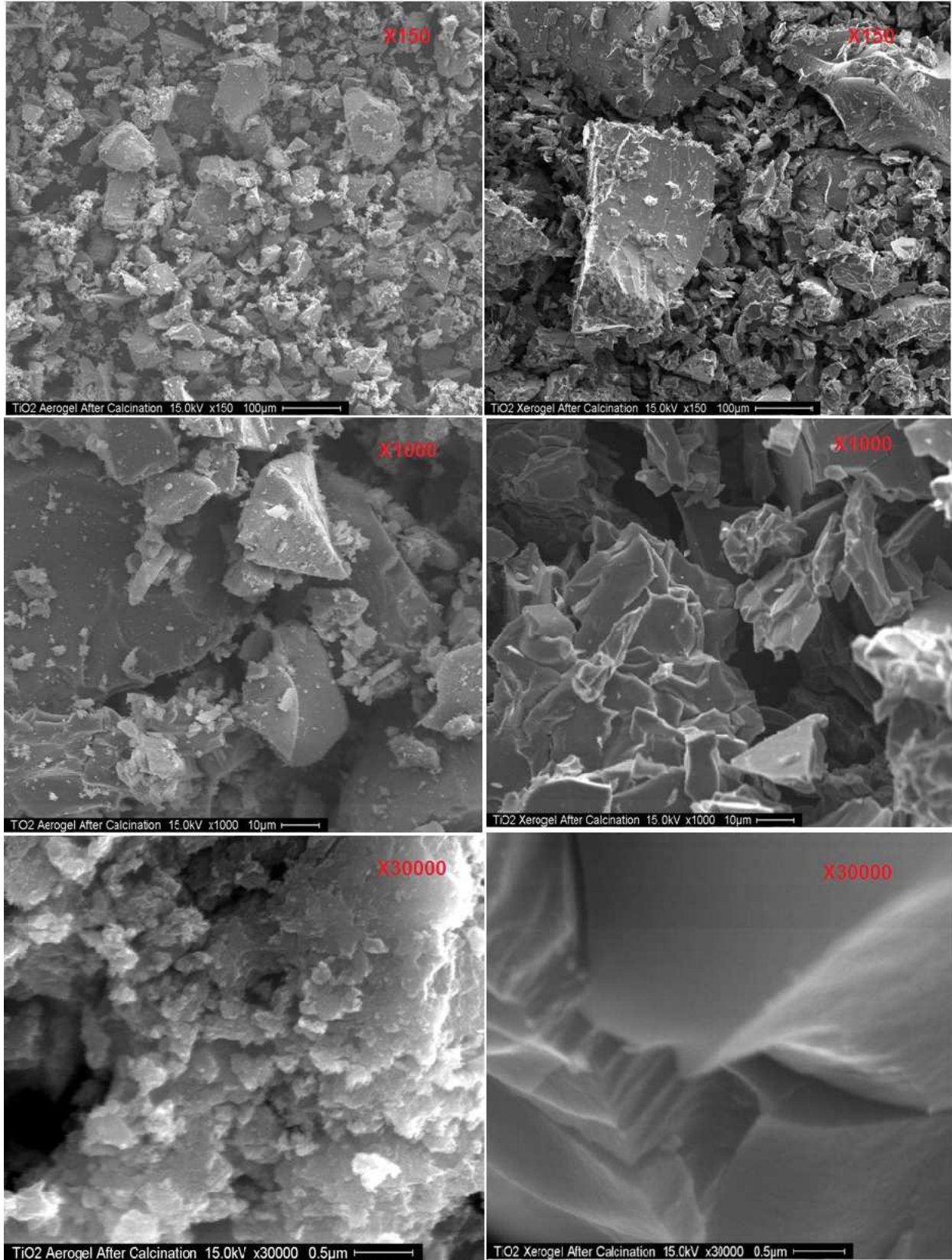


Figure 5.6 (b) TiO<sub>2</sub> Templated Calcined Aerogel (Left) and Xerogel (Right) SEM Images

b. SCF flow rate

The surfactant template, other solutes and solvent are removed from alcogel at supercritical condition resulting in formation of a highly porous aerogel. When supercritical conditions were reached, subsequently, a supercritical solution composed of carbon dioxide, ethanol and surfactant were removed from autoclave by depressurization. In fact, this extraction and drying process is a Solvent Exchange process in which the pore liquid was replaced with CO<sub>2</sub> which has a much lower critical temperature and pressure than alcohols. Solubility of ethanol and surfactant template Triton X-114 in supercritical CO<sub>2</sub> is a key element for designing the supercritical extraction and drying procedure conditions. Chany-Yih Day et al. [198] published results showing that ethanol is soluble in supercritical carbon dioxide at relatively low pressures and at various compositions. Brandon Smeltzer's works [178] showed Triton X-114 alone is insoluble in supercritical CO<sub>2</sub> from 35 °C to 50 °C up to 4600 psi. However, the addition of ethanol as an entrainer to the carbon dioxide-Triton X-114 mixtures allows Triton X-114 to become soluble in supercritical carbon dioxide at certain pressure and temperature, and molar ratio of Triton X-114. The solubility of Triton X-114 increases with the molar ratio of ethanol. Brandon's results are shown in Table 5.5.

**Table 5.5 Observed Cloud Point Pressures of Triton X-114 Mixtures [178]**

Mix	x1 (CO <sub>2</sub> )	x2 (EtOH)	x3 (X-114)	Cloud Point Pressure (CCP) in bars		
				35 °C	40 °C	45 °C
1	0.9769	0.0229	0.0002	99.9 ± 0.2588	114.65 ± 0.1225	128.63 ± 0.1095
2	0.9466	0.0530	0.0005	95.6 ± 0.1222	107.43 ± 0.2074	122.2 ± 0.0707
3	0.9321	0.0675	0.0004	One phase	One Phase	129.1 ± 0.2345

The initial molar ratio of CO<sub>2</sub>: Ethanol: Triton X-114 (x<sub>1</sub>:x<sub>2</sub>:x<sub>3</sub>) in typical aerogel preparation is 0.8560:0.1433:0.0007. In order to ensure the removal of the ethanol and surfactant template during supercritical drying and extraction procedure leaving the porous matrix intact, experimental running conditions selected were based upon the above cloud point of the ternary system.

Mass balance was calculated in order to estimate appropriate experimental running time and CO<sub>2</sub> feed flow rates. The following reasonable assumptions were made before the mass balance calculations:

- No extra co-solvent ethanol flow;
- Under certain pressure (1800 psi) and temperature (40°C), ethanol and CO<sub>2</sub> is completely miscible, even in the presence of a small percentage of other solutes existing;
- Total capacity of autoclave V is 1000ml, total initial ethanol amount is 175ml, and the volume of solid pores and other pore liquids is neglected.
- Ethanol and CO<sub>2</sub> are well mixed. The ethanol concentration inside the autoclave is uniformly distributed, and equal to the concentration at the outlet.

The experimental flow rates were assumed as a constant R:

$$R_{in} = R_{out} = R \quad (5.1)$$

where  $R_{in}$  and  $R_{out}$  represent the flow rate at flow in and flow out, respectively. The concentration of ethanol at flow in  $C_{in}$  equals to 0; the concentration of ethanol at flow out  $C_{out}$  equals to the concentration of ethanol C inside the autoclave.

The general mass balance of the supercritical fluid extraction and drying can be expressed as follow:

$$C_{in}R_{in} - C_{out}R_{out} = V \frac{dC}{dt} \quad (5.2)$$

$$0 - C R = V \frac{dC}{dt} \quad (5.3)$$

$$\int_0^t -\frac{R}{V} dt = \int_{C_0}^C \frac{dC}{C} \quad (5.4)$$

$$C = C_0 e^{-\frac{R}{V}t} \quad (5.5)$$

Four different CO<sub>2</sub> flow rates (R= 5, 10, 15, 20 ml/min) have been chosen to be compared, Total running time t=480 minutes, Initial concentration of ethanol C<sub>0</sub>=0.175,. Mass balance calculation results shown in Figure 5.7.

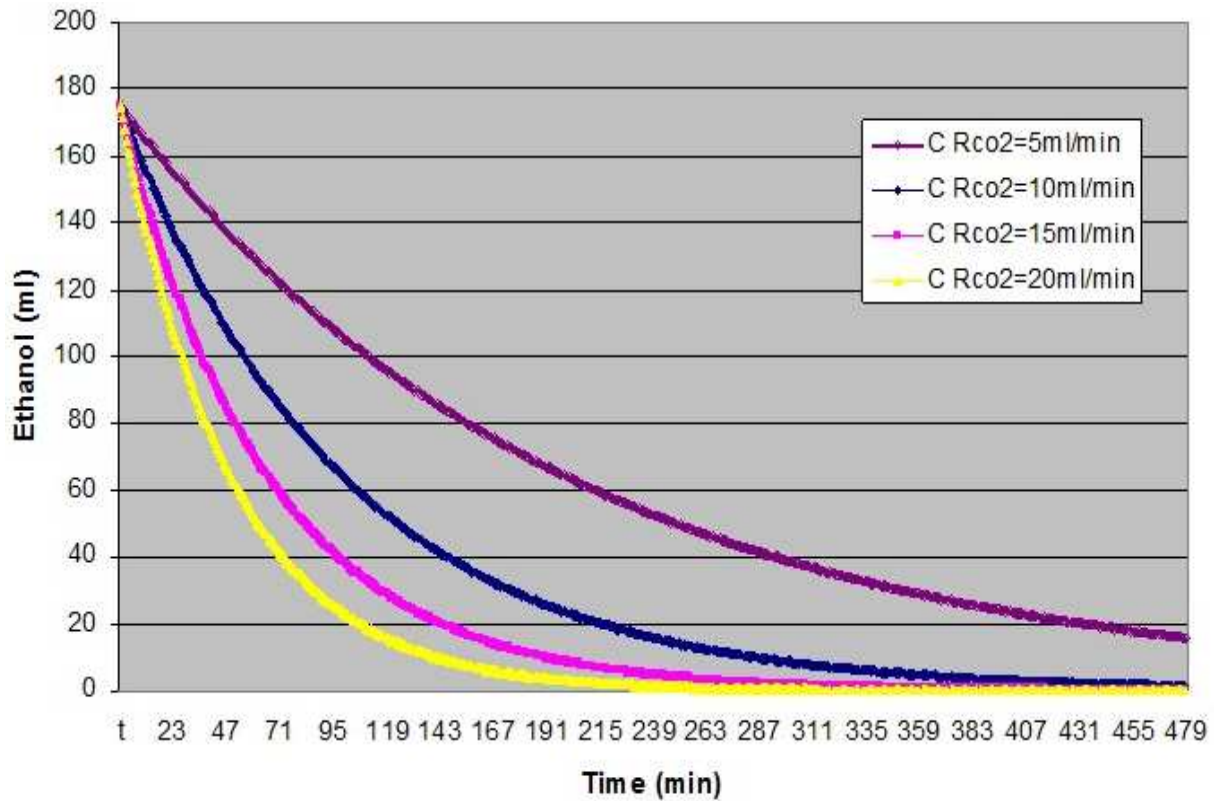


Figure 5.7 Mass Balance Calculations with Different CO<sub>2</sub> Flow Rate

Theoretical calculation estimates that it requires at least 4.5 hours to remove 99% of ethanol from the system if flow rate is 20 ml/min. Two experiments were run at different flow rates with the same running time. No Results are shown in Table 5.6.

**Table 5.6 Textural Properties for Templated TiO<sub>2</sub> Aerogel with Different CO<sub>2</sub> Flow Rate (Uncalcined)**

<b>Sample (t=8 hrs)</b>	<b>Multiplepoint BET surface area (m<sup>2</sup>/g)</b>	<b>Total Pore Volume (cc/g)</b>	<b>Average Pore (Å)</b>
R= 20 ml/min	365.0	2.652	290.7
R= 5 ml/min	98.1	0.379	154.4

The aerogel sample obtained from low CO<sub>2</sub> flow rate did not appeared totally dried, and the low SSA, TPV and APD value are attributed to the fact that the majority of porous structure of second sample is still occupied by solvent and other solutes. Making the entire supercritical extraction and drying process more efficient and time-saving is always an important goal for aerogel preparation.

#### **5.1.4 Heat Treatment**

During heat treatment, amorphous aerogel undergoes phase transformations resulting in different crystal and morphological structure. Meanwhile, the pore structure and mechanical strength significantly change.

At relative low temperature (room temperature to 100 °C), the residue of volatile alcoholic components including ethanol and N-butanol, and water were evaporated and carried out of the calcination tube by air flow. While calcination temperature ramped up to 250 °C, the entrapped trace amount of viscous liquids such as surfactant and nitric acid started being vaporized and removed from calcination tube. At relative high temperature (>250 °C), thermal unstable compounds including hydroxide and salts decompose under gas evolution, and alkyl groups react with air and eventually fully oxidizing to become water vapor and carbon dioxide.

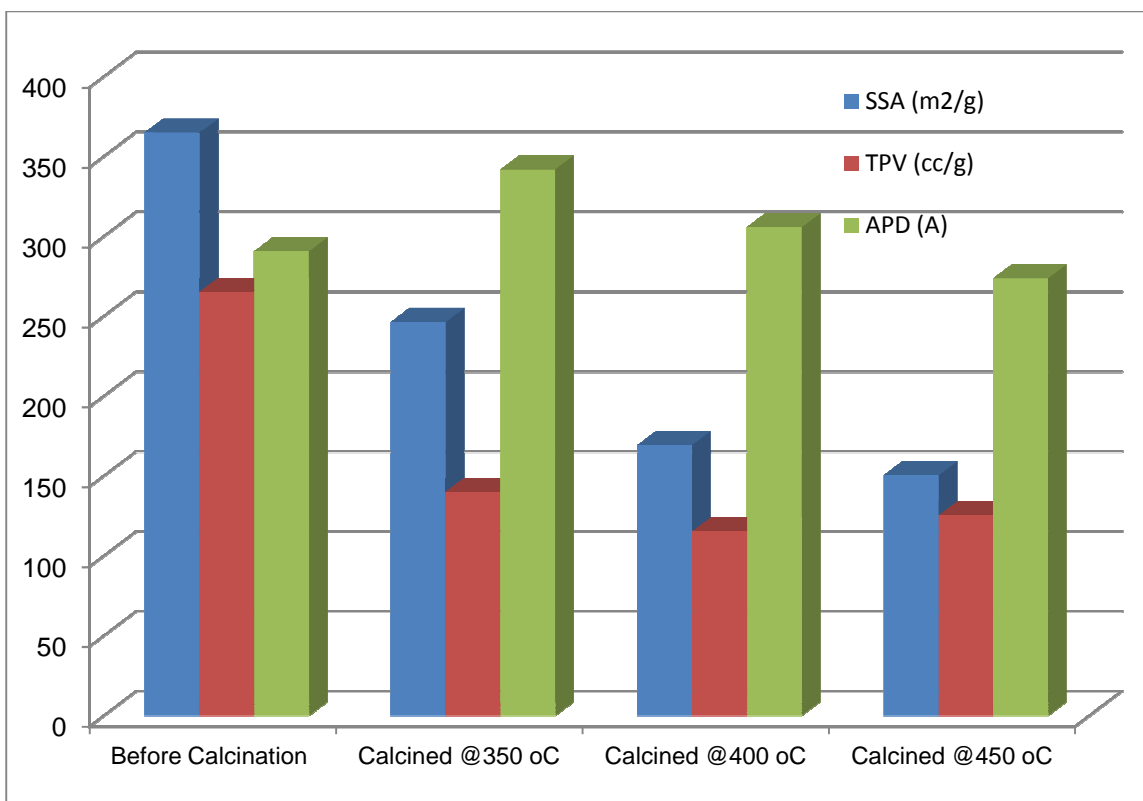
The internal surface area was reduced due to pore sintering and collapse to close cells. Pore physical strength and thermal stability increase. The amorphous TiO<sub>2</sub> structure first undergoes transformation to the anatase crystal phase. Theoretically, pure anatase phase transforms to the equilibrium rutile phase at temperatures between 550 and about 1000 °C, However, The transformation temperature of anatase to rutile strongly depends on the impurities or dopants present in the material as well as on the morphology of the sample [199].

Table 5.7 and Figure 5.8 show the textural property changes for same templated TiO<sub>2</sub> aerogel for calcination at 350 °C, 400 °C, and 450 °C.

**Table 5.7 Textural Properties for Templated TiO<sub>2</sub> Aerogel after Calcination**

<b>Sample</b>	<b>Multiplepoint BET surface area (m<sup>2</sup>/g)</b>	<b>Total Pore Volume (cc/g)</b>	<b>Average Pore (Å)</b>
Before Calcination	365.0	2.652	290.7
Calcined @350 °C	246.5	1.400	341.9
Calcined @400 °C	169.3	1.154	305.8
Calcined @450 °C	150.5	1.255	273.7

The aerogel sample's SSA and TPV decreased with calcination temperature increase. This phenomena is attributed to the decomposition of thermally unstable structure and transition of the amorphous phase to crystalline. The phenomena of APD increasing first at relative low temperature then decreasing can be explained as the occurrence of micropore elimination before sintering of larger pore structures. Calcination time is also one of the very important impact factors for determination of final degree of crystallization. It is obvious that the time required for both phase transformation completion and full crystalline growth depends on calcination temperature. To avoid any incomplete phase transformation or partial crystallizations, calcination time was fixed to 3 hours.



**Figure 5.8 SSA, APV and APD of Templated TiO<sub>2</sub> Aerogel before Calcination and after Calcination at Different Temperature**

### 5.1.5 XPS Survey

XPS elemental surveys were also used to characterize TiO<sub>2</sub> aerogel for comparison to commercialized photocatalyst *Degussa* P25. The XPS elemental survey showed that synthesized TiO<sub>2</sub> aerogel samples consisted mainly of Ti, C, and O which is very similar to *Degussa* P25. The Ti 2p<sub>3/2</sub> and 3p seems to be in the form of TiO<sub>2</sub> and the carbon in various alcohol, and other alkyl groups. Examples of XPS surveys of both P25 and sol-gel synthesized TiO<sub>2</sub> calcined aerogel are shown in Figure 5.9. Additional data are shown in Appendix C.

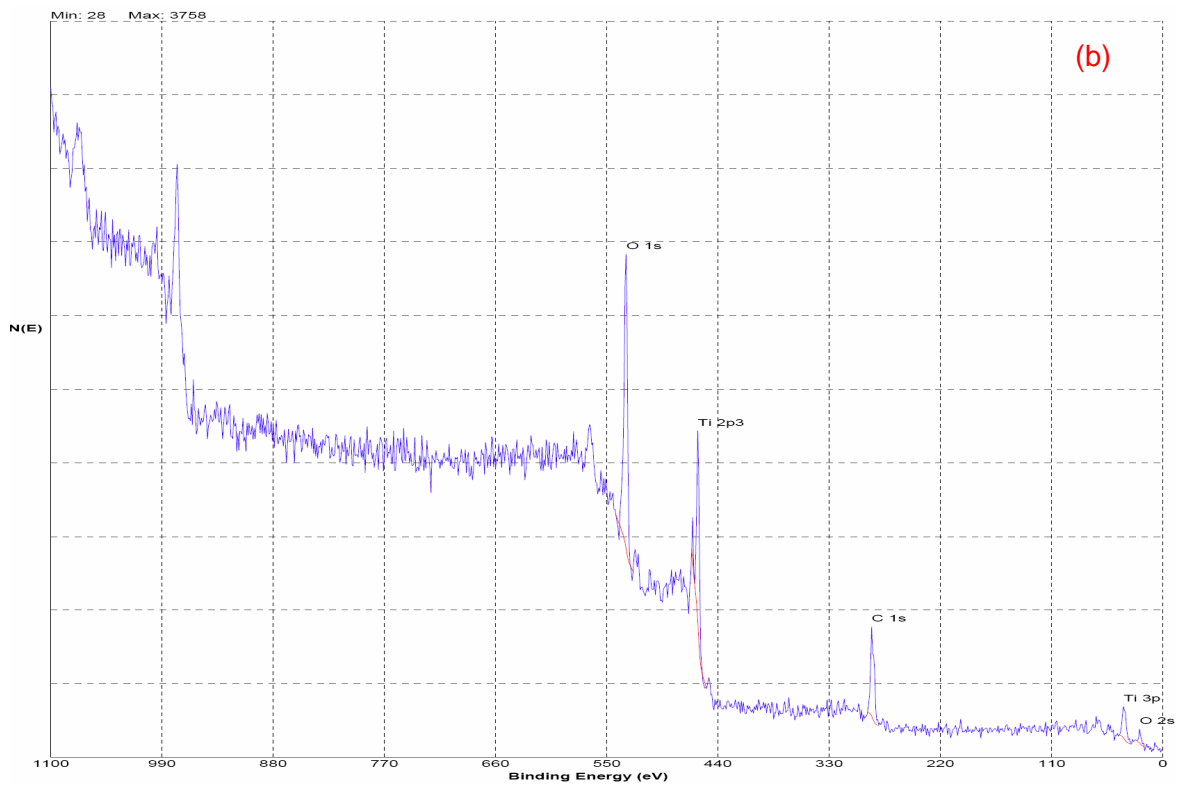
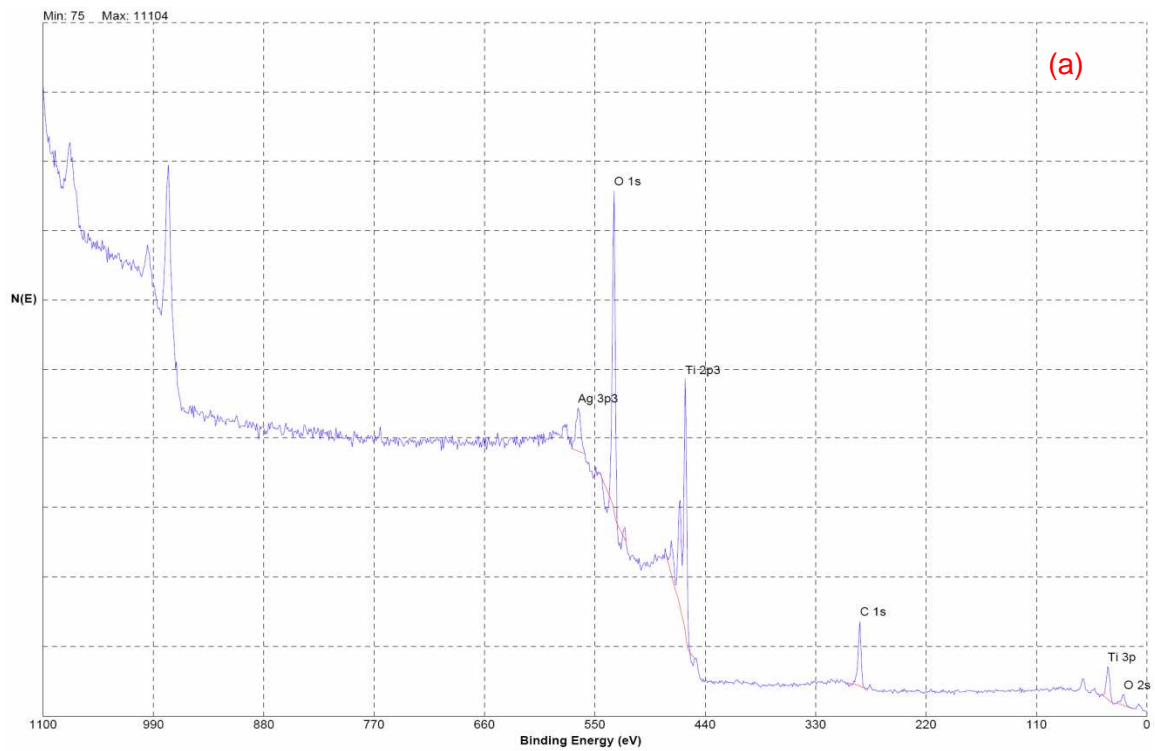


**Figure 5.9 XPS Elemental Survey of Different Sample (a) Degussa P25; (b) Calcined Templated TiO<sub>2</sub> Aerogel**

## 5.2 Co-precipitated Aerogel Preparation

The details of the preparation procedures and experimental setup for TiO<sub>2</sub> based co-precipitated aerogel are described in Chapter 4. Sample textural properties including specific surface area, total pore volume, average pore diameter and pore size distribution were examined by BET and BJH methods in Nitrogen Adsorption-Desorption analysis. Sample crystal structure as characterized by XRD is discussed in the next chapter.

### 5.2.1 TiO<sub>2</sub>/WO<sub>3</sub> Co-precipitated Aerogel

The textural properties were determined and reported in the section below. Two samples with and without the template were prepared in an identical fashion. They were aged for the same period of time and underwent the same supercritical extraction and drying process, with the only exception being the extraction and drying time. Regular co-precipitated TiO<sub>2</sub>/WO<sub>3</sub> sol-gel was only dried by supercritical CO<sub>2</sub> (20mL/min) for 6 hours, whereas, the templated co-precipitate TiO<sub>2</sub>/WO<sub>3</sub> sol-gel underwent an 8-hour long supercritical extraction and drying process. Tungstic acid (H<sub>2</sub>WO<sub>4</sub>) mixed with 30% Hydrogen peroxide (H<sub>2</sub>O<sub>2</sub>) solution was initially tested as the WO<sub>3</sub> precursor for preparing co-precipitated samples, but the gel produced exhibited thermal instability and low surface area even before heat treatment. Tungsten chloride (WCl<sub>6</sub>) exhibits water hydrolysis reactions, which are very similar to the TiO<sub>2</sub> precursor hydrolysis reactions. The results for textural analysis of regular and templated aerogel samples before and after calcination are summarized and plotted in Table 5.8 and Figure 5.10. BJH pore size distribution results are shown in Figure 5.11.

**Table 5.8 Textural Properties for Regular  $\text{TiO}_2/\text{WO}_3$  3 mol% Aerogel and Templated  $\text{TiO}_2/\text{WO}_3$  3 mol% Aerogel (Uncalcined and Calcined)**

sample		BET surface area ( $\text{m}^2/\text{g}$ )	Total Pore Volume ( $\text{cc}/\text{g}$ )	Average Pore ( $\text{\AA}$ )
Templated $\text{TiO}_2/\text{WO}_3$ 3mol% Aerogel	Uncalcined	292.0	1.339	183.5
	Calcined	191.1	1.081	305.1
Regular $\text{TiO}_2/\text{WO}_3$ 3mol% Aerogel	Uncalcined	231.1	0.151	26.1
	Calcined	132.7	0.213	49.1

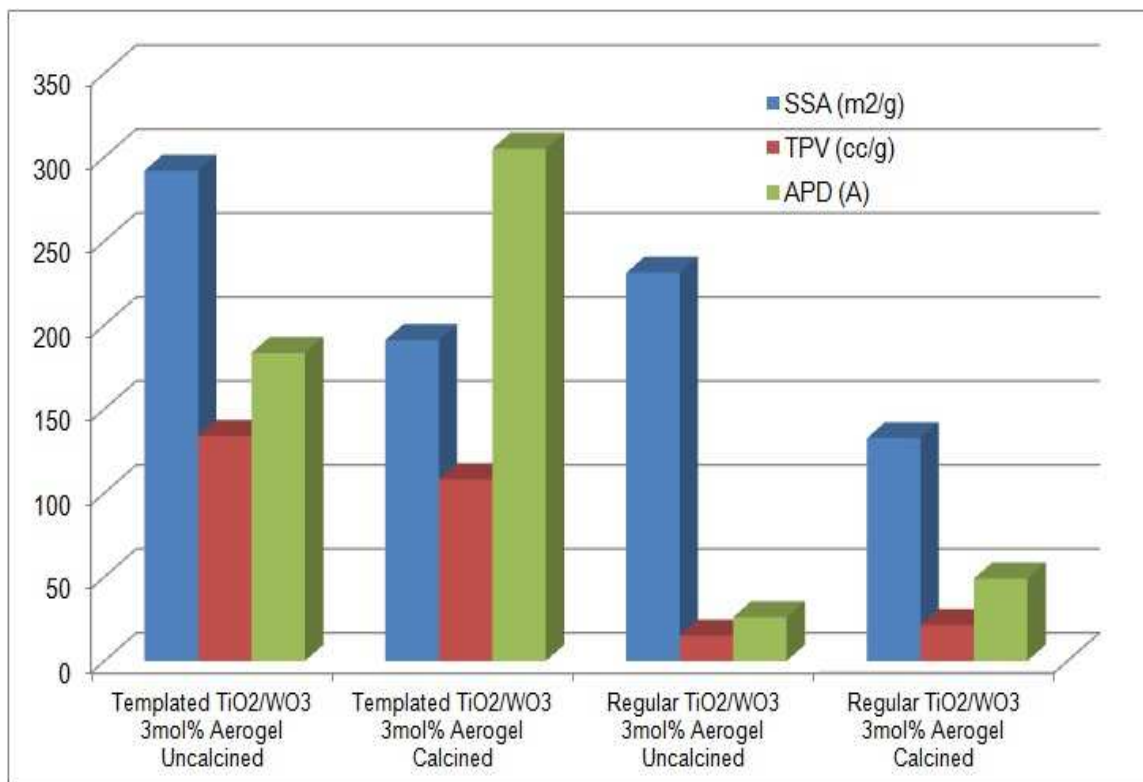


**Figure 5.10 Textural Properties for Regular  $\text{TiO}_2/\text{WO}_3$  3 mol% Aerogel and Templated  $\text{TiO}_2/\text{WO}_3$  3 mol% Aerogel (Uncalcined and Calcined)**

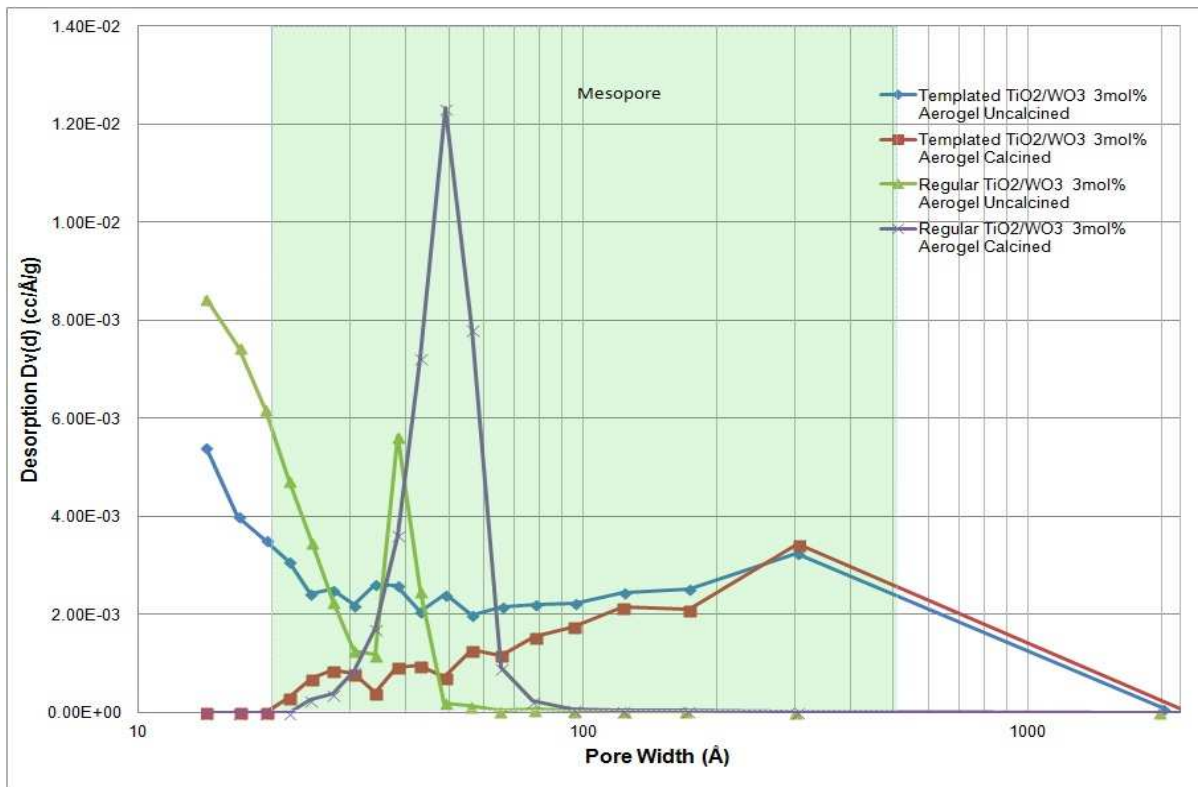


**Figure 5.11 Pore Size Distribution of Regular  $\text{TiO}_2/\text{WO}_3$  3 mol% Aerogel and Templated  $\text{TiO}_2/\text{WO}_3$  3 mol% Aerogel (Uncalcined and Calcined)**

This results comparison is very similar to that between regular and templated  $\text{TiO}_2$  aerogel. Surfactant template tailored the pore size of the product aerogel and created the desired mesoporous structure. The calcination process eliminated microporous structure and made the pore size distribution more uniform. Mesopores around 30 nm representing the majority of pore volume showed strong thermal stability and did not have significant change. It was assumed that  $\text{WO}_3$  branches chemically bonded to the  $\text{TiO}_2$  porous network and did not have any negative impact on the pore strength.

The XPS elemental survey (Shown in Figure 5.12) indicated that Calcined Co-precipitated  $\text{TiO}_2/\text{WO}_3$  aerogel samples consisted mainly of Ti, O, C, and W where atomic percentage of W was about 2.7%. Pure  $\text{TiO}_2$  and  $\text{WO}_3$  appear in white and yellow color,

respectively. The color of synthesized  $\text{TiO}_2/\text{WO}_3$  aerogel is light yellow, which represents stoichiometric  $\text{WO}_3$  in which W has an oxidation state of  $\text{W}^{6+}$ .

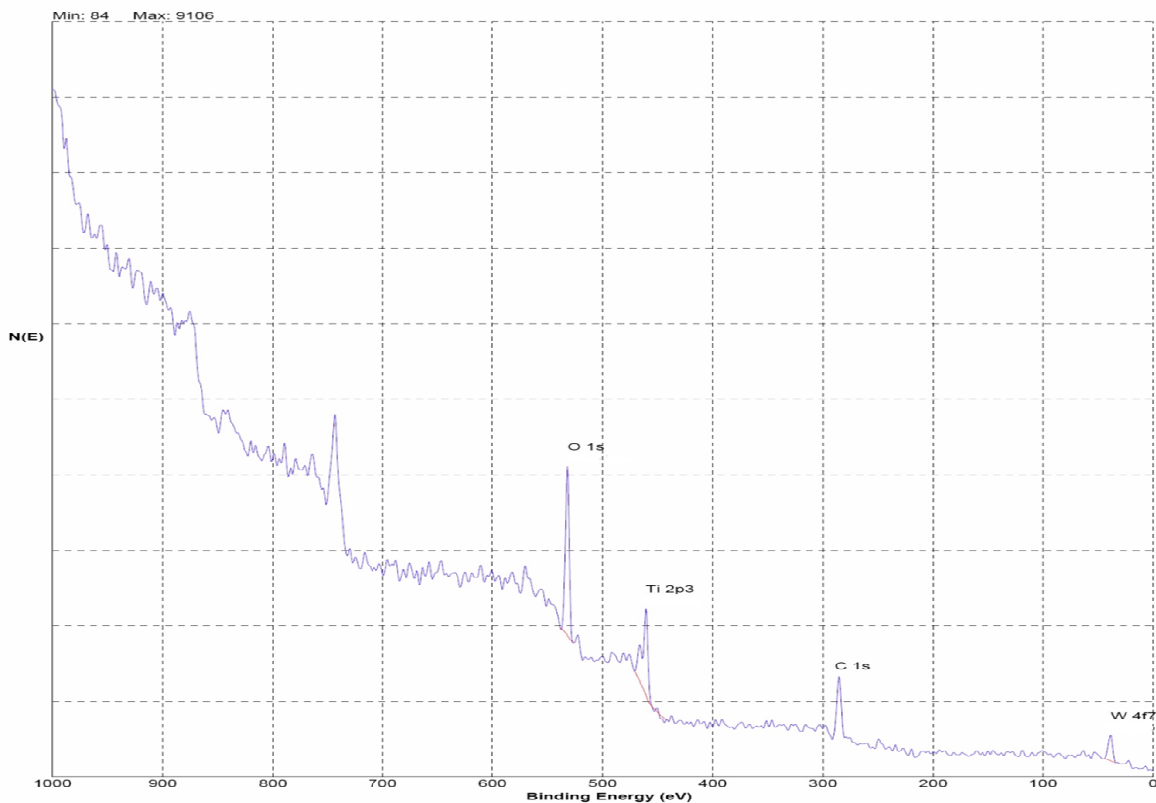


**Figure 5.12 XPS Elemental Survey of Calcined Co-precipitated  $\text{TiO}_2/\text{WO}_3$  Aerogel**

### 5.2.2 $\text{TiO}_2/\text{Fe}^{3+}$ Co-precipitated Aerogel

Ferric nitrate crystal ( $\text{Fe}(\text{NO}_3)_3 \cdot 9\text{H}_2\text{O}$ ) was used as Iron ion precursor in preparation of Iron ion doped  $\text{TiO}_2$  based aerogels in the sol-gel process. In order to minimize the influence of other components on textural properties, in this experimental preparation, Tungsten chloride solution (solution three) was not applied. 3 mol%  $\text{Fe}(\text{NO}_3)_3$  (1.21g) was directly dissolved into de-ionized water to create solution four. Table 5.9 summarized the textural characterization results of 3 mol% iron ion doped templated  $\text{TiO}_2$  aerogel before and after calcination at  $450^\circ\text{C}$ .

**Table 5.9 Textural Properties for Templated TiO<sub>2</sub>/Fe<sup>3+</sup> 3 mol% Aerogel (Uncalcined and Calcined)**

Sample		BET surface area (m <sup>2</sup> /g)	Total Pore Volume (cc/g)	Average Pore (Å)
Templated TiO <sub>2</sub> /Fe <sup>3+</sup> 3mol% Aerogel	Uncalcined	266.9	1.744	261.4
	Calcined	163.9	1.114	304.4

In comparison with TiO<sub>2</sub>/WO<sub>3</sub> aerogel characterization results, the results shown in Table 5.9 suggest that low dosage of single dopant introduced within the sol-gel synthesis process does not have a strong impact on textural properties of final aerogels. Specific surface area of aerogel reduce 30-40% after calcination. Also about 30-40% sample weight loss was observed during calcination in multiple samples.

### 5.2.3 TiO<sub>2</sub>/WO<sub>3</sub>/Fe<sup>3+</sup> Co-precipitated Aerogel

Designed Iron ion doped TiO<sub>2</sub>/WO<sub>3</sub> composite semiconductor was prepared as described in chapter 4. 3 mol% WCl<sub>6</sub> was used as WO<sub>3</sub> precursor in this section. 1, 3 and 5 mol% of Fe(NO<sub>3</sub>)<sub>3</sub> crystal were used as Iron ion precursor in this series of prepared samples, TiO<sub>2</sub>/WO<sub>3</sub>/Fe<sup>3+</sup> co-precipitated aerogels textural characterization, including SSA, TPV and TPD results are presented in Table 5.10 and Figure 5.13. Co-precipitated aerogel sample, composed of 3 mol% W and 3 mol% Fe, underwent calcination at 3 different temperatures in order to verify the calcination process and conditions effects on the structure of the doped aerogels. For practical reasons, calcination at and above 750 °C is not recommended. The stainless steel calcination tube showed severe signs of corrosion after calcination at 750 °C with airflow loaded with water vapor generated from hydroxide decomposition. As a result, the samples were contaminated with impurities from the calcination tube.

**Table 5.10 Textural Properties for Templated TiO<sub>2</sub>/3% WO<sub>3</sub>/Fe<sup>3+</sup> Aerogel with Different Amount of Iron Ion (Uncalcined and Calcined)**

sample	BET surface area (m <sup>2</sup> /g)	Total Pore Volume (cc/g)	Average Pore (Å)
Uncalcined	255.7	1.189	186.0
1mol % Fe <sup>3+</sup> Calcined (@ 450 °C)	158.1	0.704	174.1
Uncalcined	379.4	1.222	128.9
3mol % Fe <sup>3+</sup> Calcined (@ 450 °C)	163.6	0.632	171.9
Calcined (@ 550 °C)	146.5	0.532	174.3
Calcined (@ 750 °C)	44.3	0.389	300.2
Uncalcined	110.5	0.564	204.1
5mol % Fe <sup>3+</sup> Calcined (@ 450 °C)	131.2	0.637	174.6

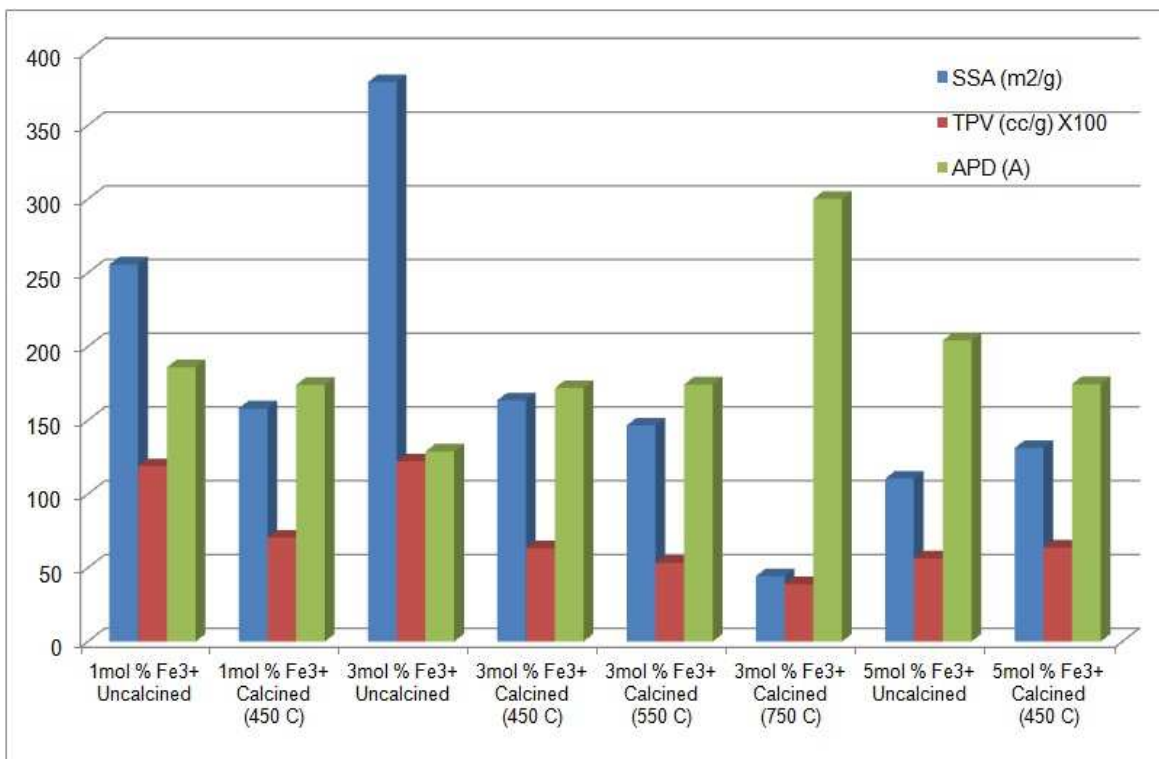


**Figure 5.13 Textural Properties of Templated TiO<sub>2</sub>/3%WO<sub>3</sub>/Fe<sup>3+</sup> Aerogel with Different Amount of Iron Ion (Uncalcined and Calcined)**

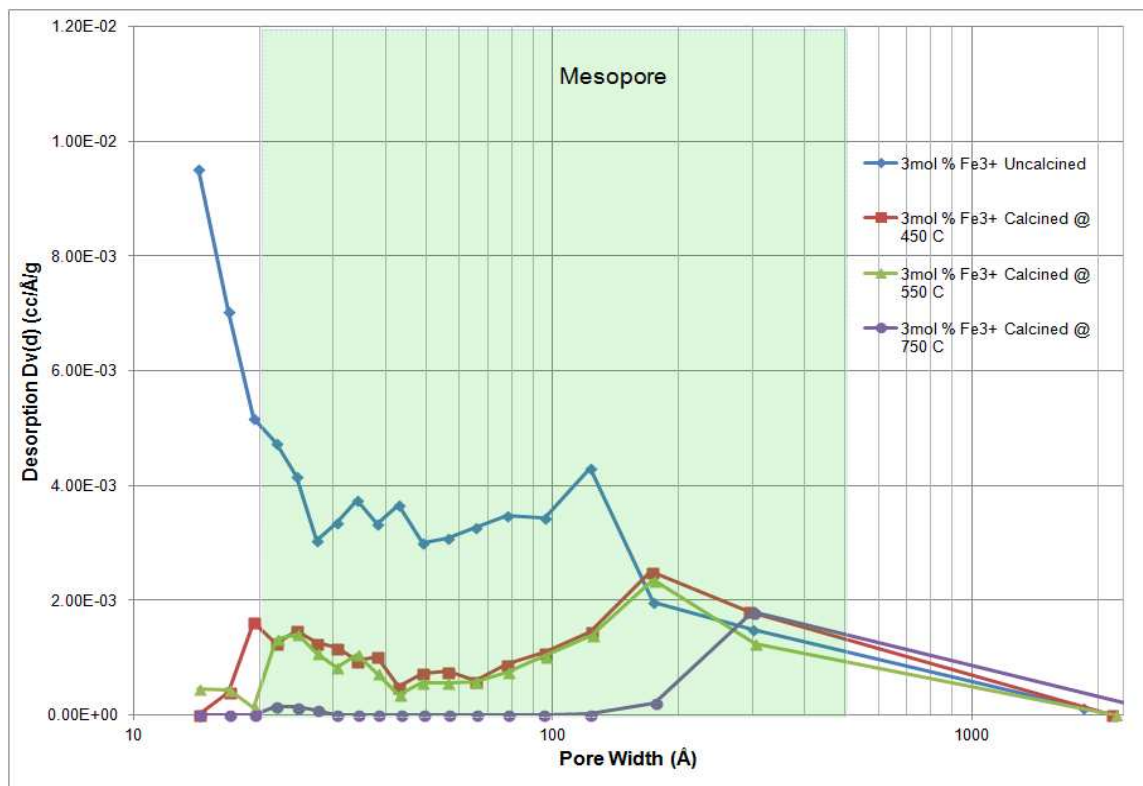


**Figure 5.14 Pore Size Distribution of Templated  $\text{TiO}_2/3\% \text{WO}_3/3\% \text{Fe}^{3+}$  Aerogel before and after Calcination at 450 °C, 550 °C, and 750 °C**

The BJH desorption pore size distributions of templated  $\text{TiO}_2/3\% \text{WO}_3/3\% \text{Fe}^{3+}$  aerogels were plotted in Figure 5.14. When initial concentration of Iron dopant was not higher than 3 mol%, there is no obvious impact on surface area and total pore volume of the synthesized co-precipitated aerogel. Microporous structures were eliminated after calcination due to pore sintering and pore collapse caused by hydroxide decomposition and amorphous phase crystallization. However, at higher temperature (above 550 °C),  $\text{WO}_3$  and Iron ion, which are considered as impurities to the pure  $\text{TiO}_2$  crystal structure, induced early phase transformation from the anatase to the rutile phase, and the crystals elongated and increased in size [200]. Even mesopores under 20nm sintered together and formed few larger pores. Internal specific surface area appeared dramatically reduced. When initial concentration of Iron dopant

increased to 5 mol%, there is more tendency for the Fe ion to strongly bind with W, Ti and O to create new comprehensive metal oxides with smaller crystal size.

The normal typical form of isotherm adsorption-desorption hysteresis loops plotted in Figure 5.15 indicated that this type of hysteresis is associated with wedge-shaped pores with open ends [201], which can be considered as direct evidence of the porous network structure of aerogels. Normally, SEM images only show surface profiles of solid particle samples. In SEM-FIB analysis, a focused ion beam drills out a cross-section on a sample to compare the profile of the bulk to that of the surface. A set of SEM-FIB images shown in Figure 5.16 further depict the uniform mesoporous structure and diameter of templated aerogel photocatalyst.

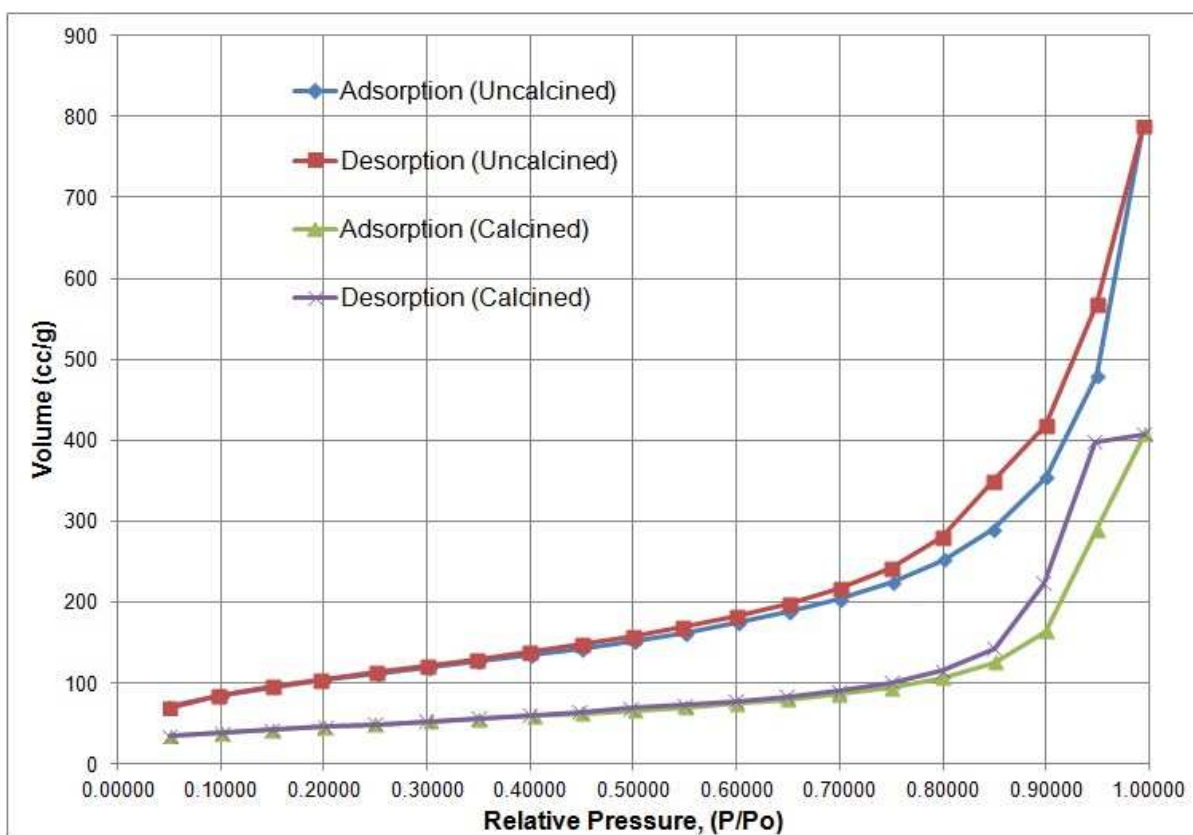
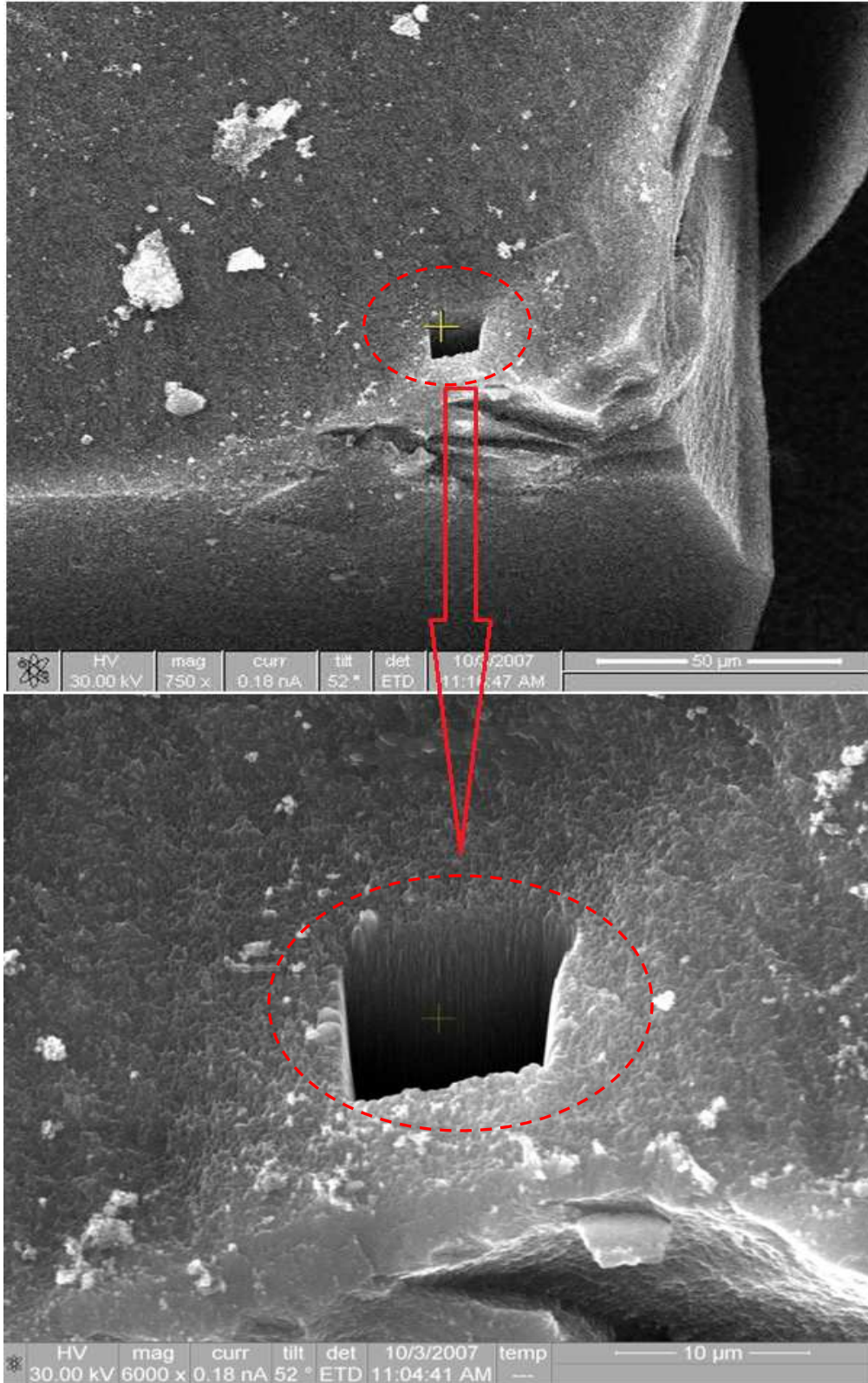


Figure 5.15 Isotherm Plots of Uncalcined Templated Co-precipitated  $\text{TiO}_2/\text{WO}_3/\text{Fe}^{3+}$  Aerogel



**Figure 5.16 SEM-FIB Images of Templated Co-precipitated Aerogel Photocatalyst at Varying Magnifications**

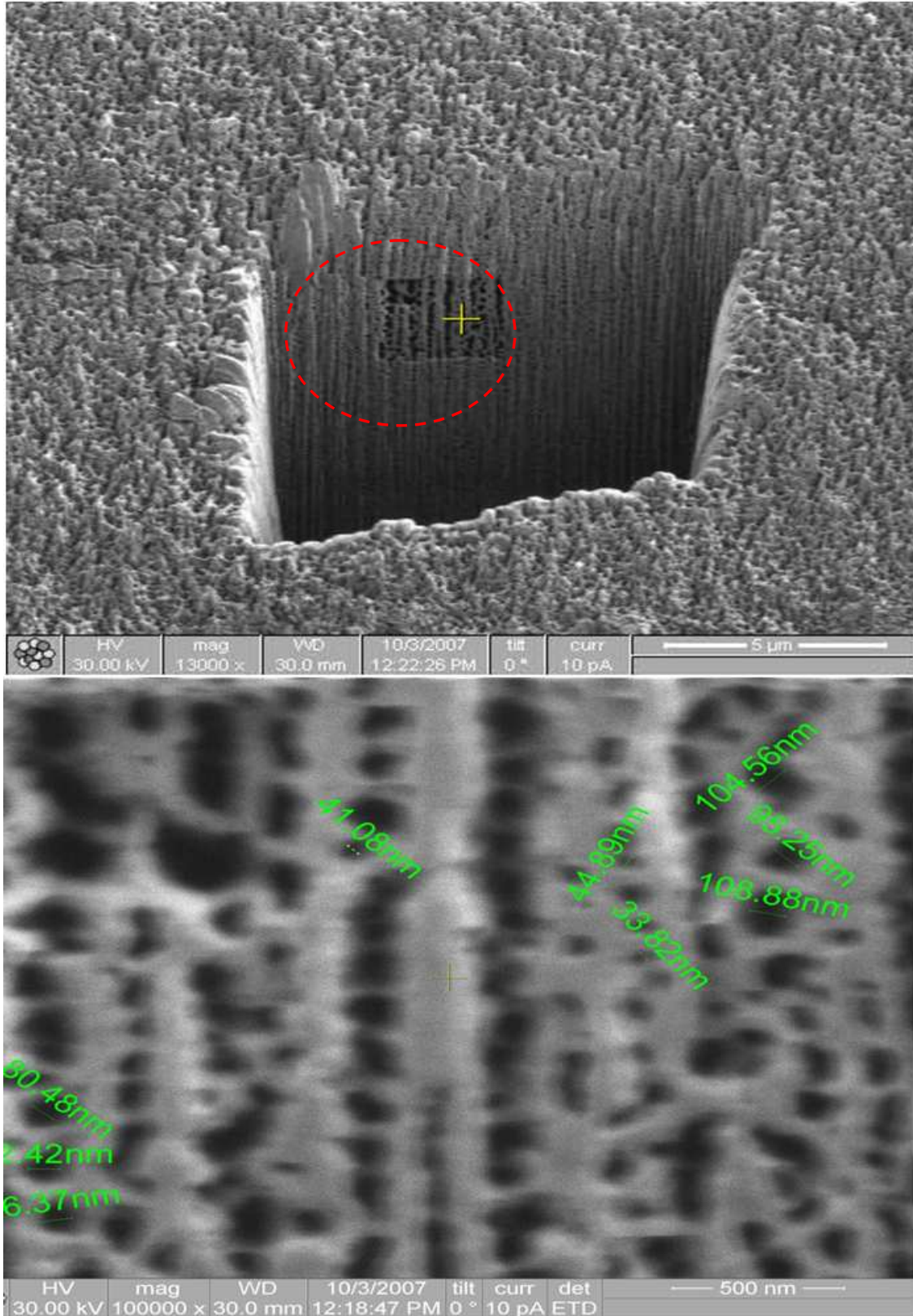


Figure 5.16 (Continued)

### 5.3 Supercritical Impregnation

Besides co-precipitation, doping and self-assembly, impregnation is also another important and effective approach to chemical functionalization of porous matrices. It not only functionalize surfaces but also allow tuning of the surface texture and structure. Compared to conventional liquid phase impregnation, with excellent characteristics of supercritical fluid, such as low viscosities, enhanced permeability, high diffusivities of solutes, and easily tunable solubility, has allowed the use of supercritical impregnation for a wide range of product functionalization purposes, and offers a very attractive and superior approach for achieving highly homogeneous dispersed surfaces. One of the earliest applications of the technology was the simultaneous permeation of diffusion of monomers/polymers into porous wood matrix in the supercritical carbon dioxide for synthesis of wood polymer composites [202]. Many other research works have applied this technique for functionalization of other mesoporous materials/aerogels [203-206].

As for catalyst functionalization, the templated co-precipitated  $\text{TiO}_2/\text{WO}_3/\text{Fe}^{3+}$  aerogel catalyst has a uniform Iron ion distribution throughout the entire sample matrix, however, a number of  $\text{Fe}^{3+}$  ion can be embedded in the bulk after hydrolysis and poly-condensation during gel aging, which may become new electron and hole recombination centers after further heat treatment. Because catalytic reactions take place on the surface and near surface regions only, it is critical to bring dopant to the area that can be accessible during photocatalytic reaction. The surface of the porous catalyst includes two parts: external surface and internal surface, with the latter providing a bigger percentage of the total surface area compared to the external surface. Hence, locating metal complex precursor particle uniformly on the internal surface instead of only on the external surface as in traditional pathways is the objective of supercritical fluid based impregnation.

Ferrocene is one Iron complex that can be dissolved in supercritical CO<sub>2</sub> without the need for entrainers. Referring to solubility data (Shown in Table 5.11) published in the book by Gupta et al. [207], Ferrocene's solubility in supercritical CO<sub>2</sub> can be tuned by adjusting either temperature or pressure. When temperature is fixed, Ferrocene's solubility increase with system pressure increase, on the contrary, when pressure is fixed, solubility decreases with increase of the system temperature. However, from a practical point of view, pressure manipulation is much more effective and quicker than changing system temperature, especially for big reactor/autoclave setups. For this work, supercritical fluid impregnation was performed at a constant temperature.

**Table 5.11 Ferrocene Solubility in Supercritical Carbon Dioxide [207]**

T(°C)	P(Bar)	S (g/L)	y x 10 <sup>6</sup>
40	97.5	2.070	799
	117.3	3.860	1280
	134.1	5.040	1580
50	97.5	0.582	381
	114.0 <sup>1</sup>	1.853	796
	117.3	2.130	881
	134.1	3.840	1380
60	97.5	0.301	256
	117.3	1.060	599
	134.1	2.290	1010

1: Obtained by digitizing the graph in the original article.

After preparation of highly porous TiO<sub>2</sub>/WO<sub>3</sub> aerogel, functionalization of the porous catalyst support needs to be performed. Templated TiO<sub>2</sub>/WO<sub>3</sub> aerogel before and after calcination were used in the supercritical impregnation process. The textural properties of supercritical impregnated aerogel and co-precipitated aerogel samples, both before and after calcination, were summarized in Table 5.12 and plotted in Figure 5.17.

**Table 5.12 Textural Properties of Different Titania Based Photocatalysts under Different Conditions**

sample		BET surface area (m <sup>2</sup> /g)	Total Pore Volume (cc/g)	Average Pore (Å)
Templated TiO <sub>2</sub> /WO <sub>3</sub> 3mol% Aerogel	Uncalcined	292.0	1.339	183.5
	Calcined	191.1	1.081	305.1
Co-precipitated TiO <sub>2</sub> /3%WO <sub>3</sub> /3%Fe <sup>3+</sup> Aerogel	Uncalcined	379.4	1.222	128.9
	Calcined	163.6	0.632	171.9
TiO <sub>2</sub> /WO <sub>3</sub> Uncalcined + SCF impreg	Uncalcined	140.8	0.663	188.4
	Calcined	153.1	0.610	174.1
TiO <sub>2</sub> /WO <sub>3</sub> Calcined + SCF impreg	Uncalcined	134.6	0.721	174.9
	Calcined	155.9	0.787	172.7

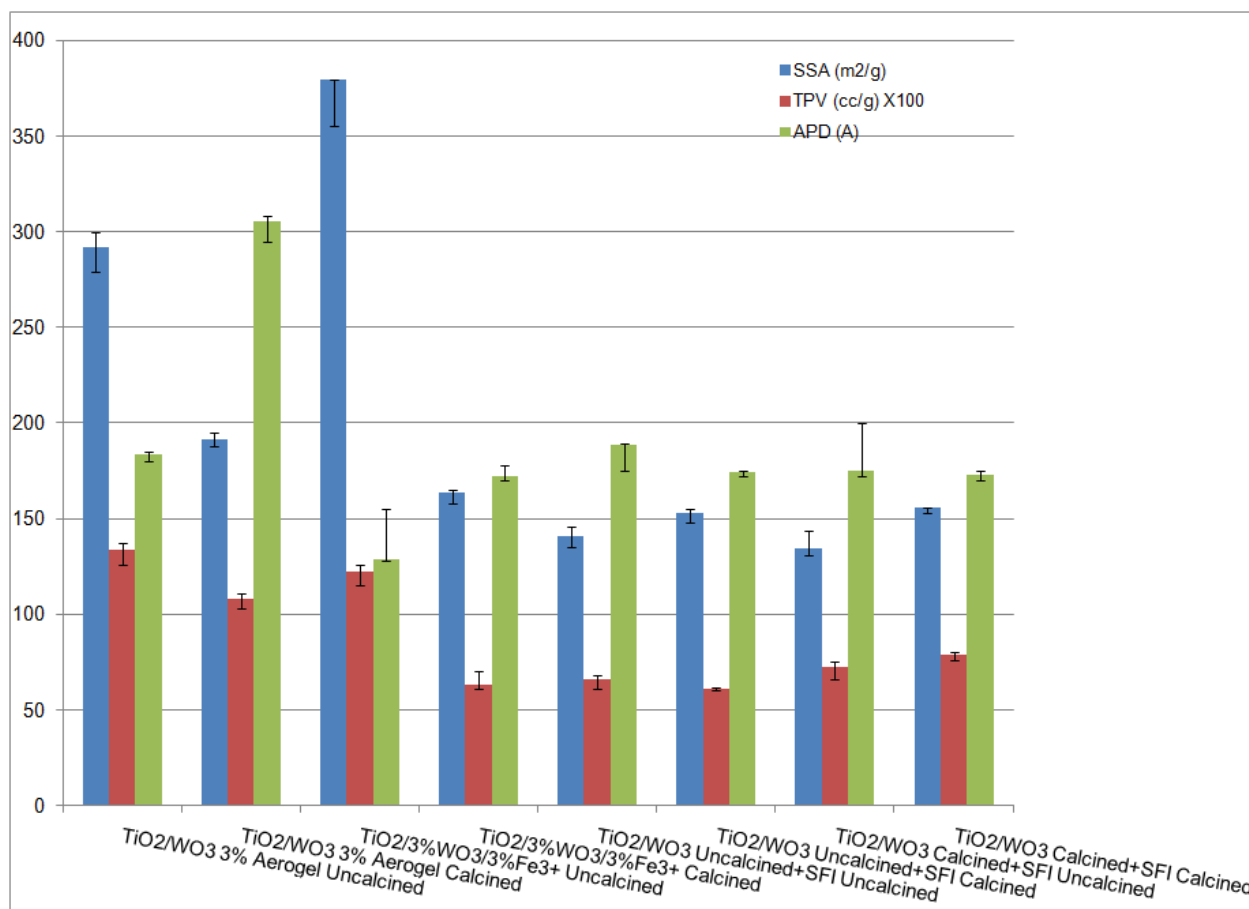


**Figure 5.17 Textural Properties of Different Titania Based Photocatalysts under Different Conditions**

Supercritical fluids impregnation was carried out at 1650 psi and 50 °C where SCCO<sub>2</sub> density is 0.53848 g/ml and viscosity is 39.587 uPa\*S. As the results shown in Table 5.12 indicate, there is no apparent correlation between the type of the aerogel to be supercritical impregnated and the textural properties of finalized supercritical impregnated TiO<sub>2</sub>/WO<sub>3</sub>/Fe<sup>3+</sup> catalyst system. The BET surface area of impregnated uncalcined aerogel was reduced more than 50% when uncalcined TiO<sub>2</sub>/WO<sub>3</sub> aerogel was used. However, the BET surface area was only reduced 30% when calcined TiO<sub>2</sub>/WO<sub>3</sub> aerogel was used. Both samples had very similar SSA, TPV and APD after heat treatment. This phenomenon indicates that even more solute being precipitated inside the pore structure of the uncalcined TiO<sub>2</sub>/WO<sub>3</sub> aerogel, the difference of concentration level of dopant did not induce significant difference in the textural properties of the finalized impregnated TiO<sub>2</sub>/WO<sub>3</sub>/Fe<sup>3+</sup> catalyst systems. The surface area and average pore sizes of co-precipitated aerogels and supercritical impregnated aerogels are almost same after calcination. The supercritical fluid impregnation process successfully introduces iron ion dopant into targeted highly porous aerogel without disturbing the original textural structure. A set of high resolution SEM-FIB images at different magnification for cross-section of calcined supercritical impregnated aerogel (Figure 5.18) showed very similar nanoporous structures and pore size distributions as what calcined co-precipitated aerogels have (Shown in Figure 5.16). Additional SEM-FIB images of TiO<sub>2</sub> based photocatalysts at different angles and magnifications are presented in Appendix D.

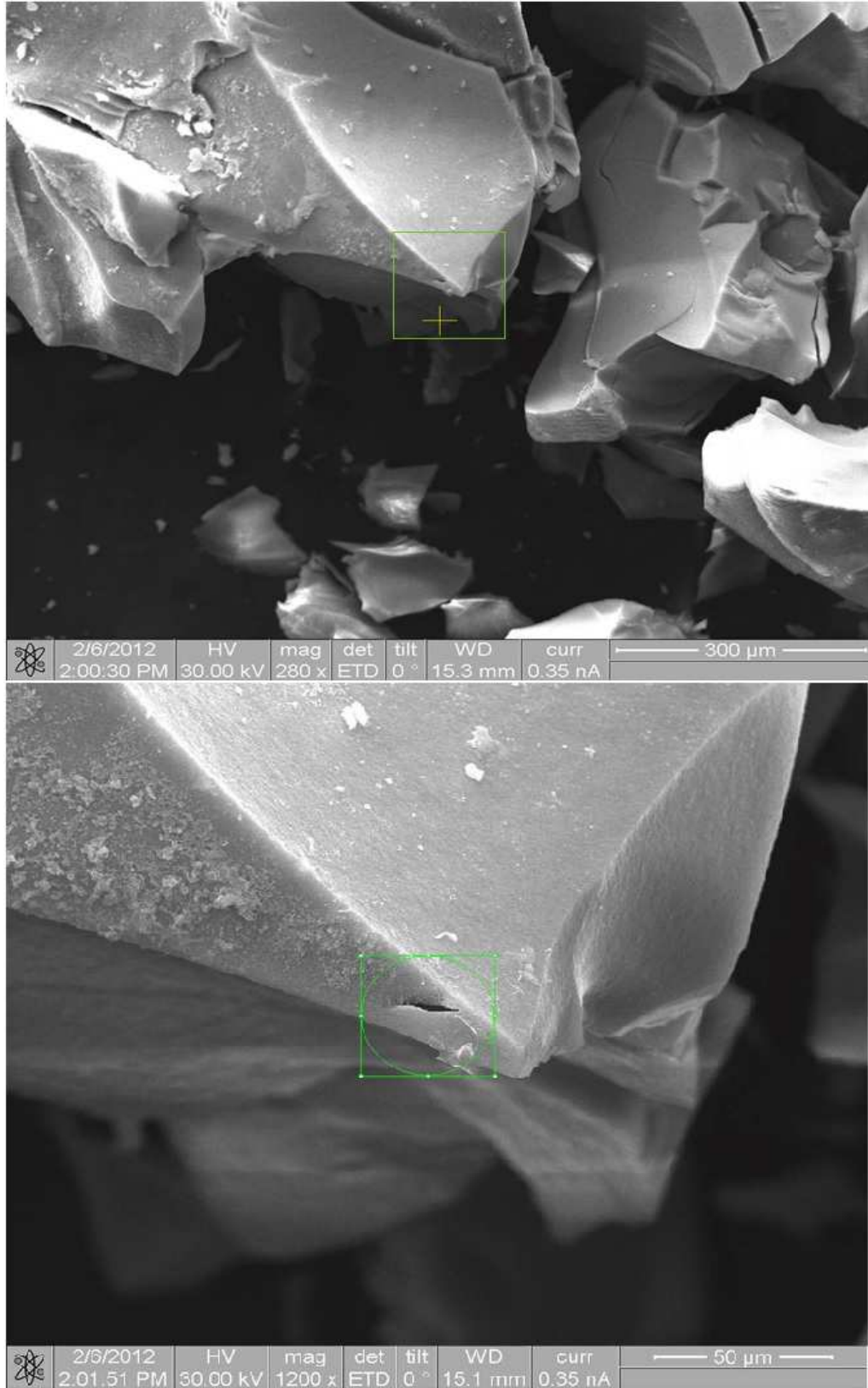


**Figure 5.18 SEM-FIB Images of Templated Supercritical Impregnated Aerogel Photocatalyst at Varying Magnifications.**

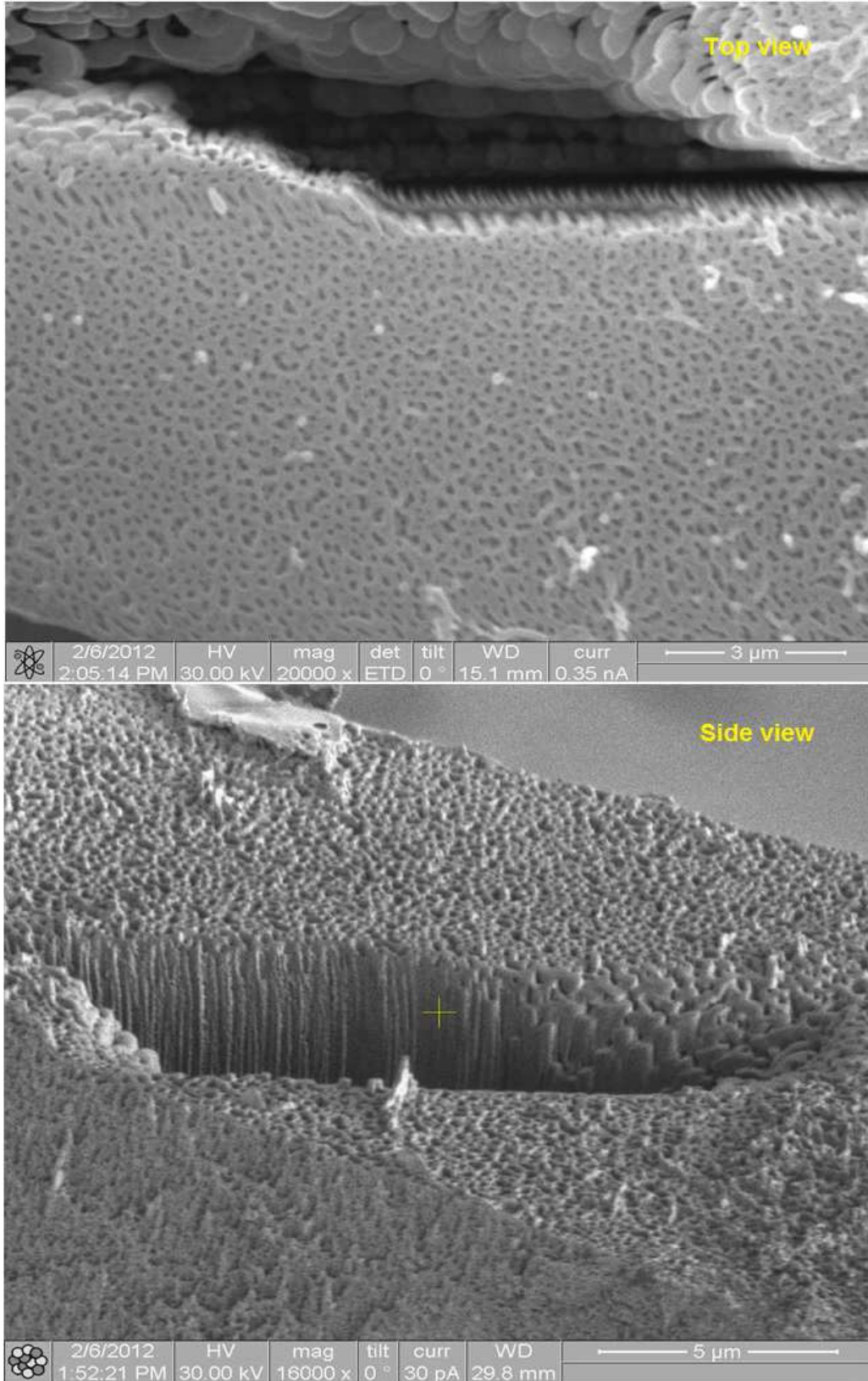


**Figure 5.18 (Continued)**

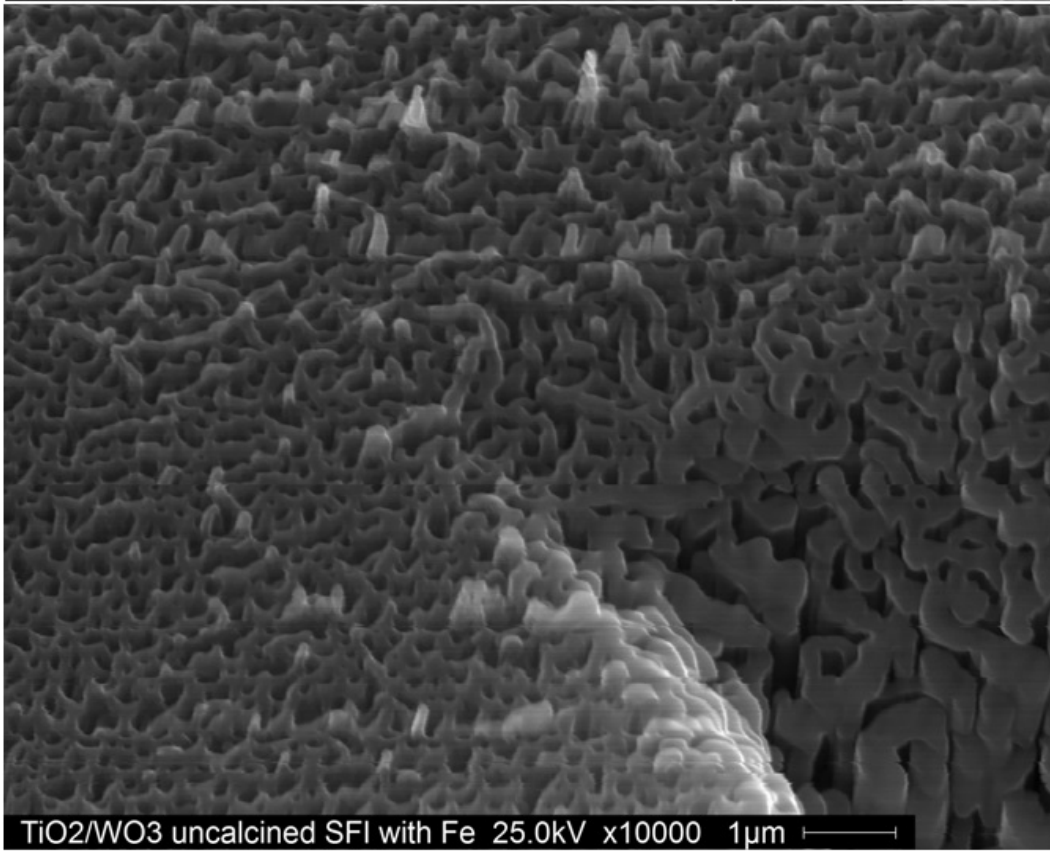
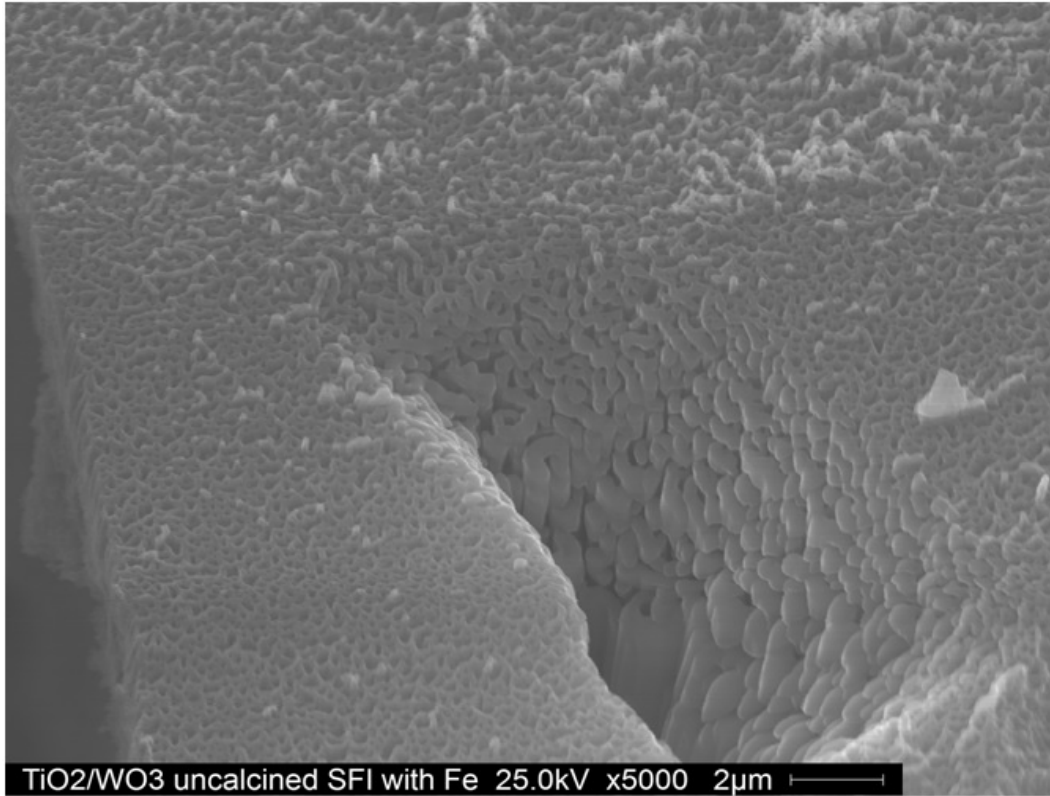
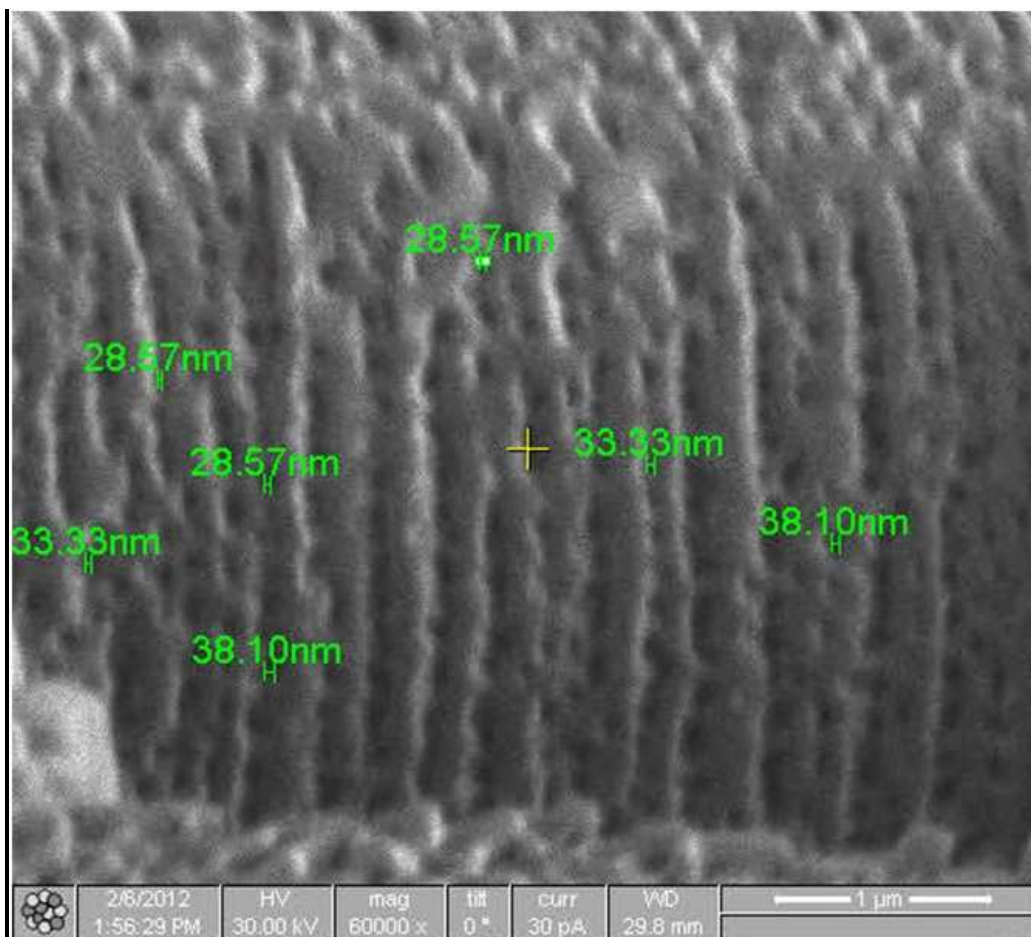


Figure 5.18 (Continued)



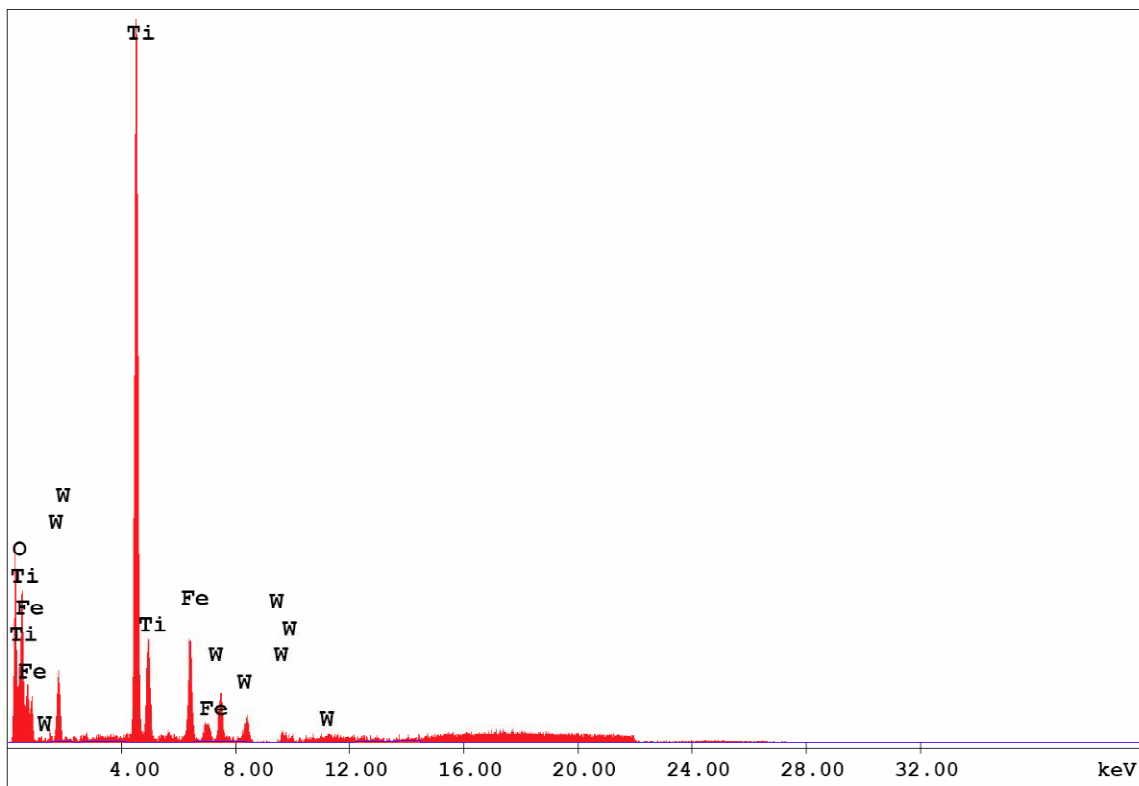
**Figure 5.18 (Continued)**

The most important reasons for using supercritical impregnation instead of co-precipitation are to minimize the consumption of dopant precursor, to fully control the amount of dopant precursor precipitated inside the porous aerogel matrix and to achieve uniform distribution of dopant on a sample's external and internal surface at same time but not in the bulk of the aerogel. Impregnation is a diffusion dominated mass transfer process. The diffusivity of solute determines how much solute is able to permeate into the porous matrix and finally deposit inside the pores. The solubility of the iron complex in supercritical CO<sub>2</sub>, the process pressure, the process temperature, the impregnation/cycle time and the system homogeneity are the key influencing factors for the impregnation process. In batch process, once system

pressure decreases, the solubility of iron complex will rapidly decrease. The insoluble portion of iron complex will then precipitate in the pores.

Diffusivity of solute depends on the solubility of solute in the solvent. In other words, it is determined by the dissolving properties of the solvent. Different temperature and pressure will result in different densities and dissolving strengths of supercritical fluids. In addition, a target aerogel's textural properties, especially internal surface area, total pore volume and pore size, also determine how much dopant precipitate inside the porous matrix in a certain period of time. Larger pore volume and larger pore size will allow more solute to deposit. An amorphous structure surface is more amendable to organometallic material adsorption of precipitate than any crystalline phase, because, microscopically, the crystal phase has atoms in a near-perfect periodic arrangement.

The SEM-EDS quantitative element analysis reveals the elemental composition of a sample's surface. The EDS elemental analysis spectra results are shown in Figure 5.19 (a) and (b). The results indicate that, at the same experimental conditions, more than 20 mol% Fe:Ti was impregnated into uncalcined  $\text{TiO}_2/\text{WO}_3$  aerogel matrix, while only about 3 mol% Fe:Ti was found on calcined  $\text{TiO}_2/\text{WO}_3$  aerogel surface after supercritical impregnation. Also, by modifying experimental time and pressure, the molar ratio of impregnated Iron inside the uncalcined  $\text{TiO}_2/\text{WO}_3$  aerogel matrix exhibited concentrations ranging from 5 mol% up to 23 mol%. The wide range of percentage of dopant exhibited by different samples directly indicates that supercritical fluid impregnation is an effective, environmental friendly, doping method that can introduce supercritical fluid soluble dopant into a porous material. Better control of the amount of introduced dopant can be achieved by manipulating supercritical conditions including time, temperature, pressure, flow rate and limited initial loading of dopant in the feed cell. In this research, only a low percentage of loading (less than 3 mol%) of Iron ion is preferred for further photocatalytic activity test.



**EDAX ZAF Quantification (Standardless)**

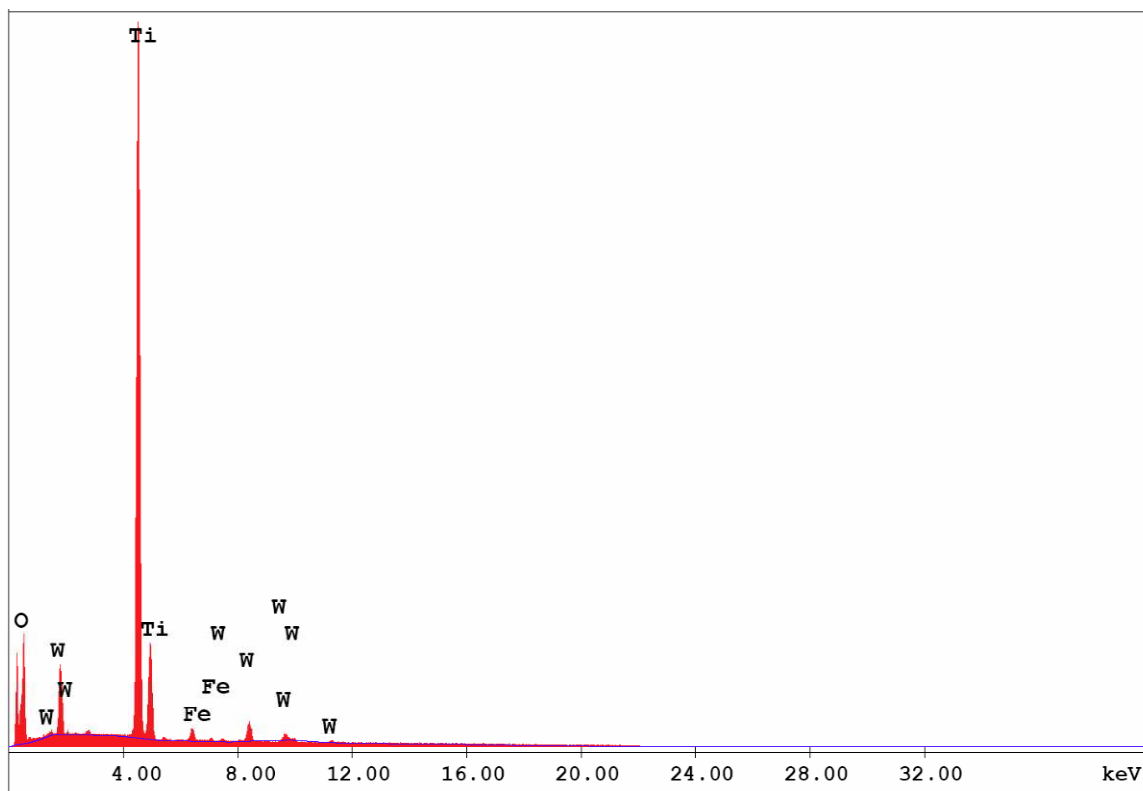
Element Normalized

SEC Table : Default

Element	Wt %	At %	K-Ratio	Z	A	F
O K	25.01	54.61	0.0396	1.1260	0.1405	1.0003
TiK	47.45	34.60	0.4514	0.9712	0.9646	1.0156
FeK	12.75	7.98	0.1186	0.9742	0.9415	1.0144
W L	14.78	2.81	0.1164	0.7856	1.0023	1.0000
Total	100.00	100.00				

Element	Net Intc.	Bkgd Intc.	Intc. Error	P/B
O K	62.86	0.07	1.15	946.45
TiK	498.62	0.28	0.41	1766.56
FeK	81.31	0.37	1.02	217.64
W L	21.12	0.47	2.03	44.63

**Figure 5.19 (a) EDS Elemental Analysis of Uncalcined TiO<sub>2</sub>/WO<sub>3</sub> Aerogel after Supercritical Impregnation with Ferrocene (Calcined)**



EDAX ZAF Quantification (Standardless)  
 Element Normalized  
 SEC Table : Default

Element	Wt %	At %	K-Ratio	Z	A	F
O K	36.85	67.16	0.0433	1.1021	0.1067	1.0001
TiK	49.29	30.00	0.4481	0.9491	0.9534	1.0047
FeK	1.77	0.92	0.0152	0.9514	0.8920	1.0109
W L	12.09	1.92	0.0948	0.7656	1.0236	1.0000
Total	100.00	100.00				

Element	Net Inte.	Bkgd Inte.	Inte. Error	P/B
O K	167.66	5.32	0.84	31.52
TiK	1767.58	25.42	0.25	69.55
FeK	37.80	18.78	2.42	2.01
W L	60.82	21.33	1.76	2.85

**Figure 5.19 (b) EDS Elemental Analysis of Calcined TiO<sub>2</sub>/WO<sub>3</sub> Aerogel after Supercritical Impregnation with Ferrocene (Calcined)**

Examples of SEM-EDS element distribution mapping images are shown in Figure 5.20. Uniform tungsten and iron distributions were found in both (A) and (B) of Figure 5.20 illustrating that supercritical fluid impregnation achieved uniform distribution of dopant in a porous matrix.

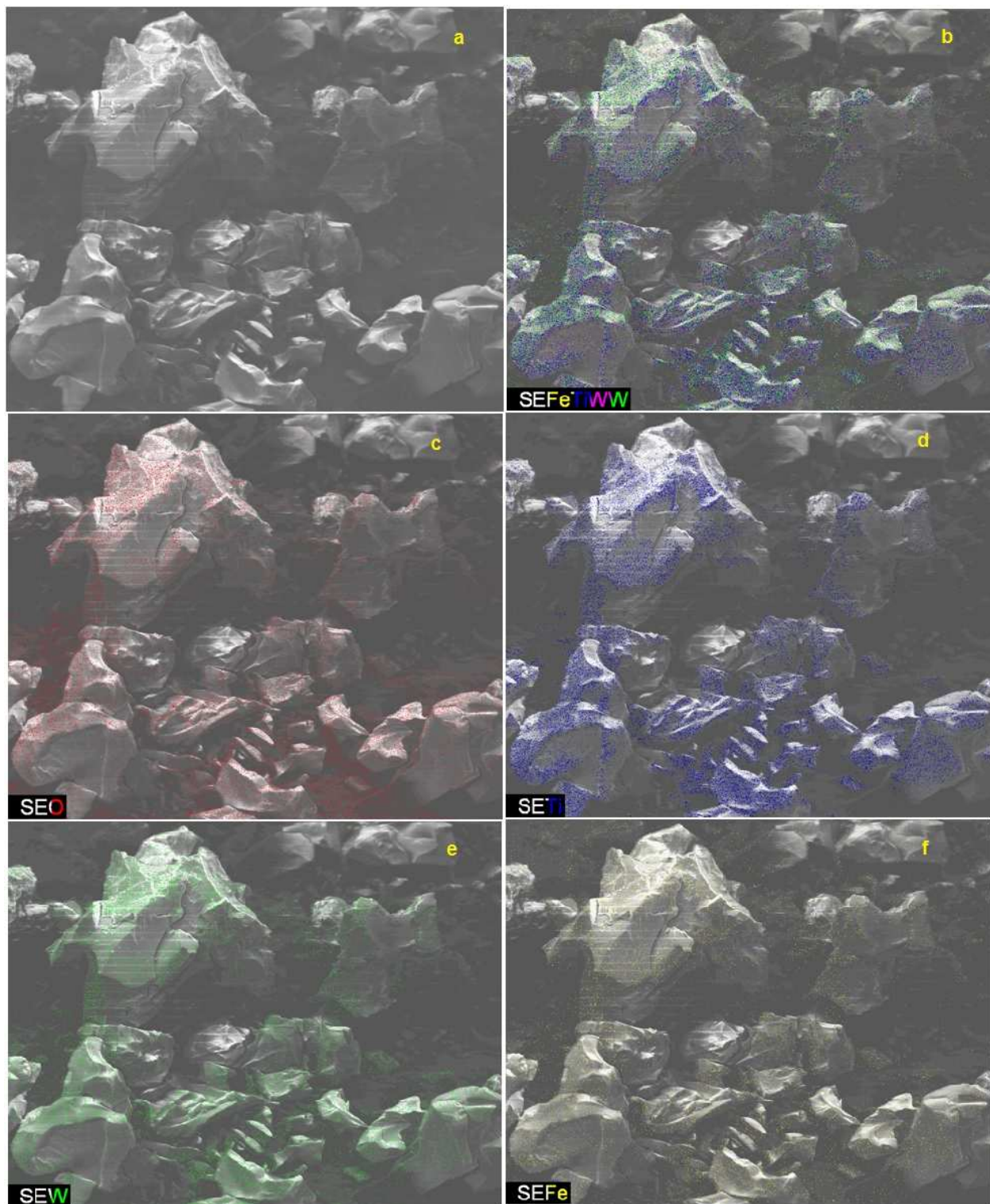


Figure 5.20 (a) SEM-EDS Elements Mapping Images of Uncalcined  $\text{TiO}_2/\text{WO}_3$  Aerogel after Supercritical Impregnation with Ferrocene (Calcined). (a) SEM Image; (b) Ti-O-W-Fe Overlap; (c) O Overlap; (d) Ti Overlap; (e) W Overlap; (f) Fe Overlap

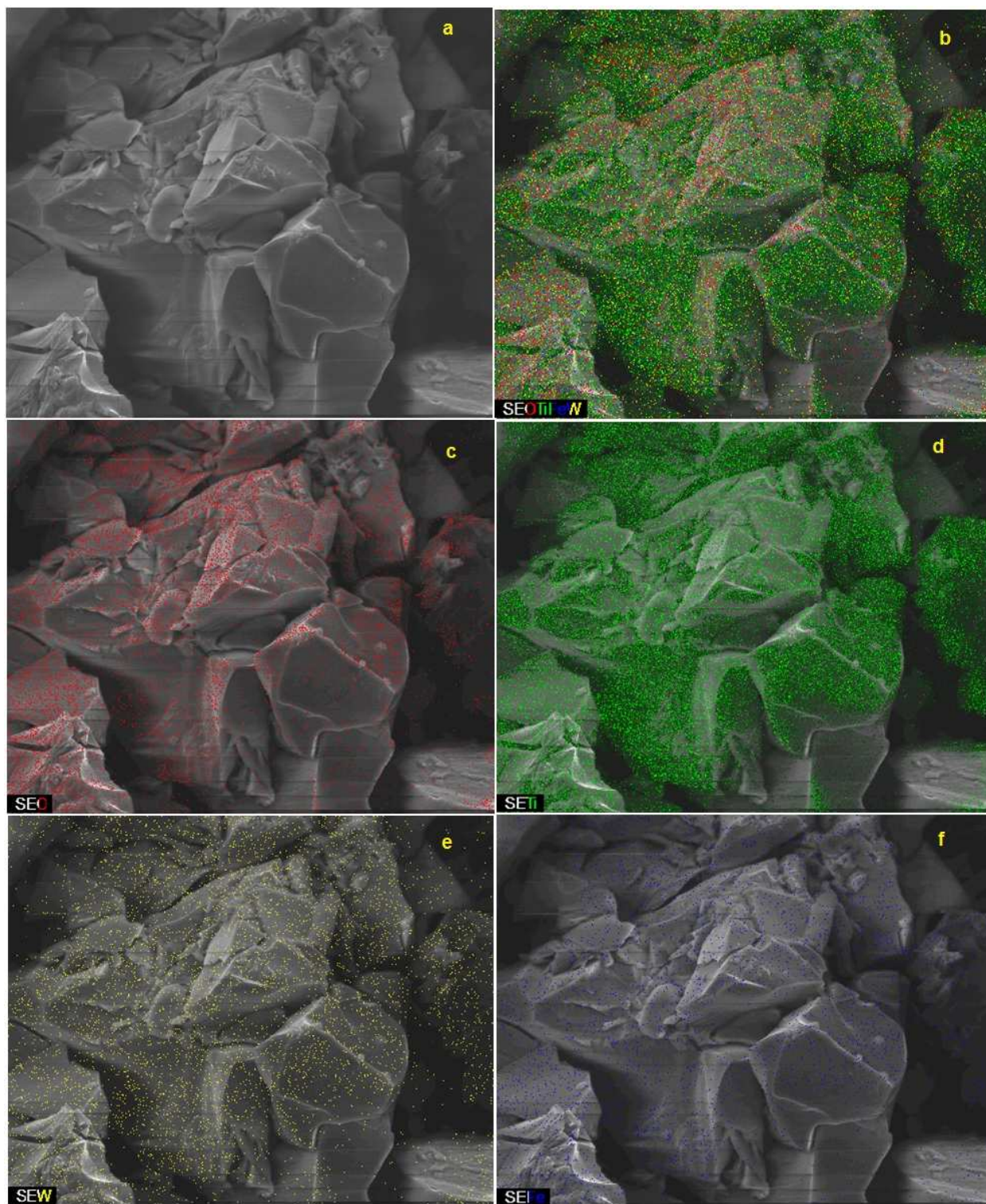


Figure 5.20 (b) SEM-EDS Elements Mapping Images of Calcined  $\text{TiO}_2/\text{WO}_3$  Aerogel after Supercritical Impregnation with Ferrocene (Calcined). (a) SEM Image; (b) Ti-O-W-Fe Overlap; (c) O Overlap; (d) Ti Overlap; (e) W Overlap; (f) Fe Overlap

## CHAPTER 6

### PHOTOCATALYST CHARACTERIZATION AND PHOTOCATALYTIC ACTIVITY RESULTS AND DISCUSSION

In this chapter, the experimental results from crystal structure analysis and band gap measurement of different synthesized TiO<sub>2</sub> based aerogel photocatalysts will be presented and discussed first. Different composition and doping of synthesized photocatalyst definitely result in different crystal structures and band gap shifts. In addition, heat treatment conditions may also affect crystal structures of product photocatalysts. Finally, the photocatalytic activity (PCA) of experimentally prepared TiO<sub>2</sub> based aerogel photocatalysts is evaluated and compared to the PCA performance results of commercially available *Degussa* P25 photocatalyst on exposure to both UV and visible light.

#### 6.1 Photocatalyst Characterization

In chapter 5, the results for the morphological, physicochemical and elemental characterization and analysis of prepared aerogel test specimens of co-precipitated TiO<sub>2</sub> based aerogel photocatalysts and supercritical impregnated TiO<sub>2</sub> based aerogel photocatalysts were presented and discussed. The suite of analytical and observational test procedures included nitrogen physisorption (SSA, TPV, APD and pore size distribution), SEM, FIB, EDS and XPS. In this section, the results from crystal structure analysis (XRD) and band gap measurement (Diffuse Reflectance Spectroscopy, DRS) will be presented and discussed.

## 6.1.1 Crystal Structure

### 6.1.1.1 Templated Pure TiO<sub>2</sub> Photocatalyst

Proper crystalline phase is critical for photocatalytic activity. In order to investigate the crystal structure, X-Ray diffraction patterns were taken for representative photocatalytic aerogel samples. All samples were observed to be in the amorphous phase after supercritical extraction and drying process. The XRD spectral pattern of uncalcined templated TiO<sub>2</sub> aerogel does not show any strong diffraction peak except strong noise (Shown in Figure 6.1).

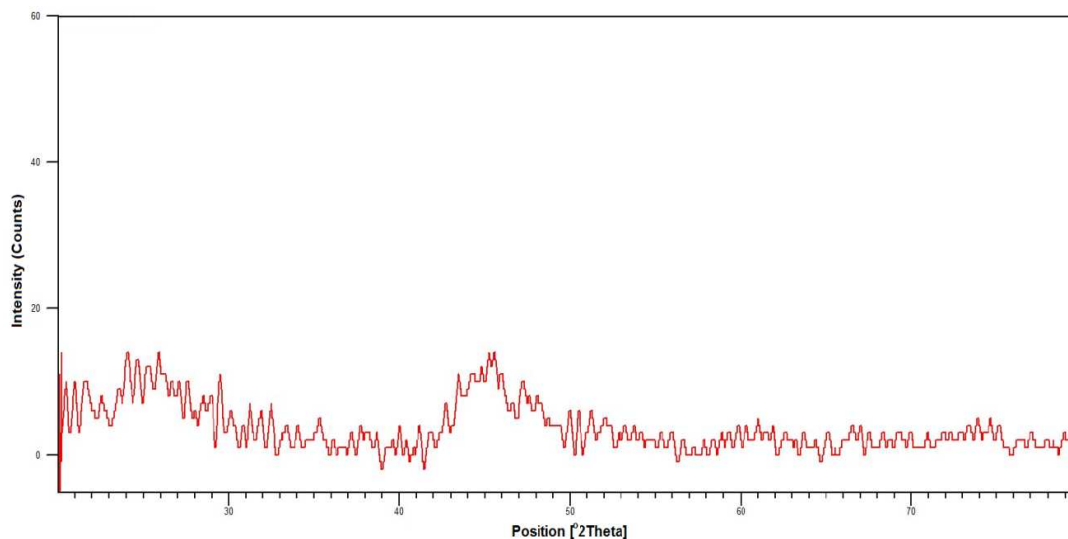


**Figure 6.1 XRD Patterns of Uncalcined Templated TiO<sub>2</sub> Aerogel**

Drying methods were observed to strongly influence the synthesized sol-gel crystal structure. Both aerogels dried under supercritical conditions and xerogels dried under ambient pressure were calcined at 450 °C for 3 hours. Figure 6.2 shows the XRD patterns of calcined xerogel and aerogel (The diffractions of anatase and rutile phase are labeled in the figure as 'A' and 'R', respectively). Anatase dominant peaks were observed at  $2\theta$  equal to 25.3°, 37.8° and 48.0° in both samples, these are diffractions peaks of the anatase phase corresponding to (1 0 1), (0 0 4), and (2 0 0), respectively. Furthermore, the xerogel XRD pattern shows a large

proportion of rutile phase co-existed with the anatase phase. The results suggest that the probability of preferentially establishing the anatase phase is much higher for supercritical fluid extracted and dried aerogels due to influence of high-pressure on network cross-linking and the tendency of the supercritical process to preserve integral porous structure without wall collapse caused by surface tension. The degree of photocatalytic activity of  $\text{TiO}_2$  is proportional to the number of electrons emitted by incident light energy. The probability of electron emission is strongly related to the electron density near the semiconductor's Fermi energy. Therefore, the higher photocatalytic efficiency of the anatase phase compared with rutile phase is expected since anatase has more electrons available for emission near the Fermi energy as compared with the rutile phase. Also, a large percentage of anatase is preferable in  $\text{TiO}_2$  based photocatalyst because its indirect band gap properties are more desirable in photocatalysis.

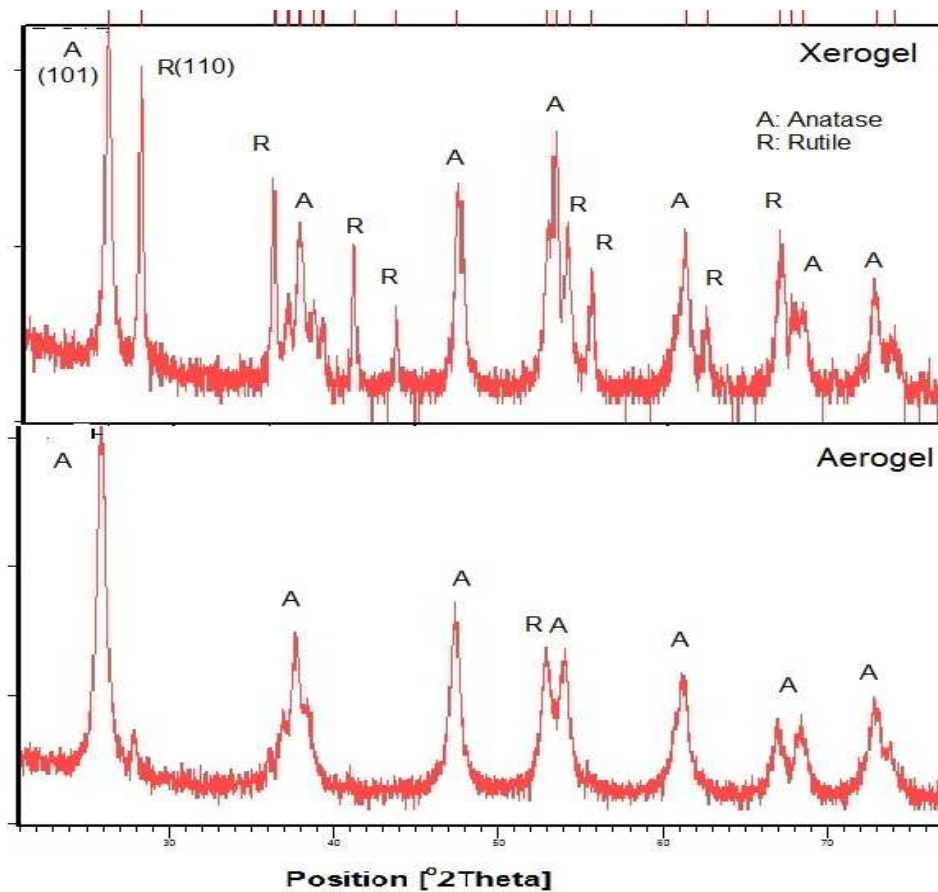


Figure 6.2 XRD Patterns of Calcined Aerogel and Xerogel

### 6.1.1.2 Co-precipitated TiO<sub>2</sub>/WO<sub>3</sub>/Fe<sup>3+</sup> Aerogel

Figure 6.3 illustrates the XRD patterns of Degussa P25 and the calcined co-precipitated templated TiO<sub>2</sub>/ 3 mol%WO<sub>3</sub>/3 mol%Fe<sup>3+</sup> aerogel. Both anatase and rutile phases are observed in P25 which has been previously reported about 80% anatase and 20% rutile, whereas, anatase phase predominantly showed in co-precipitated aerogel catalyst prepared by the sol-gel method. Anatase/rutile phase ratios of both samples were calculated by using Spurr equation and were confirmed by further Rietveld quantitative phase analysis. The anatase/rutile ratio of P25 was 82.3% vs 17.7%, and the anatase/rutile ratio of calcined co-precipitated templated TiO<sub>2</sub>/ 3 mol%WO<sub>3</sub>/3 mol%Fe<sup>3+</sup> aerogel was 99.7% vs 0.3%. Reflections corresponding to crystalline Tungsten oxide and iron oxide are seen in the XRD pattern of aerogel; however, the pattern match scores are relatively low due to their concentrations in the experimental co-precipitated photocatalyst. X-Ray diffraction of the aerogel shows smaller FWHM (Full Width at Half Maximum), which is characteristic for the crystallite size of the corresponding phase, implying a slightly larger anatase crystallite size than found in P25 (Shown in Table 6.1). Tungsten oxide and Iron oxide also made the bases of anatase peaks wider but peak height lower in the experimental photocatalyst specimen. This is attributed to an increase in lattice defect density which will limit full growth of the perfect anatase crystalline while increasing the concentration of carriers and the numbers of electrons and holes.

**Table 6.1 FWHM of Photocatalyst Samples at Anatase Phase Diffraction Peak and Anatase/Rutile Phase Ratio**

Sample	Crystal Phase	Position (2 θ)	FWHM(2 θ)	Anatase/Rutile Ratio
Degussa P25	Anatase	25.2948	0.6544	82.3:17.7
Co-precipitated TiO <sub>2</sub> /WO <sub>3</sub> /Fe <sup>3+</sup> Aerogel	Anatase	25.5124	0.6298	99.7:0.3

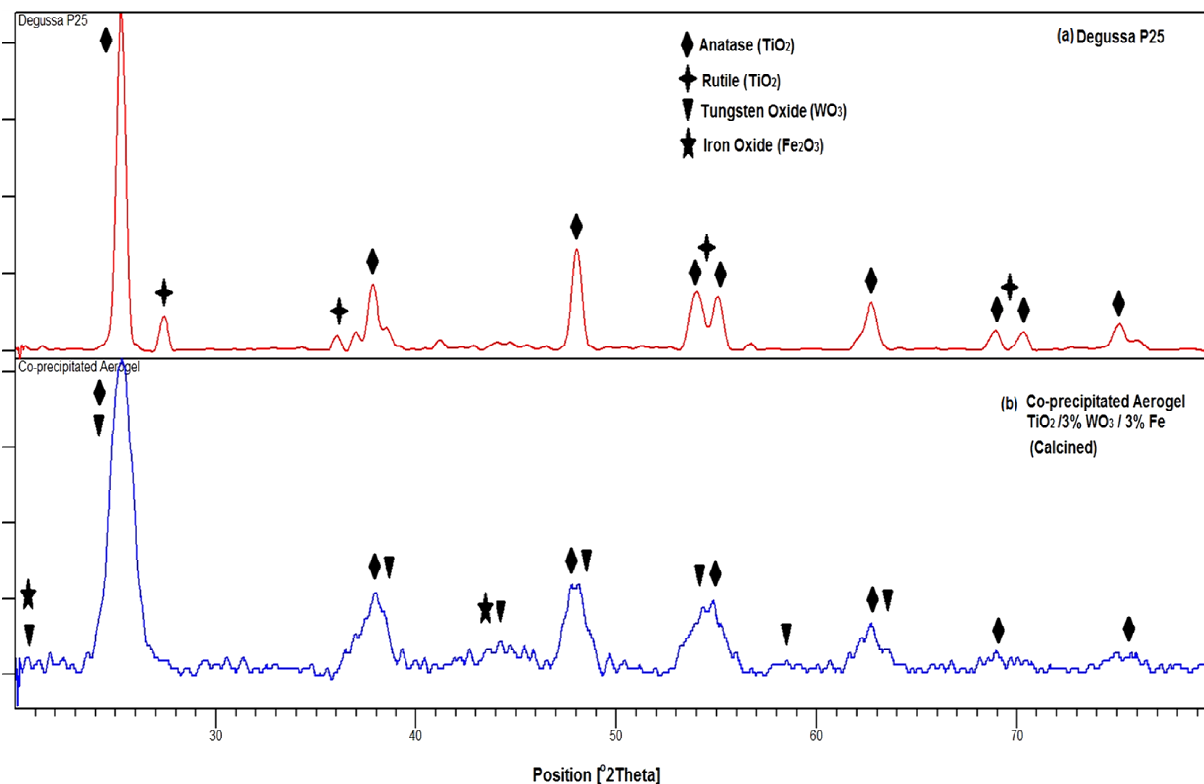


**Figure 6.3 XRD Patterns of Photocatalyst Samples. (a) Degussa P25 (b) Co-precipitated  $\text{TiO}_2/\text{WO}_3/\text{Fe}^{3+}$  Aerogel after Calcination at 450 °C**

Due to introducing various dopants such as anions, metal ions and composite semiconductors, the transformation condition from anatase to rutile may be modified [208-211], especially the transformation temperature. A number of researchers [212-214] had reported that different calcination temperatures and times achieved different ratios of anatase and rutile in titanium dioxide. Figure 6.4 shows the XRD patterns of co-precipitated aerogel calcined at different temperatures.

Both XRD patterns are similar to each other, but the aerogel calcined at higher temperature (550 °C) shows smaller FWHM corresponding to larger crystallite size. This agrees well with the BET results, which showed a decrease of the SSA with increase in calcination temperature. A weak metal Iron reflection also appeared in pattern (b). It can be explained as decomposed iron ion precursor was with an absence of oxygen in a closed pore.

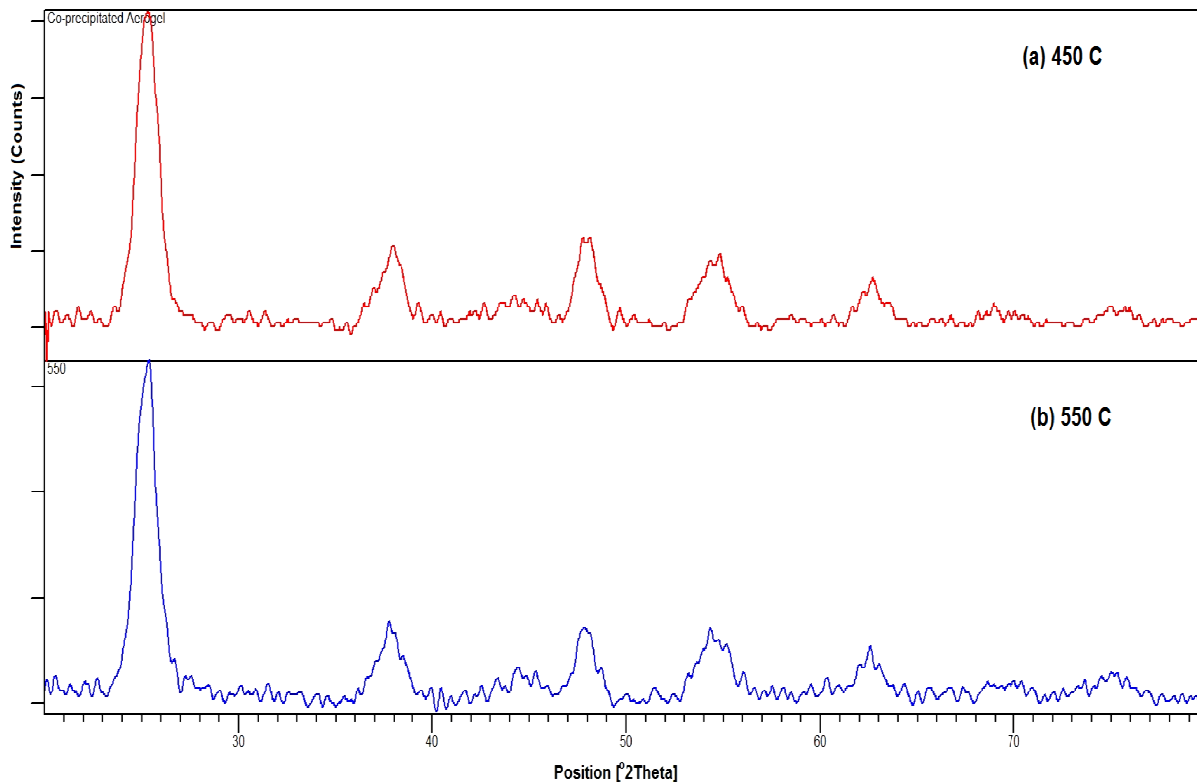


**Figure 6.4 XRD Patterns of Co-precipitated  $\text{TiO}_2/\text{WO}_3/\text{Fe}^{3+}$  Aerogel Photocatalyst Samples Calcined at Different Temperatures. (a) 450 °C (b) 550 °C**

### 6.1.1.3 Supercritical Impregnated $\text{TiO}_2/\text{WO}_3/\text{Fe}^{3+}$ Aerogel

Figure 6.5 shows the XRD pattern comparison of co-precipitated aerogel and supercritical impregnated aerogel. Both XRD patterns are very similar to each other, which matches with the BET results and the EDS elemental analysis results, which indicate similar 3 mol% Fe was presented in both co-precipitated templated  $\text{TiO}_2/\text{WO}_3/\text{Fe}^{3+}$  aerogel and supercritical impregnated  $\text{TiO}_2/\text{WO}_3/\text{Fe}^{3+}$  aerogel. XRD sample were ground to fine powder before mounting on the sample plate. Therefore, both the embedded Fe in co-precipitated aerogel and the Fe in the supercritical impregnated aerogel, both on the surface and inside the pores, will have same chance to be examined in X-ray scan.

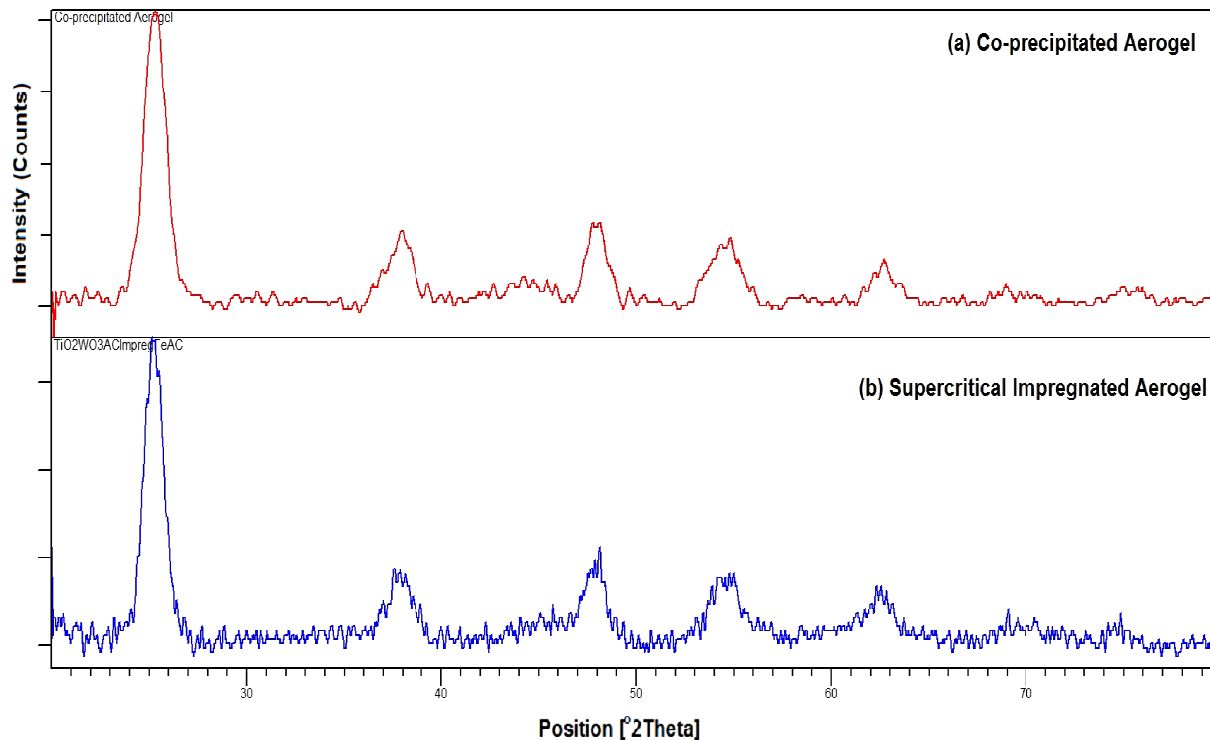


**Figure 6.5 XRD Patterns of Co-precipitated  $\text{TiO}_2/\text{WO}_3/\text{Fe}^{3+}$  Aerogel Photocatalyst and Supercritical Impregnated  $\text{TiO}_2/\text{WO}_3/\text{Fe}^{3+}$  Aerogel Photocatalyst**

### 6.1.2 Band Gap

Figure 6.6 reports the UV-Vis diffuse reflectance spectra (DRS) for Sigma-Aldrich 99% pure  $\text{TiO}_2$  powder, *Degussa* P25 and various kinds of sol-gel synthesized  $\text{TiO}_2$  aerogels. This UV-Vis DRS provides both an indication of the characteristic wavelength of light absorption by a semiconductor, as well as a method for estimating the band gap energy [215-217]. This method is based on extrapolating the spectrum steepest lines of each UV-Vis spectrum until interception with wavelength x-axis. This intercept wavelength defines the band gap energy for the semiconductors corresponding to the absorbed light wavelength (see Equation (4.13)). Table 6.2 summarized the correlated band gap energy of each of the experimental samples (Only calcined aerogel samples are listed).

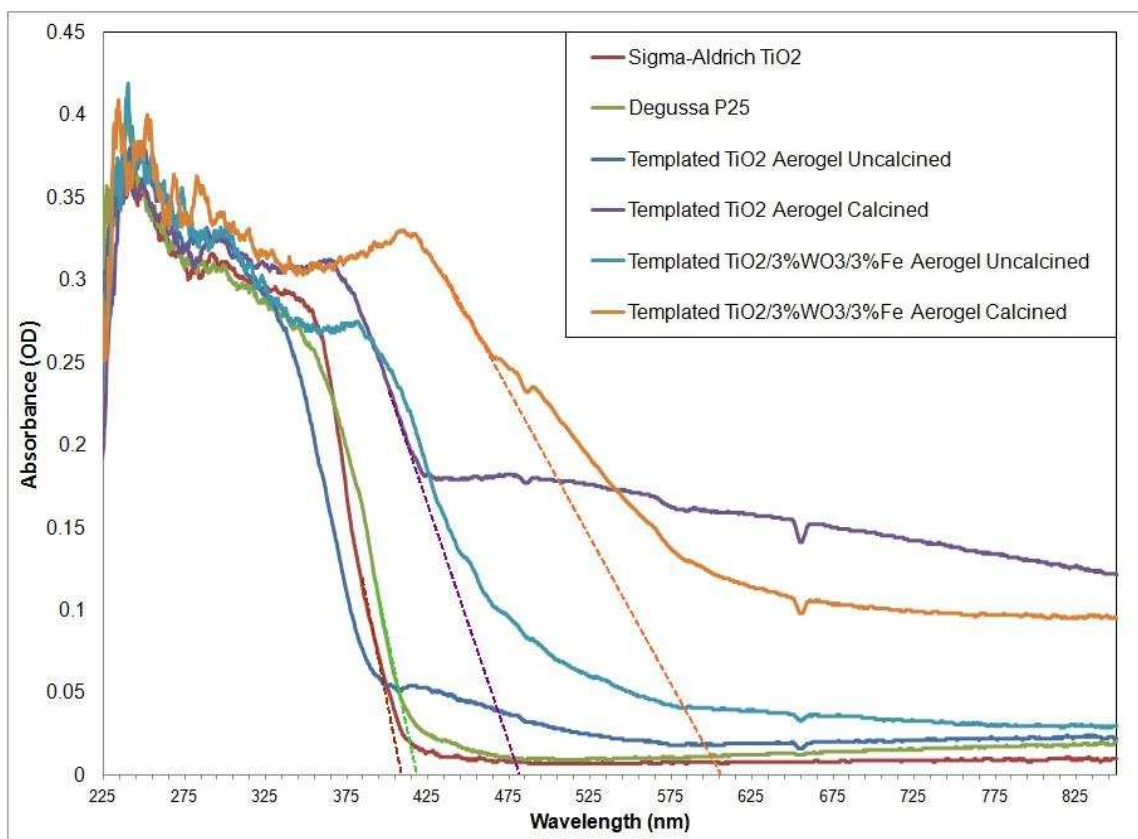


**Figure 6.6 Diffuse Reflectance Spectra of Different Photocatalysts**

**Table 6.2 Band-gap of Different Photocatalysts (Co-precipitated)**

Sample	Wavelength(nm)	Band gap(eV)
Degussa P25	416	2.98
Sigma-Aldrich TiO <sub>2</sub>	402	3.08
Aerogel TiO <sub>2</sub> (Calcined)	485	2.56
Aerogel TiO <sub>2</sub> /WO <sub>3</sub> /Fe <sup>3+</sup> (Calcined)	602	2.06

The results tabulated in Table 6.2 and illustrated in Figure 6.6 depict that the aerogel samples band gap is indeed reduced to visible light region. Calcined composite photocatalysts show additional broad absorption in the visible light region.

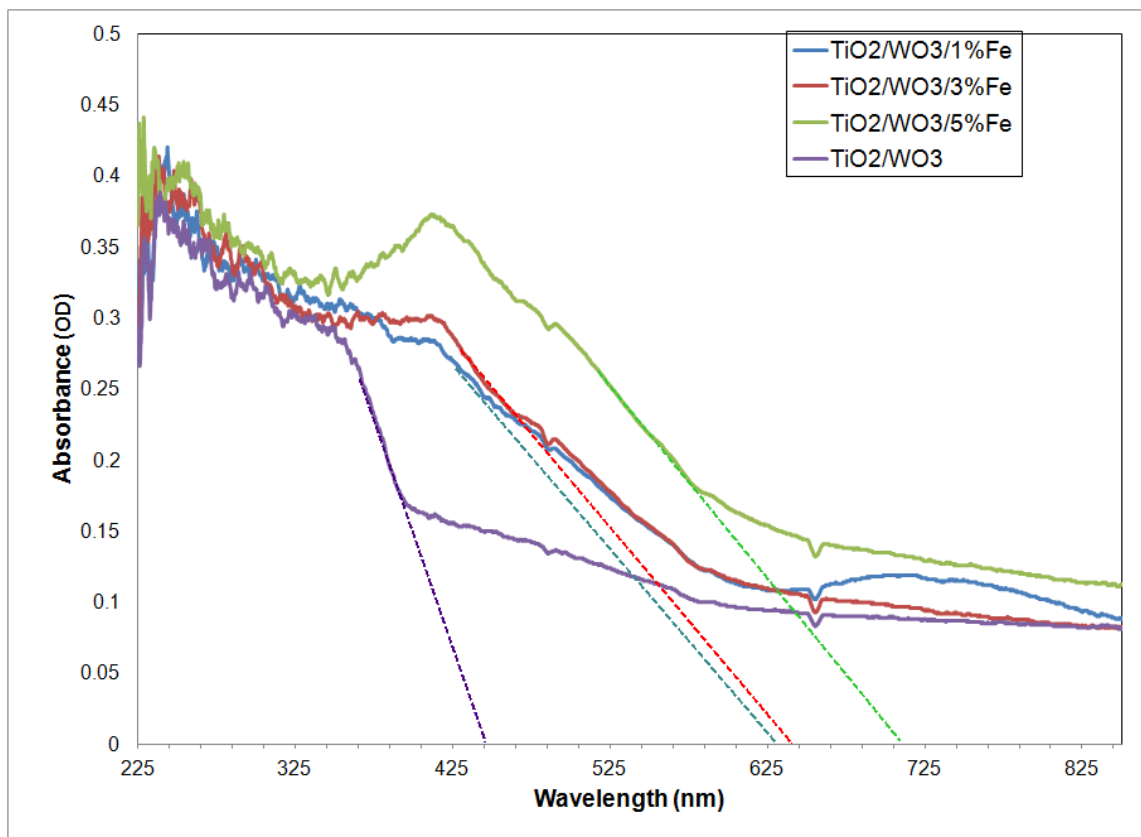


**Figure 6.7 Diffuse Reflectance Spectra of Co-precipitated  $\text{TiO}_2/\text{WO}_3$  with Different Amounts of Iron**

Figure 6.7 shows DRS of co-precipitated  $\text{TiO}_2/\text{WO}_3$  aerogel with different amounts of iron. Aerogel with 1 mol% and 3 mol% co-precipitated Iron, exhibited similar band gap red shifting, whereas, larger band gap shifting was observed in aerogels with 5 mol% iron. Over-reduced band gap promotes easier and faster electron-hole recombination, which will be harmful to photocatalytic activity.

Figure 6.8 shows the DRS of co-precipitated  $\text{TiO}_2/\text{WO}_3/\text{Fe}^{3+}$  aerogels at different calcination temperatures. The x-axis intercepts slightly increase with increasing calcination temperature and possibly correspond to an increase of rutile and  $\text{WO}_3$  crystalline ratio in the photocatalyst.

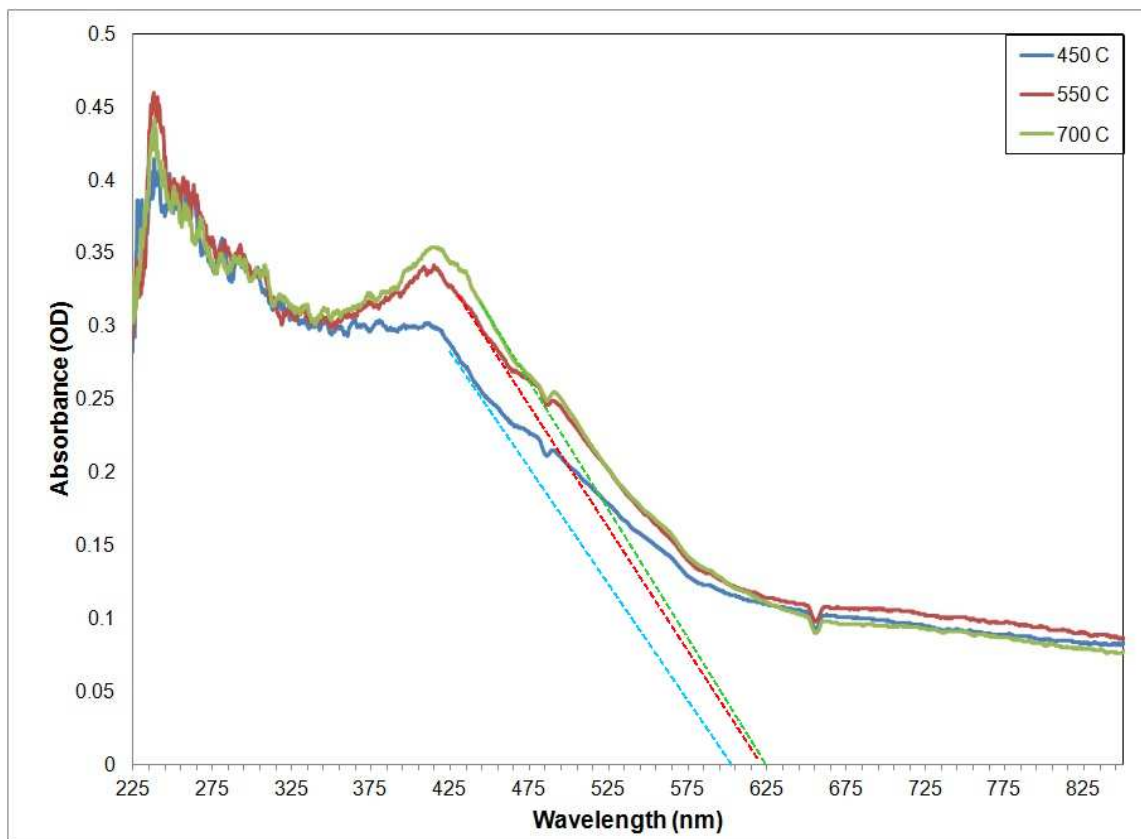


**Figure 6.8 Diffuse Reflectance Spectra of Co-precipitated  $\text{TiO}_2/\text{WO}_3/\text{Fe}^{3+}$  with Different Calcination Temperatures**

Figure 6.9 shows the DRS of supercritical impregnated  $\text{TiO}_2/\text{WO}_3/\text{Fe}^{3+}$  aerogels with different  $\text{TiO}_2/\text{WO}_3$  aerogel conditions. The results summarized in Table 6.3 depict that supercritical impregnated uncalcined  $\text{TiO}_2/\text{WO}_3$  has a higher percentage Fe impregnated, which is attributed to the increasing value of the absorbing light red shift and corresponds a narrower band gap and lower band gap energy.

**Table 6.3 Band-gap of Different Photocatalysts (Supercritical Impregnated)**

Sample	Wavelength (nm)	Band gap (eV)	Fe (mol %):Ti
Degussa P25	416	2.98	0
Aerogel $\text{TiO}_2/\text{WO}_3$ Calcined SCI $\text{Fe}^{3+}$ (Calcined)	630	1.98	~3
Aerogel $\text{TiO}_2/\text{WO}_3$ Uncalcined SCI $\text{Fe}^{3+}$ (Calcined)	666	1.85	~22

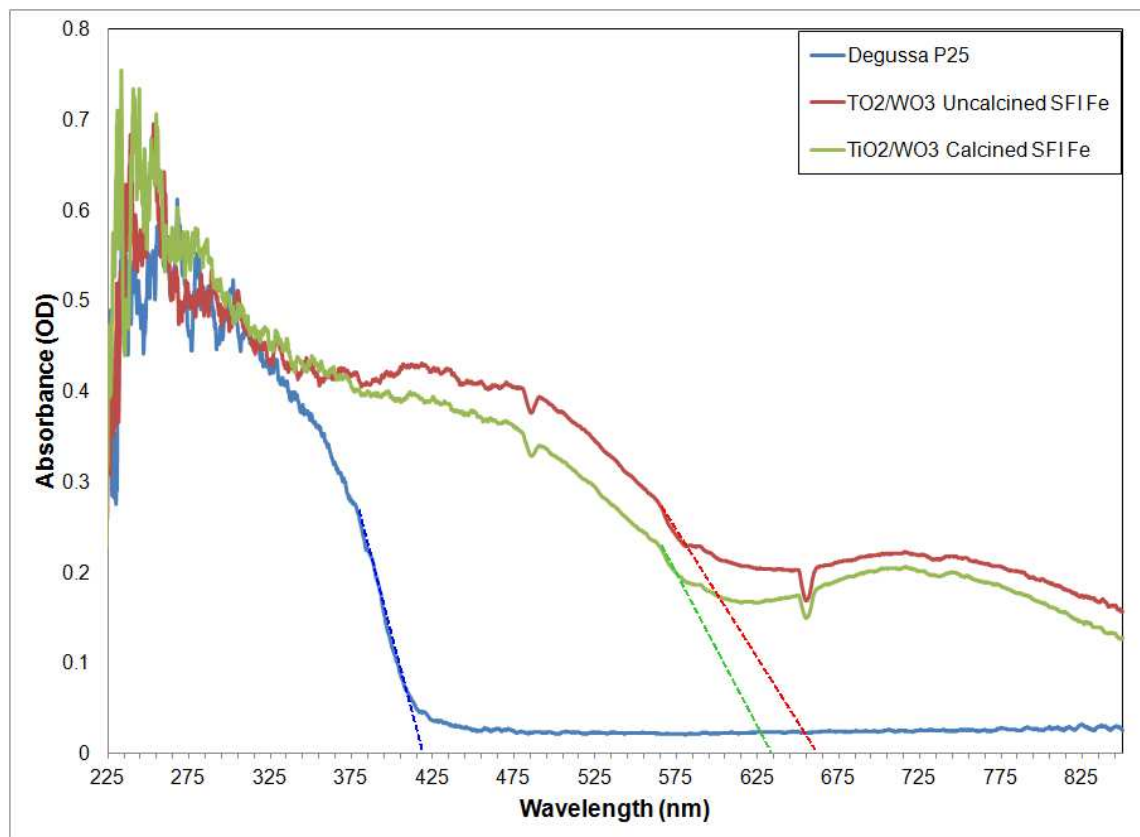


**Figure 6.9 Diffuse Reflectance Spectra of Supercritical Impregnated  $\text{TiO}_2/\text{WO}_3/\text{Fe}^{3+}$  with Different  $\text{TiO}_2/\text{WO}_3$  Conditions**

## 6.2 Photocatalyst Activity

The photocatalytic performance of calcined  $\text{TiO}_2$  based aerogel composite photocatalyst was evaluated in comparison with Degussa P25 and other experimental prepared photocatalyst samples in the model degradation of methylene blue (MB) under UV and visible light. Detailed experimental setup and procedure were described in Chapter 4. Experiments were run at room temperature and pressure with 500 ml 10 ppm MB in water solution. This solution was used to evaluate the effectiveness of the photocatalysts in decomposition of MB. The experimental system consisted of a water-cooling jacketed batch stirred reactor where 200 mg catalysts were used. The reaction is carried out for 12 hours. The UV light source used was Spectroline ENB-260C (6 W with UVA=365 nm and UVB=312 nm). The visible light source used was 250 W

IWASAKI Self-ballasted mercury lamp with UV cut-off filter film (>400 nm). The MB calibration curve is given in Figure 6.10.

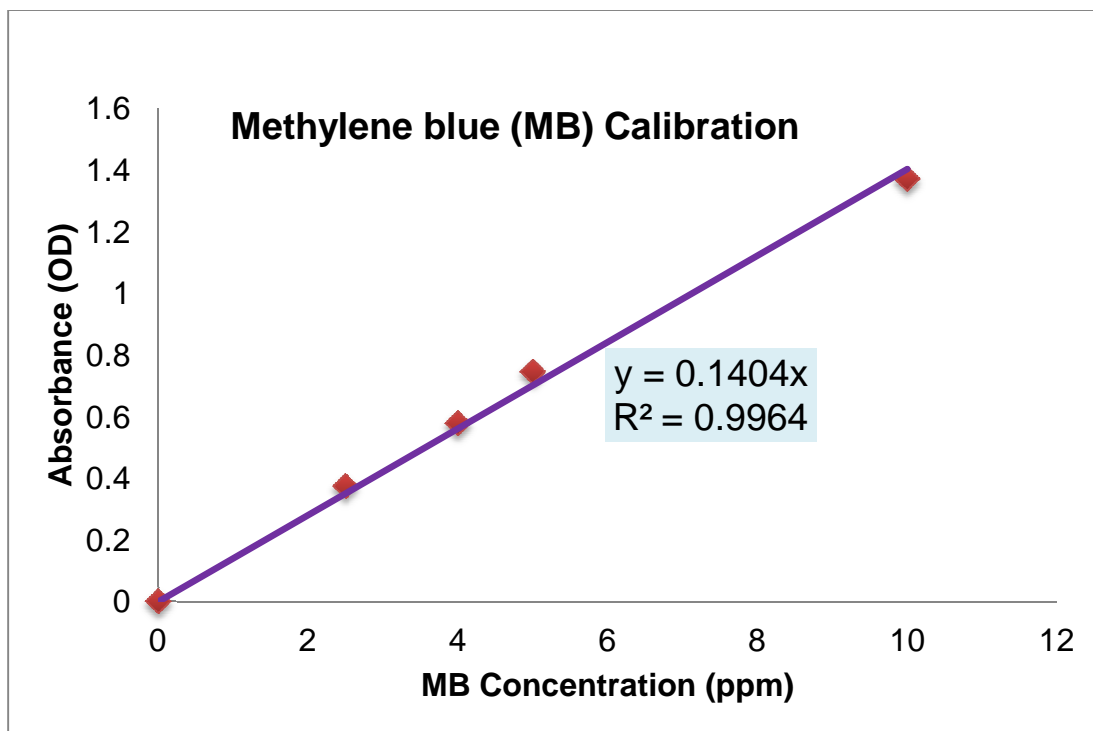


**Figure 6.10 Calibration Curve for Methylene Blue Absorption Peak at 297nm in UV-Vis Spectrum**

### 6.2.1 Under UV Light

For MB photodegradation experiments, four different composition of co-precipitated templated  $\text{TiO}_2$  based aerogel were chosen to be examined in comparison to the PCA of *Degussa* P25 under same experimental conditions as described in chapter 4. Incident light intensity, concentration of photocatalyst and targeted reactant/pollutant, reactor system pH value and oxygen availability are all considered as significant extrinsic factors that can affect the photocatalytic activity evaluation. Therefore, the photodegradation experimental conditions were designed to maintain constant conditions in order to minimize any unnecessary influence from those parameters. Figure 6.11 and 6.12 showed the typical changes of the UV-Vis absorbance

peak of MB (wavelength=297nm) over time for the photocatalytic degradation of MB. Associated with the decrease in intensity of the characteristic UV-Vis spectral peaks is also the fading of the MB blue solution color with time.

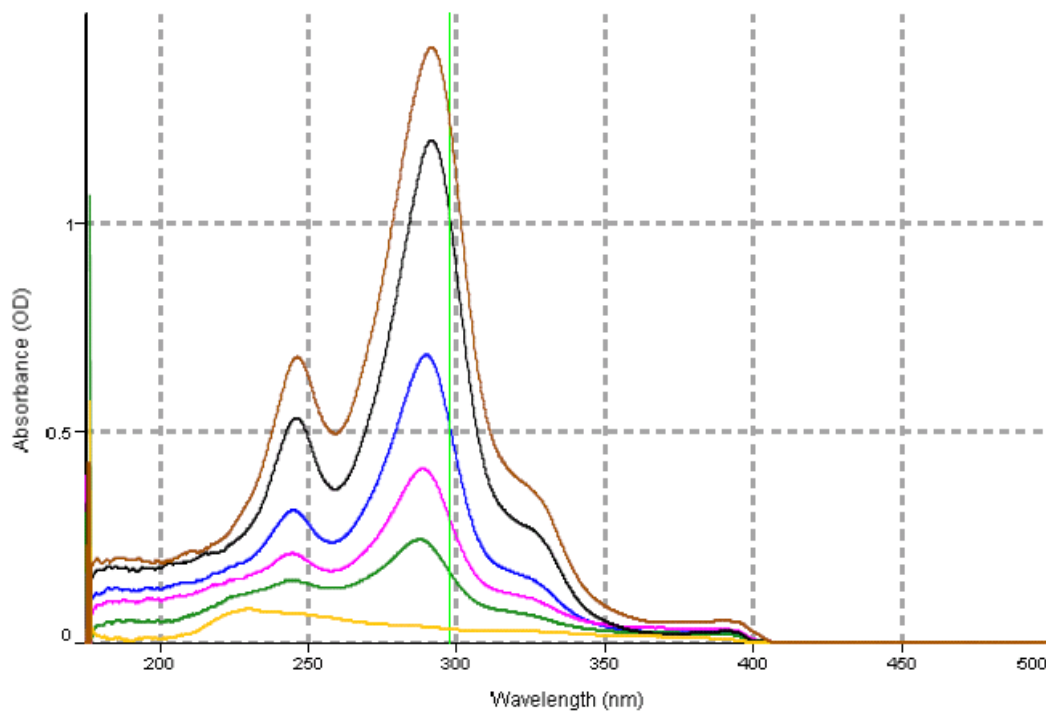


**Figure 6.11 Typical UV-Vis Absorbance Peak of MB (wavelength=297nm) Reduction during Photodegradation under UV Light**

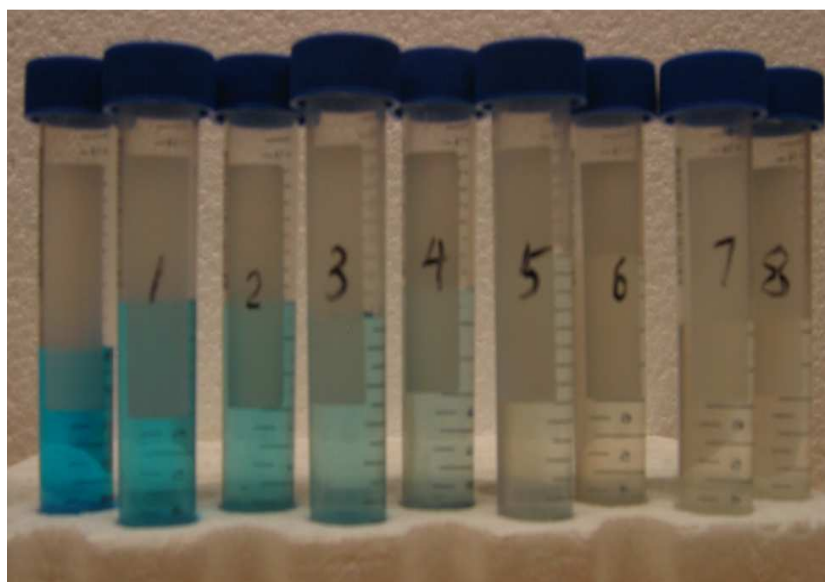


**Figure 6.12 Color Fading of MB Solution during Photodegradation under UV Light**

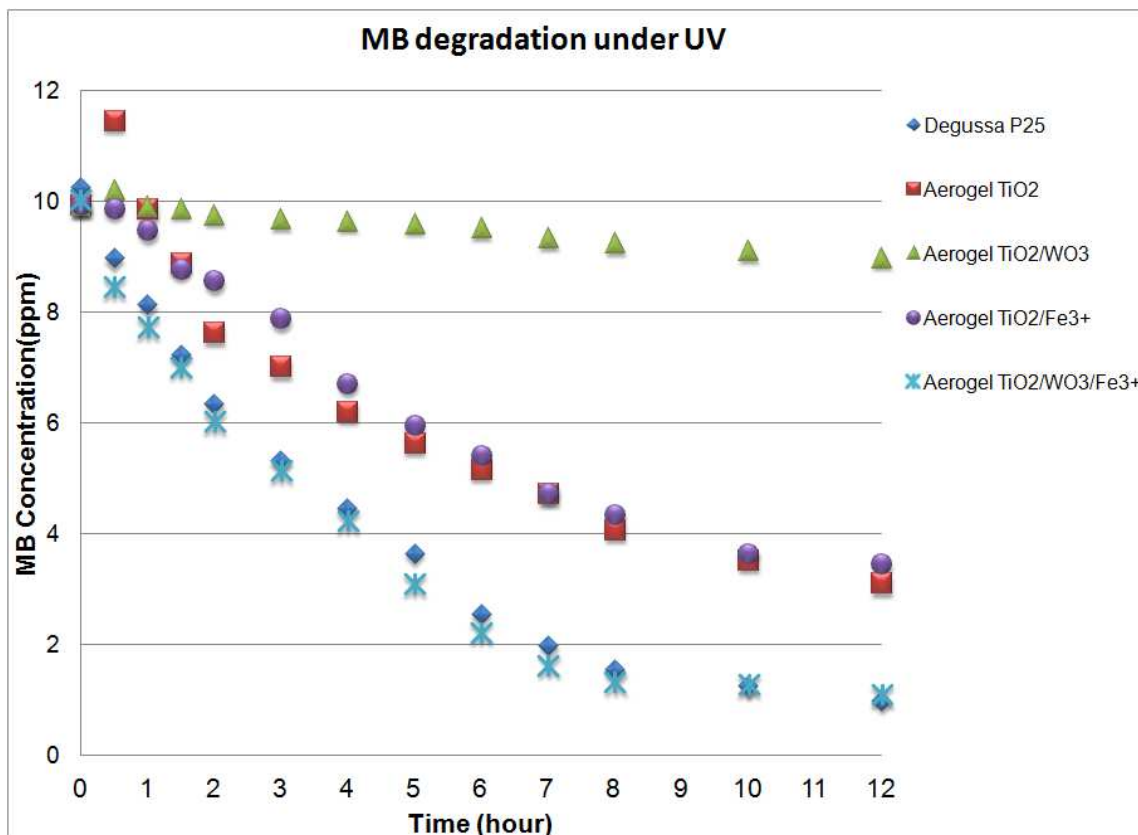


**Figure 6.13 Methylene Blue Degradation under UV Light (P25 and Co-precipitated Aerogel)**

No obvious detectable degradation of MB occurs without either photocatalyst or UV radiation alone. As can be seen from Figures 6.11, the co-precipitated  $\text{TiO}_2/3\% \text{WO}_3/3\% \text{Fe}^{3+}$  aerogel performed comparable to *Degussa* P25 catalyst under UV light while pure titanium oxide aerogel and  $\text{TiO}_2/3\% \text{Fe}^{3+}$  aerogel also performed relatively well. About 77% of MB was decomposed after 6 hours photodegradation. However, aerogels that contained 3 mol%  $\text{WO}_3$  without the  $\text{Fe}^{3+}$  did not show any appreciable activity, which has been previously report in similar work [140]. Because the heterogeneous reaction mechanism is dictated by the adsorption kinetics, it is better to consider to use the modified solid-liquid interface *Langmuir-Hinshelwood (L-H)* kinetic adsorption model, which relates the rate of photodegradation to the reaction rate constant ( $k$ ), equilibrium adsorption co-efficient ( $K$ ) and the initial concentration of

the reactant/pollutant (C) to follow the degradation kinetics and to access the rate expression in terms of disappearance of reactant:

$$r = -\frac{dC}{dt} = k\theta = \frac{kKC}{(1+KC)} \quad (6.1)$$

where  $\theta$  is the fraction of the surface covered by the reactant ( $\theta=KC/(1+KC)$ ). However, at low reactant concentration, the common first-order rate law of reaction is significantly similar to *L-H* model, the rate  $r$  is proportional to the surface coverage  $\theta$  which becomes proportional to reactant concentration  $C$ . Matthews R.W reported that the low concentration reactants under liquid phase degradation obey the first-order rate law with reasonable precision [218-220]. So, the reactant concentration over time can be expressed as:

$$r = -\frac{dC}{dt} = k'C \quad (6.2)$$

Integration of Equation 6.2 yields the first-order reaction equation as follow:

$$\ln\left(\frac{C}{C_0}\right) = -k't \quad (6.3)$$

The reaction rate constant  $k'$  can be obtained from the slope of the linear regression plot of  $-\ln(C/C_0)$  vs  $t$ .

The reaction rate constant corresponds to how well the photogenerated charge carriers separate without fast recombination. Theoretically, after being separated, photoexcited electrons and holes are trapped in conduction band and valence band, respectively, in very short times (normally in ns or ps scale). Electrons transfer to electron acceptors such as oxygen to become  $O_2^-$  and holes reacts with water to generate hydroxyl radicals. Trapping the electron with bubbled oxygen is a very slow process and will retard MB degradation. So that, trapping

electrons with another compound that is close to photocatalyst surface is very important.  $W^{6+}$  can be reduced by an electron to become  $W^{5+}$  if no other electron trap is available. The unstable  $W^{5+}$  will then act as an electron donor and push the electrons back to recombine with holes due to repulsive forces. Therefore, the presence of  $W^{6+}$ - $W^{5+}$  pairs change the physical and chemical properties of the reduced  $WO_3$  species, which has negative influence on photocatalyst PCA. This effect has been reported previously [221], and agrees well with the observations made in this research. However, the surface of  $WO_3/TiO_2$  is more acidic than that of regular  $TiO_2$ . This acidity will induce a higher concentration of  $OH^-$  on photocatalyst surface, which is favorable for  $OH$  radical formation which is necessary for photooxidation reaction. Dopant  $Fe^{3+}$  can trap electrons and be easily reduced by electrons to  $Fe^{2+}$ , which prevents fast electron-hole fast recombination. So combining  $WO_3$  and  $Fe^{3+}$  makes the  $TiO_2$  based photocatalyst PCA obviously higher than those without any dopant or with a single dopant.

### 6.2.2 Under Visible Light

Figure 6.14 depicts the performance of various photocatalysts under visible light.  $TiO_2/WO_3/Fe^{3+}$  aerogel outperformed all while *Degussa* P25 photocatalyst did not exhibit much activity under visible light. Titanium oxide aerogel did induce some degradation while  $TiO_2/WO_3$  aerogel photocatalyst had similar performance. It is obvious that  $TiO_2/3\% WO_3/3\% Fe^{3+}$  aerogel shows improved PCA compared to *Degussa* P25. The number of photoexcited electron-hole pairs is proportional to the absorbed photon energy, which directly correlates to the photodegradation rate, which can explained the slower MB degradation rate under visible light.

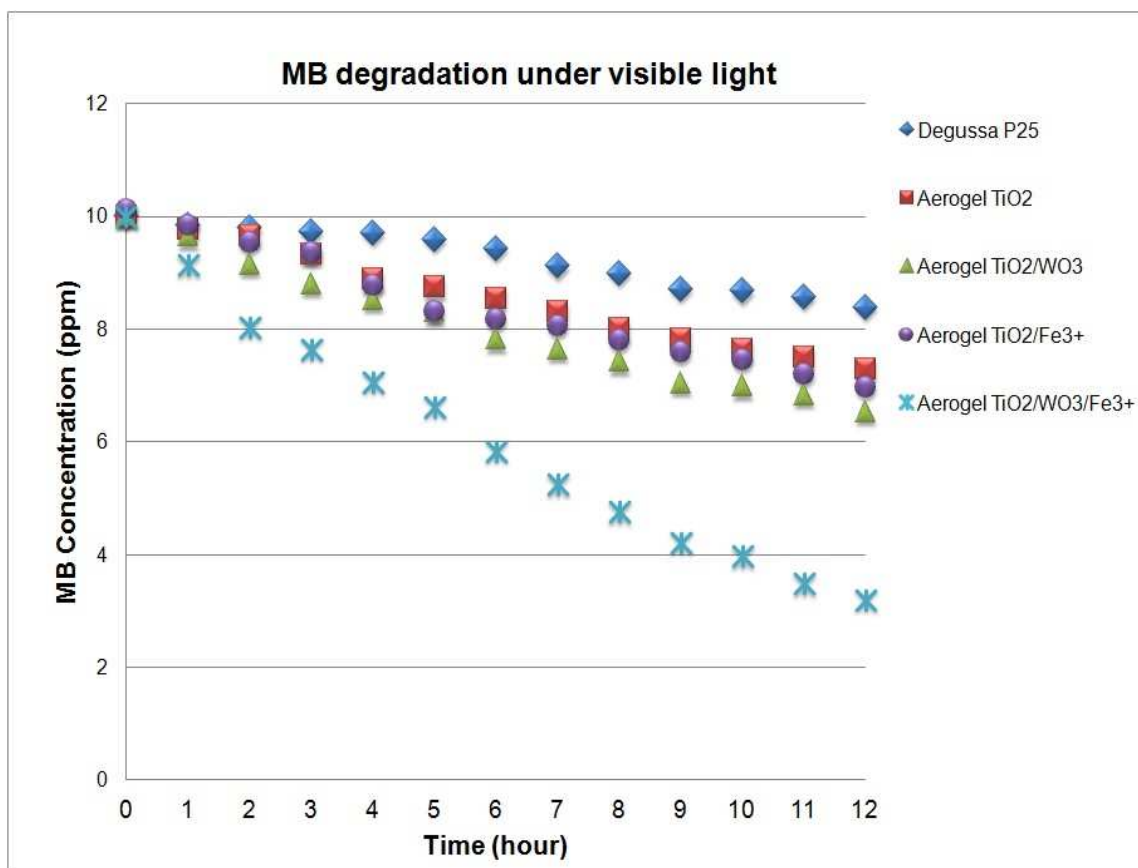


**Figure 6.14 Methylene Blue Degradation under Visible Light (P25 and Co-precipitated Aerogel)**

### 6.2.3 Supercritical Impregnated Aerogel Photocatalysts

Figure 6.14 and 6.15 depict the performance of supercritical impregnated aerogel photocatalysts compared to *Degussa P25* and co-precipitated aerogel photocatalysts under UV and visible light, respectively. Under UV light, performance of all samples are similar. Under visible light, as expected from previous observations, the experimental photocatalyst aerogel sample both performed significantly better than the *Degussa P25* standard. Also, the PCA performance for both experimental aerogel samples were essentially the same. It is therefore reasonable to assume that both experimental aerogels had similar composition, textural, physical and chemical properties, and band gap.

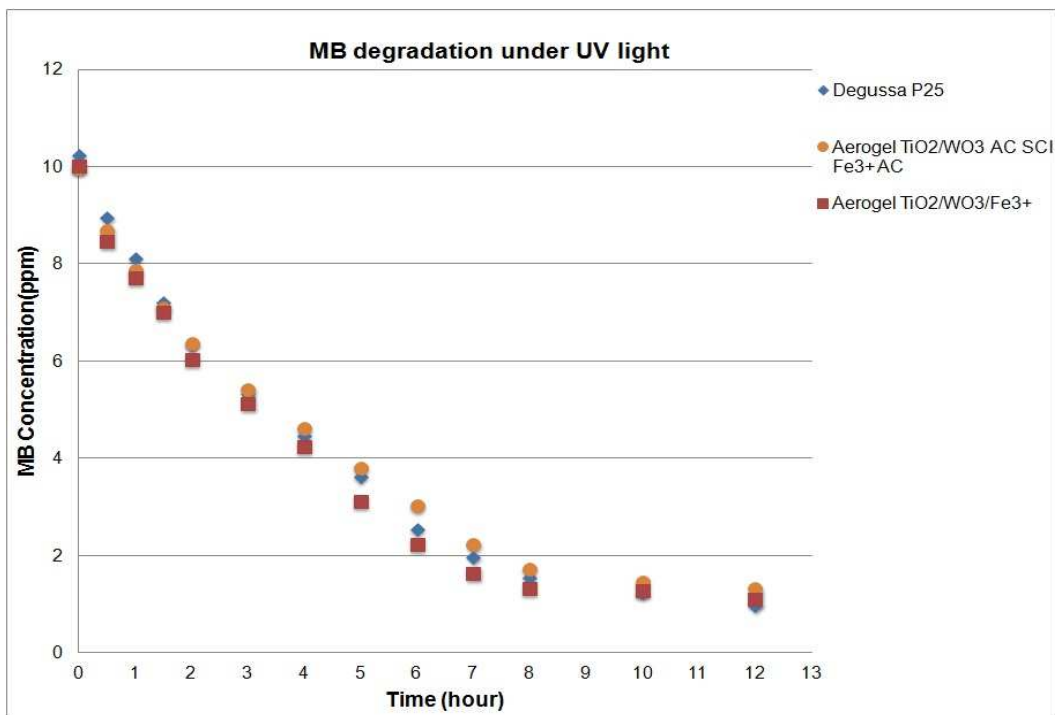


Figure 6.15 Methylene Blue Degradation under UV Light (P25, Supercritical Impregnated Aerogel and Co-precipitated Aerogel)

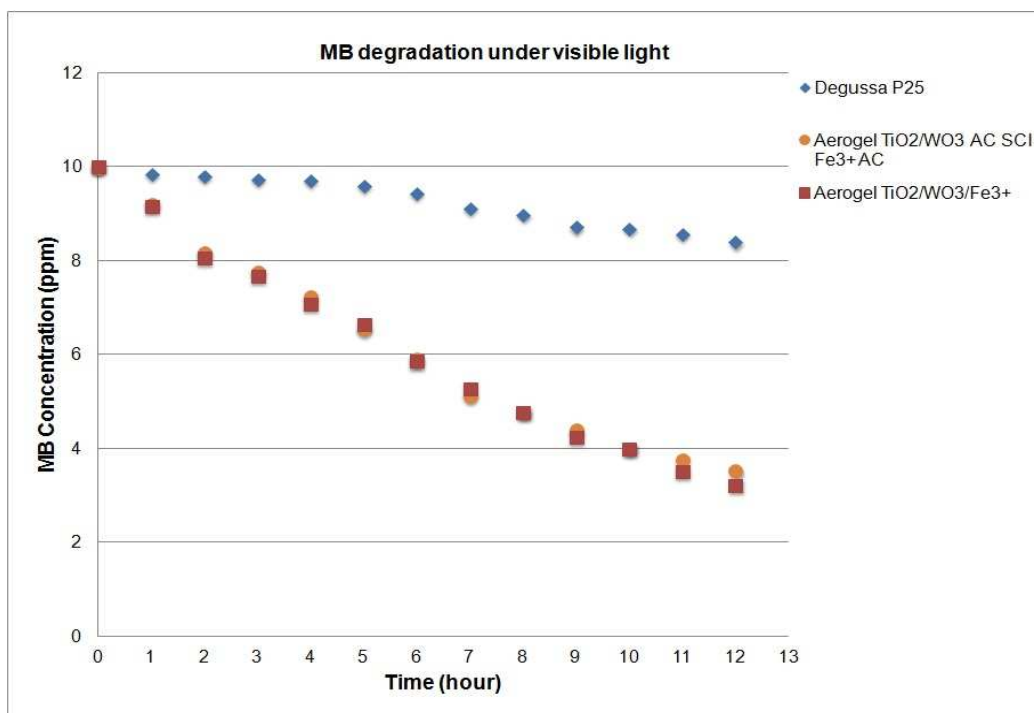
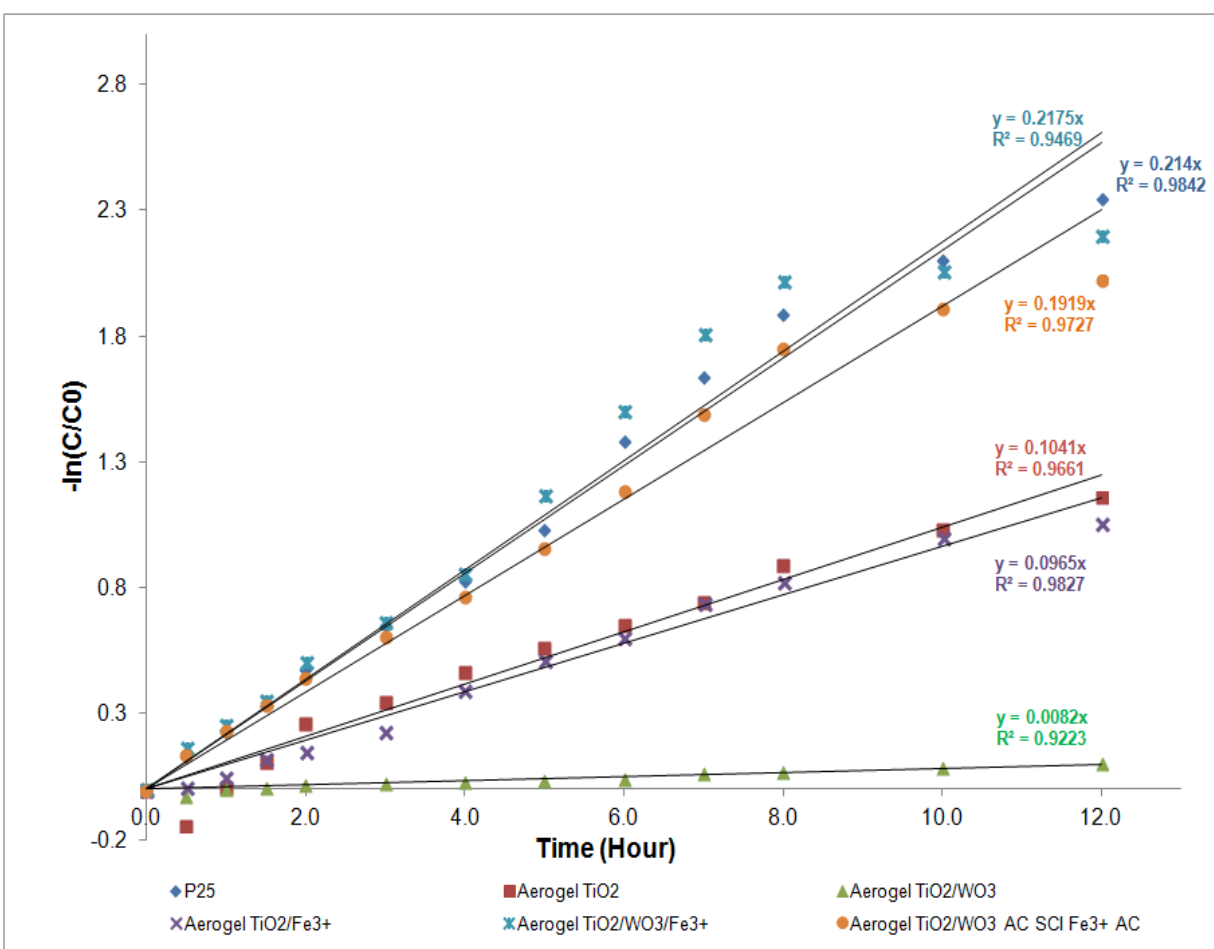


Figure 6.16 Methylene Blue Degradation under Visible Light (P25, Supercritical Impregnated Aerogel and Co-precipitated Aerogel)

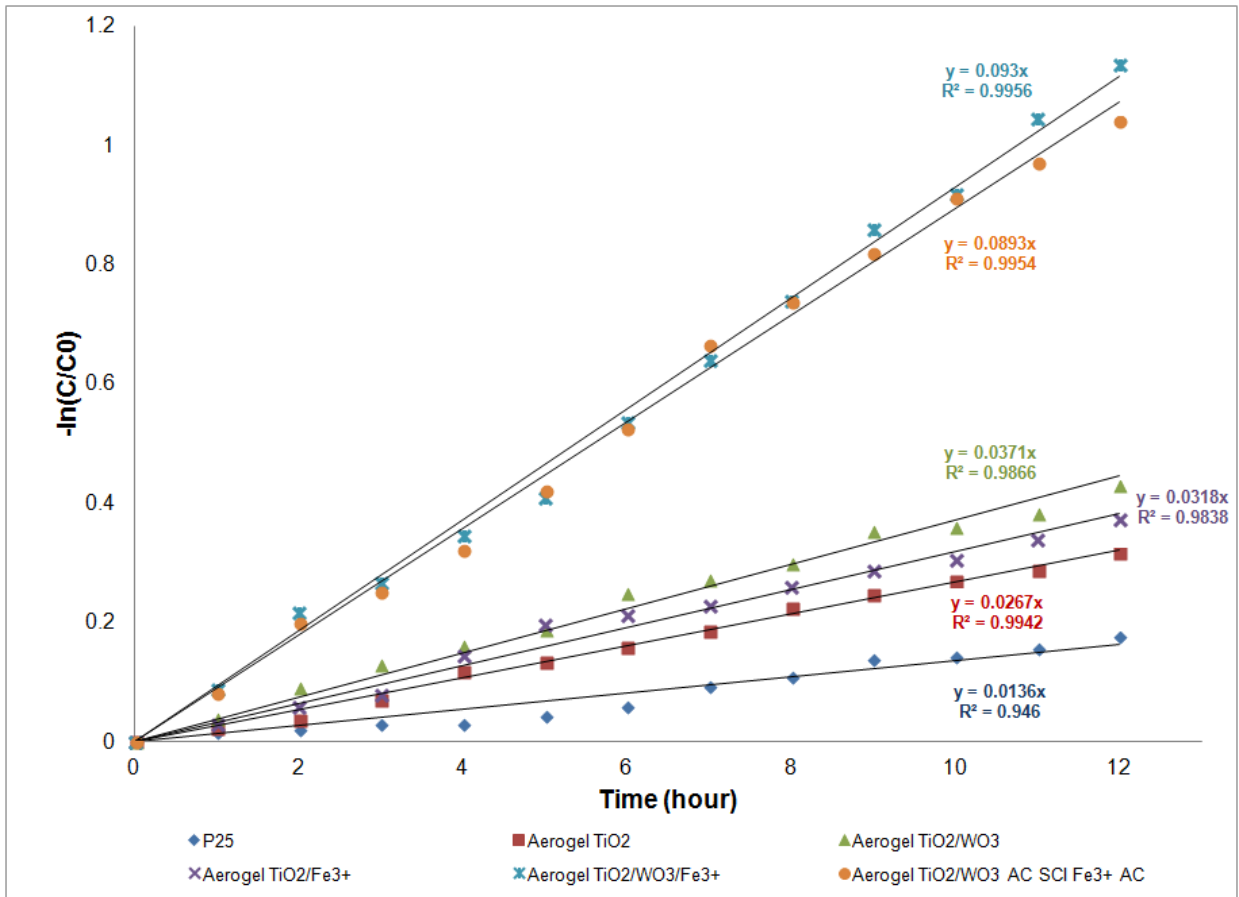
## 6.2.4 Kinetics of Photocatalytic Reaction

Figure 6.17 (a) and (b) depict the linear regression of the normalized MB relative concentration ( $\ln(C/C_0)$ ) decline as function of time following the Equation 6.3 for experiments running under UV light and visible light, respectively. It is worth to mention that linear regression trend lines fit the experimental data well at relative higher concentration ( $C > 2$  ppm), but observed experimental results show slower reaction rates at lower MB concentration. It could be explain as photodegradation reaction became more like a diffusion-controlled reaction than an activation-controlled reaction when the concentration of reactant MB is lower and lower.



(a)

Figure 6.17 Kinetics of Photodegradation of MB with Different Photocatalysts under (a) UV Light; (b) Visible Light



(b)

Figure 6.17 (Continued)

## CHAPTER 7

### CONCLUSIONS AND RECOMMENDATIONS

The conclusions of this dissertation are summarized in this chapter, which further includes recommendations for future work.

#### 7.1 Conclusions

The overall aim of this doctoral research is to design and synthesize a  $\text{TiO}_2$  based photocatalyst that has tailored and tunable nano-porous structure to capture environmental pollutants and enable their in-situ decomposition to smaller benign molecules, preferably under both UV and visible light through photo-oxidation.

A novel and environmental friendly method was developed to prepare unique surfactant templated aerogel composite photocatalysts. The process operating conditions, sol-gel chemistry, and the dopant precursors can be flexibly tuned to tailor the chemical and mechanical performance of the aerogel photocatalyst.

A second composite semiconductor  $\text{WO}_3$  and transition metal ion  $\text{Fe}^{3+}$  were successfully incorporated within the  $\text{TiO}_2$  porous matrix through sol-gel feed preparation and supercritical extraction and drying stages. XRD analysis of these samples show that subsequent heat treatment at  $450\text{ }^\circ\text{C}$  results in titanium dioxide with desirable anatase crystal structure, and tailored tungsten oxide and iron oxide composition. If the calcination step is carried out at temperatures above  $550\text{ }^\circ\text{C}$ , the presence of rutile phase is observed. A neutral surfactant template, Triton X-114, is used for tuning of the mesoporous structure and surface properties in

an effort to enhance the ability of the nano structured photocatalysts to capture and retain pollutants for their subsequent photocatalytic destruction.

The surface area, the pore volume per gram and the average pore size of the developed aerogel photocatalysts are about an order of magnitude higher in comparison to the industry standard *Degussa* P25. The surface areas were about three times greater for aerogels while the pore volumes per gram increased by about five times. Average pore diameters ranged between 20 to 30 nm. The cross-section of aerogels, as seen in SEM-FIB images, clearly show an open cell mesoporous structure.

A technique for supercritical fluid impregnation of dopant precursors was developed as an alternative to the co-precipitated aerogel preparation pathways. The tunable supercritical fluid impregnation process allows incorporation of the desirable concentration of organic iron complex and uniform dispersion of the dopant within the targeted highly porous  $\text{TiO}_2/\text{WO}_3$  aerogel matrix while retaining the original textural structure. Through judicious selection of the aerogel, the system pressure and temperature, the processing time and the initial amount of organic metal complex, wide range of Fe loadings was achieved through the supercritical impregnation approach.

X-Ray diffraction of the aerogel implies slightly larger anatase crystallite size than *Degussa* P25. Tungsten oxide and Iron oxide introduced as dopants induce an increase in lattice defect density which will limit the fully growth of the perfect anatase crystalline while increasing the concentration of carriers and the numbers of electrons and holes. The UV-Vis diffuse reflectance spectra depict that calcined composite aerogel photocatalysts,  $\text{TiO}_2/\text{WO}_3/\text{Fe}^{3+}$  particles have a band gap of about 2.06 eV which is indeed within the visible light region.

Several of aerogel photocatalyst were tested for a model photo-catalytic reaction. The model system employed Methylene Blue (MB) photo-oxidation reaction under UV and visible light. Aerogel  $\text{TiO}_2$  particles that contain three mole percent  $\text{WO}_3$  and three mole percent  $\text{Fe}^{3+}$  exhibit photocatalytic capability comparable to *Degussa* P25 under UV light exposure and extend the activity to visible light range at which P25 activity is negligible. Pure  $\text{TiO}_2$  aerogels and  $\text{TiO}_2$  aerogels with three mole percent  $\text{Fe}^{3+}$  did also perform relatively well under UV light, but exhibit very limited activity under visible light. Interestingly,  $\text{TiO}_2$  aerogels with three mole percent  $\text{WO}_3$  but no  $\text{Fe}^{3+}$  did not show any appreciable activity under neither UV nor visible light.

## 7.1 Recommendations

There are several future directions possible as a result of this research including the techniques, composition, and the intended use. These include:

- The sol-gel synthesis step, the supercritical extraction and drying process, the supercritical fluid impregnation stage and even the final heat treatment stages may be integrated. The pilot plant can be configured to carry with an automated component feed and control loops. This will be ideal for larger scale industrial production.
- Transparent porous catalyst support such as silica may help enhance the adsorption capability and allow more light into the internal porous nano structure that have the active catalyst sites. Silica aerogel mixed with 25% *Degussa* P25 was synthesized in trial experiments, the surface area of product aerogels was about  $700 \text{ m}^2/\text{g}$ . However, these achieved aerogel particles were opaque white due to light scattering by dispersed P25 nanoparticles. However, using  $\text{TiO}_2$  and silica precursors together in sol-gel preparation may result a totally different aerogel. Even if transparent  $\text{TiO}_2$ /Silica are synthesized, the photocatalytic activity of these nano structured particles may remain

limited under visible light since silica band gap is much larger than  $\text{TiO}_2$ . Thus, composite semiconductor or other dopant additions may still be necessary.

- Sorption and mass transfer limitations may limit liquid phase, particularly aqueous, photocatalytic reaction applications, due to higher surface tension and resulting capillary forces associated with such systems. Instead, photodegradation of gaseous systems are expected to be potentially superior compared to liquid phase.

## REFERENCES

1. Plotnikov, J., (1936) "Allgerneine Photochernie," 2nd Ed., Walter de Gruyter, West Berlin.
2. BBC Research Report (2010), Photocatalysts: Technologies and Global Markets
3. Pozzo, R. L., Baltanas, M. A., & Cassano, A. E. (1997). Supported titanium oxide as photocatalyst in water decontamination: state of the art. *Catalysis Today*, 39(3), 219-231.
4. Ollis, D. F., & Al-Ekabi, H. (1993). Photocatalytic purification and treatment of water and air: *proceedings of the 1st International Conference on TiO<sub>2</sub> Photocatalytic Purification and Treatment of Water and Air*, London, Ontario, Canada, 8-13 November, 1992. Elsevier Science Ltd.
5. Vohra, A., Goswami, D. Y., Deshpande, D. A., & Block, S. S. (2006). Enhanced photocatalytic disinfection of indoor air. *Applied Catalysis B: Environmental*, 64(1), 57-65.
6. Guillard, C., Bui, T. H., Felix, C., Moules, V., Lina, B., & Lejeune, P. (2008). Microbiological disinfection of water and air by photocatalysis. *Comptes Rendus Chimie*, 11(1), 107-113.
7. Berry, R. J., & Mueller, M. R. (1994). Photocatalytic Decomposition of Crude Oil Slicks Using TiO<sub>2</sub> on a Floating Substrate. *Microchemical journal*, 50(1), 28-32.
8. Nair, M., Luo, Z., & Heller, A. (1993). Rates of photocatalytic oxidation of crude oil on salt water on buoyant, cenosphere-attached titanium dioxide. *Industrial & engineering chemistry research*, 32(10), 2318-2323.
9. Tan, S. S., Zou, L., & Hu, E. (2006). Photocatalytic reduction of carbon dioxide into gaseous hydrocarbon using TiO<sub>2</sub> pellets. *Catalysis today*, 115(1), 269-273.
10. Blossey, R. (2003). Self-cleaning surfaces—virtual realities. *Nature materials*, 2(5), 301-306.
11. Ni, M., Leung, M. K., Leung, D. Y., & Sumathy, K. (2007). A review and recent developments in photocatalytic water-splitting using TiO<sub>2</sub> for hydrogen production. *Renewable and Sustainable Energy Reviews*, 11(3), 401-425.
12. Fujishima A and Honda K (1972) Electrochemical Photolysis of Water at a Semiconductor Electrode *Nature* 238 37

13. Fujishima, A., Rao, T. N., & Tryk, D. A. (2000). Titanium dioxide photocatalysis. *Journal of Photochemistry and Photobiology C: Photochemistry Reviews*, 1(1), 1-21.
14. Chatterjee, D., & Dasgupta, S. (2005) Visible light induced photocatalytic degradation of organic pollutants. *Journal of Photochemistry and Photobiology C: Photochemistry Reviews*, 6(2), 186-205.
15. Litter, M. I. (1999). Heterogeneous photocatalysis: transition metal ions in photocatalytic systems. *Applied Catalysis B: Environmental*, 23(2), 89-114.
16. Fujishima, A., Zhang, X., & Tryk, D. A. (2008). TiO<sub>2</sub> photocatalysis and related surface phenomena. *Surface Science Reports*, 63(12), 515-582.
17. Carp, O., Huisman, C. L., & Reller, A. (2004). Photoinduced reactivity of titanium dioxide. *Progress in Solid State Chemistry*, 32(1), 33-177.
18. Ni, M., Leung, M. K., Leung, D. Y., & Sumathy, K. (2007). A review and recent developments in photocatalytic water-splitting using TiO<sub>2</sub> for hydrogen production. *Renewable and Sustainable Energy Reviews*, 11(3), 401-425.
19. Wang, S., Ang, H. M., & Tade, M. O. (2007). Volatile organic compounds in indoor environment and photocatalytic oxidation: State of the art. *Environment international*, 33(5), 694-705.
20. Choi, W. (2006). Pure and modified TiO<sub>2</sub> photocatalysts and their environmental applications. *Catalysis surveys from Asia*, 10(1), 16-28.
21. Agrios, A. G., & Pichat, P. (2005). State of the art and perspectives on materials and applications of photocatalysis over TiO<sub>2</sub>. *Journal of Applied Electrochemistry*, 35(7), 655-663.
22. Chen, X., & Mao, S. S. (2007). Titanium dioxide nanomaterials: synthesis, properties, modifications, and applications. *Chemical reviews*, 107(LBNL--59769).
23. Chen, X. (2009). Titanium dioxide nanomaterials and their energy applications. *Chinese Journal of Catalysis*, 30(8), 839-851.
24. Litter, M. I. (1999). Heterogeneous photocatalysis: transition metal ions in photocatalytic systems. *Applied Catalysis B: Environmental*, 23(2), 89-114.
25. Palmisano, G., Augugliaro, V., Pagliaro, M., & Palmisano, L. (2007). Photocatalysis: a promising route for 21st century organic chemistry. *Chemical Communications*, (33), 3425-3437.
26. Serpone, N. (1995). Brief introductory remarks on heterogeneous photocatalysis. *Solar energy materials and solar cells*, 38(1-4), 369-379.
27. Ollis, D. F., Pelizzetti, E., & Serpone, N. (1991). Photocatalyzed destruction of water contaminants. *Environmental science & technology*, 25(9), 1522-1529.

28. Diebold, U. (2003). The surface science of titanium dioxide. *Surface science reports*, 48(5), 53-229.
29. Chen, Y., Crittenden, J. C., Hackney, S., Sutter, L., & Hand, D. W. (2005). Preparation of a novel TiO<sub>2</sub>-based pn junction nanotube photocatalyst. *Environmental science & technology*, 39(5), 1201-1208.
30. Park, J. H., Kim, S., & Bard, A. J. (2006). Novel carbon-doped TiO<sub>2</sub> nanotube arrays with high aspect ratios for efficient solar water splitting. *Nano letters*, 6(1), 24-28.
31. Pan, J. H., Cai, Z., Yu, Y., & Zhao, X. S. (2011). Controllable synthesis of mesoporous F-TiO<sub>2</sub> spheres for effective photocatalysis. *Journal of Materials Chemistry*, 21(30), 11430-11438.
32. Liu, S., Yu, J., & Jaroniec, M. (2010). Tunable photocatalytic selectivity of hollow TiO<sub>2</sub> microspheres composed of anatase polyhedra with exposed {001} facets. *Journal of the American Chemical Society*, 132(34), 11914-11916.
33. Li, Y., Sasaki, T., Shimizu, Y., & Koshizaki, N. (2008). A Hierarchically Ordered TiO<sub>2</sub> Hemispherical Particle Array with Hexagonal-Non-Close-Packed Tops: Synthesis and Stable Superhydrophilicity Without UV Irradiation. *Small*, 4(12), 2286-2291.
34. Li, Y., Sasaki, T., Shimizu, Y., & Koshizaki, N. (2008). Hexagonal-close-packed, hierarchical amorphous TiO<sub>2</sub> nanocolumn arrays: transferability, enhanced photocatalytic activity, and superamphiphilicity without UV irradiation. *Journal of the American Chemical Society*, 130(44), 14755-14762.
35. Kitano, M., Mitsui, R., Eddy, D. R., El-Bahy, Z. M., Matsuoka, M., Ueshima, M., & Anpo, M. (2007). Synthesis of nanowire TiO<sub>2</sub> thin films by hydrothermal treatment and their photoelectrochemical properties. *Catalysis Letters*, 119(3-4), 217-221.
36. Cozzoli, P. D., Kornowski, A., & Weller, H. (2003). Low-temperature synthesis of soluble and processable organic-capped anatase TiO<sub>2</sub> nanorods. *Journal of the American Chemical Society*, 125(47), 14539-14548.
37. Wu, J. J., & Yu, C. C. (2004). Aligned TiO<sub>2</sub> nanorods and nanowalls. *The Journal of Physical Chemistry B*, 108(11), 3377-3379.
38. Zhang, M., Bando, Y., & Wada, K. (2001). Sol-gel template preparation of TiO<sub>2</sub> nanotubes and nanorods. *Journal of materials science letters*, 20(2), 167-170.
39. Fu, N., Wu, Y., Jin, Z., & Lu, G. (2009). Structural-dependent photoactivities of TiO<sub>2</sub> nanoribbon for visible-light-induced H<sub>2</sub> evolution: the roles of nanocavities and alternate structures. *Langmuir*, 26(1), 447-455.
40. Pan, K., Zhang, Q., Wang, Q., Liu, Z., Wang, D., Li, J., & Bai, Y. (2007). The photoelectrochemical properties of dye-sensitized solar cells made with TiO<sub>2</sub> nanoribbons and nanorods. *Thin Solid Films*, 515(7), 4085-4091.

41. Zukalova, M., Zukal, A., Kavan, L., Nazeeruddin, M. K., Liska, P., & Grätzel, M. (2005). Organized mesoporous TiO<sub>2</sub> films exhibiting greatly enhanced performance in dye-sensitized solar cells. *Nano Letters*, 5(9), 1789-1792.
42. Wang, Z. S., Yamaguchi, T., Sugihara, H., & Arakawa, H. (2005). Significant efficiency improvement of the black dye-sensitized solar cell through protonation of TiO<sub>2</sub> films. *Langmuir*, 21(10), 4272-4276.
43. Choi, W., Termin, A., & Hoffmann, M. R. (1994). The role of metal ion dopants in quantum-sized TiO<sub>2</sub>: correlation between photoreactivity and charge carrier recombination dynamics. *The Journal of Physical Chemistry*, 98(51), 13669-13679.
44. Baan, R., Straif, K., Grosse, Y., Secretan, B., El Ghissassi, F., & Coglianò, V. (2006). Carcinogenicity of carbon black, titanium dioxide, and talc. *The Lancet Oncology*, 7(4), 295-296.
45. Moon, S. C., Mametsuka, H., Suzuki, E., & Nakahara, Y. (1998). Characterization of titanium-boron binary oxides and their photocatalytic activity for stoichiometric decomposition of water. *Catalysis today*, 45(1), 79-84.
46. Antonelli, D. M., & Ying, J. Y. (1995). Synthesis of hexagonally packed mesoporous TiO<sub>2</sub> by a modified sol-gel method. *Angewandte Chemie International Edition in English*, 34(18), 2014-2017.
47. Vorontsov, A. V., Savinov, E. N., & Zhensheng, J. (1999). Influence of the form of photodeposited platinum on titania upon its photocatalytic activity in CO and acetone oxidation. *Journal of Photochemistry and Photobiology A: Chemistry*, 125(1), 113-117.
48. Ohtani, B., Kakimoto, M., Nishimoto, S. I., & Kagiya, T. (1993). Photocatalytic reaction of neat alcohols by metal-loaded titanium (IV) oxide particles. *Journal of Photochemistry and Photobiology A: Chemistry*, 70(3), 265-272.
49. Chen, J., Ollis, D. F., Rulkens, W. H., & Bruning, H. (1999). Photocatalyzed oxidation of alcohols and organochlorides in the presence of native TiO<sub>2</sub> and metallized TiO<sub>2</sub> suspensions. Part (I): photocatalytic activity and pH influence. *Water Research*, 33(3), 661-668.
50. Chan, S. C., & Barteau, M. A. (2005). Preparation of highly uniform Ag/TiO<sub>2</sub> and Au/TiO<sub>2</sub> supported nanoparticle catalysts by photodeposition. *Langmuir*, 21(12), 5588-5595.
51. Behnajady, M. A., Modirshahla, N., Shokri, M., & Rad, B. (2008). Enhancement of photocatalytic activity of TiO<sub>2</sub> nanoparticles by silver doping: photodeposition versus liquid impregnation methods. *Global NEST Journal*, 10(1), 1-7.
52. Jacobs, J. W. M., Kampers, F. W. H., Rikken, J. M. G., Bulle-Lieuwma, C. W. T., & Koningsberger, D. C. (1989). Copper photodeposition on TiO<sub>2</sub> studied with HREM and EXAFS. *Journal of The Electrochemical Society*, 136(10), 2914-2923.

53. Yin, Y., Jin, Z., & Hou, F. (2007). Enhanced solar water-splitting efficiency using core/sheath heterostructure CdS/TiO<sub>2</sub> nanotube arrays. *Nanotechnology*, 18(49), 495608.
54. Jang, J. S., Gyu Kim, H., Borse, P. H., & Lee, J. S. (2007). Simultaneous hydrogen production and decomposition of H<sub>2</sub>S dissolved in alkaline water over CdS–TiO<sub>2</sub> composite photocatalysts under visible light irradiation. *International journal of hydrogen energy*, 32(18), 4786-4791.
55. Liu, L., Hensel, J., Fitzmorris, R. C., Li, Y., & Zhang, J. Z. (2009). Preparation and photoelectrochemical properties of CdSe/TiO<sub>2</sub> hybrid mesoporous structures. *The Journal of Physical Chemistry Letters*, 1(1), 155-160.
56. Lo, S. C., Lin, C. F., Wu, C. H., & Hsieh, P. H. (2004). Capability of coupled CdSe/TiO<sub>2</sub> for photocatalytic degradation of 4-chlorophenol. *Journal of hazardous materials*, 114(1), 183-190.
57. Papp, J., Soled, S., Dwight, K., & Wold, A. (1994). Surface acidity and photocatalytic activity of TiO<sub>2</sub>, WO<sub>3</sub>/TiO<sub>2</sub>, and MoO<sub>3</sub>/TiO<sub>2</sub> photocatalysts. *Chemistry of materials*, 6(4), 496-500.
58. Martin, C., Solana, G., Rives, V., Marci, G., Palmisano, L., & Sclafani, A. (1997). Physico-chemical properties of WO<sub>3</sub>/TiO<sub>2</sub> systems employed for 4-nitrophenol photodegradation in aqueous medium. *Catalysis letters*, 49(3-4), 235-243.
59. Paramasivam, I., Nah, Y. C., Das, C., Shrestha, N. K., & Schmuki, P. (2010). WO<sub>3</sub>/TiO<sub>2</sub> nanotubes with strongly enhanced photocatalytic activity. *Chemistry-A European Journal*, 16(30), 8993-8997.
60. Yongjing, L. F. G. (1999). Enhanced Rates of Photocatalytic Behavior Using WO<sub>3</sub>/TiO<sub>2</sub> Coupled Semiconductor Nanopowder [J]. *Chinese Journal Of Environmental Science*, 4.
61. Mohapatra, S. K., Banerjee, S., & Misra, M. (2008). Synthesis of Fe<sub>2</sub>O<sub>3</sub>/TiO<sub>2</sub> nanorod–nanotube arrays by filling TiO<sub>2</sub> nanotubes with Fe. *Nanotechnology*, 19(31), 315601.
62. Shaogui, Y., Xie, Q., Xinyong, L., Yazhi, L., Shuo, C., & Guohua, C. (2004). Preparation, characterization and photoelectrocatalytic properties of nanocrystalline Fe<sub>2</sub>O<sub>3</sub>/TiO<sub>2</sub>, ZnO/TiO<sub>2</sub>, and Fe<sub>2</sub>O<sub>3</sub>/ZnO/TiO<sub>2</sub> composite film electrodes towards pentachlorophenol degradation. *Physical Chemistry Chemical Physics*, 6(3), 659-664.
63. Marci, G., Augugliaro, V., Lopez-Munoz, M. J., Martin, C., Palmisano, L., Rives, V., & Venezia, A. M. (2001). Preparation characterization and photocatalytic activity of polycrystalline ZnO/TiO<sub>2</sub> systems. 1. Surface and bulk characterization. *The Journal of Physical Chemistry B*, 105(5), 1026-1032.

64. Marci, G., Augugliaro, V., Lopez-Munoz, M. J., Martin, C., Palmisano, L., Rives, V., ... & Venezia, A. M. (2001). Preparation characterization and photocatalytic activity of polycrystalline ZnO/TiO<sub>2</sub> systems. 2. Surface, bulk characterization, and 4-nitrophenol photodegradation in liquid-solid regime. *The Journal of Physical Chemistry B*, 105(5), 1033-1040.
65. Vinodgopal, K., Bedja, I., & Kamat, P. V. (1996). Nanostructured semiconductor films for photocatalysis. Photoelectrochemical behavior of SnO<sub>2</sub>/TiO<sub>2</sub> composite systems and its role in photocatalytic degradation of a textile azo dye. *Chemistry of materials*, 8(8), 2180-2187.
66. Hirano, M., & Ota, K. (2004). Preparation of photoactive anatase-type TiO<sub>2</sub>/silica gel by direct loading anatase-type TiO<sub>2</sub> nanoparticles in acidic aqueous solutions by thermal hydrolysis. *Journal of materials science*, 39(5), 1841-1844.
67. Hofstadler, K., Bauer, R., Novalic, S., & Heisler, G. (1994). New reactor design for photocatalytic wastewater treatment with TiO<sub>2</sub> immobilized on fused-silica glass fibers: photomineralization of 4-chlorophenol. *Environmental science & technology*, 28(4), 670-674.
68. Ding, Z., Hu, X., Lu, G. Q., Yue, P. L., & Greenfield, P. F. (2000). Novel silica gel supported TiO<sub>2</sub> photocatalyst synthesized by CVD method. *Langmuir*, 16(15), 6216-6222.
69. Anpo, M., Takeuchi, M., Ikeue, K., & Dohshi, S. (2002). Design and development of titanium oxide photocatalysts operating under visible and UV light irradiation.: The applications of metal ion-implantation techniques to semiconducting TiO<sub>2</sub> and Ti/zeolite catalysts. *Current Opinion in Solid State and Materials Science*, 6(5), 381-388.
70. Klaas, J., Schulz-Ekloff, G., & Jaeger, N. I. (1997). UV-visible diffuse reflectance spectroscopy of zeolite-hosted mononuclear titanium oxide species. *The Journal of Physical Chemistry B*, 101(8), 1305-1311.
71. Torimoto, T., Okawa, Y., Takeda, N., & Yoneyama, H. (1997). Effect of activated carbon content in TiO<sub>2</sub>-loaded activated carbon on photodegradation behaviors of dichloromethane. *Journal of Photochemistry and photobiology A: Chemistry*, 103(1), 153-157.
72. Arana, I., Dona-Rodriguez, J. M., Rendón, E. T., Cabo, C. G. I., Gonzalez-Diaz, O., Herrera-Melián, J. A., & Navio, J. A. (2003). TiO<sub>2</sub> activation by using activated carbon as a support-Part II. Photoreactivity and FTIR study. *Applied Catalysis B: Environmental*, 44(2), 153-160.
73. Matthews, R. W. (1987). Solar-electric water purification using photocatalytic oxidation with TiO<sub>2</sub> as a stationary phase. *Solar Energy*, 38(6), 405-413.
74. Mogyorósi, K., Farkas, A., Dékány, I., Ilisz, I., & Dombi, A. (2002). TiO<sub>2</sub>-based photocatalytic degradation of 2-chlorophenol adsorbed on hydrophobic clay. *Environmental science & technology*, 36(16), 3618-3624.

75. Cun, D., Lianyun, D., Chuanbao, W., Xianping, X., & Youchang, X. (1992). Preparation of Complex Support  $\text{TiO}_2/\gamma\text{-Al}_2\text{O}_3$  by Gas Phase Adsorption and State of  $\text{TiO}_2$  on  $\gamma\text{-Al}_2\text{O}_3$  Surface [J]. *Journal of Molecular Catalysis*, 1, 002.
76. Monneyron, P., Manero, M. H., Foussard, J. N., Benoit-Marquie, F., & Maurette, M. T. (2003). Heterogeneous photocatalysis of butanol and methyl ethyl ketone—characterization of catalyst and dynamic study. *Chemical engineering science*, 58(3), 971-978.
77. Kontos, G. A., Soulintzis, A. L., Karahaliou, P. K., Psarras, G. C., Georga, S. N., Krontiras, C. A., & Pisanias, M. N. (2007). Electrical relaxation dynamics in  $\text{TiO}_2$ —polymer matrix composites. *Express Polym Lett*, 1(12), 781-789.
78. Xue, C. H., Jia, S. T., Chen, H. Z., & Wang, M. (2008). Superhydrophobic cotton fabrics prepared by sol-gel coating of  $\text{TiO}_2$  and surface hydrophobization. *Science and Technology of Advanced Materials*, 9(3), 035001.
79. Mikula, M., Brezova, V., Čěppan, M., Pach, L., & Karpinský, L. (1995). Comparison of photocatalytic activity of sol-gel  $\text{TiO}_2$  and P25  $\text{TiO}_2$  particles supported on commercial fibreglass fabric. *Journal of materials science letters*, 14(9), 615-616.
80. Iguchi, Y., Ichiura, H., Kitaoka, T., & Tanaka, H. (2003). Preparation and characteristics of high performance paper containing titanium dioxide photocatalyst supported on inorganic fiber matrix. *Chemosphere*, 53(10), 1193-1199.
81. Ohno, T., Tsubota, T., Toyofuku, M., & Inaba, R. (2004). Photocatalytic activity of a  $\text{TiO}_2$  photocatalyst doped with  $\text{C}^{4+}$  and  $\text{S}^{4+}$  ions having a rutile phase under visible light. *Catalysis letters*, 98(4), 255-258.
82. Kim, S. W., Khan, R., Kim, T., & Kim, W. (2008). Synthesis, Characterization, and Application of Zr, S Co-doped  $\text{TiO}_2$  as Visible-light Active Photocatalyst. *BULLETIN-KOREAN CHEMICAL SOCIETY*, 29(6), 1217.
83. Hench, L. L., & West, J. K. (1990). The sol-gel process. *Chemical Reviews*, 90(1), 33-72.
84. Pajonk, G. M. (1991). Aerogel catalysts. *Applied Catalysis*, 72(2), 217-266.
85. Kistler, S.S. (1931) Coherent expanded aerogels and jellies. *Nature*, 127, 741.
86. Kemmere, M. F., & Meyer, T. (Eds.). (2006). *Supercritical carbon dioxide*. John Wiley & Sons.
87. Ertl, G., Knözinger, H., & Weitkamp, J. (Eds.). (2008). *Preparation of solid catalysts*. Wiley. com.
88. Anderson, M. T., Martin, J. E., Odinek, J. G., Newcomer, P. P., & Wilcoxon, J. P. (1997). Monolithic periodic mesoporous silica gels. *Microporous materials*, 10(1), 13-24.

89. Sunol, A. K., & Sunol, S. G. (2004). Templating Aerogels for Tunable Nanoporosity. In *Dekker Encyclopedia of Nanoscience and Nanotechnology* (pp. 3843-3851).
90. Zhang, Y., & Erkey, C. (2006). Preparation of supported metallic nanoparticles using supercritical fluids: a review. *The Journal of supercritical fluids*, 38(2), 252-267.
91. Yoda, S., Otake, K., Takebayashi, Y., Sugeta, T., & Sato, T. (2001). Effects of supercritical impregnation conditions on the properties of silica–titania aerogels. *Journal of non-crystalline solids*, 285(1), 8-12.
92. Kikic, I., & Vecchione, F. (2003). Supercritical impregnation of polymers. *Current Opinion in Solid State and Materials Science*, 7(4), 399-405.
93. Muth, O., Hirth, T., & Vogel, H. (2000). Polymer modification by supercritical impregnation. *The Journal of Supercritical Fluids*, 17(1), 65-72.
94. Cooper, A. I. (2000). Polymer synthesis and processing using supercritical carbon dioxide. *Journal of Materials Chemistry*, 10(2), 207-234.
95. Howdle, S. M., Ramsay, J. M., & Cooper, A. I. (1994). Spectroscopic analysis and in situ monitoring of impregnation and extraction of polymer films and powders using supercritical fluids. *Journal of Polymer Science Part B: Polymer Physics*, 32(3), 541-549.
96. Zhou, H., Fang, J., Yang, J., & Xie, X. (2003). Effect of the supercritical CO<sub>2</sub> on surface structure of PMMA/PS blend thin films. *The Journal of supercritical fluids*, 26(2), 137-145.
97. Morere, J., Tenorio, M. J., Torralvo, M. J., Pando, C., Renuncio, J. A. R., & Cabanas, A. (2011). Deposition of Pd into mesoporous silica SBA-15 using supercritical carbon dioxide. *The Journal of Supercritical Fluids*, 56(2), 213-222.
98. Zhang, J., Han, B., Hou, Z., Liu, Z., He, J., & Jiang, T. (2003). Novel method to load nanoparticles into mesoporous materials: Impregnation of MCM-41 with ZnS by compressed CO<sub>2</sub>. *Langmuir*, 19(18), 7616-7620.
99. Acda, M. N., Morrell, J. J., & Levien, K. L. (2001). Supercritical fluid impregnation of selected wood species with tebuconazole. *Wood science and technology*, 35(1-2), 127-136.
100. Serpone, N., & Emeline, A. V. (2002). Suggested terms and definitions in photocatalysis and radiocatalysis. *International Journal of Photoenergy*, 4(3), 91-131.
101. Salomon, R. G. (1983). Homogeneous metal-catalysis in organic photochemistry. *Tetrahedron*, 39(4), 485-575.
102. Linsebigler, A. L., Lu, G., & Yates Jr, J. T. (1995). Photocatalysis on TiO<sub>2</sub> surfaces: principles, mechanisms, and selected results. *Chemical Reviews*, 95(3), 735-758.

103. Kominami, H., Murakami, S. Y., Kato, J. I., Kera, Y., & Ohtani, B. (2002). Correlation between some physical properties of titanium dioxide particles and their photocatalytic activity for some probe reactions in aqueous systems. *The Journal of Physical Chemistry B*, 106(40), 10501-10507.
104. Reyes-Coronado, D., Rodriguez-Gattorno, G., Espinosa-Pesqueira, M. E., Cab, C., De Coss, R., & Oskam, G. (2008). Phase-pure TiO<sub>2</sub> nanoparticles: anatase, brookite and rutile. *Nanotechnology*, 19(14), 145605.S
105. Navrotsky, A., Jamieson, J. C., & Kleppa, O. J. (1967). Enthalpy of transformation of a high-pressure polymorph of titanium dioxide to the rutile modification. *Science*, 158(3799), 388-389.
106. Fujishima, A., Hashimoto, K., Watanabe, T. (1999) TiO<sub>2</sub> photocatalysis. Fundamentals and applications, 1st ed. Tokyo: BKC.
107. Halley, J. W., Kozlowski, M., Michalewicz, M., Smyrl, W., & Tit, N. (1991). Photoelectrochemical spectroscopy studies of titanium dioxide surfaces: theory and experiment. *Surface science*, 256(3), 397-408.
108. Bacsa, R. R., & Kiwi, J. (1998). Effect of rutile phase on the photocatalytic properties of nanocrystalline titania during the degradation of p-coumaric acid. *Applied Catalysis B: Environmental*, 16(1), 19-29.
109. Muggli, D. S., & Ding, L. (2001). Photocatalytic performance of sulfated TiO<sub>2</sub> and Degussa P-25 TiO<sub>2</sub> during oxidation of organics. *Applied Catalysis B: Environmental*, 32(3), 181-194.
110. Ohno, T., Sarukawa, K., Tokieda, K., & Matsumura, M. (2001). Morphology of a TiO<sub>2</sub> Photocatalyst (Degussa, P-25) Consisting of Anatase and Rutile Crystalline Phases. *Journal of Catalysis*, 203(1), 82-86.
111. Inel, Y., & Ökte, A. N. (1996). Photocatalytic degradation of malonic acid in aqueous suspensions of titanium dioxide: an initial kinetic investigation of CO<sub>2</sub> photogeneration. *Journal of Photochemistry and Photobiology A: Chemistry*, 96(1), 175-180.
112. Fox, M. A., & Dulay, M. T. (1993). Heterogeneous photocatalysis. *Chemical reviews*, 93(1), 341-357.
113. Lakshmi, B. B., Dorhout, P. K., & Martin, C. R. (1997). Sol-gel template synthesis of semiconductor nanostructures. *Chemistry of materials*, 9(3), 857-862.
114. Mann, S., Burkett, S. L., Davis, S. A., Fowler, C. E., Mendelson, N. H., Sims, S. D., ... & Whilton, N. T. (1997). Sol-gel synthesis of organized matter. *Chemistry of materials*, 9(11), 2300-2310.
115. Nguyen-Phan, T. D., Pham, H. D., Kim, S., Oh, E. S., Kim, E. J., & Shin, E. W. (2010). Surfactant removal from mesoporous TiO<sub>2</sub> nanocrystals by supercritical CO<sub>2</sub> fluid extraction. *Journal of Industrial and Engineering Chemistry*, 16(5), 823-828.

116. Fu, X., Zeltner, W. A., & Anderson, M. A. (1995). The gas-phase photocatalytic mineralization of benzene on porous titania-based catalysts. *Applied Catalysis B: Environmental*, 6(3), 209-224.
117. Klare, M., Scheen, J., Vogelsang, K., Jacobs, H., & Broekaert, J. A. C. (2000). Degradation of short-chain alkyl-and alkanolamines by TiO<sub>2</sub> and Pt/TiO<sub>2</sub> assisted photocatalysis. *Chemosphere*, 41(3), 353-362.
118. Blaková, A., Csölleová, L., & Brezova, V. (1998). Effect of light sources on the phenol degradation using Pt/TiO<sub>2</sub> photocatalysts immobilized on glass fibres. *Journal of Photochemistry and Photobiology A: Chemistry*, 113(3), 251-256.
119. Takeuchi, M., Tsujimaru, K., Sakamoto, K., Matsuoka, M., Yamashita, H., & Anpo, M. (2003). Effect of Pt loading on the photocatalytic reactivity of titanium oxide thin films prepared by ion engineering techniques. *Research on chemical intermediates*, 29(6), 619-629.
120. Bowker, M., James, D., Stone, P., Bennett, R., Perkins, N., Millard, L., ... & Dickinson, A. (2003). Catalysis at the metal-support interface: exemplified by the photocatalytic reforming of methanol on Pd/TiO<sub>2</sub>. *Journal of Catalysis*, 217(2), 427-433.
121. Moonsiri, M., Rangsunvigit, P., Chavadej, S., & Gulari, E. (2004). Effects of Pt and Ag on the photocatalytic degradation of 4-chlorophenol and its by-products. *Chemical Engineering Journal*, 97(2), 241-248.
122. Orlov, A., Jefferson, D. A., Macleod, N., & Lambert, R. M. (2004). Photocatalytic properties of TiO<sub>2</sub> modified with gold nanoparticles in the degradation of 4-chlorophenol in aqueous solution. *Catalysis letters*, 92(1-2), 41-47.
123. Orlov, A., Chan, M. S., Jefferson, D. A., Zhou, D., Lynch, R. J., & Lambert, R. M. (2006). Photocatalytic degradation of water-soluble organic pollutants on TiO<sub>2</sub> modified with gold nanoparticles. *Environmental technology*, 27(7), 747-752.
124. Sakatani, Y.; Koike, H. 2001, Japan Patent, P2001-72419A,.
125. Ihara, T., Ando, M., & Sugihara, S. (2001). Preparation of visible light active TiO<sub>2</sub> photocatalysis using wet method. *Photocatalysis*, 5, 19.
126. Asahi, R., Morikawa, T., Ohwaki, T., Aoki, K., & Taga, Y. (2001). Visible-light photocatalysis in nitrogen-doped titanium oxides. *science*, 293(5528), 269-271.
127. Irie, H., Watanabe, Y., & Hashimoto, K. (2003). Carbon-doped anatase TiO<sub>2</sub> powders as a visible-light sensitive photocatalyst. *Chemistry Letters*, 32(8), 772-773.
128. Lettmann, C., Hildenbrand, K., Kisch, H., Macyk, W., & Maier, W. F. (2001). Visible light photodegradation of 4-chlorophenol with a coke-containing titanium dioxide photocatalyst. *Applied Catalysis B: Environmental*, 32(4), 215-227.

129. Chen, C., Long, M., Zeng, H., Cai, W., Zhou, B., Zhang, J., ... & Wu, D. (2009). Preparation, characterization and visible-light activity of carbon modified TiO<sub>2</sub> with two kinds of carbonaceous species. *Journal of Molecular Catalysis A: Chemical*, 314(1), 35-41.
130. Sakthivel, S.; Kisch, H., (2003) Daylight photocatalysis by carbon-modified titanium dioxide' *Angewandte Chemie*, International Edition, 42, 4908
131. Umebayashi, T., Yamaki, T., Itoh, H., & Asai, K. (2002). Band gap narrowing of titanium dioxide by sulfur doping. *Applied Physics Letters*, 81(3), 454-456.
132. Ohno, T., Akiyoshi, M., Umebayashi, T., Asai, K., Mitsui, T., & Matsumura, M. (2004). Preparation of S-doped TiO<sub>2</sub> photocatalysts and their photocatalytic activities under visible light. *Applied Catalysis A: General*, 265(1), 115-121.
133. Choi WY, Termin A, Hoffmann MR. (1994)The role of metal ion dopants in quantum-sized TiO<sub>2</sub>: correlation between photoreactivity and charge carrier recombination dynamics. *J Phys Chem* 84:13669–79.
134. Serpone, N., Maruthamuthu, P., Pichat, P., Pelizzetti, E., & Hidaka, H. (1995). Exploiting the interparticle electron transfer process in the photocatalysed oxidation of phenol, 2-chlorophenol and pentachlorophenol: chemical evidence for electron and hole transfer between coupled semiconductors. *Journal of Photochemistry and Photobiology A: Chemistry*, 85(3), 247-255.
135. Doong RA, Chen CH, Maithreepala RA, Chang SM. (2001) The influence of pH and cadmium sulfide on the photocatalytic degradation of 2-chlorophenol in titanium dioxide suspensions. *Water Res* ;35(12): 2873–80
136. Zou, Z., Liu, Y., Li, H., Liao, Y., & Xie, C. (2010). Synthesis of TiO<sub>2</sub>/WO<sub>3</sub>/MnO<sub>2</sub> composites and high-throughput screening for their photoelectrical properties. *Journal of Combinatorial Chemistry*, 12(3), 363-369.
137. Chen, D., Zhang, H., Hu, S., & Li, J. (2008). Preparation and enhanced photoelectrochemical performance of coupled bicomponent ZnO-TiO<sub>2</sub> nanocomposites. *The Journal of Physical Chemistry C*, 112(1), 117-122.
138. Davis, R. J., & Liu, Z. (1997). Titania-silica: a model binary oxide catalyst system. *Chemistry of materials*, 9(11), 2311-2324.
139. Shiyanovskaya, I., & Hepel, M. (1999). Bicomponent WO<sub>3</sub>/TiO<sub>2</sub> Films as Photoelectrodes. *Journal of the Electrochemical Society*, 146(1), 243-249.
140. Lin, C. F., Wu, C. H., & Onn, Z. N. (2008). Degradation of 4-chlorophenol in TiO<sub>2</sub>, WO<sub>3</sub>, SnO<sub>2</sub>, TiO<sub>2</sub>/WO<sub>3</sub> and TiO<sub>2</sub>/SnO<sub>2</sub> systems. *Journal of hazardous materials*, 154(1-3), 1033-1039.
141. Chai, S. Y., Kim, Y. J., & Lee, W. I. (2006). Photocatalytic WO<sub>3</sub>/TiO<sub>2</sub> nanoparticles working under visible light. *Journal of electroceramics*, 17(2-4), 909-912.

142. Song, K. Y., Park, M. K., Kwon, Y. T., Lee, H. W., Chung, W. J., & Lee, W. I. (2001). Preparation of transparent particulate MoO<sub>3</sub>/TiO<sub>2</sub> and WO<sub>3</sub>/TiO<sub>2</sub> films and their photocatalytic properties. *Chemistry of materials*, 13(7), 2349-2355.
143. Ohno, T., Miyamoto, Z., Nishijima, K., Kanemitsu, H., & Xueyuan, F. (2006). Sensitization of photocatalytic activity of S-or N-doped TiO<sub>2</sub> particles by adsorbing Fe<sup>3+</sup> cations. *Applied Catalysis A: General*, 302(1), 62-68.
144. Ohno, T. (2006). Development of visible light sensitive TiO<sub>2</sub> photocatalysts and their sensitization using Fe<sup>3+</sup> ions. *Journal of the Japan Petroleum Institute*, 49(4), 168-176.
145. Li, H., Sunol, S. G., & Sunol, A. K. (2012). Development of titanium-dioxide-based aerogel catalyst with tunable nanoporosity and photocatalytic activity. *Nanotechnology*, 23(29), 294012.
146. Perrut, Michel, (1994) Advances in Supercritical Fluid Chromatographic Process, *Journal of Chromatography A*, 658, 293-313.
147. Chordia, L; Martinez, J.L., (2002) What's So Hot About Supercritical Fluids? *Laboratory Focus*, Vol. 6, No. 1
148. Teja, A.S., Eckert, C.A., (2000) Commentary on Supercritical Fluids: Research and Applications, *Ind. Eng. Chem. Res.*, 39, 4442-4444.
149. Taylor, L. T., (1996) *Supercritical Fluids Extraction*, John Wiley and Sons, New York
150. Peng, D. Y., & Robinson, D. B. (1976). A new two-constant equation of state. *Industrial & Engineering Chemistry Fundamentals*, 15(1), 59-64.
151. Falk, R., Randolph, T. W., Meyer, J. D., Kelly, R. M., & Manning, M. C. (1997). Controlled release of ionic compounds from poly (L-lactide) microspheres produced by precipitation with a compressed antisolvent. *Journal of controlled release*, 44(1), 77-85.
152. Young, T. J., Johnston, K. P., Mishima, K., & Tanaka, H. (1999). Encapsulation of lysozyme in a biodegradable polymer by precipitation with a vapor-over-liquid antisolvent. *Journal of pharmaceutical sciences*, 88(6), 640-650
153. Reverchon, E. (1999). Supercritical antisolvent precipitation of micro-and nano-particles. *The journal of supercritical fluids*, 15(1), 1-21.
154. Rantakylä, M., Jäntti, M., Aaltonen, O., & Hurme, M. (2002). The effect of initial drop size on particle size in the supercritical antisolvent precipitation (SAS) technique. *The Journal of Supercritical Fluids*, 24(3), 251-263.
155. Chang, C. J., Day, C. Y., Ko, C. M., & Chiu, K. L. (1997). Densities and P-x-y diagrams for carbon dioxide dissolution in methanol, ethanol, and acetone mixtures. *Fluid Phase Equilibria*, 131(1), 243-258

156. Day, C. Y., Chang, C. J., & Chen, C. Y. (1996). Phase equilibrium of ethanol+ CO<sub>2</sub> and acetone+ CO<sub>2</sub> at elevated pressures. *Journal of Chemical & Engineering Data*, 41(4), 839-843.
157. Perrut, M. (2000). Supercritical fluid applications: Industrial developments and economic issues. *Industrial & engineering chemistry research*, 39(12), 4531-4535.
158. Brinker, C. Jeffery; Smith, Douglas M.; Desphande, Ravindra, (1992) Preparation of low-density aerogels at ambient pressure, *Materials Research Society*, 271, 567-572.
159. Kistler, S. S., (1932) Coherent Expanded Aerogels, *Journal of Physical Chemistry*, vol. 36, 1932, 52-64.
160. Tewari, Param H.; Hunt, Arlon J. and Lofftus, Kevin D., (1985) Ambient-Temperature Supercritical Drying of Transparent Silica Aerogels, *Materials letters*, 3, No.9-10, 363-367.
161. Saus, W., Knittel, D., & Schollmeyer, E. (1993). Dyeing of textiles in supercritical carbon dioxide. *Textile Research Journal*, 63(3), 135-142.
162. Knittel, D., Saus, W., & Schollmeyer, E. (1993). Application of supercritical carbon dioxide in finishing processes. *Journal of the Textile Institute*, 84(4), 534-552.
163. Kazarian, S. G., Brantley, N. H., West, B. L., Vincent, M. F., & Eckert, C. A. (1997). In situ spectroscopy of polymers subjected to supercritical CO<sub>2</sub>: Plasticization and dye impregnation. *Applied Spectroscopy*, 51(4), 491-494
164. Ngo, T. T., Liotta, C. L., Eckert, C. A., & Kazarian, S. G. (2003). Supercritical fluid impregnation of different azo-dyes into polymer: in situ UV/Vis spectroscopic study. *The Journal of supercritical fluids*, 27(2), 215-221
165. Kikic, I., & Vecchione, F. (2003). Supercritical impregnation of polymers. *Current Opinion in Solid State and Materials Science*, 7(4), 399-405.
166. Muth, O., Hirth, T., & Vogel, H. (2000). Polymer modification by supercritical impregnation. *The Journal of Supercritical Fluids*, 17(1), 65-72.
167. Rest, A.J., (1990) "Infra Dig Matrix Media", *J. Mol. Struct.*, 222, 87-93.
168. Yoda, S., Hasegawa, A., Suda, H., Uchimaru, Y., Haraya, K., Tsuji, T., & Otake, K. (2004). Preparation of a platinum and palladium/polyimide nanocomposite film as a precursor of metal-doped carbon molecular sieve membrane via supercritical impregnation. *Chemistry of materials*, 16(12), 2363-2368.
169. Lucas, S., González, E., Calvo, M. P., Palencia, C., Alonso, E., & Cocero, M. J. (2007). Supercritical CO<sub>2</sub> impregnation of Radiata pine with organic fungicides: Effect of operating conditions and two-parameters modeling. *The Journal of supercritical fluids*, 40(3), 462-469.

170. Kazarian, S. G., & Martirosyan, G. G. (2002). Spectroscopy of polymer/drug formulations processed with supercritical fluids: in situ ATR-IR and Raman study of impregnation of ibuprofen into PVP. *International journal of pharmaceuticals*, 232(1), 81-90.
171. Braga, M. E., Pato, M. T. V., Silva, H. S., Ferreira, E. I., Gil, M. H., Duarte, C. M., & de Sousa, H. C. (2008). Supercritical solvent impregnation of ophthalmic drugs on chitosan derivatives. *The Journal of Supercritical Fluids*, 44(2), 245-257.
172. Yoda, S., Takebayashi, Y., Sugeta, T., & Otake, K. (2004). Platinum-silica aerogels via supercritical drying and impregnation. *Journal of non-crystalline solids*, 350, 320-325.
173. Yoda, S., Ohtake, K., Takebayashi, Y., Sugeta, T., Sako, T., & Sato, T. (2000). Preparation of SiO<sub>2</sub>-TiO<sub>2</sub> aerogels using supercritical impregnation. *Journal of Sol-Gel Science and Technology*, 19(1-3), 719-723.
174. McHugh, M. A., Seckner, A. J., & Yogan, T. J. (1984). High-pressure phase behavior of binary mixtures of octacosane and carbon dioxide. *Industrial & engineering chemistry fundamentals*, 23(4), 493-499.
175. Penninger, J. M., McHugh, M. A., Radosz, M., & Krukoniš, V. J. (1985). Supercritical fluid technology.
176. Kiszka, M. B., Meilchen, M. A., & McHugh, M. A. (1988). Modeling high-pressure gas-polymer mixtures using the Sanchez-Lacombe equation of state. *Journal of applied polymer science*, 36(3), 583-597.
177. McHugh, M. A., & Krukoniš, V. J. (1986). Supercritical fluid extraction. Principles and practice.
178. Smeltzer, Brandon, (2005) Solubility of Surfactant Templates and Inorganic Complexes in Supercritical Carbon Dioxide Solutions, *Master's Thesis*, University of South Florida
179. Bradley, D. C., (1989) Metal alkoxides as precursors for electronic and ceramic materials, *Chemical Reviews*, vol. 89, 1317-1322.
180. Livage, J.; Henry, M. and Sanchez, C., (1988) Sol-gel chemistry of transition metal oxides, *Progress in Solid State Chemistry*, v 18, 259-341
181. Scherer, George W. and Brinker, C. Jeffery, (1990) Sol-Gel Science The Physical and Chemistry of Sol-Gel Processing, Academic press, New York.
182. Yao, Nan; Xiong, Guoxing; Yuhong; He, Mingyuan and Yang, Weishen, (2001) Preparation of novel uniform mesoporous alumina catalysts by the sol-gel method, *Catalysis Today*, vol. 68, 97-109.
183. Wijngaarden, R. J.; Kronberg A. and Westerterp K. R., (1998) Industrial catalysis Optimizing Catalysts and Processes, Wiley-VCH,.

184. Suh, Dong Jin and Park, Tae-Jin, (1996) sol-gel strategies for pore control of high-surface-area transition-metal oxide aerogels”, *Chemistry of Materials*, vol. 8, 509-513.
185. Ying, J.V.; Mehnert, C.P.; Wong, M.S. (1999), Synthesis and Applications of Supramolecular-templated Mesoporous Materials, *Angew. Chem., Intl. Ed.*, 38, 56-77.
186. Gerbeleu, N.V.; Arion, V.B. and Burgess, J., (1999) Template Synthesis of Macrocyclic Compounds, Wiley-VCH
187. Pinnavaia, Thomas and Tanev, P. T., (1995), A neutral templating route to mesoporous molecular sieves”, *Science*, 267, 865-867
188. Liu, J.; Han, B.; Li, G.; Zhang, X.; He, J.; Liu, Z. (2001), Investigation of non-ionic surfactant dynol-604 based reverse microemulsions formed in supercritical carbon dioxide. *Langmuir*, 17, 8040-8043.
189. Liu, J.; Han, B.; Li, G.; Liu, Z.; He, J.; Yang, G. (2001) Solubility of the non-ionic surfactant tetraethylene glycol n-laurel ether in supercritical CO<sub>2</sub> with n-pentanol. *Fluid Phase Equilibria*, 187-188, 247-254.
190. Al-Ghamdi, A.; Carvallo, R.; Sunol, S.G.; Sunol, A.K. (2003) Supercritical Fluid Aided Synthesis of Surfactant Templated Aerogels. *AIChE Annual Meeting*, San Francisco, CA, Nov. 16-22
191. Golubko, N. V., Yanovskaya, M. I., Romm, I. P., & Ozerin, A. N. (2001). Hydrolysis of titanium alkoxides: thermochemical, electron microscopy, saxs studies. *Journal of sol-gel science and technology*, 20(3), 245-262.
192. Li, H (2005) Supercritical Carbon Dioxide Aided Preparation of Nickel Oxide/Alumina Aerogel Catalyst, *Master Thesis*
193. Caruso, R. A., & Schattka, J. H. (2000). Cellulose acetate templates for porous inorganic network fabrication. *Advanced Materials*, 12(24), 1921-1923.
194. Brunauer, S., Emmett, P. H., & Teller, E. (1938). Adsorption of gases in multimolecular layers. *Journal of the American Chemical Society*, 60(2), 309-319.
195. Barrett, E. P., Joyner, L. G., & Halenda, P. P. (1951). The determination of pore volume and area distributions in porous substances. I. Computations from nitrogen isotherms. *Journal of the American Chemical Society*, 73(1), 373-380.
196. LaMer, V. K., & Dinegar, R. H. (1950). Theory, production and mechanism of formation of monodispersed hydrosols. *Journal of the American Chemical Society*, 72(11), 4847-4854.
197. Yao, N.; Xiong, G.; He, Y.M.; Yang, W. (2001) Preparation of novel mesoporous alumina catalysts by the sol-gel method. *Catalysis Today*, 68, 97-109.

198. Chany-Yih Day, & Chang, Chiehming J. & Chen, Chiu-Yang. (1996). Phase Equilibrium of Ethanol + CO<sub>2</sub> and Acetone + CO<sub>2</sub> Elevated Pressures. *The Journal of Chemical and Engineering Data*, 41, 839-843.
199. Hanaor, Dorian A. H.; Sorrell, Charles C. (2011). "Review of the anatase to rutile phase transformation". *Journal of Materials Science* 46 (4): 855–874.
200. Gribb, A. A., & Banfield, J. F. (1997). Particle size effects on transformation kinetics and phase stability in nanocrystalline TiO<sub>2</sub>. *American Mineralogist*, 82(7), 717-728.
201. De Boer, J. H., & Lippens, B. (1964). Studies on pore systems in catalysts II. The shapes of pores in aluminum oxide systems. *Journal of Catalysis*, 3(1), 38-43.
202. Sunol, A. K. (1992). *U.S. Patent No. 5,169,687*. Washington, DC: U.S. Patent and Trademark Office.
203. Kluson, P., Kacer, P., Cajthaml, T., & Kalaji, M. (2001). Preparation of titania mesoporous materials using a surfactant-mediated sol-gel method. *J. Mater. Chem.*, 11(2), 644-651.
204. Lu, X.B.; Zhang, W.H.; He, R. (2002) Simultaneous removal of surfactant template from MCM-41 and implantation of transition metal complexes into mesopores with supercritical fluid. *Chinese Chemical Letters*, 13(5), 480-483.
205. Tsang, S.C.; Yu, K.M.K.; Steele, A.M.; Zhu, J.; Fu, Q.J. (2003) Solid supported micellar catalysis: some syntheses and characterizations. *Catalysis Today*, 81, 573-591.
206. Wakayama, H., Goto, Y., & Fukushima, Y. (2003). A novel method for tailoring porous structures of nanoporous materials using supercritical solvents. *Physical Chemistry Chemical Physics*, 5(17), 3784-3788.
207. Gupta, R. B., & Shim, J. J. (2006). *Solubility in supercritical carbon dioxide*. CRC press. 351-354
208. Kim, J., Kim, H. R., & Choung, S. J. (2011). The characterization and hydrogen production from water decomposition with methanol in a semi-batch type reactor using In, P-TiO<sub>2</sub> s. *International Journal of Photoenergy*, 2011.
209. Zeng, Q. G., Ding, Z. J., & Zhang, Z. M. (2007). Observation of an ultraviolet emission band in TiO<sub>2</sub> nanocrystals doped with Eu<sup>3+</sup>. *Journal of materials science*, 42(11), 3778-3782.
210. Luu, C. L., Nguyen, Q. T., & Ho, S. T. (2010). Synthesis and characterization of Fe-doped TiO<sub>2</sub> photocatalyst by the sol-gel method. *Advances in Natural Sciences: Nanoscience and Nanotechnology*, 1(1), 015008.
211. Vijayan, B. K., Dimitrijevic, N. M., Wu, J., & Gray, K. A. (2010). The effects of Pt doping on the structure and visible light photoactivity of titania nanotubes. *The Journal of Physical Chemistry C*, 114(49), 21262-21269

212. Gemelli, E., & Camargo, N. H. A. (2007). Oxidation kinetics of commercially pure titanium. *Revista matéria*, 12(3), 525-531.
213. Ramakrishna, S., Jose, R., Archana, P. S., Nair, A. S., Balamurugan, R., Venugopal, J., & Teo, W. E. (2010). Science and engineering of electrospun nanofibers for advances in clean energy, water filtration, and regenerative medicine. *Journal of materials science*, 45(23), 6283-6312.
214. Wang, J., Li, R., Zhang, Z., Sun, W., Wang, X., Xu, R., ... & Zhang, X. (2008). Degradation of hazardous dyes in wastewater using nanometer mixed crystal TiO<sub>2</sub> powders under visible light irradiation. *Water, Air, and Soil Pollution*, 189(1-4), 225-237.
215. Subramanian, V., Wolf, E. E., & Kamat, P. V. (2004). Catalysis with TiO<sub>2</sub>/gold nanocomposites. Effect of metal particle size on the Fermi level equilibration. *Journal of the American Chemical Society*, 126(15), 4943-4950.
216. Kundu, S., Ciston, J., Senanayake, S. D., Arena, D. A., Fujita, E., Stacchiola, D., ... & Rodriguez, J. A. (2012). Exploring the Structural and Electronic Properties of Pt/Ceria-Modified TiO<sub>2</sub> and Its Photocatalytic Activity for Water Splitting under Visible Light. *The Journal of Physical Chemistry C*, 116(26), 14062-14070.
217. Colón, G., Maicu, M., Hidalgo, M. C., Navío, J. A., Kubacka, A., & Fernández-García, M. (2010). Gas phase photocatalytic oxidation of toluene using highly active Pt doped TiO<sub>2</sub>. *Journal of Molecular Catalysis A: Chemical*, 320(1), 14-18.
218. Matthews, R. W. (1987). Photooxidation of organic impurities in water using thin films of titanium dioxide. *Journal of Physical Chemistry*, 91(12), 3328-3333.
219. Matthews, R. W. (1988). Kinetics of photocatalytic oxidation of organic solutes over titanium dioxide. *Journal of Catalysis*, 111(2), 264-272.
220. Matthews, R. W. (1989). Photocatalytic oxidation and adsorption of methylene blue on thin films of near-ultraviolet-illuminated TiO<sub>2</sub>. *J. Chem. Soc., Faraday Trans. 1*, 85(6), 1291-1302.
221. Do, Y. R., Lee, W., Dwight, K., & Wold, A. (1994). The Effect of WO<sub>3</sub> on the Photocatalytic Activity of TiO<sub>2</sub>. *Journal of Solid State Chemistry*, 108(1), 198-201.

## APPENDICES

## Appendix A: Nomenclature

Å	Angstrom ( $10^{-10}$ m)
atm%	Atomic Percentage
APD	Average Pore Diameter
ASM	As-made
BET	Brunauer-Emmett-Teller Surface Area Analysis
BJH	Barrett-Joyner-Halenda Pore Size Distribution
C	Concentration
CAL	Calcined
CB	Conduction Band
DRS	Diffuse Reflectance Spectroscopy
EDS	Energy-Dispersion X-ray Spectroscopy
$e^- - h^+$	Negative Charged Electron and Positive Charged Hole Pair
EOS	Equation of State
EtOH	Ethanol
eV	Electron Volt
$Fe_2O_3$	Iron Oxide
FIB	Focused Ion Beam
FWHM	Full Width at Half Maximum
HPLC	High Performance Liquid Chromatography
MB	Methylene Blue
mol%	Molar Percentage
M.W.	Molecular Weight
MSDS	Material Safety Data Sheet
NHE	Normal Hydrogen Electrode

## Appendix A (Cont.)

P	Pressure
$P_c$	Critical Pressure
PCA	Photocatalyst Activity
PI	Pressure Indicator
SCCO <sub>2</sub>	Supercritical Carbon Dioxide
SCF	Supercritical Fluid
SFE	Supercritical Extraction
SFI	Supercritical Fluid Impregnation
SSA	Specific Surface Area
SEM	Scanning Electron Microscopy
$t$	Time
T	Temperature
$T_c$	Critical Temperature
TI	Temperature Indicator
TiO <sub>2</sub>	Titania, Titanium Dioxide
Ti(OBu) <sub>4</sub>	Titanium Butoxide
TSA	Total Surface Area
TPV	Total Pore Volume
UV	Ultraviolet
VB	Valence Band
Vis	Visible
Vol	Volume
WO <sub>3</sub>	Tungsten Oxide
wt%	Weight Percentage
$x$	Mole Fraction

## Appendix A (Cont.)

XPS X-ray Photoelectron Spectroscopy

XRD X-ray Diffraction Spectroscopy

$\gamma$  Solubility

$\lambda$  Wavelength

$\rho$  Density

## Appendix B: Textural Properties Analysis Results

The BET isotherm plots and BJH desorption  $D(v)$  pore size distribution plots of various samples show as following.

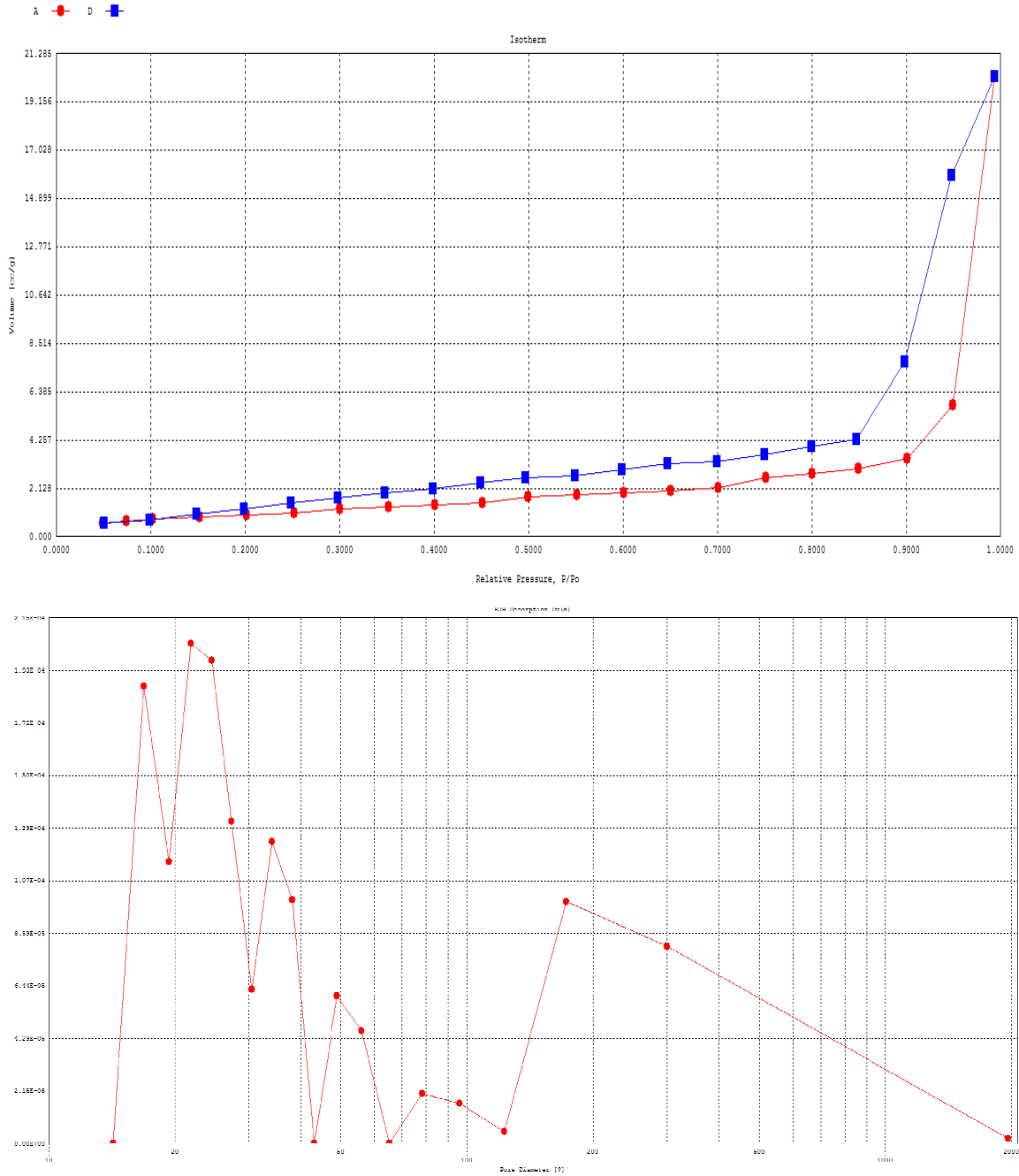
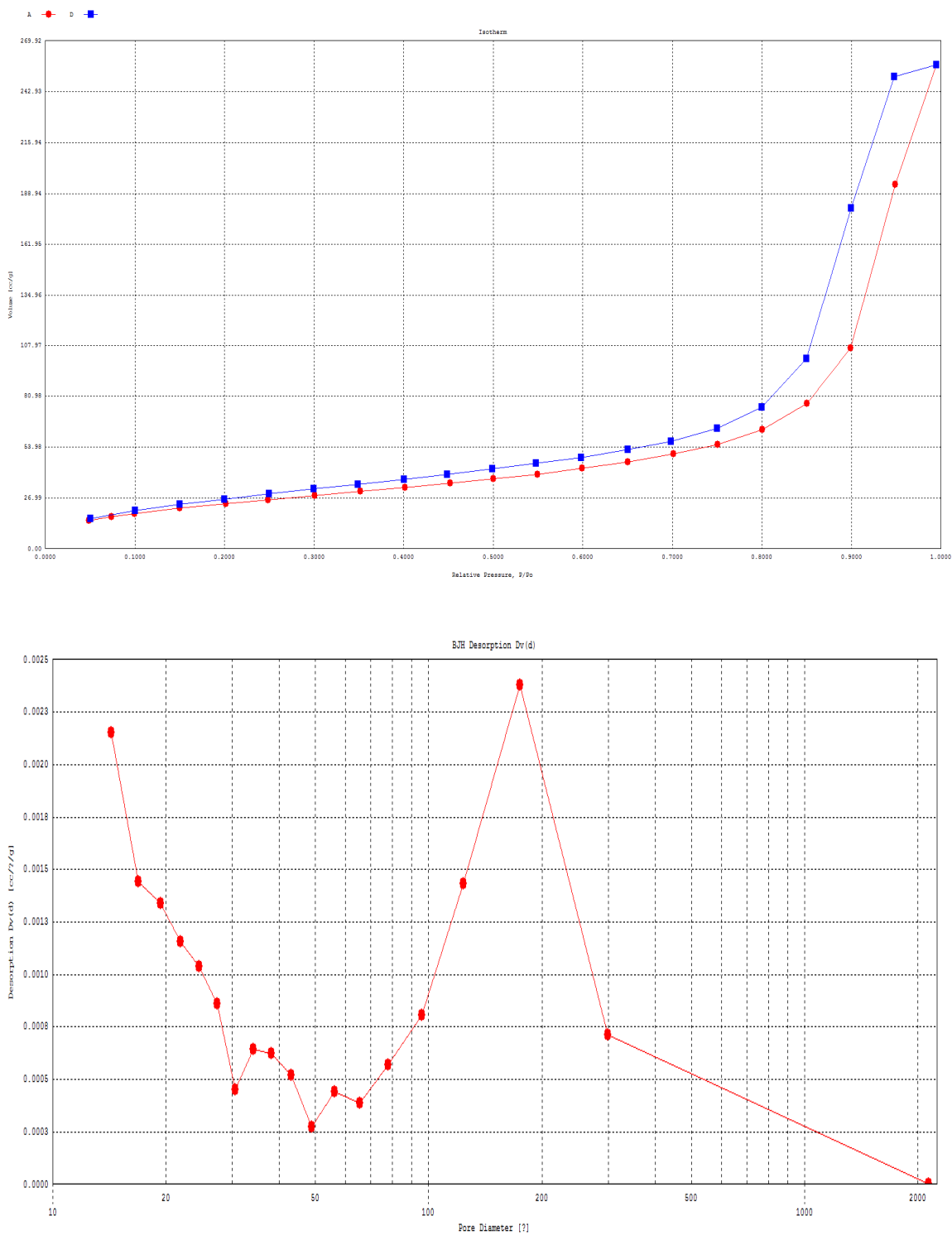


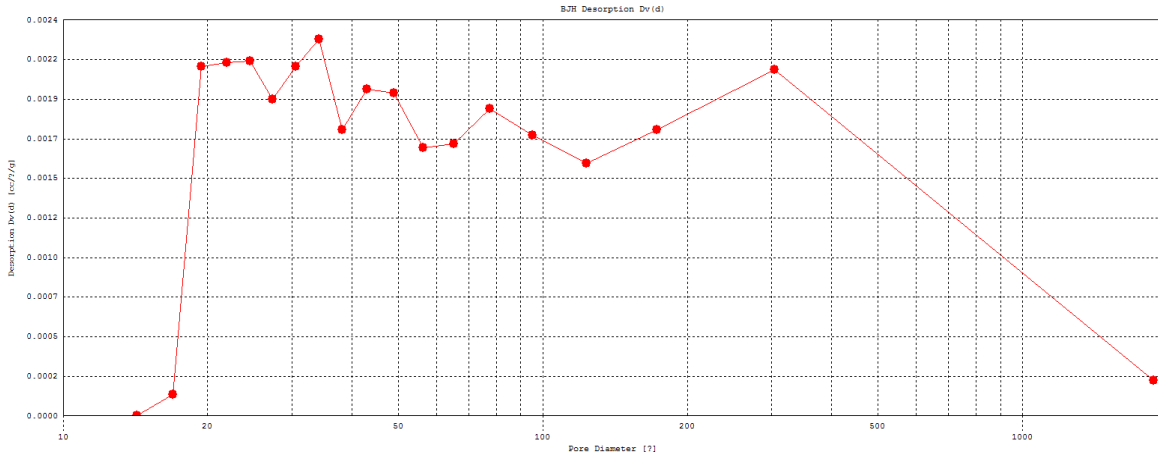
Figure B.1 BET and BJH Plots of TiO<sub>2</sub> Aerogel after Aging 120 Hours

## Appendix B (Cont.)

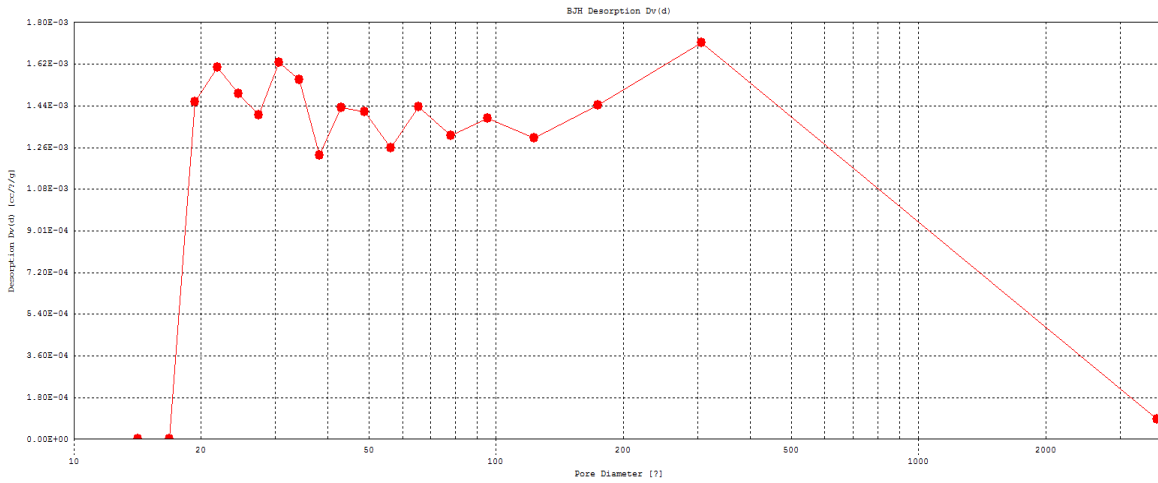


**Figure B.2 BET and BJH Plots of TiO<sub>2</sub> Aerogel after Supercritical Extraction and Drying (8 hours @ R<sub>CO<sub>2</sub></sub> = 5 ml/min)**

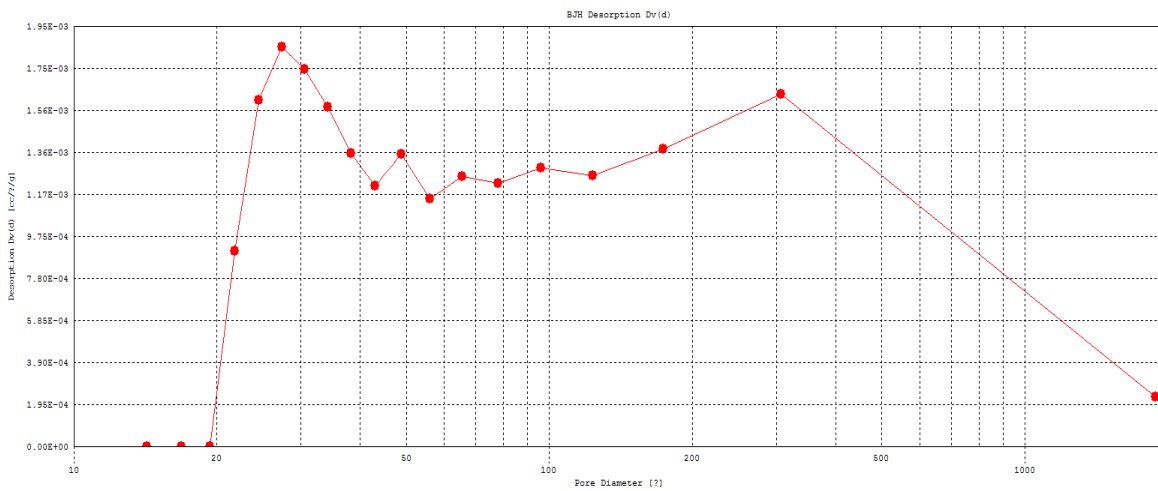
**Appendix B (Cont.)**



**(a)**



**(b)**



**(c)**

**Figure B.3 BJH Pore Size Distribution Plots of TiO<sub>2</sub> Aerogel at Different Calcination Temperature (a: 350 °C; b: 400 °C; c: 450 °C)**

**Appendix B (Cont.)**

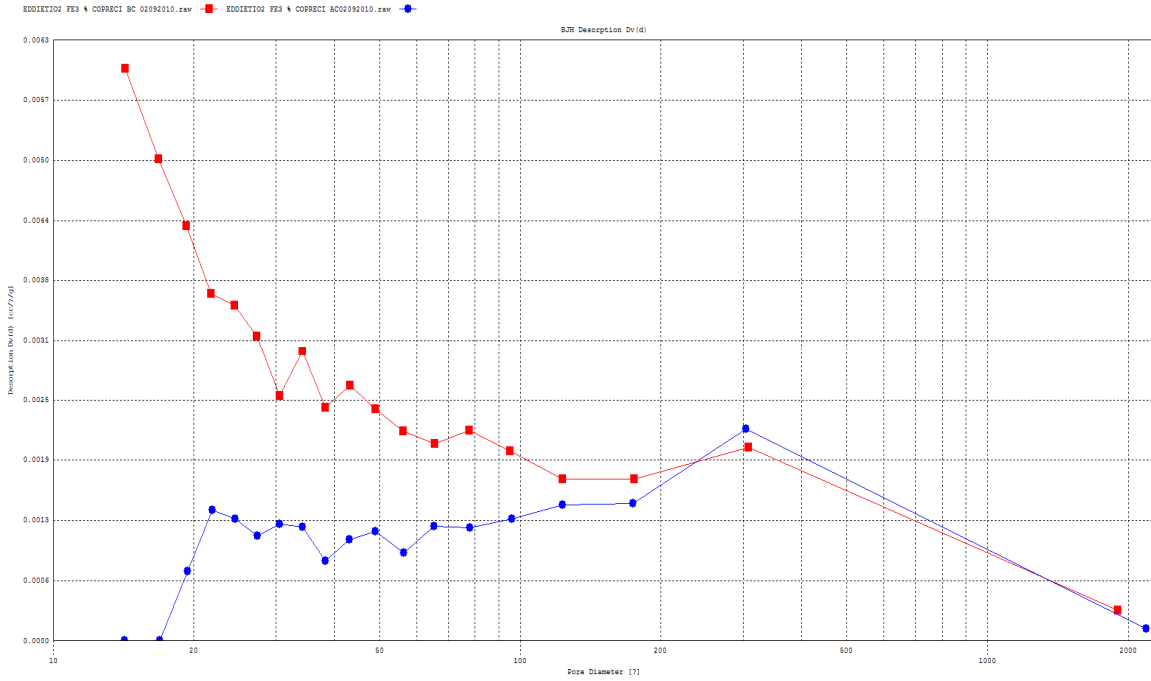


**Figure B.4 BJH Pore Size Distribution Plots of TiO<sub>2</sub>/Fe<sup>3+</sup> 3 mol% Aerogel (Uncalcined (Red) and Calcined (Blue))**

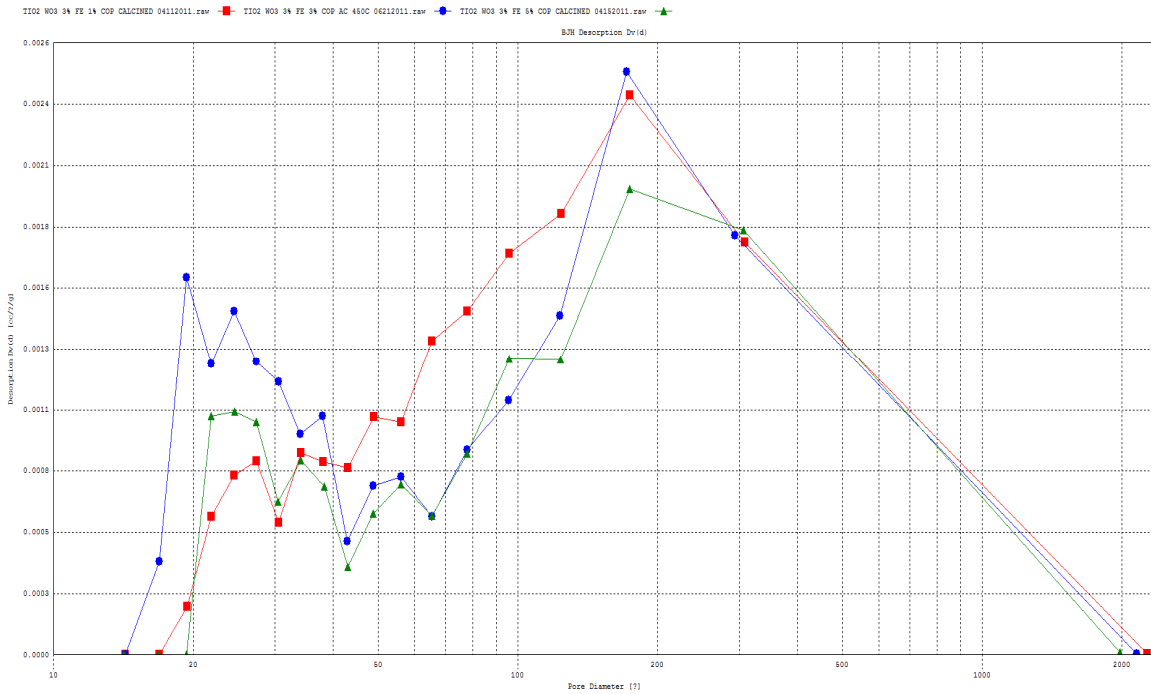


**Figure B.5 BJH Pore Size Distribution Plots of TiO<sub>2</sub>/3%WO<sub>3</sub>/Fe<sup>3+</sup> Aerogel with Different Amount of Iron Ion (1% (Red), 3% (Blue), and 5% (Green))**

## Appendix B (Cont.)

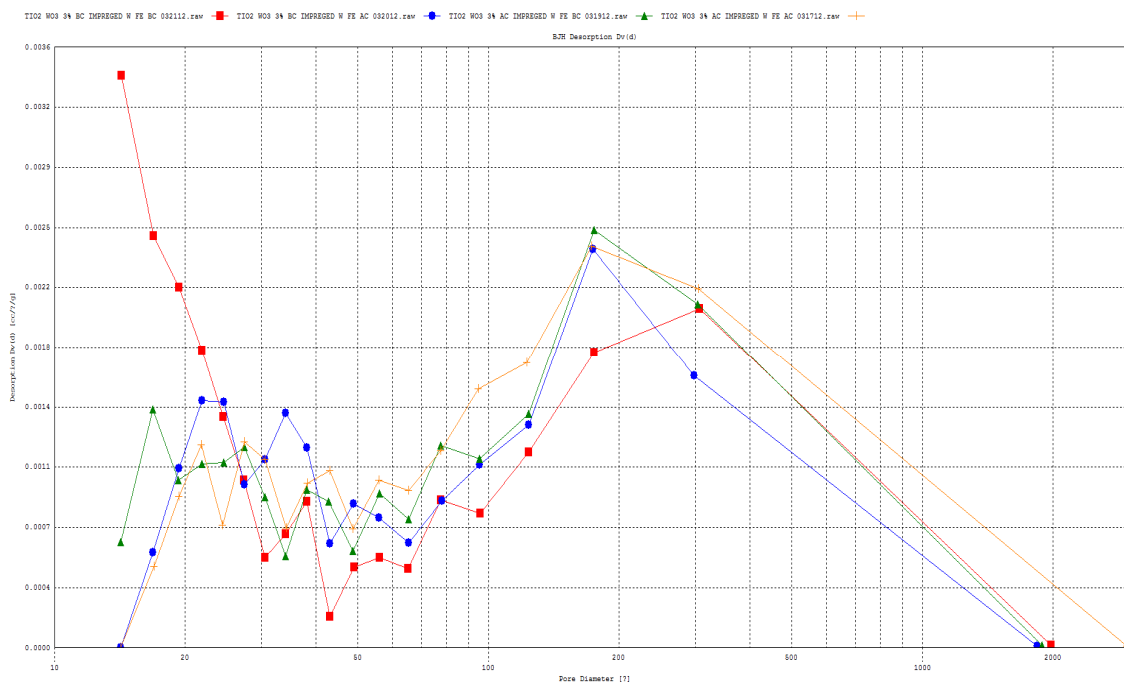


**Figure B.6 BJH Pore Size Distribution Plots of Different Titania Based Photocatalysts under Different Conditions (TiO<sub>2</sub>/WO<sub>3</sub> Uncalcined+SFI Uncalcined(Red), TiO<sub>2</sub>/WO<sub>3</sub> Uncalcined+SFI Calcined (Blue), TiO<sub>2</sub>/WO<sub>3</sub> Calcined+SFI Uncalcined (Green) and TiO<sub>2</sub>/WO<sub>3</sub> Calcined+SFI Calcined(Orange))**

## Appendix C: Additional XPS Surveys Patterns

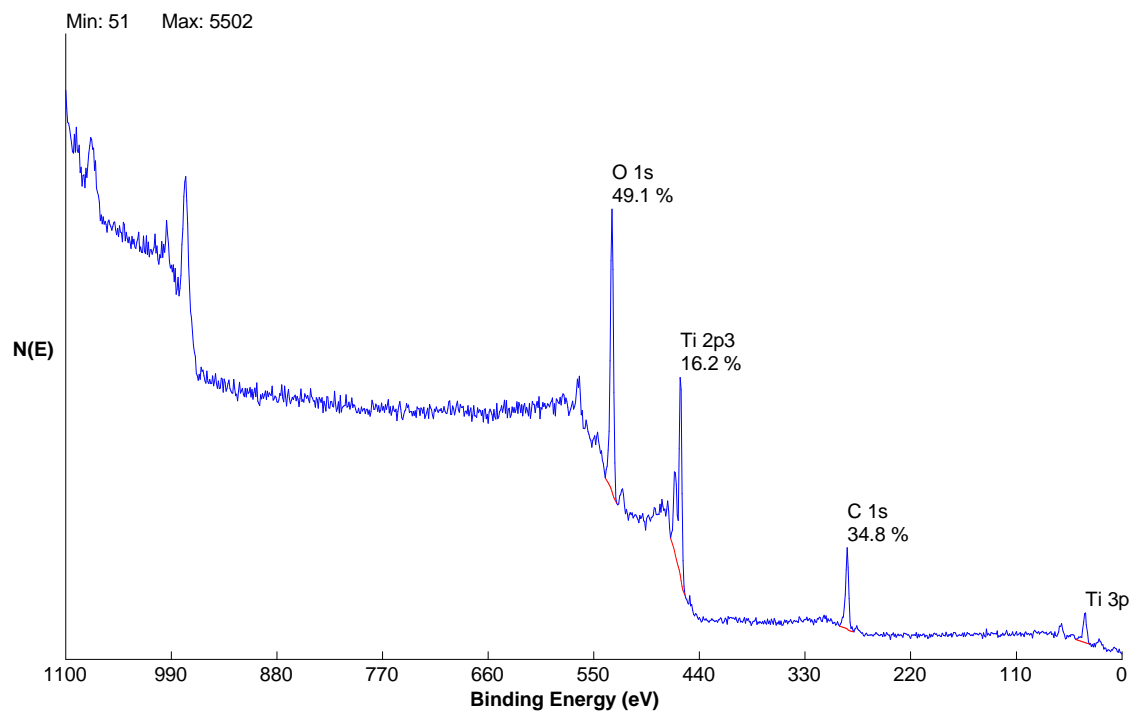
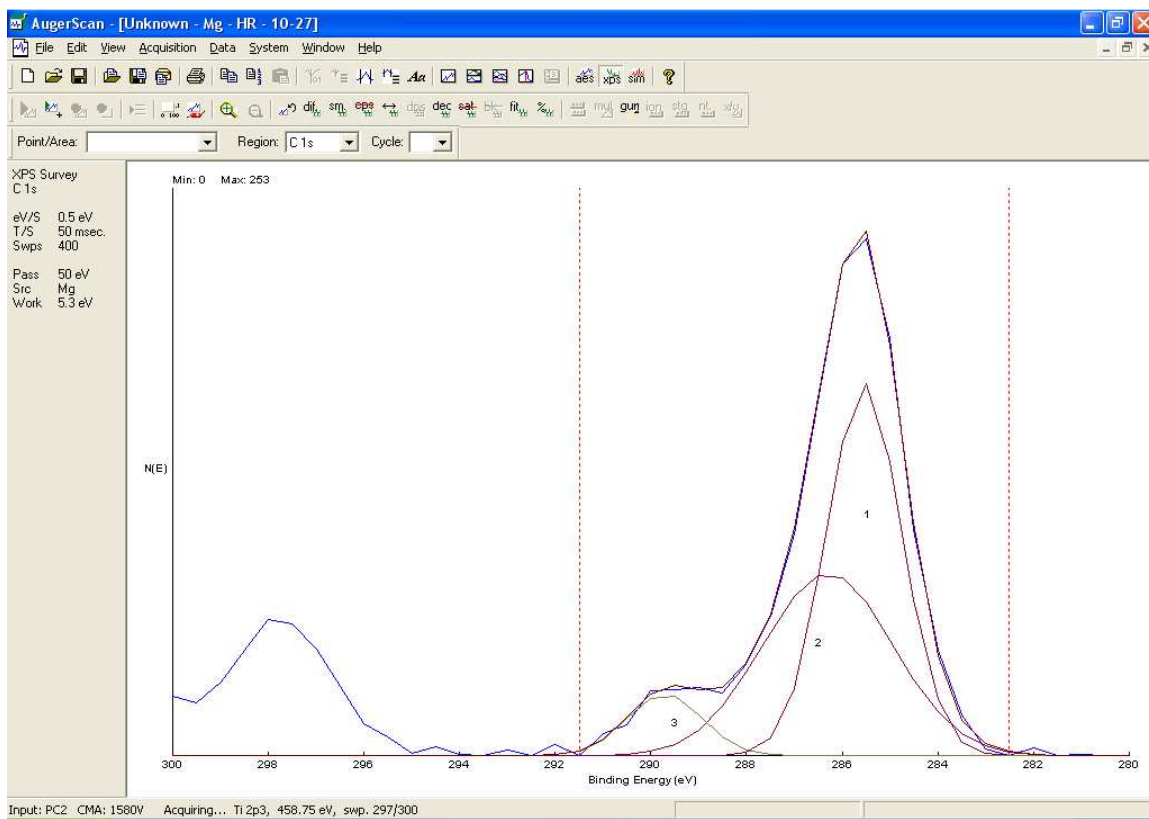
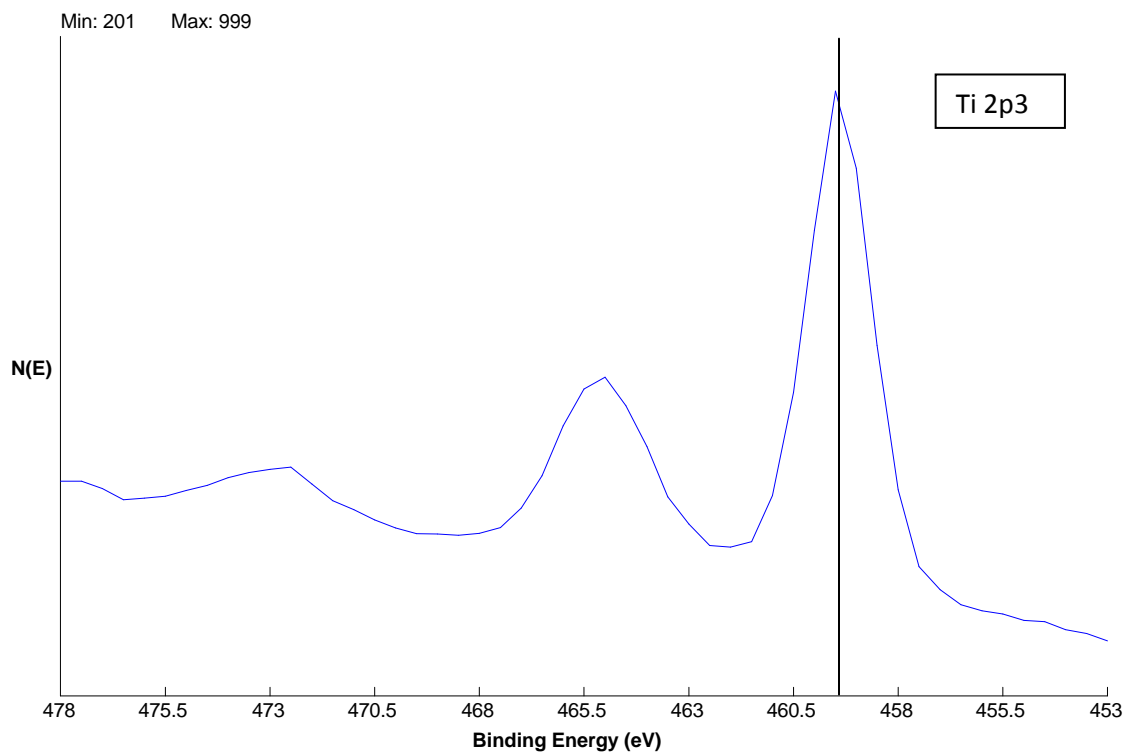
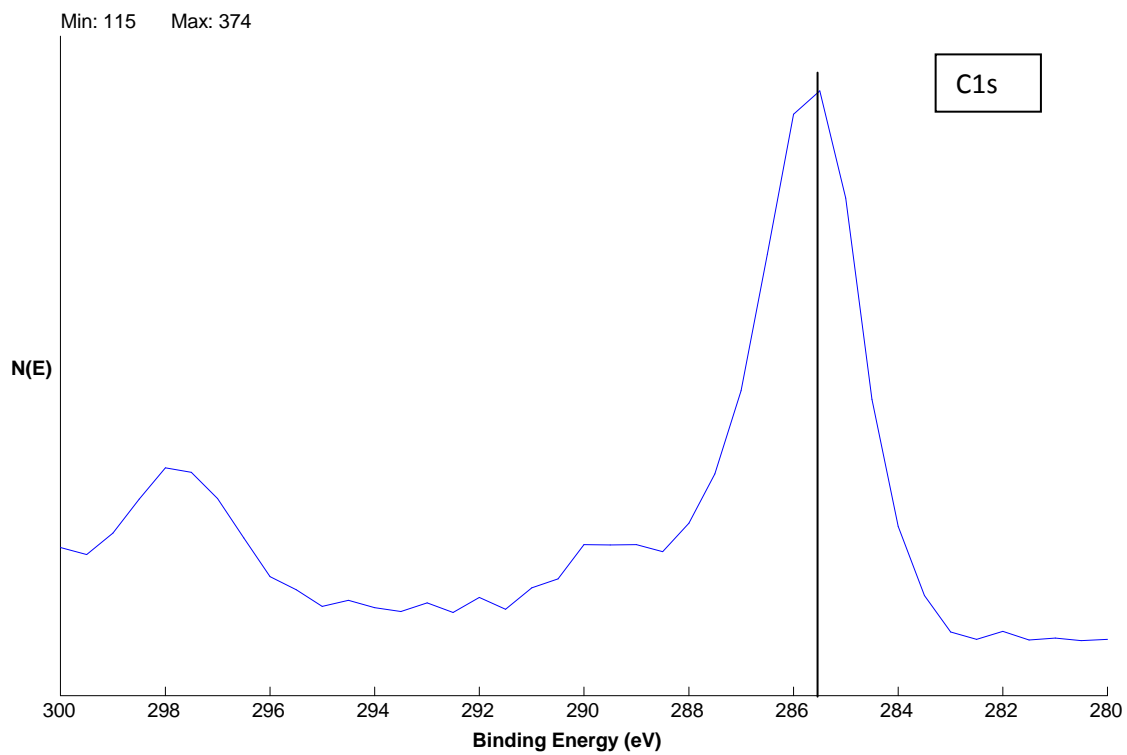


Figure C.1 XPS High Resolution Elemental Survey of Sol-gel Synthesized  $\text{TiO}_2$  Aerogel

### Appendix C (Cont.)



**Figure C.1 (Continued)**

## Appendix D: Additional SEM/FIB Images

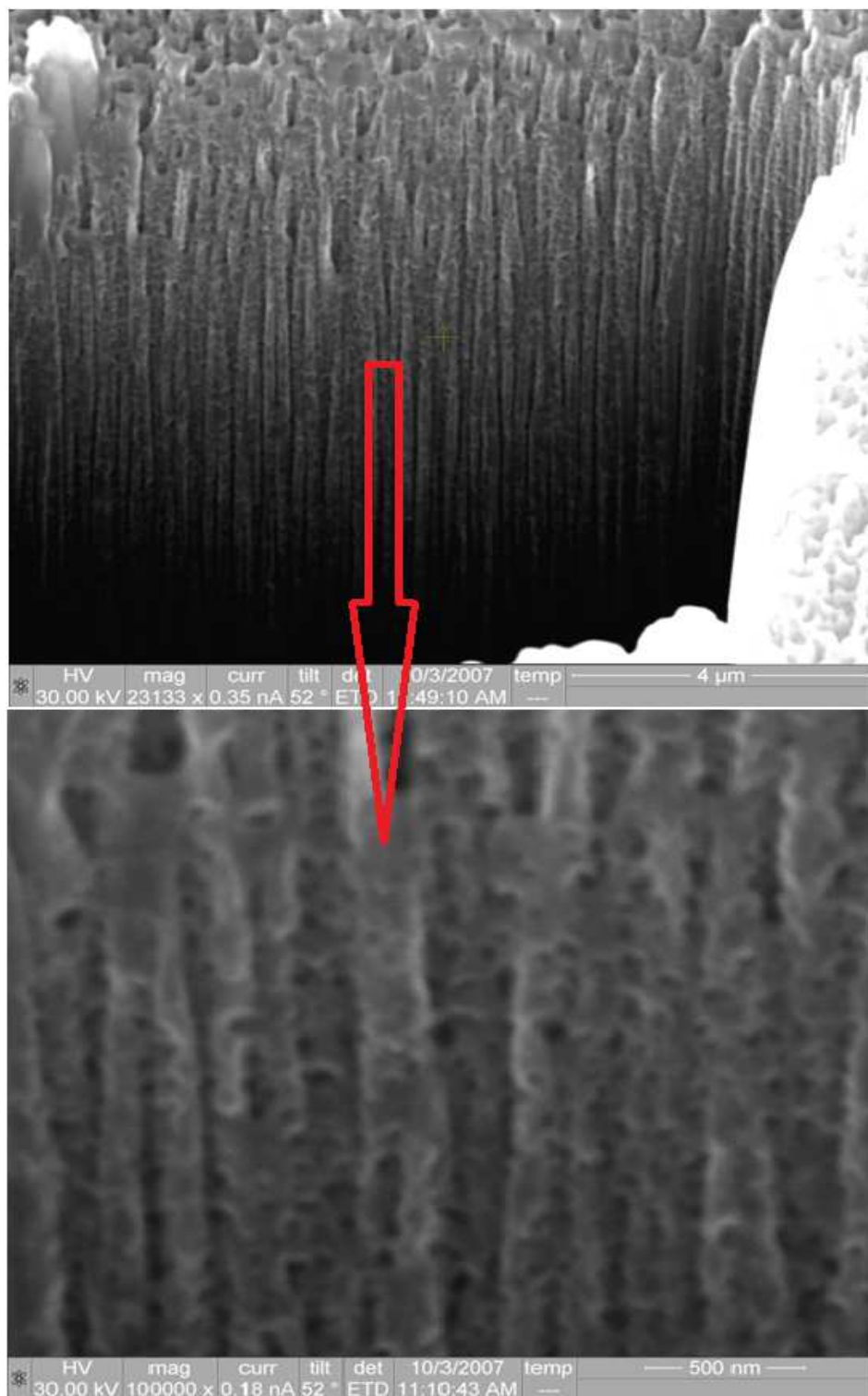


**Figure D.1 SEM-FIB Images of Templated Co-precipitated Aerogel Photocatalyst at Varying Magnifications and Processes**

Appendix D (Cont.)

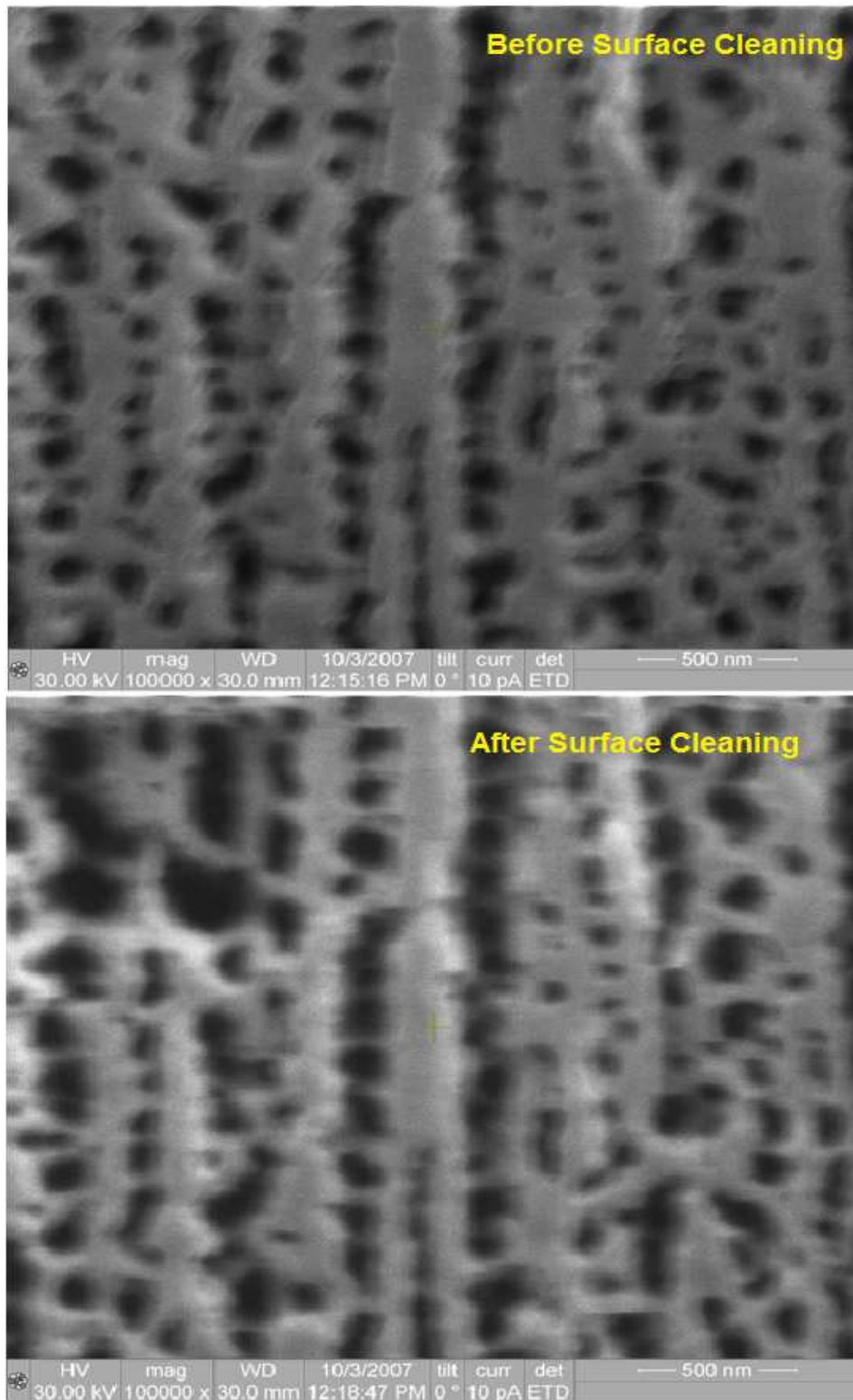


Figure D.1 (Continued)

Appendix D (Cont.)

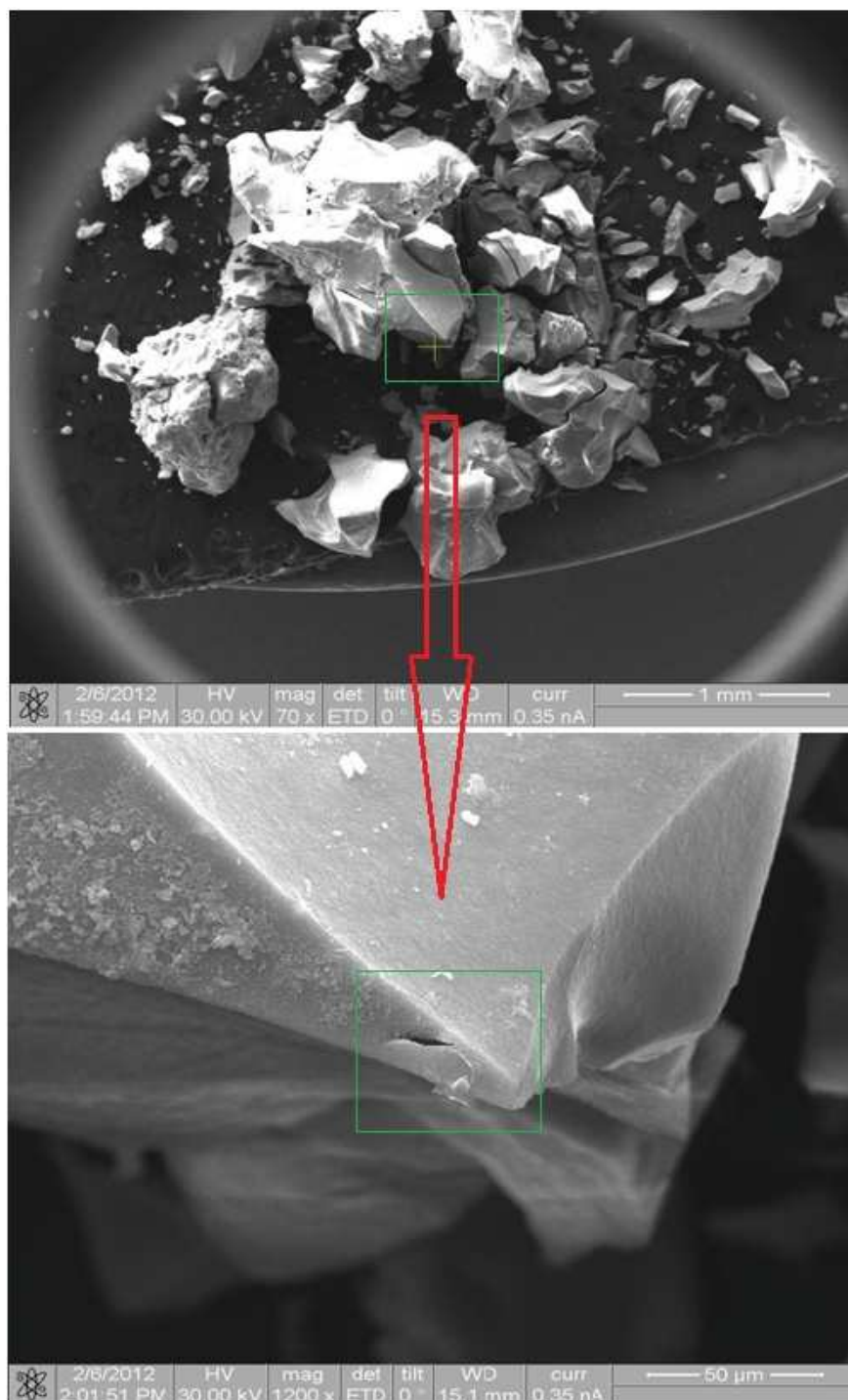


Figure D.2 SEM-FIB Images of Templated Supercritical Impregnated Aerogel Photocatalyst at Varying Magnifications.

Appendix D (Cont.)

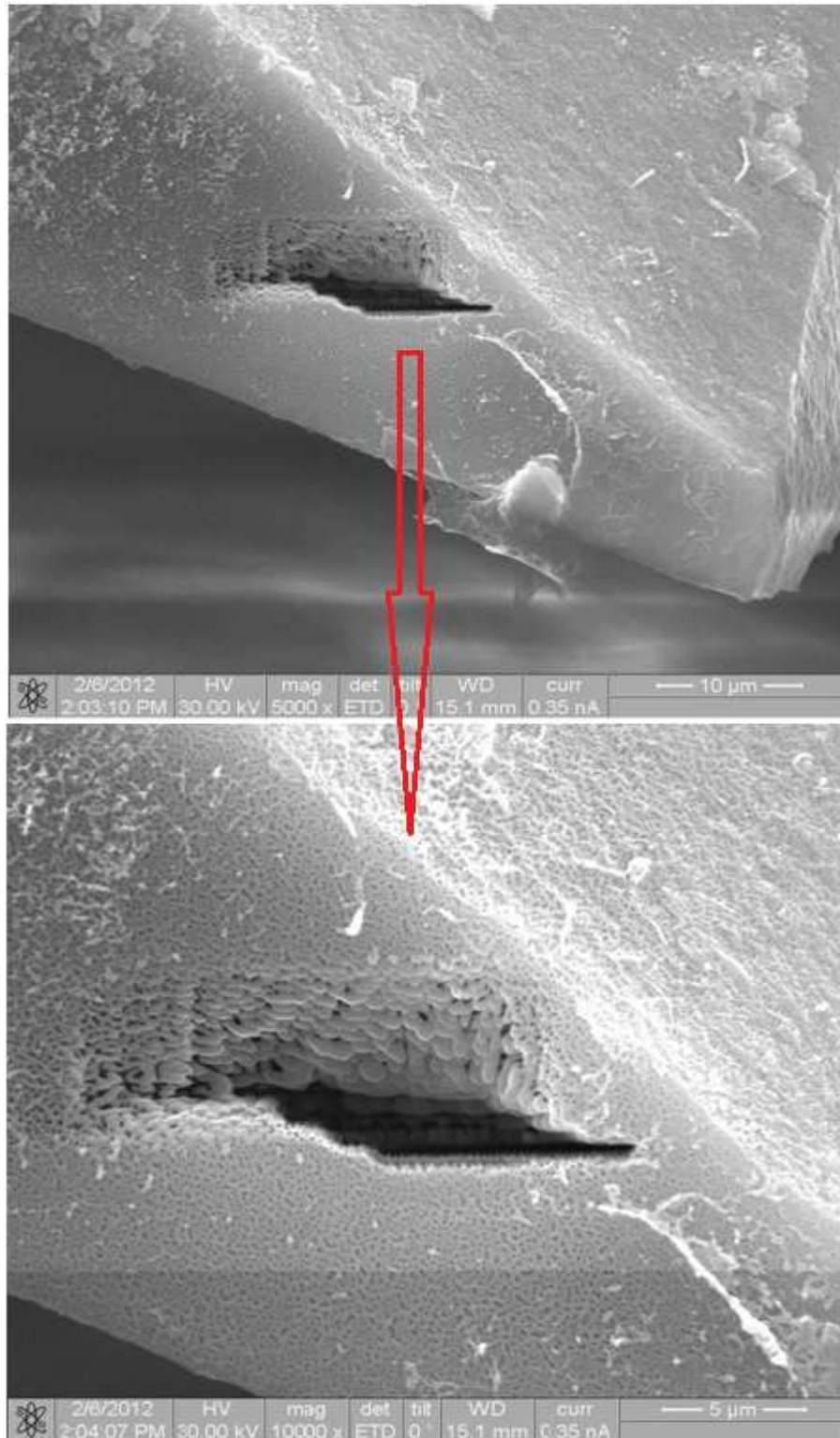


Figure D.2 (Continued)

Appendix D (Cont.)

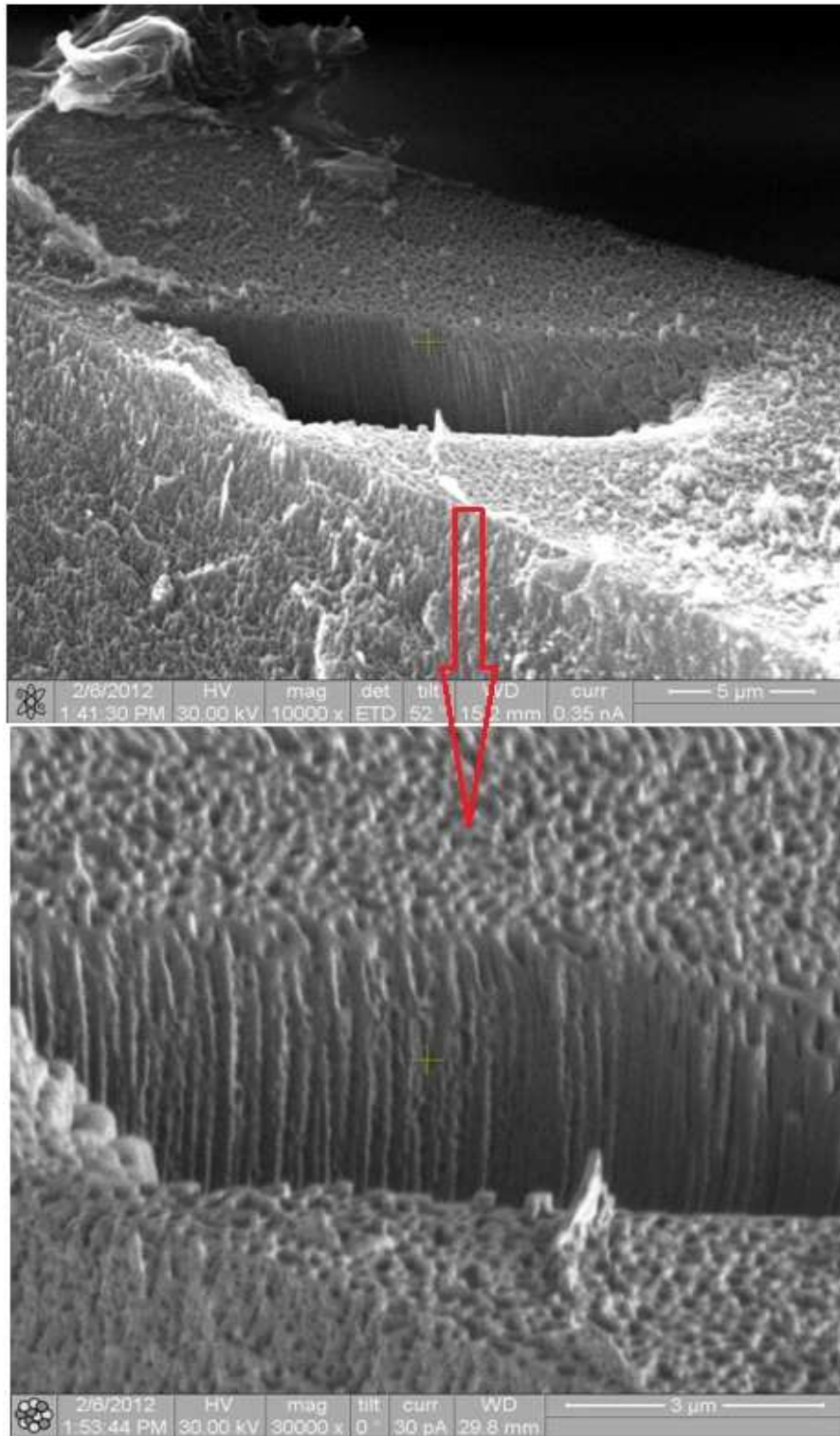


Figure D.2 (Continued)

Appendix D (Cont.)

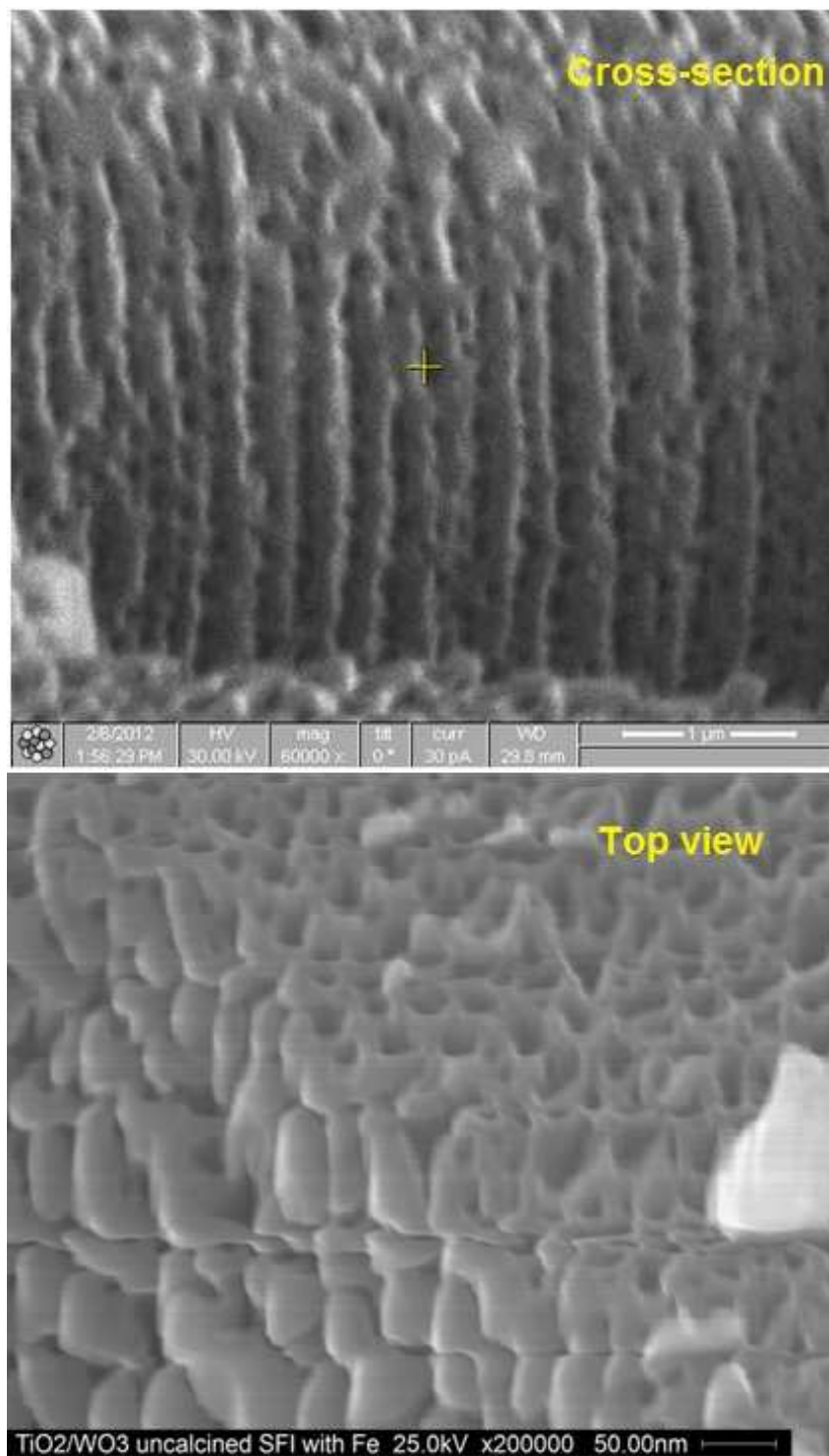


Figure D.2 (Continued)

## Appendix E: Additional XRD Patterns

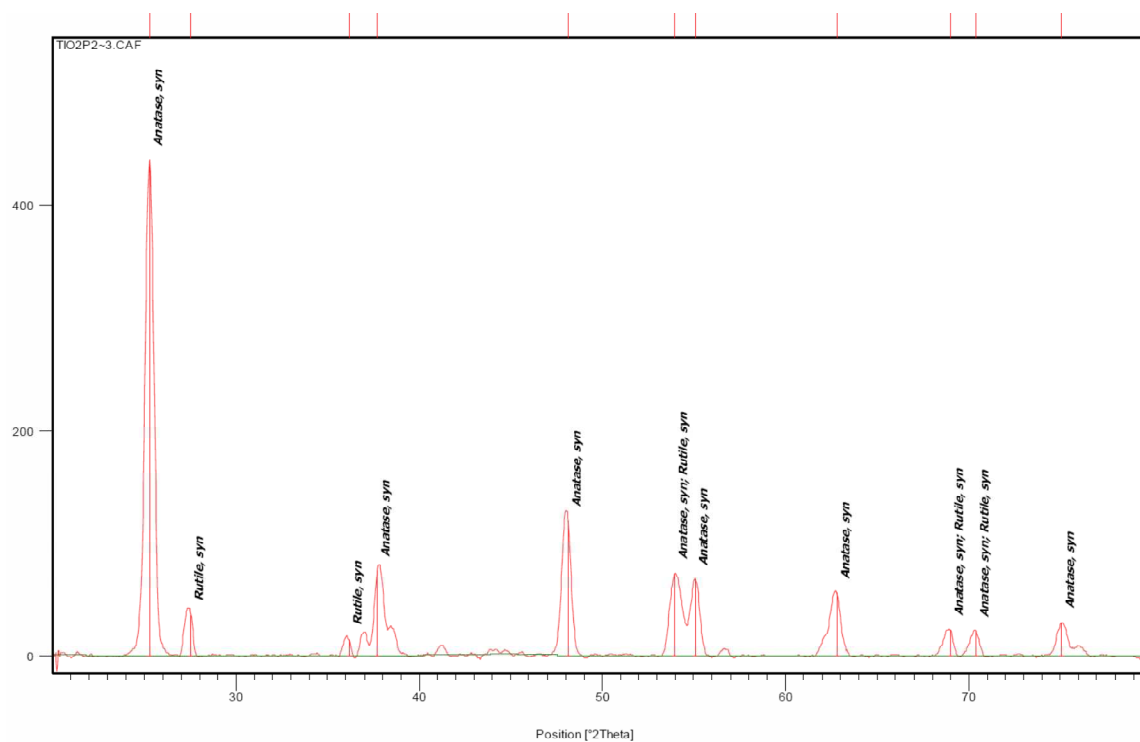


Figure E.1 XRD Pattern of Degussa P25

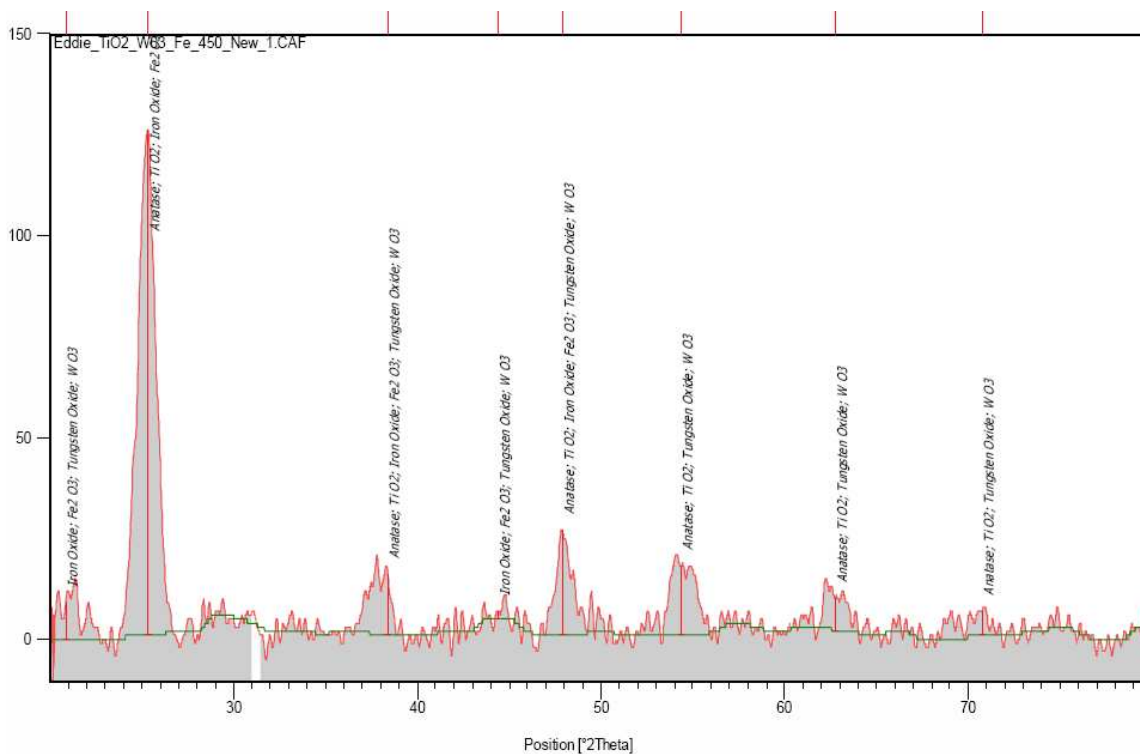


Figure E.2 XRD Pattern of Co-precipitated TiO<sub>2</sub>/WO<sub>3</sub>/Fe<sup>3+</sup> Aerogel after Calcination at 450 °C

## Appendix E (Cont.)

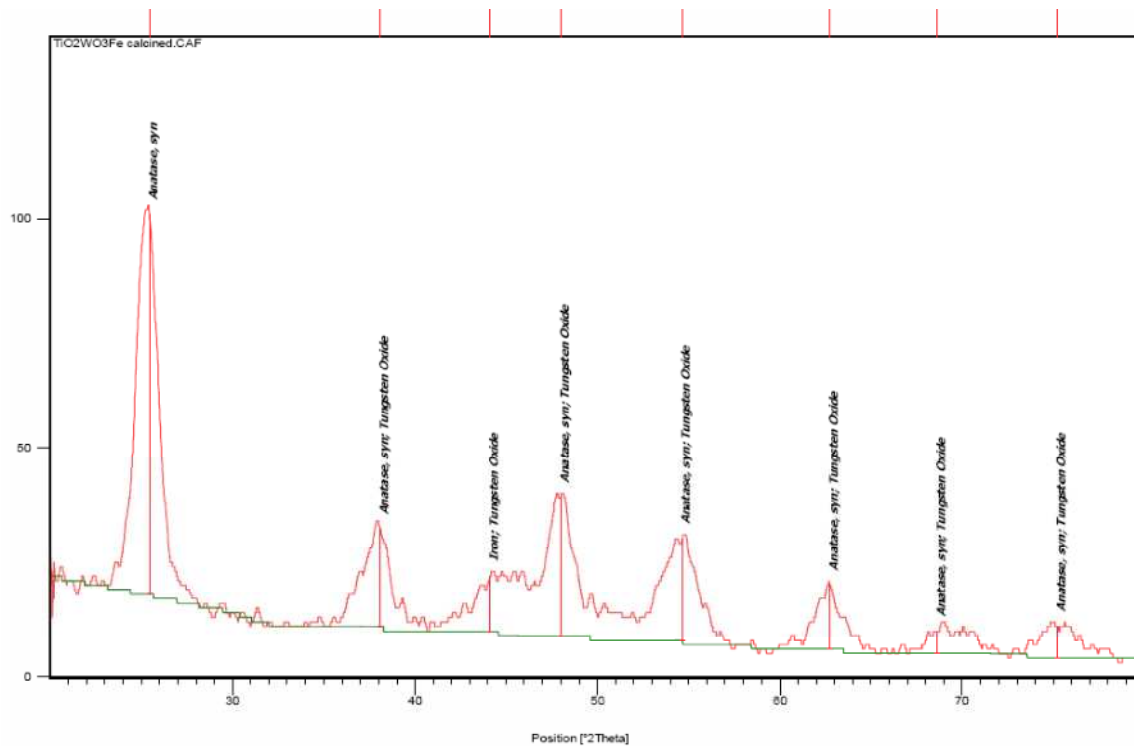


Figure E.3 XRD Pattern of Co-precipitated  $\text{TiO}_2/\text{WO}_3/\text{Fe}^{3+}$  Aerogel after Calcination at 550 °C

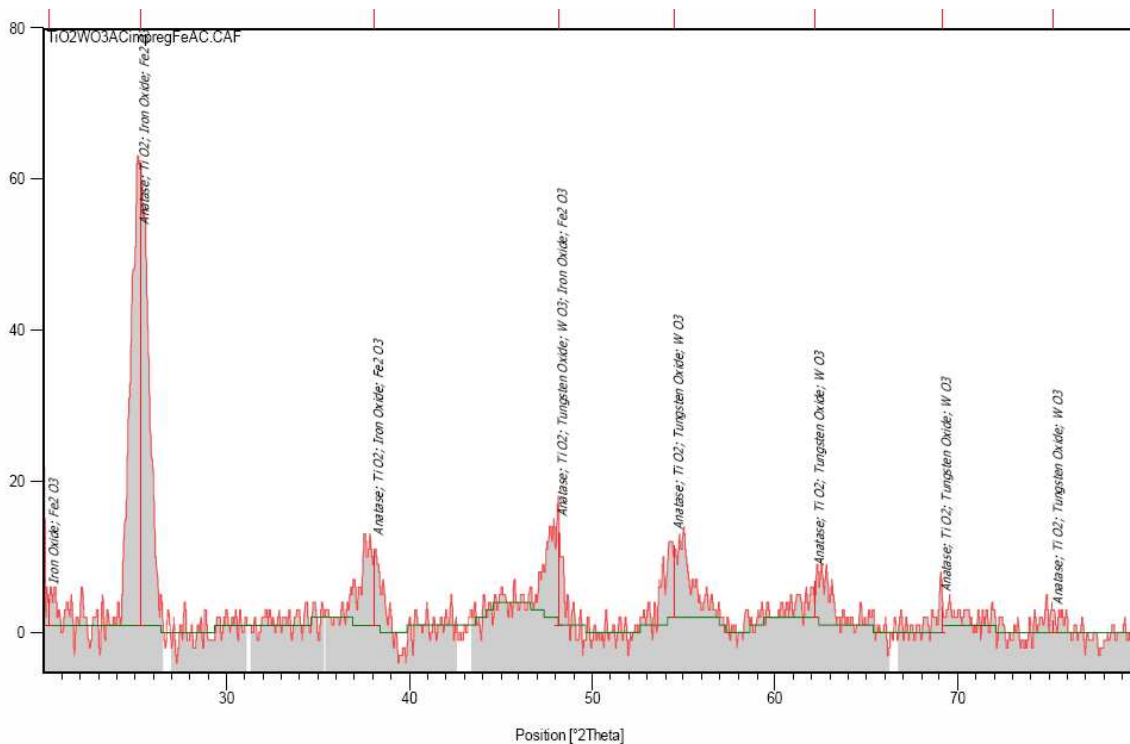


Figure E.4 XRD Pattern of Supercritical Impregnated  $\text{TiO}_2/\text{WO}_3/\text{Fe}^{3+}$  Aerogel after Calcination

## Appendix F Photocatalytic Activity Evaluation

Photocatalytic activity of different photocatalysts under different reaction conditions are listed in here individually.

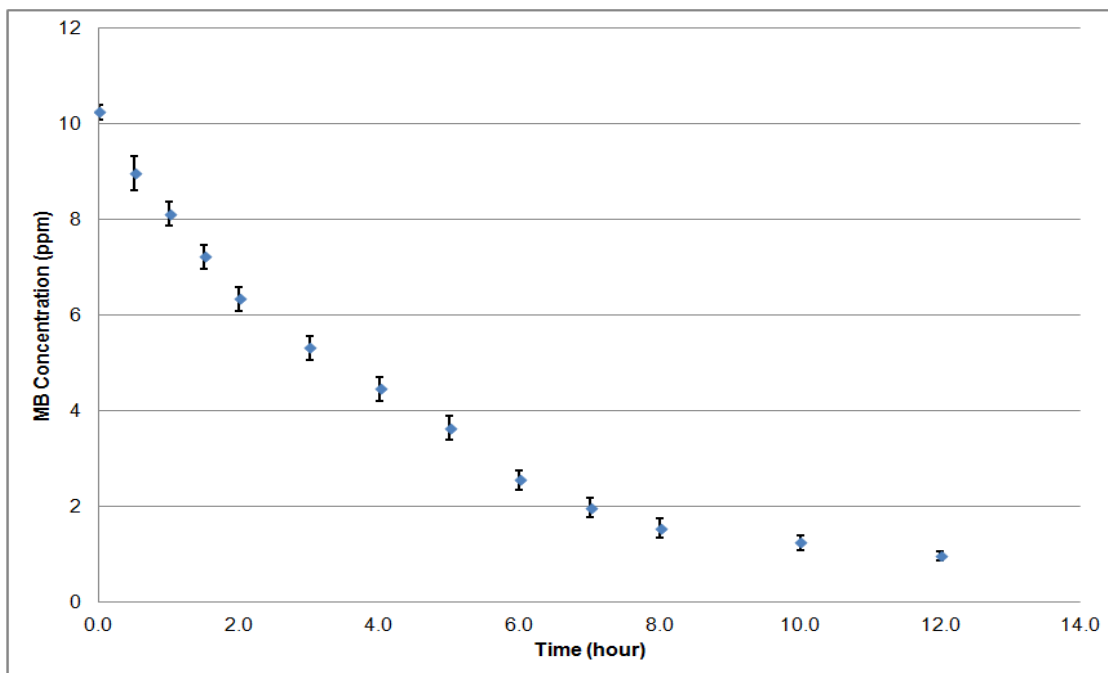


Figure F.1 Methylene Blue Degradation under UV Light with P25

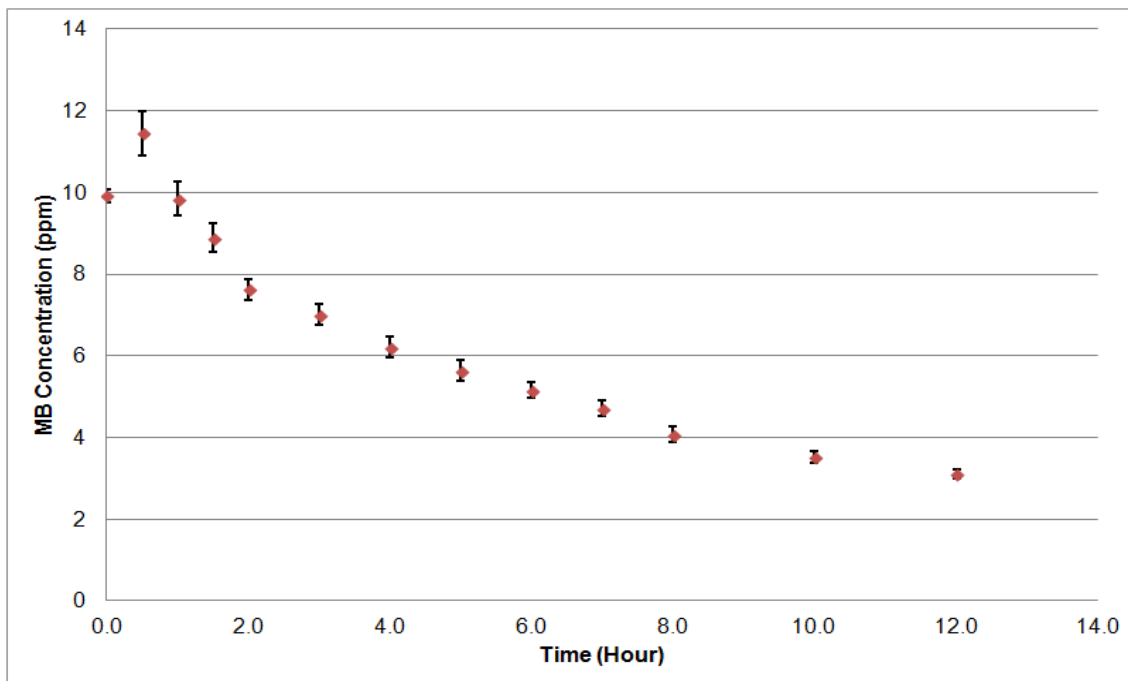


Figure F.2 Methylene Blue Degradation under UV Light with TiO<sub>2</sub> Aerogel

Appendix F (Cont.)

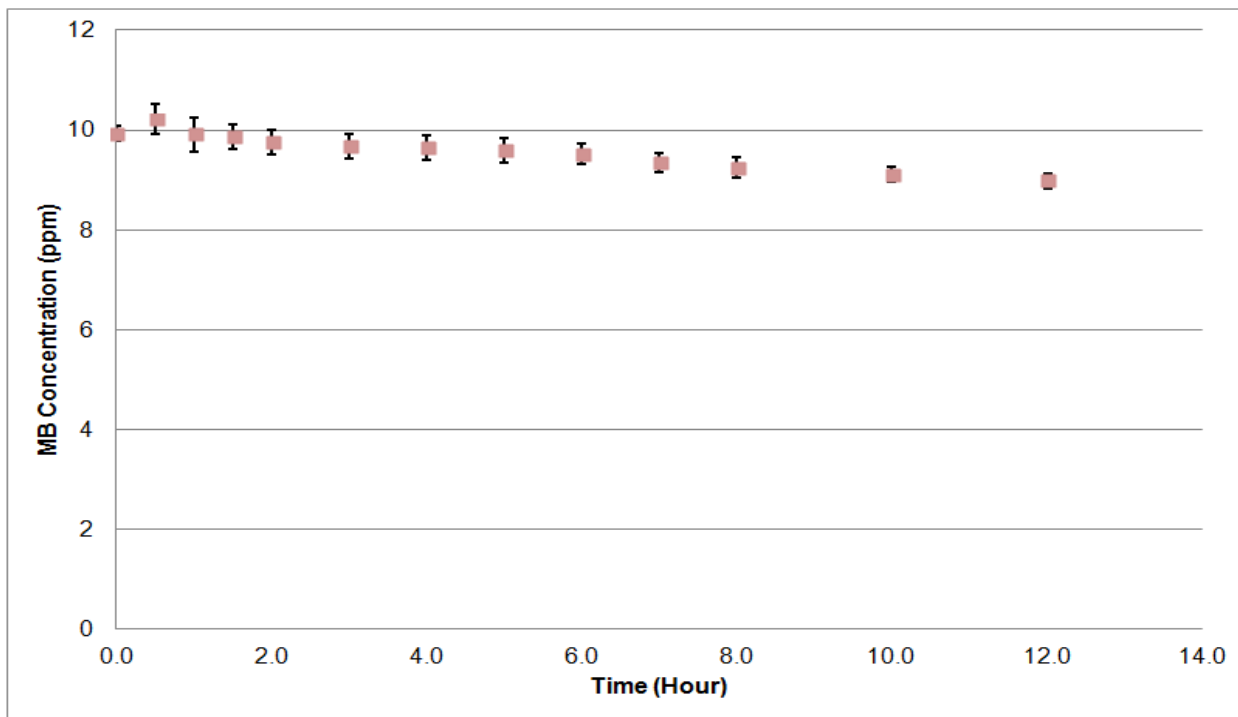


Figure F.3 Methylene Blue Degradation under UV Light with TiO<sub>2</sub>/WO<sub>3</sub> Aerogel

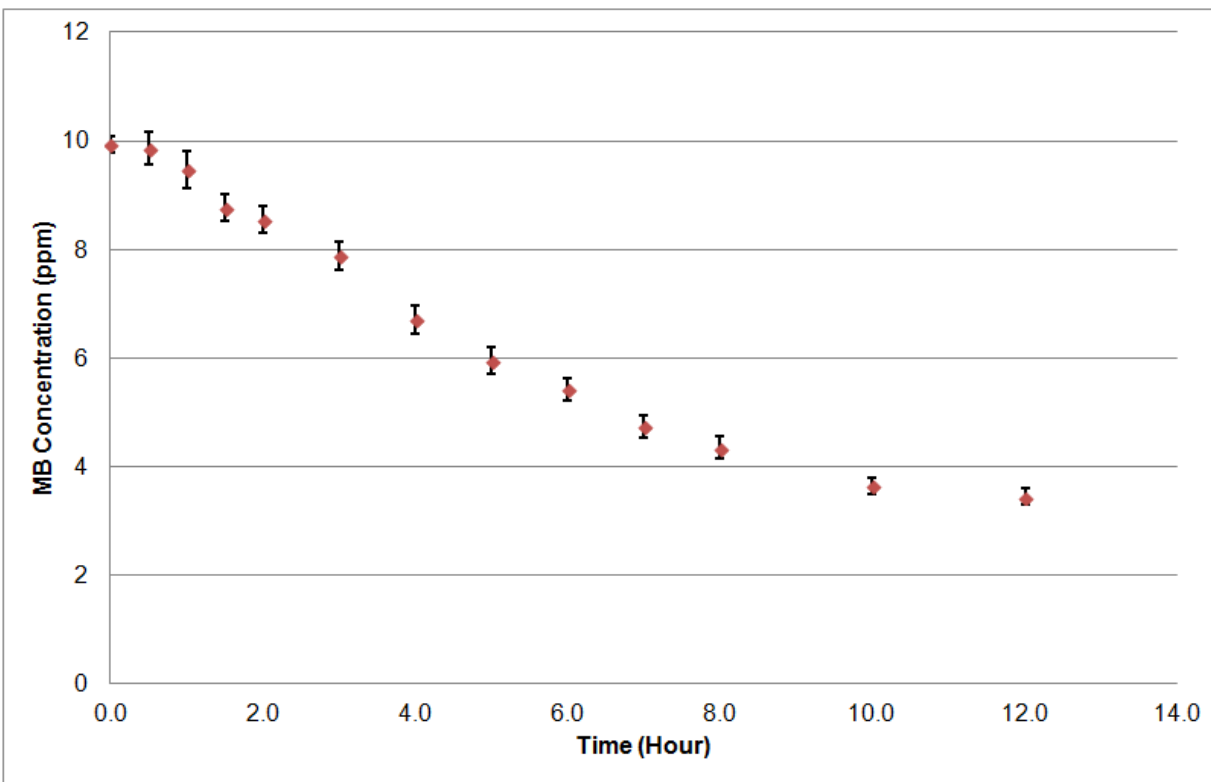


Figure F.4 Methylene Blue Degradation under UV Light with TiO<sub>2</sub>/Fe<sup>3+</sup> Aerogel

Appendix F (Cont.)

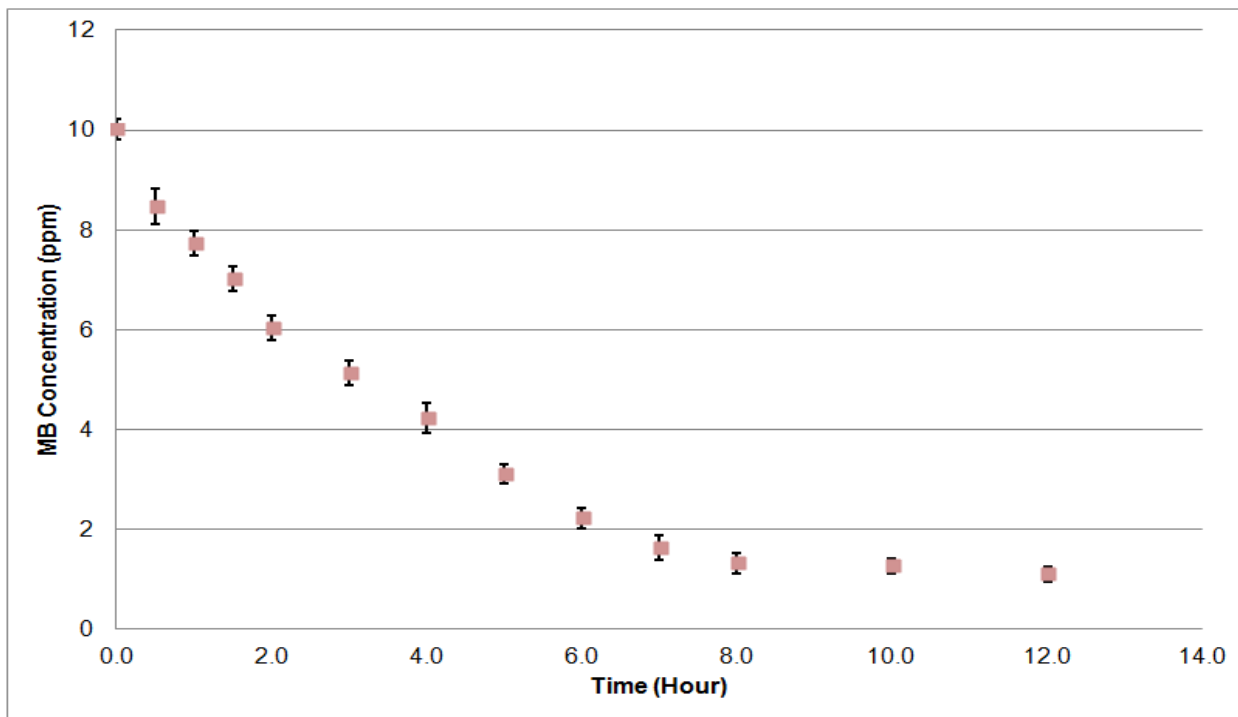


Figure F.5 Methylene Blue Degradation under UV Light with Co-precipitated  $\text{TiO}_2/\text{WO}_3/\text{Fe}^{3+}$  Aerogel

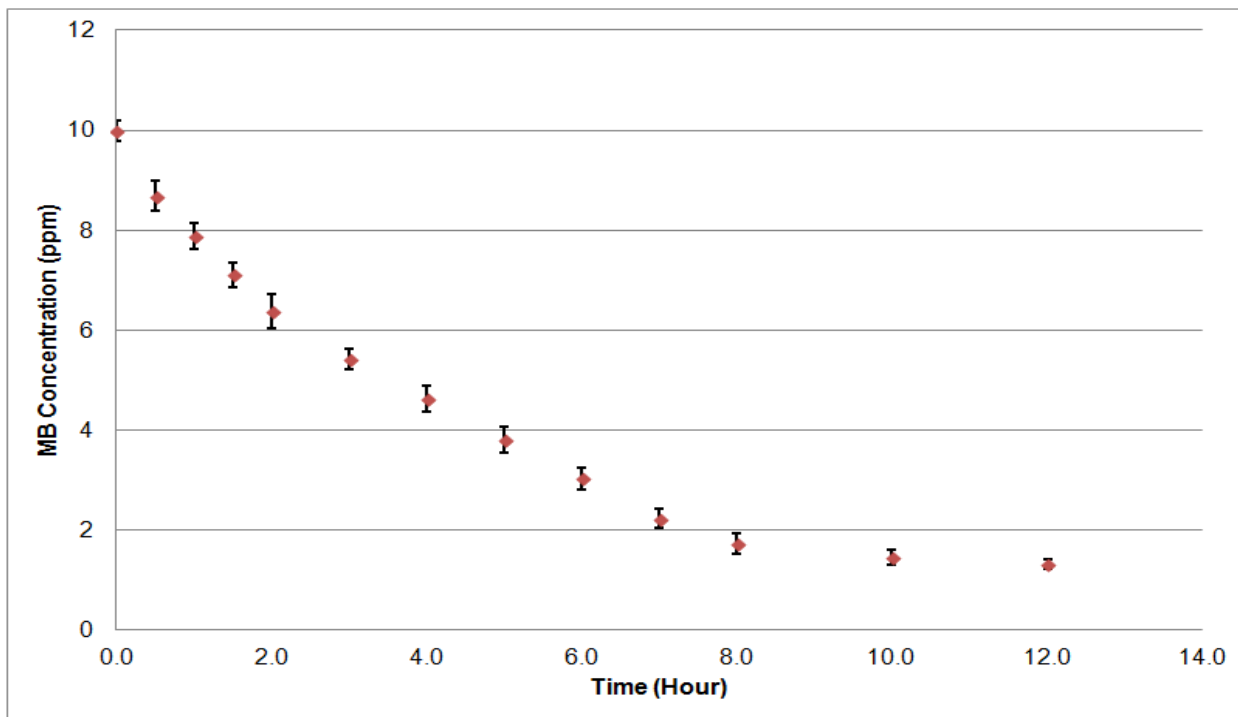


Figure F.6 Methylene Blue Degradation under UV Light with Supercritical Impregnated  $\text{TiO}_2/\text{WO}_3/\text{Fe}^{3+}$  Aerogel

Appendix F (Cont.)

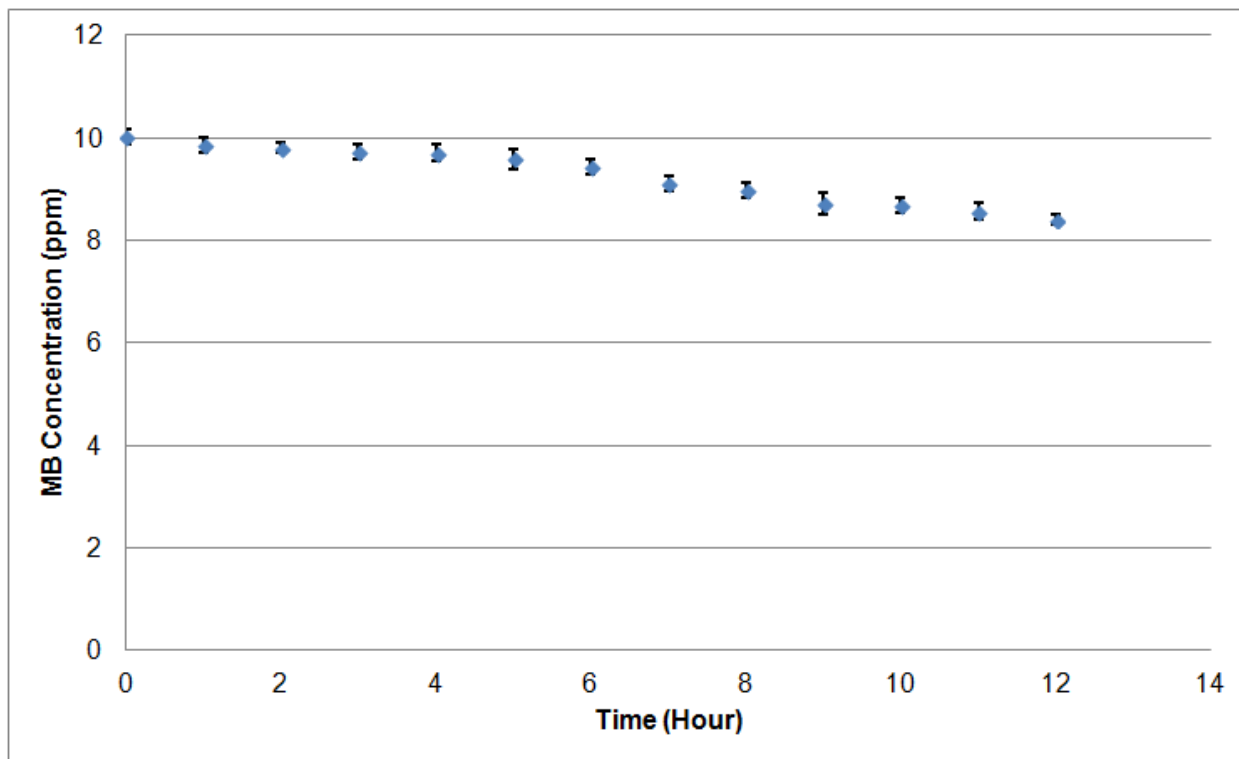


Figure F.7 Methylene Blue Degradation under Visible Light with P25

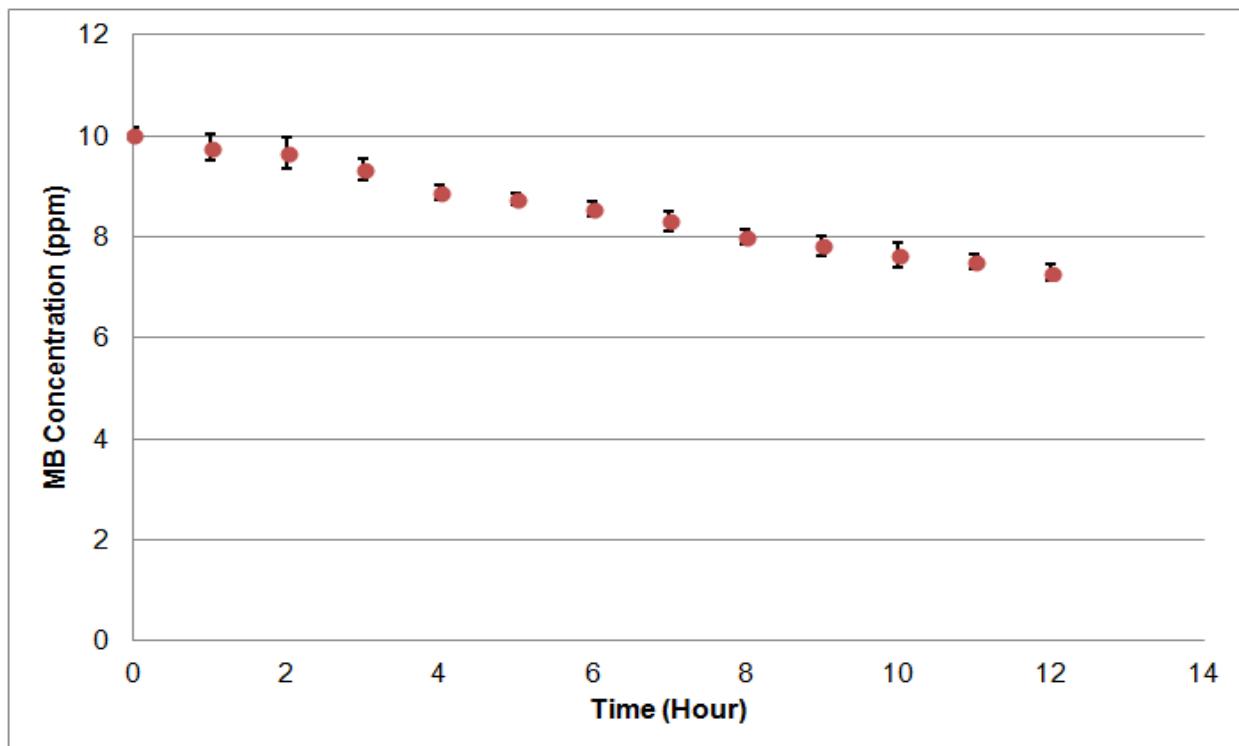


Figure F.8 Methylene Blue Degradation under Visible Light with TiO<sub>2</sub> Aerogel

Appendix F (Cont.)

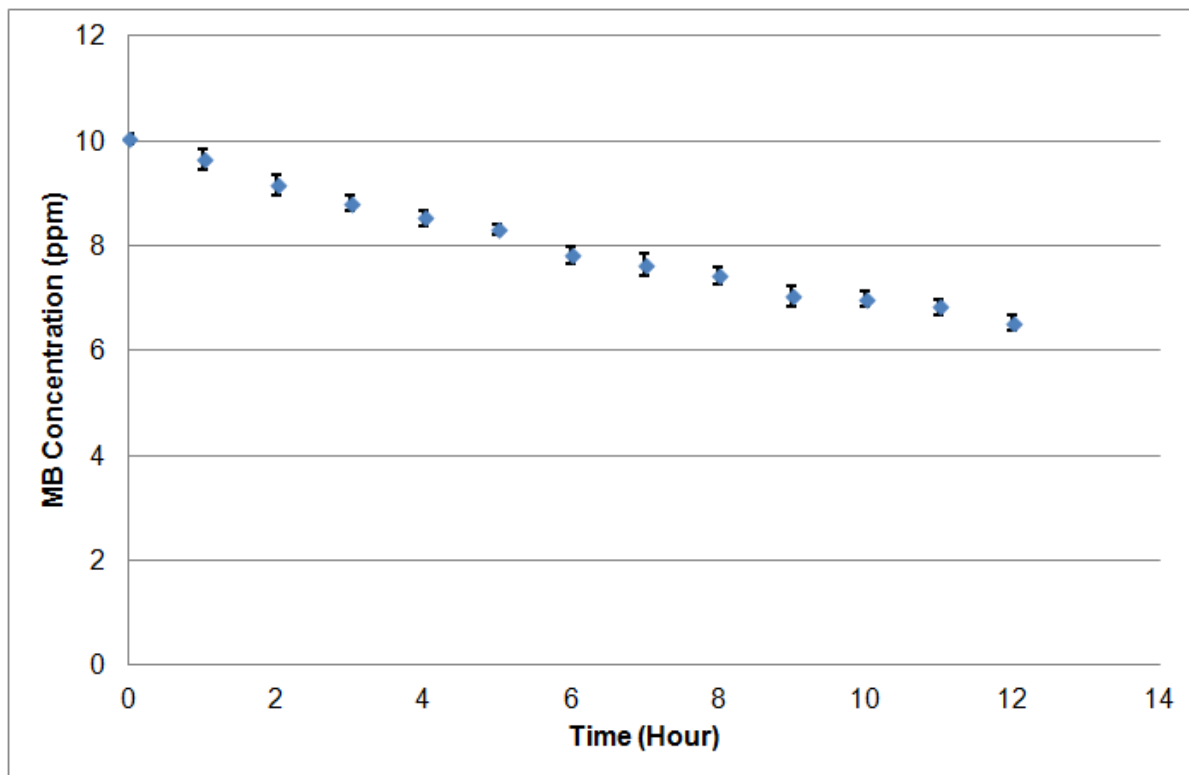


Figure F.9 Methylene Blue Degradation under Visible Light with TiO<sub>2</sub>/WO<sub>3</sub> Aerogel

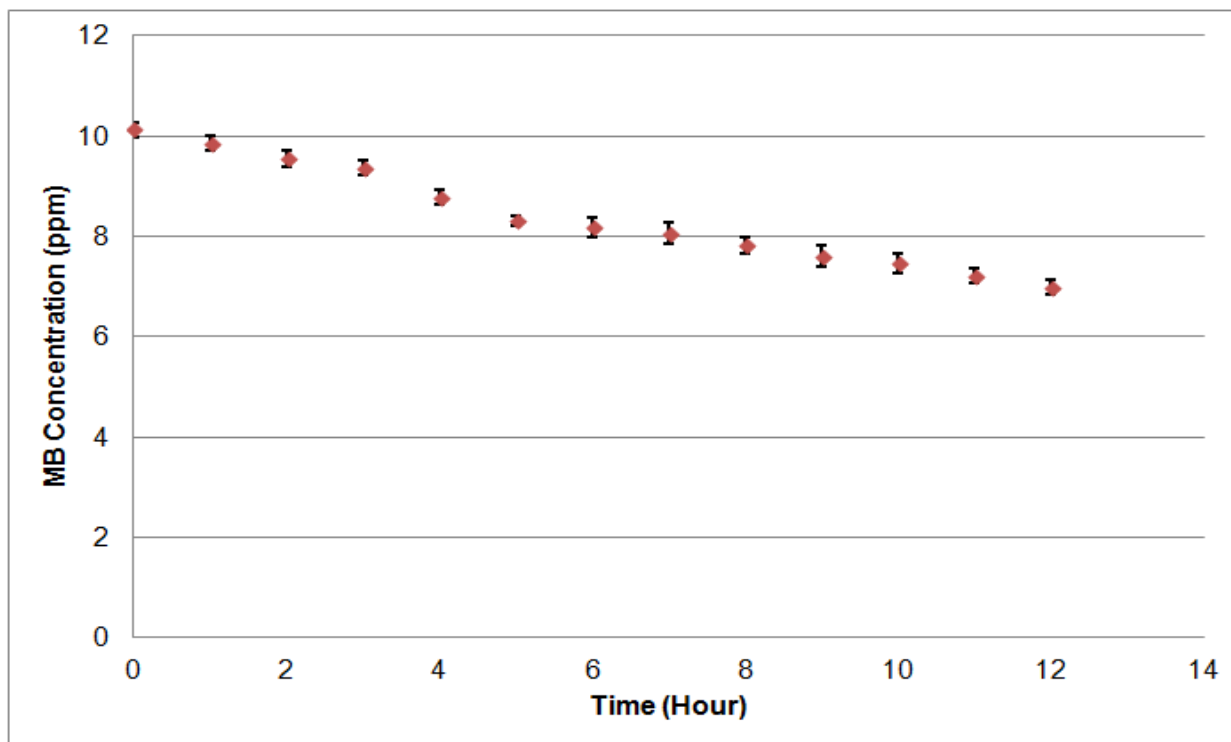


Figure F.10 Methylene Blue Degradation under Visible Light with TiO<sub>2</sub>/Fe<sup>3+</sup> Aerogel

Appendix F (Cont.)

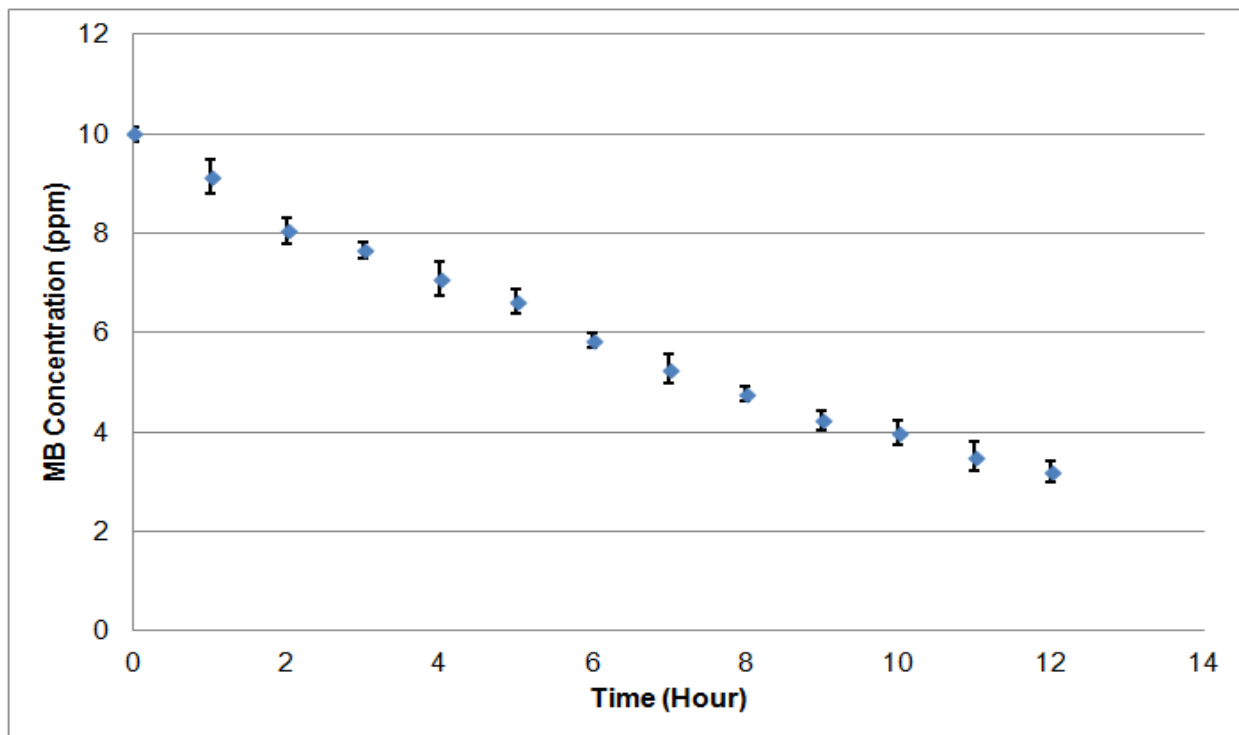


Figure F.11 Methylene Blue Degradation under Visible Light with Co-precipitated  $\text{TiO}_2/\text{WO}_3/\text{Fe}^{3+}$  Aerogel

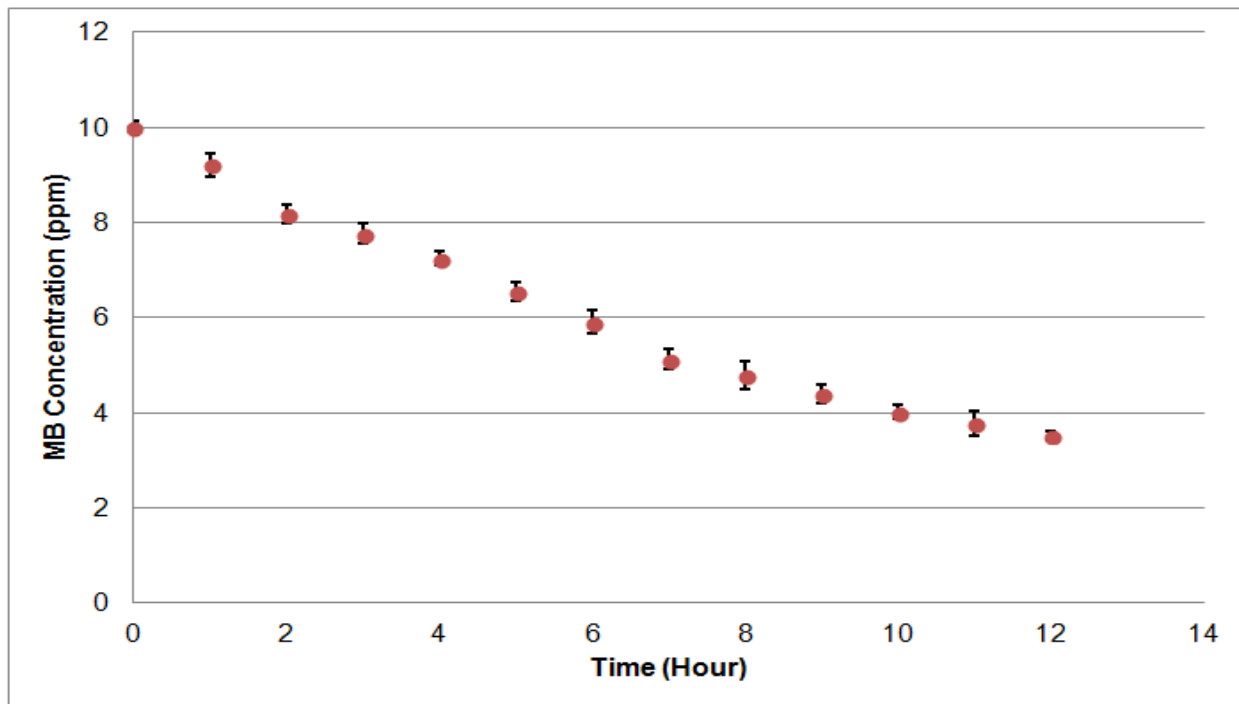


Figure F.12 Methylene Blue Degradation under Visible Light with Supercritical Impregnated  $\text{TiO}_2/\text{WO}_3/\text{Fe}^{3+}$  Aerogel